STUDIES ON HYDRODYNAMICS OF SURFACE AERATION TANKS

Submitted in partial fulfilment of the requirements
for the award of the degree of

Doctor of Philosophy

in

CIVIL ENGINEERING

by

Mr. DEVARAJAN K.

(Roll No. 716111)

Supervisor

Dr. AJEY KUMAR PATEL

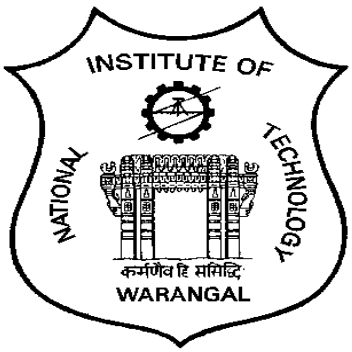

DEPARTMENT OF CIVIL ENGINEERING

NATIONAL INSTITUTE OF TECHNOLOGY WARANGAL

WARANGAL-506004, TELANGANA, INDIA

2022

DEDICATED

TO

MY PARENTS

APPROVAL SHEET

This Dissertation Work entitled **"Studies on Hydrodynamics of Surface Aeration Tanks"** by **Mr. Devarajan K** is approved for the degree of Doctor of Philosophy

Examiners

_____

_____

_____

Supervisor

Dr. Ajey Kumar Patel

Associate Professor

Department of Civil Engineering, NIT Warangal

Chairman

Professor & Head

Department of Civil Engineering, NIT Warangal

Date:_____ Place:_____

NATIONAL INSTITUTE OF TECHNOLOGY WARANGAL

CERTIFICATE

This is to certify that the thesis entitled **"Studies on Hydrodynamics of Surface Aeration Tanks"** being submitted by **Mr. Devarajan K.** for the award of the degree of Doctor of Philosophy (Ph.D) in Civil Engineering to the National Institute of Technology Warangal, India is a record of the bonafide research work carried out by him under my supervision. The thesis has fulfilled the requirements according to the regulations of this Institute and in my opinion has reached the standards for submission. The results embodied in the thesis have not been submitted to any other University or Institute for the award of any degree or diploma.

Date:

Dr. Ajey Kumar Patel

Thesis Supervisor

Associate Professor

Department of Civil Engineering,

National Institute of Technology Warangal

DECLARATION

This is to certify that the work presented in the thesis entitled **"Studies on Hydrodynamics of Surface Aeration Tanks"** is a bonafide work done by me under the supervision of Dr. Ajey Kumar Patel and was not submitted elsewhere for the award of any degree.

I declare that this written submission represents my ideas in my own words and where others' ideas or words have been included, I have adequately cited and referenced the original sources. I also declare that I have adhered to all principles of academic honesty and integrity and have not misrepresented or fabricated or falsified any idea/data/fact/source in my submission. I understand that any violation of the above will be a cause for disciplinary action by the institute and can also evoke penal action from the sources which have thus not been properly cited or from whom proper permission has not been taken when needed.

Mr. Devarajan K.

Roll No. 716111

Date:

Abstract

The present study analyses the physical reasons causing variation in the performance goals and flow pattern associated with circular baffled surface aeration tanks under various geometric and dynamic conditions using the Computational Fluid Dynamics (CFD) technique for the optimal design of aeration vessels. The Reynolds Averaged Navier Stokes (RANS) approach with standard k-ε turbulence model closure was adopted for modelling the flow field characteristics. The impeller rotation was modelled using the Multiple Reference Frame (MRF) technique and the entrainment of air into the reactor vessels was modelled using implcit Volume of Fluid (VOF) method.

The numerical errors arising from grid resolution, grid type and numerical discretization scheme were properly minimized in the present study. The hybrid grid outperforms the tetrahedral grid for modelling the surface aeration tank. The second order upwind scheme provides accurate prediction of flow field which are comparable with third order schemes. The radial and axial extents of MRF boundary were varied in the tank domain and optimal extents of the same were found. The proper balance between the power number computed from the torques of impeller and tank periphery was derived as the general criterion for selecting the optimal position of MRF boundary. The predictions from the completely verified CFD model matched closely with the corresponding results from the experimental studies and LES model respectively.

The tank parameters such as impeller clearance, tank diameter, impeller speed, number of blades and number of baffles were varied and the respective influence on the flow field and performance goals were analysed. The standard reactor vessel working in the turbulent regime develops double loop pattern and large trailing vortices behind the blades. On the other hand, the low clearance vessels, high clearance vessels and the vessels with large diameter generates distinct low pressure region around the impeller which results in single loop pattern and small trailing vortices behind the blades. The small trailing vortices provide weak flow separation region behind the blades which results in small impeller form drag and power number as compared to the standard reactor vessel. The high clearance vessels and the standard reactor vessel agitated at high impeller speeds produces high vortex and turbulence activity near the free liquid surface which deforms the same and increases the oxygen transfer into the aeration vessels. The double loop pattern produces bulk mixing of the fluid while the single loop

pattern provides localized mixing either near bottom or top surfaces of the reactor vessels. Thus, the distribution of pressure and trailing vortices surrounding the impeller controls the flow pattern and power characteristics of the aeration vessels. The aeration tank with four baffles and the Rushton Turbine (RT) impeller with six blades were found to be optimal for the mixing purposes due to the development of high vortex and turbulence activity in the reactor vessels.

Contents

List of Figures

List of Tables

Abbreviation Notation and Nomenclature

AFT	Adaptive Force Field Technique
AIAA	American Institute of Aeronautics and Astronautics
ASM	Algebraic Stress Model
ASME	American Society of Mechanical Engineers
ASP	Activated Sludge Process
BOD	Biochemical Oxygen Demand
CARPT	Computer Automated Radioactive Particle Tracking
CFD	Computational Fluid Dynamics
CSM	Continuum Surface Force Model
DES	Detached Eddy Simulation
DNS	Direct Numerical Simulation
DT	Disc Turbine
EASM	Explicit Algebraic Stress Model
GCI	Grid Convergence Index
IBC	Impeller Boundary Condition
IO	Inner-Outer
LDA	Laser Doppler Anemometry
LDV	Laser Doppler Velocimetry
LES	Large Eddy Simulation
MRF	Multiple Reference Frame
MUSCL	Monotone Upwind Scheme for
PBTD	Pitched Blade Down flow Turbine
PEPT	Positron Emission Particle Tracking
PIV	Particle Image Velocimetry
QUICK	Quadratic Upwind Interpolation scheme for Convective Kinetics
RANS	Reynolds Averaged Navier Stokes
RNG	Re-Normalization Group
RSM	Reynolds Stress Model
RT	Rushton Turbine
SAS	Scale Adaptive Simulation
SM	Sliding Mesh

SS	Source Sink
SST	Shear Stress Transport
VOF	Volume of Fluid
V&V	Verification & Validation

Acronyms

A	Cross-sectional area of the vessel
a	Rate of decay of $\frac{u_r}{u_{tip}}$ in the discharge stream of impeller
B	Width of baffle walls
b	Width of impeller blades
C_p	Pressure coefficient
$C_{1\varepsilon}$, $C_{2\varepsilon}$, $C_{3\varepsilon}$, C_μ	Model constants
D	Diameter of the impeller
d	Diameter of reactor vessel
D_r	Radial extent of MRF boundary
D_r^*	Optimal radial extent of MRF boundary
e	Gas hold-up
e_r	Absolute relative error
F	Froude number
F_s	Factor of safety
F_σ	Surface tension force
F_B	Body force (Coriolis and Centrifugal forces)
F_g	Gravitational force
f_1, f_2, f_3	Flow field solutions from fine, medium and coarse grids
G	Vorticity
G_k	Generation of turbulent kinetic energy from mean velocity gradients
G_b	Generation of turbulent kinetic energy from buoyancy
g	Acceleration due to gravity
H	Depth of water
H_D	Height of liquid in the presence of gas
H	Height of liquid in the absence of gas
H_r	Axial extent of MRF boundary

H_r^*	Optimal axial extent of MRF boundary
h	Clearance of the impeller from bottom surface of the vessel
$K_L a_{20}$	Volumetric oxygen transfer coefficient
k	Turbulent kinetic energy
k_p	Peak turbulent kinetic energy
k^*	Non-dimensional oxygen transfer parameter
L	Number of elements of blade
l	Length of impeller blades
M	Number of elements or control volumes
$\dot{m}_{pq}$	Mass transfer from p^{th} phase to q^{th} phase
$\dot{m}_{qp}$	Mass transfer from q^{th} phase to p^{th} phase
N	Rotational speed of the RT impeller
N_{bl}	Number of blades of the impeller
N_{bf}	Number of baffle walls of tank
N_p	Power number
N_{pt}	Power number computed from torque of rotating or stationary walls
$N_{pt}-imp$	N_{pt} computed from torques of rotating walls
$N_{pt}-baff$	N_{pt} computed from torques of stationary walls
$N_{p\varepsilon}$	Power number computed from volume integrated turbulence dissipation rate
N_q	Pumping number
P'	Impeller power drawn
p	Pressure
p_f	Formal order of accuracy of discretization scheme
$\hat{p}$	Observed order of accuracy
Q_r	Volume flow rate in the radial direction
R	Radius of impeller
R_e	Reynolds number
R^*	Convergence ratio
r	Radial direction
r^*	Normalized radial distance
r'	Grid refinement factor
S	Strain rate

$\|\|S\|\|$	Euclidean norm of strain rate tensor
S_k, S_ε	User defined source terms
$S_{\alpha q}$	Mass source term
TI	Turbulence intensity
t	Time
u	Velocity of flow
u_r	Mean radial velocity
u_{rp}	Peak mean radial velocity
u_t	Mean tangential velocity
u_{tp}	Peak mean tangential velocity
u_a	Mean axial velocity
u_{tip}	Impeller tip velocity
u_q	Velocity of q^{th} phase
v_{32}	Difference between f_3 and f_2
v_{21}	Difference between f_2 and f_1
$\|\|w\|\|$	Euclidean norm of rotation rate tensor
x	Spatial coordinate
Y_M	Contribution of fluctuating dilatation in compressible turbulence to the overall turbulence dissipation rate
z	Axial direction
z^*	Normalized axial distance

Greek letters

β	Rate of decay of $\frac{u_t}{u_{tip}}$ in the discharge stream of impeller
ρ_a	Density of air
ρ_w	Density of water
ρ_q	Density of a fluid phase q under consideration
ϑ	Kinematic viscosity of water
ε	Turbulent dissipation rate
μ	Dynamic viscosity of fluid
μ_t	Turbulence viscosity
δ_{ij}	Kronecker delta

$-\rho_q \overline{u_i' u_j'}$	Reynolds stress
$\sigma_k, \sigma_\varepsilon$	Turbulent Prandtl numbers
ω	Turbulence eddy frequency
α_q	Volume fraction of q^{th} phase
τ	Net torque on the impeller blades
θ	Tangential direction
Ω	Angular speed of impeller

Chapter 1

Introduction

1.1 Wastewater treatment- an overview

Wastewater treatment is the process by which contaminants in the wastewater is removed to enhance its quality so that the resulting effluent can be safely discharged into the water bodies without causing any negative impacts on the ecosystem. Based on the source of generation, wastewater can be classified into four categories viz. domestic wastewater (also called sewage or municipal wastewater), industrial wastewater, agricultural wastewater and leachate from the sanitary landfills. Appropriate treatment plants are installed and operated to treat each type of wastewater. The industrial wastewater is treated either in industrial wastewater treatment plant or in the sewage treatment plant itself after necessary pre-treatment process (Peavy et al. 1985). The wastewater treatment has mainly four stages viz., preliminary treatment, primary treatment, secondary treatment and tertiary treatment respectively. In the preliminary treatment, the larger materials (debris, gravel, sand) which can cause operational difficulties are removed while in the primary treatment, finer solids, oil and grease content present in the wastewater are removed. In the secondary treatment process, organic matter dissolved in the wastewater is converted into sludge using aerobic or anaerobic techniques and the sludge is then properly digested and disposed. The treated wastewater after the secondary treatment process is disinfected using chlorination or ultraviolet irradiation methods in the final treatment and then discharged into the water bodies or reused for any specific purposes (JBA 2010).

During the past century, considerable research works in the field of wastewater treatment has led to significant improvements in the Activated Sludge Process (ASP) which is regarded as the standard for biological secondary wastewater treatment process (Karpinska and Bridgeman 2018). The ASP mainly consists of a bioreactor called aeration tank in which the treatment occurs, a secondary clarifier for separating the harmless solid particles after the treatment and sludge recycle system for providing active micro-organisms from the clarifier back to the aeration tank for uninterrupted treatment process. The wastewater from the primary treatment units is carried to the aeration tank in which intimate contact is developed between particulate and suspended organic matter with the sludge re-circulated from the secondary clarifier. This sludge consists of actively growing micro-organisms which convert the organic matter present in the wastewater into sludge in the presence of oxygen (Peavy et al. 1985). The air is introduced into the wastewater either through the surface aeration system or as bubbles through the diffused aeration system. The micro-organisms present in the re-circulated sludge consume the oxygen available in the air for converting the organic matter present in the wastewater into stable, low-energy compounds such as SO_4, NO_3, CO_2 and sludge containing new bacterial cells (Peavy et al. 1985). Therefore, the required level of oxygen for the biological oxidation process should be ensured within the aeration vessel so as to achieve effective treatment of the wastewater (Karpinska and Bridgeman 2017). The effluent containing sludge from the aeration tank is transported to the secondary clarifier where the sludge is allowed to settle down by means of gravity in the bottom part of the clarifier. A small part of the sludge containing active micro-organisms from the secondary clarifier is re-circulated back to the aeration tank for continuing the ASP without any interruption. The remaining part of the sludge is processed in the sludge treatment plant and then properly disposed or reused (JBA 2010). The typical diagram showing the workflow of ASP is shown in Figure 1.1.

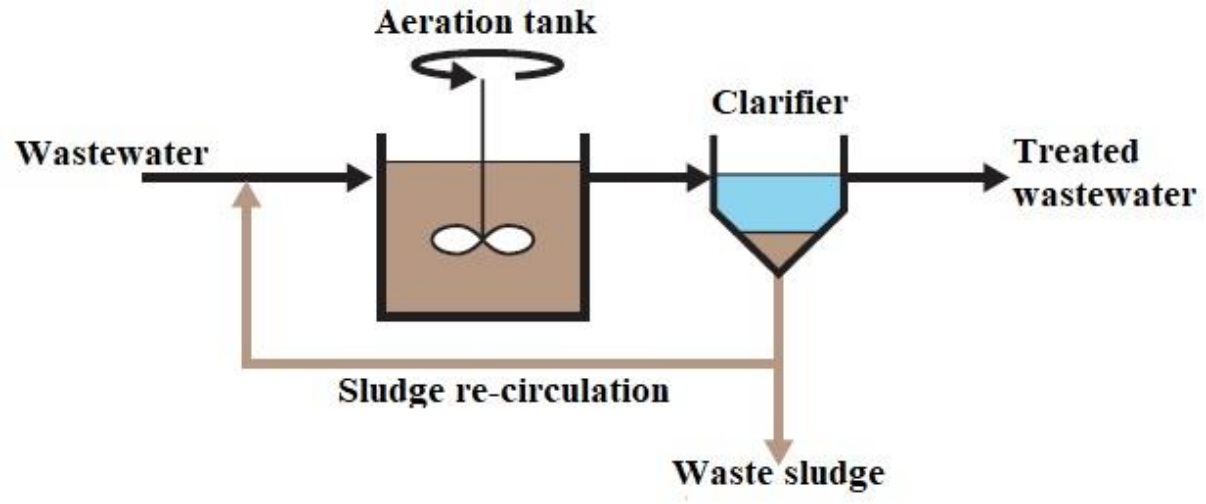

Figure 1.1: Workflow of ASP

(Source: SUEZ (2021))

1.2 Mechanisms of aeration process

The oxygen transfer into the aeration tanks is essential for efficient treatment of the wastewater and it depends upon the type of aeration system employed for the wastewater treatment process (Karpinska and Bridgeman 2017). The mechanisms causing the aeration process is classified into three categories such as shear type entrainment, vortex type entrainment and liquid fall type entrainment (Durve and Patwardhan 2012). The basic idea behind each type of aeration mechanism is to generate the flow conditions suitable for increasing the interfacial contact area between the air and liquid which increases the entrainment of air into the liquid. The underlying flow conditions then generate air bubbles within the liquid and disperse the same into the entire domain of the reactor vessel.

1. Shear type entrainment: The vigorous rotation of the impeller located near the free liquid surface develops strong discharge streams and re-circulation patterns which increases the turbulent velocities near the free liquid surface. The higher turbulence levels create significant wave action near the free liquid surface which ejects liquid droplets into the air. The movement of liquid droplets in air increases the interfacial contact area between the air and liquid leading to the entrainment of air into the liquid. When the droplets strike back at the free liquid surface, bubbles are entrapped into the liquid resulting in increase in the oxygen transfer into the reactor vessel. The re-circulation patterns present in the vessel distributes the entrapped air bubbles into the entire domain of the reactor vessel (Durve and Patwardhan

2012). The wave action near the free liquid surface and entrapment of air bubbles into the vessel are shown in Figures 1.2(a) and 1.2(b) respectively.

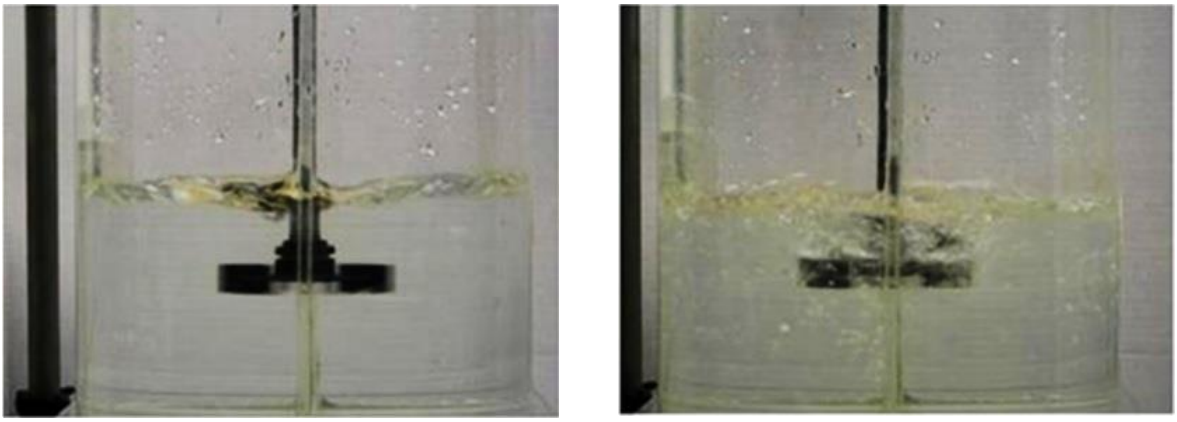

(a) **(b)**

Figure 1.2: (a) Wave action near the free liquid surface and (b) Entrapment of air bubbles into the reactor

(Source: Motamedvaziri and Armenante (2012))

2. Vortex type entrainment: The strong rotation of the impeller increases the tangential velocity and centrifugal action near the free liquid surface which results in the formation of a free surface vortex in the central part of the vessel. The formation of free surface vortex increases the interfacial contact area between the air and liquid which increases the entrainment of air into the liquid contained in the vessel. At higher impeller rotation speed, the free surface vortex reaches the impeller surface and results in the formation of large number of air bubbles. The dispersion of air bubbles into the liquid significantly increases the oxygen transfer into the reactor vessel. Since the bubble dispersion occurs in the vessel without the usage of any gas-sparger, this process is also known as self-induced aeration (Busciglio et al. 2013). The formation of free surface vortex and dispersion of air bubbles are shown in Figures 1.3(a) and 1.3(b) respectively.

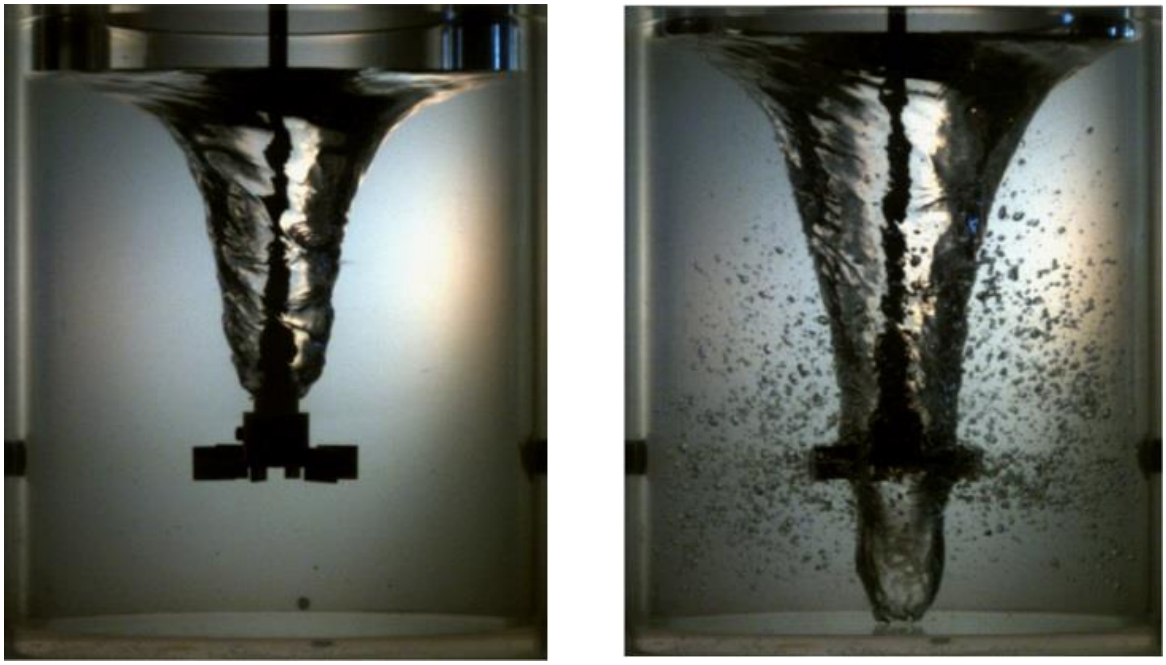

(a) **(b)**

Figure 1.3: (a) Free surface vortex around impeller shaft and (b) Entrapment of air bubbles into the reactor

(Source: Busciglio et al. (2013))

3. Liquid fall type entrainment: The high turbulent velocities generated along the free liquid surface leads to partial swelling or bulging of the free liquid surface. The discontinuity in the slope of free liquid surface at the boundary of the swollen part results in the branching of flow away from the free liquid surface and subsequent formation of air bubbles near the free liquid surface. The liquid then moves downwards through the swollen surface in the form of a small waterfall and returns back to the free liquid surface. The air bubbles thus formed are entrained into the liquid when the flow once branched away is re-entered into the free liquid surface. This phenomenon is also known as waterfall induced entrainment as the liquid flows through the swollen surface like a small waterfall (Madarame and Chiba 1990). The liquid fall type air entrainment into the reactor vessel with detailed views of free liquid surface and swollen parts are shown in Figures 1.4(a)-1.4(c) respectively.

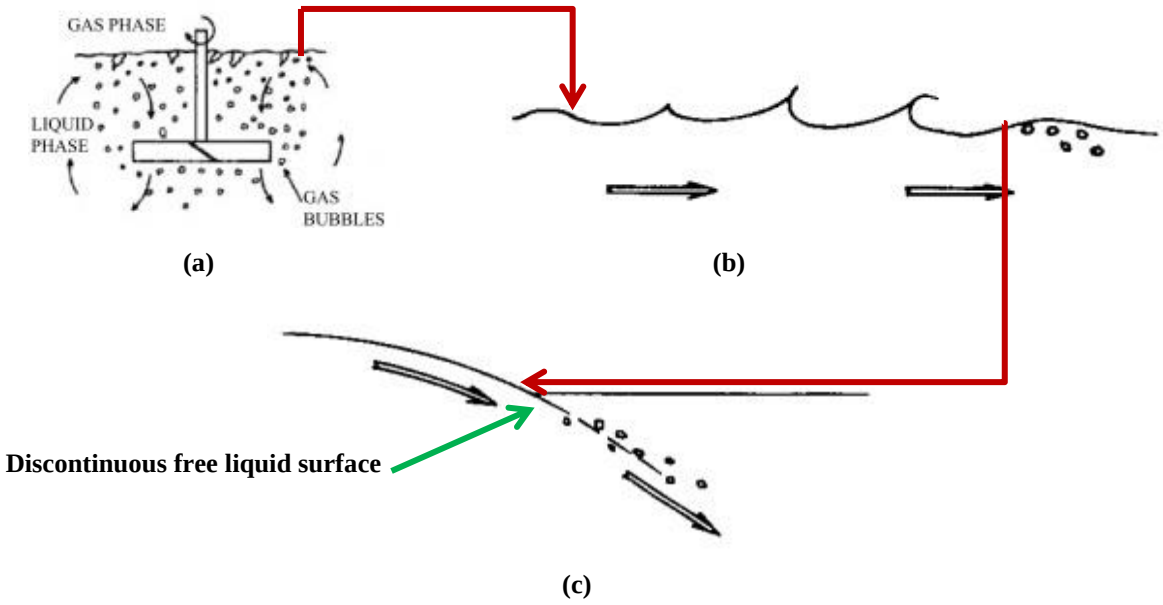

Figure 1.4: (a) Liquid fall type entrainment (Source: Yang and Mao (2014)), detailed views of (b) wavy free liquid surface and (c) liquid fall along swollen part (Source: Madarame and Chiba (1990))

1.3 Classification of aeration system

The aeration systems in the activated sludge plants are designed to deliver calculated oxygen demand of the wastewater against the available dissolved oxygen level in the incoming wastewater. Apart from providing required oxygen demand for the wastewater, the aeration systems should invariably assure necessary mixing or agitation in the vessel so that the complete mixed liquor suspended solids can be made available for the biological activity. Moreover, activated sludge should be kept in suspension throughout the entire course of the treatment process (JBA 2010). The aeration system is basically classified into three categories viz. (1) Diffused aeration system, (2) Surface aeration system and (3) Combined aeration system.

1. Diffused aeration system: In this aeration system, compressed air is introduced into the wastewater through diffusers or nozzles which are placed near the bottom surface of the vessel. The diffusers are located along one side of the aeration vessel so as to obtain a spiral flow field within the tank which helps in providing adequate mixing and solid suspension conditions within the vessel. The aeration occurs through the interfacial contact area between the air bubbles rising from bottom of the vessel and the wastewater contained in the vessel. The diffusers are placed at a height of 0.3m to 0.6m above the floor of the vessel so as to avoid clogging during shutdown and to aid in cleaning of the tank. The diffused aerators shall

be classified into two categories such as fine bubble diffuser and coarse bubble diffuser respectively (JBA 2010). The fine bubble diffusers provide superior oxygen transfer efficiency with adequate mixing of the sewage while increases the maintenance cost to reduce the underlying fouling and clogging issues. On the other hand, coarse bubble diffusers develop superior mixing conditions in the aeration tank with less maintenance cost although the oxygen transfer efficiency is lesser than that of the fine bubble diffusers (SSI 2019). The diagram of diffused aerator is shown in Figure 1.5.

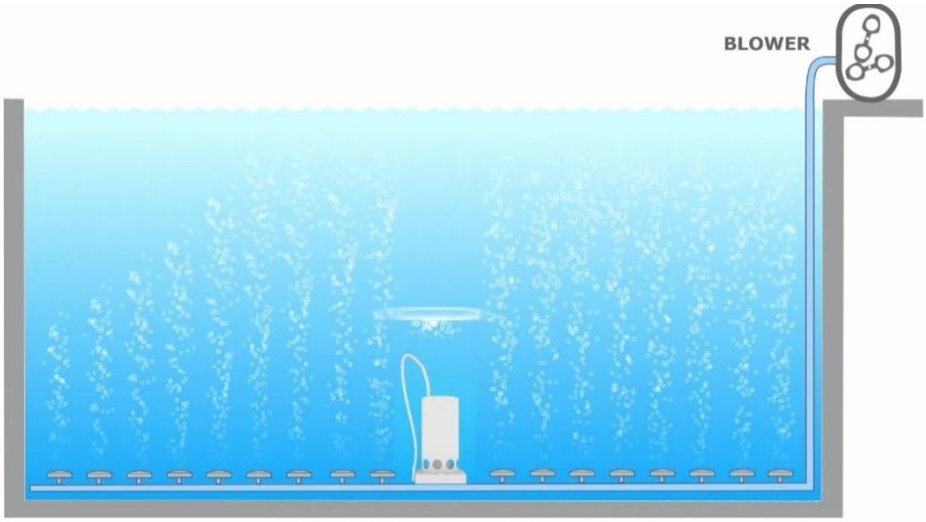

Figure 1.5: Diffused aerator

(Source: Gasion (2021))

2. Surface aeration system: In this aeration system, wastewater is filled into a vessel with or without baffle walls and vigorously agitated using an impeller which is centrally mounted inside the vessel and connected to a motor using a vertical shaft (Rao 1999). The strong agitation of the impeller disturbs the normal air-liquid interface and generates additional interfaces which increase the contact area between the air and liquid resulting in the entrainment of air into the aeration tank (Rao and Kumar 2009). The strong agitation of the impeller also increases the mixing inside the tank which helps in uniformly distributing the entrained air into whole part of the vessel and properly suspending the organic matter within the fluid contained in the vessel (Patil et al. 2004). The impeller is mostly placed near the free liquid surface so as to increase the number of additional interfaces and subsequent entrainment of air into the liquid. Surface aerator is widely preferred in the wastewater treatment process as it provides superior treatment efficiency with minimum cost for

operation and maintenance activities (JBA 2010). The diagram of surface aeration tank is shown in Figure 1.6.

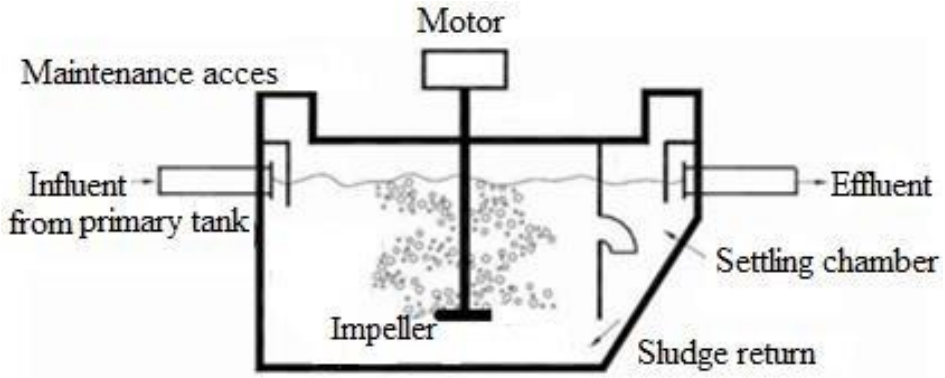

Figure 1.6: Surface aerator

(Source: Zabava et al. (2016))

3. Combined aeration system: In this aeration system, diffused and mechanical aerators are used to provide oxygen transfer into the wastewater. The diffusers are placed near the bottom surface of the vessel and the impeller for providing necessary mechanical agitation is also immersed in the liquid contained within the vessel. The air bubbles released from the diffusers travel upwards and develop strong mixing within the reactor vessel. The impeller is rotated in a direction opposite to the movement of air bubbles so as to enhance the mixing performance as well as to increase the entrainment of air through the additional air-water interfaces generated. Thus, the oxygen transfer occurs through the contact area between air bubbles and sewage as well as through the additional air-liquid interfaces developed by the strong agitation of the impeller (Engineering Articles 2022). The Dorroco aerator is a classic example for the combined aeration system and the same is shown in Figure 1.7. The main purposes of aeration such as oxygen transfer, superior mixing of sewage in the vessel and suspension of organic matter in the sewage are remarkably achieved using the combined aeration system.

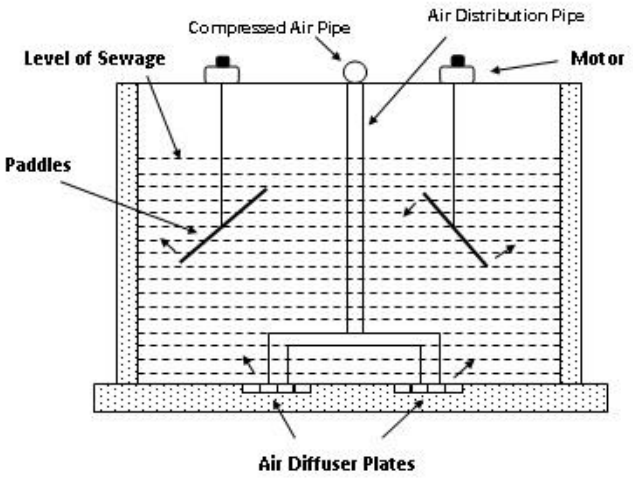

Figure 1.7: Dorrocco aerator

(Source: Engineering Articles (2022))

1.4 Surface aeration tank

The surface aeration system is widely used in the wastewater treatment industries due to its superior oxygen transfer efficiency at less operational and maintenance cost (Rao et al. 2009). Although, the diffused aerators provide higher oxygen transfer rates, troubles due to fouling and clogging of sludge and chemical build up reduces their treatment efficiencies with time and demands huge cost for the maintenance of such troubles. Moreover, the design and installation of diffused aerators are complex as compared to the mechanical aerators. Further, the diffused aerators aren't suitable for the sewage containing effluent from chemical industries and higher concentration of suspended particles (SSI 2019).

The main components of a surface aeration tank consist of a vessel with or without baffle walls and a rotating element called impeller which is connected to the motor through a vertical shaft (Rao et al. 2009). The cylindrical tank is widely preferred for the wastewater treatment as it develops superior oxygen transfer conditions as compared to the square and rectangular shaped tanks (Rao et al. 2004). Moreover, the presence of baffle walls is desirable as it avoids the formation of circular flow patterns and provides strong mixing in the radial and axial directions within the reactor vessel (Alcamo et al. 2005). A schematic diagram of a circular baffled surface aeration tank agitated using a Rushton Turbine (RT) impeller is shown in Figure 1.8. The various factors controlling the oxygen transfer process and the associated power consumption can be grouped as geometric parameters, dynamic parameters and

physical parameters respectively (Rao et al. 2009) and the corresponding functional relationship is expressed as given in the equation (1).

$$K_L a_{20}, P' = f\left(A, H, D, B, l, b, h, N, g, N_{bl}, N_{bf}, \rho_a, \rho_w, \vartheta\right) \quad (1)$$

Where $K_L a_{20}$ is the volumetric oxygen transfer coefficient, P' is the power consumed, A is the cross-sectional area of the vessel, H is the depth of water, D and N are the diameter and rotational speed of the impeller, B is the width of baffle walls, l and b are the length and width of impeller blades, h is the clearance of the impeller from bottom of the vessel, N_{bl} and N_{bf} are the number of blades of rotor and number of baffle walls of the tank, ρ_a and ρ_w are the density of air and density of water, g is the acceleration due to gravity and ϑ is the kinematic viscosity of water. The density and kinematic viscosity corresponding to the normal water are considered in this equation since the wastewater after the primary treatment exhibits highly similar physical characteristics as that of normal water and found to be invariant during the surface aeration process (Alvarado et al. 2013). The equation (1) was converted into the non-dimensional form using Buckingham pi theorem (Zlokarnik 2006) and the same was rearranged by Rao et al. (2009) as specified in the equation (2).

$$k^*, N_p = f\left(\frac{\sqrt{A}}{D}, \frac{H}{D}, \frac{l}{D}, \frac{b}{D}, \frac{h}{D}, \frac{B}{D}, \frac{N_{bf}}{N_{bl}}, \frac{\rho_a}{\rho_w}, R_e, F\right) \quad (2)$$

Where $k^* = K_L a_{20}\left(\frac{\vartheta}{g^2}\right)^{1/3}$ is the non-dimensional oxygen transfer parameter, $N_p = \frac{P'}{\rho N^3 D^5}$ is the impeller power number, $R_e = \frac{ND^2}{\vartheta}$ is the Reynolds number and $F = \frac{N^2 D}{g}$ is the Froude number respectively. The first seven non-dimensional parameters represent 'geometric similarity' and the last two parameters indicate 'dynamic similarity' of the aeration tank respectively (Rao et al. (2009)). The k^* and N_p are the fundamental performance goals associated with the surface aeration tanks.

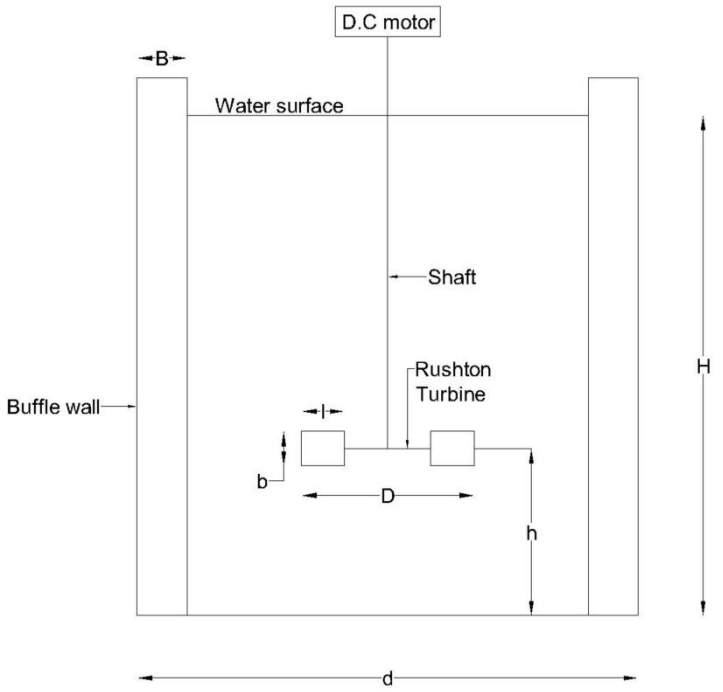

Figure 1.8: Circular surface aeration tank with baffle walls agitated using RT impeller

(Source: Rao et al. (2009))

1.5 Emerging challenges in designing energy efficient surface aeration tanks

The continuous research activities in the field of ASP have expanded its applicability from the removal of high levels of Biochemical Oxygen Demand (BOD) and total suspended solids to the removal of nutrients such as nitrogen and phosphorous contained in the wastewater. Moreover, several modifications were attempted to the ASP so as to enhance its flexibility to meet the user specific requirements (Karpinska and Bridgeman 2016). However, the ASP requires steady supply of energy for the continuous working of the surface aeration tanks and pumps used for sludge and mixed liquor re-circulation processes. The surface aeration tank consumes 45%-75% of the total energy required for the complete wastewater treatment process which increases up to 85% in the extreme cases of nutrient removal from the wastewater (Karpinska and Bridgeman 2018). Therefore, the aeration process has considerable influence on the operation as well as maintenance budget of the water utilities (WEF 2009). Considering the global prominence on the water-energy-food-climate change nexus, it is necessary to reduce the energy consumption of wastewater treatment plants by

adopting various energy conservation measures, management programmes and engineering practices (Karpinska and Bridgeman 2018). As per the guidelines provided by EPA (2013) and WEF (2009), energy consumption of the wastewater treatment plants can be reduced by optimizing the design of surface aeration tanks. The other alternatives such as operational modifications (ie, frequent on-off operation) and the usage of advanced membrane diffuser system have reduced the oxygen transfer efficiency and increased the operational and maintenance cost (Karpinska and Bridgeman 2016). Therefore, it is necessary to develop optimal configuration of the surface aeration tank which provides high treatment efficiency with less energy consumption.

In majority of the wastewater treatment industries, the design of surface aeration tank is prepared based on empirical principles (ATV-A-131 guidelines) or thumb rules or past experience of the officials working in such industries. These methods doesn't have sound theoretical basis and often result in improper design of the aeration vessels and subsequent financial loss related with the industries (Karpinska and Bridgeman 2018). Since the order of biochemical reactions occurring in the aeration tank is greater than zero, wastewater treatment efficiency associated with such non-ideal systems is governed by the hydrodynamic features present in the vessel (Karpinska and Bridgeman 2016). Therefore, accurate prediction of the local scale flow features associated with the surface aeration tanks is necessary for achieving optimal design of the same (Karpinska and Bridgeman 2017). However, the flow field characteristics associated with the aeration vessels aren't considered by the above mentioned methods for the design process. These methods assume the presence of a well-mixed flow regime in the surface aeration tank during the ASP or the flow behaviour of the surface aeration tanks are predicted using the ideal reactor models. Hence, a sophisticated analysis of the flow behaviour of the surface aeration tanks accounting for the flow patterns, turbulence characteristics and distribution of oxygen is necessary for efficient and energy optimized design of the surface aeration tanks (Karpinska and Bridgeman 2016).

The flow physics associated with the surface aeration tanks is complex due to the presence of multiphase flow (mixed liquor and air), turbulent flow generated by the impeller and scales of various lengths ranging from size of bubbles to the size of aeration tank (Karpinska et al. 2015). The fluid flow within the surface aeration tank is controlled by the geometric and dynamic parameters of the tank and at the same time, fluid flow governs the interface contact and oxygen transfer, power consumption, biochemical reactions and local concentration of

solids (Karpinska and Bridgeman 2016). Thus, it is necessary to build-up relationships connecting geometric and dynamic parameters of the tank, flow field characteristics and performance goals associated with the vessel so as to obtain efficient and energy optimized design of the surface aeration tanks.

1.6 Hydraulic design of surface aeration tanks- Experimental and Computational approaches

Substantial efforts were taken in the past to characterize the flow field conditions present in the agitated vessels using both experimental as well as Computational Fluid Dynamics (CFD) techniques. The conventional experimental techniques such as Laser Doppler Anemometry/Velocimetry (LDA/LDV) and Particle Image Velocimetry (PIV) are limited to lab-scale processes, affected by the uncertainties in the scale-up criteria for transferring the lab scale results into real full size reactor scale (Wechsler et al. 1999), poses difficulties in measuring the fluctuating quantities near the impeller (Alcamo et al. 2005) and restricted by the opacity of the fluid (Liu 2013). Although, the advanced experimental techniques such as Positron Emission Particle Tracking (PEPT) and Computer Automated Radioactive Particle Tracking (CARPT) techniques avoid some of the above mentioned drawbacks, these methods need to be developed further to analyse the complex flow conditions allied with the reactor vessels (Liu 2013).

CFD approach has drawn widespread attention during the recent periods in analysing the flow field characteristics associated with the agitated reactors. With the advent of the sophisticated workstations and supercomputers, CFD approach provides detailed characterisation of the reactor hydrodynamics which are expensive or unobtainable from the experimental studies (Karpinska and Bridgeman 2017). This is a powerful and cost effective tool which computes the flow fields by simultaneously solving the conservation equations of mass, momentum and other variables under consideration (Joshi et al. 2011). Although, the CFD modelling process has inherent assumptions and inadequacies, proper minimization of various sources of numerical error and validation of the underlying mean and turbulent flow fields with the corresponding experimental results have resulted in accurate prediction from this approach (Coroneo et al. 2011). Due to these reasons, CFD approach is widely employed for predicting the flow behaviour as well as unit processes involved in the reactor vessels.

1.7 The present work

The main aim of the present study is to build physical reasons causing variation in the performance goals under various geometric and dynamic conditions of the aeration tank which aid in effective design of the same using CFD approach. The methodology adopted for the CFD simulations was verified and validated to achieve reliable and accurate prediction of the flow field characteristics. The present thesis is divided into two main parts. The first part deals with the development of an efficient CFD model of a reactor vessel including minimization of various sources of numerical error and detailed comparison of the CFD prediction with the corresponding results from experiments and advanced computational techniques available in the literature. The second part comprises of the analysis of mean and turbulent flow fields under various geometric and dynamic conditions of the vessel so as to explain the physical reasons causing variation in the performance goals with the variation in the geometric and dynamic parameters of the tank. The physical relationship between the tank parameters and the performance goals will help in selecting the optimal configuration of the reactor vessel for the surface aeration process. Apart from the surface aeration process, the results from this study can be extended for designing the reactor vessels used in various industries requiring solid-liquid suspension and bulk mixing conditions respectively.

1.8 Layout of thesis

This thesis is structured as follows. The Chapter 2 deals with the review of relevant literature pertaining to the research topic under consideration. This includes review of literature related with the verification of various sources of numerical error and analysis of the flow field characteristics associated with various configurations of the reactor vessels. The methodology adopted for the CFD modelling of surface aeration tanks is elucidated in the Chapter 3. This chapter contains the description regarding the modelling approach, governing equations, turbulence model closures, boundary conditions, procedures adopted to minimize the various sources of numerical error and configurations of the aeration vessels analysed in the present work. The Chapters 4 and 5 describe the results obtained from the present study and the comprehensive discussion of the same. In Chapter 4, the results concerning the verification of various sources of numerical error arising from grid resolution, grid type, numerical discretization scheme and the position of MRF boundary are discussed. Further, the predictive

performance of the completely verified CFD model is analysed by comparing the respective flow field predictions with the corresponding results from the experimental techniques, LES approach and other complex turbulence models respectively. In Chapter 5, the effect of various tank parameters such as $\frac{h}{D}$, $\frac{d}{D}$, N, N_{bl} and N_{bf} on the flow fields and performance goals were analysed. The distributions of mean velocity, pressure, trailing vortices and various turbulent quantities under various configurations of the vessel were analysed. The physical reasons behind the variation in the performance goals with the variation in the above mentioned geometric and dynamic parameters of the tank are elucidated. Finally, the Chapter 6 specifies the conclusions derived from the discussion of the results and possible scope for the future work.

1.9 References

Alcamo, R., G. Micale, F. Grisafi, A. Brucato, and M. Ciofalo. 2005. “Large-eddy simulation of turbulent flow in an unbaffled stirred tank driven by a Rushton turbine.” *Chem. Eng. Sci.,* 60 (8–9): 2303–2316. https://doi.org/10.1016/j.ces.2004.11.017.

Alvarado, A., M. Vesvikar, J. F. Cisneros, T. Maere, P. Goethals, and I. Nopens. 2013. “CFD study to determine the optimal configuration of aerators in a full-scale waste stabilization pond.” *Water Res.,* 47 (13): 4528–4537. https://doi.org/10.1016/j.watres.2013.05.016.

Busciglio, A., G. Caputo, and F. Scargiali. 2013. “Free-surface shape in unbaffled stirred vessels: Experimental study via digital image analysis.” *Chem. Eng. Sci.,* 104: 868–880. https://doi.org/10.1016/j.ces.2013.10.019.

Coroneo, M., G. Montante, A. Paglianti, and F. Magelli. 2011. “CFD prediction of fluid flow and mixing in stirred tanks: Numerical issues about the RANS simulations.” *Comput. Chem. Eng.,* 35 (10): 1959–1968. https://doi.org/10.1016/j.compchemeng.2010.12.007.

Durve, A. P., and A. W. Patwardhan. 2012. “Numerical and experimental investigation of onset of gas entrainment phenomenon.” *Chem. Eng. Sci.,* 73: 140–150. https://doi.org/10.1016/j.ces.2012.01.030.

Engineering Articles. 2022. “Aeration & Methods and Types of Aeration.” *Engineering Articles: A Portal of Engg. Lectures, Notes and Software.*Accessed July 22, 2022. https://www.engineeringarticles.org/aeration-methods-and-types-of-aeration/.

EPA. 2013. *Energy Efficiency in Water and Wastewater Facilities - a Guide to Developing and Implementing Greenhouse Gas Reduction Programs*. Washington, DC: United States Environmental Protection Agency.

Gasion. 2021. “Mega Bubble Generator: Introduces Bubble Mixers for Turbulence Creation in any Liquid Tank.” *Gasion.* Accessed July 22, 2022. https://gasionairtec.com/mega-bubble-generator/.

JBA. 2010. *Manual on Sewerage & Sewage Treatment.*2nd ed. New Delhi: JBA Publishers.

Joshi, J. B., N. K. Nere, C. V. Rane, B. N. Murthy, C. S. Mathpati, A. W. Patwardhan, and V. V. Ranade. 2011. “CFD simulation of stirred tanks: Comparison of turbulence models. Part I: Radial flow impellers.” *Can. J. Chem. Eng.*, 89 (1): 23–82. https://doi.org/10.1002/cjce.20446.

Karpinska, A. M., and J. Bridgeman. 2016. “CFD-aided modelling of activated sludge systems – A critical review.” *Water Res.*, 88: 861–879. https://doi.org/10.1016/j.watres.2015.11.008.

Karpinska, A. M., and J. Bridgeman. 2017. “Towards a robust CFD model for aeration tanks for sewage treatment – a lab-scale study.” *Eng. Appl. Comput. Fluid Mech.*, 11 (1): 371–395. https://doi.org/10.1080/19942060.2017.1307282.

Karpinska, A. M., and J. Bridgeman. 2018. “CFD as a Tool to Optimize Aeration Tank Design and Operation.” *J. Environ. Eng.*, 144 (2): 05017008. https://doi.org/10.1061/(ASCE)EE.1943-7870.0001307.

Karpinska, A. M., M. M. Dias, R. A. R. Boaventura, and R. J. Santos. 2015. “Modeling of the hydrodynamics and energy expenditure of oxidation ditch aerated with hydrojets using CFD codes.” *Water Qual. Res. J. Canada*, 50 (1): 83–94. https://doi.org/10.2166/wqrjc.2014.036.

Liu, L. 2013. “Computational Fluid Dynamics Modelling of Complex Fluid Flow in Stirred Vessels.” Ph.D. thesis, School of Chemical Engineering, College of Engineering and Physical Sciences, The University of Birmingham.

Madarame, H., and T. Chiba. 1990. “Gas Entrainment Inception at the Border of a Flow-Swollen Liquid Surface.” *Nucl. Eng. Des.*, 120: 193–201.

Motamedvaziri, S., and P. M. Armenante. 2012. “Flow regimes and surface air entrainment in partially filled stirred vessels for different fill ratios.” *Chem. Eng. Sci.*, 81: 231–250. https://doi.org/10.1016/j.ces.2012.05.050.

Patil, S. S., N. A. Deshmukh, and J. B. Joshi. 2004. “Mass-transfer characteristics of surface aerators and gas-inducing impellers.” *Ind. Eng. Chem. Res.*, 43 (11): 2765–2774. https://doi.org/10.1021/ie030428h.

Peavy, H. S., D. R. Rowe, and G. Tchobanoglous. 1985. *Environmental Engineering.* International ed. 1985. Singapore: McGraw-Hill Book Company.

Ramakrishna Rao, A., B. B. V. Laxmi, and S. K. Narasiah. 2004. "Simulation of Oxygen Transfer Rates in Circular Aeration Tanks." *Water Qual. Res. J. Canada*, 39 (3): 237–244.

Rao, A. R. 1999. "Prediction of reaeration rates in square stirred tanks." *J. Environ. Eng.*, 125 (March): 215–223.

Rao, A. R., and B. Kumar. 2009. "Resistance Characteristics of Surface Aerators." *J. Hydraul. Eng.*, 135 (January): 38–45.

Rao, A. R., A. K. Patel, and B. Kumar. 2009. "Oxygen transfer in circular surface aeration tanks." *Environ. Technol.*, 30 (7): 747–753. https://doi.org/10.1080/09593330902911705.

SSI. 2019. "Diffused Air vs. Mechanical Wastewater Aeration Systems." *SSI Smart Ideas for Water*. Accessed July 22, 2022. https://www.ssiaeration.com/diffused-air-vs-mechanical-aeration/#gref.

SUEZ. 2021. "Activated sludge reactor: type and configurations." *suez degremont water handbook.* Accessed July 22, 2022. https://www.suezwaterhandbook.com/processes-and-technologies/biological-processes/suspended-growth-cultures/activated-sludge-reactor-type-and-configurations.

Wechsler, K., M. Breuer, and F. Durst. 1999. "Steady and Unsteady Computations of Turbulent Flows Induced by a 4/45° Pitched-Blade Impeller." *J. Fluids Eng.*, 121 (2): 318–329. https://doi.org/10.1115/1.2822210.

WEF. 2009. *Energy Conservation in Water and Wastewater Treatment Facilities*. Water Environment Federation Manual of Practice No. 32. New York: McGraw-Hill, Inc.

Yang, C., and Z. S. Mao. 2014. "Multiphase stirred reactors." *Numer. Simul. Multiph. React. with Contin. Liq. Phase*, 75–151. Elsevier.

Zabava, B. Ștefania, G. Voicu, V. V. Safta, N. Ungureanu, M. Dinca, I. Mariana, and M. Munteanu. 2016. "*Types of aerators used in wastewater treatment plants.*" In *Proc., 5th Int. Conf. Therm. Equipment, Renew. Energy Rural Dev.*, 455–460. Golden Sands, Bulgaria.

Zlokarnik, M. 2006. *Scale-Up in Chemical Engineering*. 2nd ed. Germany: WILEY-VCH Verlag GmbH & Co. KGaA.

Chapter 2

Review of Literature

2.1 Energy efficient design of surface aeration tanks

The surface aeration tanks are the popular choice among various aeration systems for the wastewater treatment process due to its superior treatment efficiency at lesser operating and maintenance cost (Rao 1999). However, the surface aeration tanks are energy intensive units in a wastewater treatment plant and the development of energy efficient design of the same is a challenge faced by the research community as well as the practicing engineers (Karpinska and Bridgeman 2016). The energy efficient design of the surface aeration tank requires detailed knowledge of the underlying flow field characteristics. However, such details of the flow field characteristics aren't considered in the present design procedures (Karpinska and Bridgeman 2018). The past studies of Deshmukh and Joshi 2006, Patil et al. 2004 and Rao et al. 2009 have focussed in developing correlations for predicting the oxygen transfer and power consumption at various configurations of the reactor vessels so as to assist in the proper design of the same. But the variables affecting mixing or flow field characteristics weren't considered in such studies although these variables play a crucial role in the performance of the surface aeration tanks (Karpinska and Bridgeman 2018).

The surface aeration tanks consist of high velocity and turbulence fields which promote entrainment of air as well as uniform distribution of the entrained air in the entire domain of the reactor vessel so as to achieve superior treatment efficiency. The geometric and dynamic parameters of the aeration tank control the underlying flow patterns and turbulence characteristics. The flow patterns and turbulence characteristics developed in the aeration tank in turn governs the corresponding performance goals such as oxygen transfer, power

consumption and mixing conditions (Karpinska and Bridgeman 2016) respectively. The surface aeration tank is basically a reactor vessel in which the liquid is pumped using an impeller and is transported to other parts of the reactor vessel so as to generate a flow pattern (or circulation pattern) within the vessel (Liu 2013). Moreover, the rotation of the impeller creates turbulence conditions in the vessel which governs the oxygen transfer into the reactor vessel (Rao 1999). Therefore, it is necessary to obtain detailed insight into the linkage between tank parameters, flow field characteristics and performance goals of the aeration tank so as to achieve energy efficient design of the same. In this regard, the literature review was done to understand the way in which the performance goals of the surface aeration tank vary with the variations in the tank parameters and flow field characteristics.

2.2 Relationships between aeration tank parameters, flow field characteristics and performance goals

In the present section, literature concerned with the variations in the oxygen transfer, power consumption and mixing performance of the reactor vessels with variations in the reactor parameters and flow field characteristics were reviewed. The inferences from these studies were used to identify the research gaps and subsequent outlining of the objectives for the present research work.

2.2.1 Flow patterns and power number

The reactor vessels with RT impeller at one third height (standard configuration) as well as mid-height have developed strong discharge streams behind the blades which propagate radially towards the tank periphery to generate two circulation loops above and below the impeller centre-plane. This flow pattern is known as double re-circulation or double loop pattern (Kresta and Wood 1993; Yapici et al. 2008) which is characterised by complex three dimensional velocity fields, periodic trailing vortices behind the blades and random turbulence fields away from the impeller (Escudié and Liné 2003; Yianneskis et al. 1987). Extensive research works have been performed by various scholars in the past using experimental and CFD techniques for studying the velocity fields (Lee and Yianneskis 1998; Molen and Maanen 1978; Yianneskis et al. 1987), trailing vortices (Escudié et al. 2004; Escudié and Liné 2006; Stoots and Calabrese 1995) and turbulence characteristics (Başbuğ et al. 2017; Cutter 1966; Delafosse et al. 2008; Wu and Patterson 1989) associated with these

reactor configurations. The above mentioned studies have found high magnitude of mean velocity near the impeller indicating jet action of the discharge stream, adequate velocity magnitude in the bulk flow region, significant transfer of kinetic energy from trailing vortices to random turbulence fields and dissipation of the same in the bulk flow region and near the periphery of the tank. These flow field characteristics provide bulk mixing of the fluid contained within the reactor vessel which makes it suitable for various operations associated with chemical, biochemical, petroleum, metal, metallurgical and wastewater treatment industries (Joshi et al. 2011).

However, the RT impeller located near the bottom surface of the reactor vessel (low clearance vessel) has produced completely different flow pattern and mixing conditions as compared to the standard reactor vessel. The low clearance vessel develops discharge streams which move axially downwards and strike on the bottom surface of the vessel to generate two major re-circulation loops in the vessel. This flow pattern is known as single re-circulation pattern or single loop pattern (Nienow 1968) or single loop down-pumping pattern (Iyer and Patel 2022) respectively. Single loop down-pumping pattern is characterised by higher velocities and turbulence fields near the bottom surface of the vessel which helps in lifting the solid particles and suspending the same in the liquid contained within the reactor vessel (Montante et al. 1999). Thus, the low clearance vessel is widely preferred for the solid-liquid suspension processes in the industries (Conti et al. 1981). As a consequence, the transition from double loop pattern to single loop down-pumping pattern leads to decrease in the N_p by 25%-30% (Montante et al. 1999; Yapici et al. 2008) and mixing time by 16.37% (Ochieng et al. 2008; Ochieng and Onyango 2008) respectively. Several research works (Armenante et al. 1998; Armenante and Nagamine 1998; Conti et al. 1981; Galletti et al. 2003; Li et al. 2011; Montante et al. 1999, 2001; Zhu et al. 2019) have been performed to determine the critical impeller clearance at which the transition from double loop to single loop down-pumping pattern occurs. The double loop to single loop down-pumping pattern transition was found to occur within a range of impeller clearance rather than at a single clearance level and the flow patterns became unstable within this range and switched back and forth between single loop down-pumping and double loop patterns with a well-defined periodicity. The flow field characteristics associated with the single loop down-pumping pattern such as axial velocity fields, inclination of discharge streams and secondary circulation loops have been analysed using experimental and CFD approaches by various researchers (Li et al. 2011; Montante et al. 1999, 2001; Ochieng et al. 2008; Zhu et al. 2019). The downward moving discharge

streams and trailing vortices have caused substantial transfer of energy from the impeller region to the bottom surface of the reactor vessel (Li et al. 2011) resulting in significant increase in the vortex and turbulence activity in the entire bottom surface of the reactor vessel (Montante et al. 1999). The localized mixing produced near the bottom surface of the reactor vessel has led to poor bulk mixing of the liquid contained within the reactor vessel (Rashidifar and Rashidifar 2013). Li et al. (2011) and Montante et al. (1999) have increased the impeller speed of low clearance vessels and found insignificant changes in the underlying single loop down-pumping pattern. On the other hand, the larger impellers at low clearance conditions develop double loop pattern instead of single loop down-pumping pattern as compared to the smaller sized impellers (Li et al. 2011; Zhu et al. 2019). Moreover, the single loop down-pumping pattern associated with the RT impeller was found to be weaker than that produced by the Pitched Blade Turbine (PBT) impeller (Zhu et al. 2019). Although, the past research works have analysed the geometric and dynamic conditions causing double loop to single loop down-pumping pattern transition and corresponding decrease in the N_p, physical reasons behind the same is still a mystery among the research community.

The reactor vessel with RT impeller located near the free liquid surface (high clearance vessel) has generated the discharge streams which move axially upwards and strike on the free liquid surface to provide two major re-circulation loops within the vessel. This flow pattern is known as single re-circulation pattern or single loop pattern (Motamedvaziri and Armenante 2012) or single loop up-pumping pattern (Iyer and Patel 2022) respectively. As a consequence, the transition from double loop pattern to single loop up-pumping pattern leads to decrease in the N_p by 40% and pumping number (N_q) by 75% respectively (Motamedvaziri and Armenante 2012). The single loop up-pumping pattern is characterised by higher velocities and turbulence fields near the top surface of the vessel which causes deformation of the free liquid surface and entrainment of air into the reactor vessel (Ryma et al. 2013). Thus, the high clearance vessels are widely adopted for the surface aeration process in the wastewater treatment industries (Deshmukh and Joshi 2006). Motamedvaziri and Armenante (2012) have specified a critical impeller submergence ratio below which the double loop pattern changes into single loop up-pumping pattern and this ratio was found to be unaffected by the rotational speed of the impeller. The characteristics of single loop up-pumping pattern such as axial velocity fields, inclination of discharge streams and secondary re-circulation loops were studied by various researchers such as Ryma et al. (2013) and Motamedvaziri and Armenante (2012) using experimental and CFD approaches. The upward discharge streams

associated with the high clearance vessels have increased the vortex and turbulence activity near the top surface of the vessel which in turn enhanced the localized mixing effects near the top surface of the reactor vessel. Even though, the earlier research works have studied the geometric and dynamic conditions of the reactor vessel causing double loop to single loop up-pumping pattern transition and corresponding reduction in the N_p, the physical reasons causing the same aren't investigated by the research community so far. The flow patterns produced by the reactor vessels under standard, low and high clearance conditions are shown in Figures 2.1(a)-2.1(c) respectively.

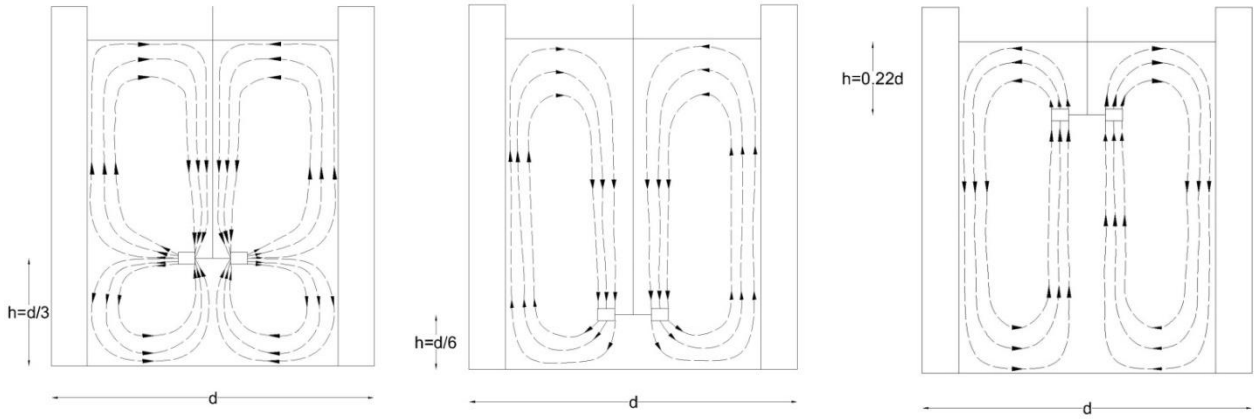

(a) Standard reactor vessel $\left(\boldsymbol{h = \frac{d}{3}}\right)$ **(b) Low clearance vessel** $\left(\boldsymbol{h = \frac{d}{6}}\right)$ **(c) High clearance vessel** $(\boldsymbol{h = 0.22d})$

Figure 2.1: Flow patterns associated with (a) Standard reactor vessel, (b) Low clearance vessel and (c) High clearance vessel

The R_e of flow is a crucial dynamic parameter which significantly affects the mixing and power characteristics associated with the reactor vessels. Bates et al. (1963) have provided a 'power curve' which shows the variation of N_p with the R_e of flow for various types of impellers having different sizes agitated in a standard baffled reactor vessel. N_p linearly decreases in the laminar regime, slightly increases in the transitional regime and becomes constant in the turbulent regime of the baffled reactor vessels. However, in the case of unbaffled reactor vessels, N_p and N_q decreases with increase in the R_e under the turbulent flow regime as compared to the baffled reactor vessels (Myers et al. 2002). The mean velocity, velocity fluctuations and turbulent kinetic energy have exhibited Reynolds independent behaviour in the turbulent flow regime for standard as well as low clearance vessels respectively (Basavarajappa et al. 2015; Yapici et al. 2008; Zhang et al. 2017b). Moreover, the variations of mixing time and mixing energy associated with the reactor vessels

with variations in the R_e have been discussed in the research works of Lu et al. (1997) and Molnár et al. (2014) respectively. Although, the power curve is widely used for the design of industrial reactor vessels, physical reasons causing the variation of N_p with the R_e aren't analysed so far.

The research works of Molnár et al. (2014) and Wu et al. (2001) have studied the effect of N_{bl} on the performance features and the impeller with six blades was found to provide superior mixing and dispersion of liquid within the reactor vessel as compared to the remaining impeller configurations. On the other hand, Lu and Yang (1998) have illustrated the suitability of the RT impeller with four blades for the aeration process due to the development of strong mean deformation rates, longer trailing vortices and higher turbulence fields as compared to the RT impeller with six blades. Backhurst et al. (1988) have observed that the aeration performance of the reactor vessel increases with increase in the N_{bl} from zero to eight and remains constant thereafter. The authors have preferred the impeller with eight blades for the mixing process in the aeration vessels. The inferences from these literature regarding the optimal N_{bl} is mutually contradicting in nature and hence detailed flow field analysis of the reactor vessels agitated using the RT impeller with various N_{bl} is necessary for determining the optimal N_{bl} for the mixing process.

The reactor vessel with four baffle walls is considered as a standard for majority of the industrial processes due to the development of superior mixing and dispersion conditions (Myers et al. 2002; Rao et al. 2009; Wu and Patterson 1989; Yianneskis et al. 1987; Zlokarnik 2006). Also, the reactor vessel with four baffles generates fully baffled conditions and superior mechanical stability which enhances the mixing performance of the same (Myers et al. 2002). On the other hand, Lu et al. (1997) have recommended providing N_{bf} between four and eight for achieving superior mixing conditions in the vessel while Nishikawa et al. (1979) have specified to adopt vessel with three baffle walls to derive the fully baffled condition. The issues allied with the fluid mixing in the tanks having excessive baffling conditions were discussed by Lu et al. (1997). The controversy persisting in the optimal N_{bf} for achieving superior mixing conditions in the reactor vessel from these literature necessitates the detailed flow field analyses of the reactor vessels with various N_{bf} to determine the optimal N_{bf} for the mixing process.

2.2.2 Oxygen transfer

The phenomenon of surface aeration and the flow field characteristics under the aeration conditions were widely studied using experimental and CFD approaches by various researchers (Deshmukh and Joshi 2006; Kulkarni and Patwardhan 2014; Motamedvaziri and Armenante 2012; Patil et al. 2004; Ryma et al. 2013; Sun et al. 2006). The surface aeration increases with increase in $\frac{h}{D}$ and the maximum oxygen transfer was obtained when the impeller is placed near the free liquid surface (Patil et al. 2004; Sun et al. 2006). The increase in the N and D under high clearance conditions has increased the turbulent flow within the vessel which in turn resulted in superior oxygen transfer into the reactor vessel (Sun et al. 2006). On the other hand, increase in the $\frac{d}{D}$ under high clearance conditions has considerably decreased the interfacial contact area (Matsumura et al. 1982) and the oxygen transfer into the reactor vessel (Backhurst et al. 1988). Motamedvaziri and Armenante (2012) have explained that the effective surface aeration occurs when the submergence of the RT impeller is less than the critical impeller submergence for generating the single loop up-pumping pattern and the corresponding F is greater than the critical F for providing free surface vortex and necessary mixing conditions adequate for the oxygen transfer into the reactor vessel. The rotation of impeller near the free liquid surface effectively transports the energy imparted by the impeller towards the free liquid surface resulting in the formation of free surface vortex (Deshmukh and Joshi 2006). The axial velocity, turbulent kinetic energy and dissipation rate above the impeller and near the free liquid surface from the high clearance vessels were found to be higher than that related with the standard reactor vessel (Deshmukh and Joshi 2006; Ryma et al. 2013). Moreover, the additional re-circulation loop generated near the free liquid surface around the shaft accumulates the air bubbles and fill the same into the free surface vortex region thus developed (Sun et al. 2006). The formation of free surface vortex has increased the oxygen transfer across the interface into the reactor vessel (Deshmukh and Joshi 2006; Ryma et al. 2013). The increase in the N generates stronger trailing vortices behind the blades which suck the free surface vortex region towards the impeller resulting in increase in the size and depth of the same (Sun et al. 2006). As the free surface vortex touches the impeller surface, strong rotation of the impeller disperses the air bubbles into the liquid contained in the reactor vessel resulting in significant increase in the oxygen transfer into the reactor vessel (Ryma et al. 2013; Sun et al. 2006). Motamedvaziri and Armenante (2012) have referred this phenomenon as ‘flooding condition’ and correlated the same with critical F of

flow within the reactor vessel. Since, the impeller is located near the free liquid surface of the surface aeration tanks, momentum of flow as well as the liquid circulation produced near the bottom surface of the vessel were found to be inferior as compared to that near the impeller and free liquid surface respectively (Ryma et al. 2013; Sun et al. 2006). This in turn has resulted in poor gas hold-up near the bottom surface of the reactor vessel (Sun et al. 2006). Kulkarni and Patwardhan (2012, 2014) have analysed the flow field characteristics during the onset of aeration in the reactor vessels. The interfacial turbulence quantities such as radial Root Mean Square (RMS) velocity, axial RMS velocity and turbulent kinetic energy have exhibited similar magnitudes during the onset of air entrainment irrespective of scale of the vessel, type of the impeller as well as size of the impeller respectively (Kulkarni and Patwardhan 2012). On the other hand, Kulkarni and Patwardhan (2014) have found that the instantaneous axial velocity, vorticity and strain rate on the air side of the interface achieve threshold values during the onset of aeration and substantially decreases thereafter in the reactor vessels agitated using the Disc Turbine (DT) and Pitched Blade Down flow Turbine (PBTD) impellers under various agitation speeds. From this literature review, it can be concluded that the past research works have mainly focussed on analysing the variations of free surface vortex, gas hold-up profiles, entrapment of air bubbles, circulation patterns and turbulence fields with the geometric and dynamic parameters of the surface aeration tank. However, the physical reasons causing such variations aren't explored so far in the literature which can help in developing optimal configurations of the surface aeration tank.

2.2.3 Summary

In summary, the mixing and dispersion processes in the surface aeration tanks exhibit considerable complexities regardless of the flow regime. The geometric and dynamic parameters of the tank have significant impact on the flow patterns and quality of mixing. The physical reasons causing variations in the N_p, oxygen transfer and mixing conditions with variations in the geometric and dynamic parameters of the reactor vessel aren't analysed so far in the literature. The detailed knowledge regarding the linkage between geometric and dynamic parameters of the vessel, flow field characteristics and performance goals is inevitable for optimal design of the reactor vessels (Başbuğ et al. 2018). This process requires proper characterisation of mean and turbulent flow fields near the impeller as well as in the bulk circulation region of the vessel (Joshi et al. 2011). Among the various geometric

parameters, the effect of $\frac{d}{D}$, N_{bl} and N_{bf} on the mean and turbulent flow fields associated with the reactor vessels aren't studied so far which is necessary for the optimal design of the same. Moreover, the optimal N_{bl} and N_{bf} required for achieving superior mixing and oxygen transfer in the reactor vessels need to be determined from the detailed flow field analysis.

2.3 Computational Fluid Dynamics (CFD) Modelling

The principle of CFD approach is to analyse the fluid flow phenomena by solving the set of governing equations describing the fluid dynamics and associated transport processes (if any) (Versteeg and Malalasekera 1995). Although, the CFD was initially used in the field of aerospace, advancements in the computational resources and modelling approaches have resulted in the extensive usage of the same in studying the fluid dynamics associated with the various engineering applications during the past three decades (Bakker et al. 2001). CFD modelling has several advantages, for example, its ability to provide detailed fundamental conceptions which are either experimentally expensive or unobtainable, such as local hydrodynamic features, phase distribution, heat and mass transfer rates respectively. Moreover, the CFD approach is helpful to avoid scale-up issues which has caused significant uncertainties in the design of agitated reactors. Sommerfeld and Decker (2004) have evaluated the developments and recent trends in the CFD for analysing the single phase and multiphase flows associated with the agitated reactors. Paramount efforts have been attributed in developing the CFD models for studying the fluid mixing in the agitated tanks over the past two decades. Recently, considerable efforts have been made in developing the CFD models for complex phenomena such as solid-liquid suspension (Guha et al. 2008; Montante and Magelli 2007), gas-liquid mixing (Kulkarni and Patwardhan 2014; Motamedvaziri and Armenante 2012) and mixing of non-Newtonian fluids (Adams and Barigou 2007; Pakzad et al. 2008) in the agitated vessels. Although, the CFD approach is an effective tool for analysing the flow field characteristics associated with the reactor vessels, accuracy of the predictions is affected by various factors such as modelling approach, additional models related with the underlying unit processes (such as turbulence model, multiphase model, surface tension model, impeller rotation model etc.) and various sources of numerical error.

2.3.1 Modelling approach

There are three modelling approaches with which the governing equations of fluid flow can be solved viz., (1) Direct Numerical Simulation (DNS), (2) Large Eddy Simulation (LES) and (3) Reynolds Averaged Navier Stokes (RANS) approach respectively. The energy spectrum illustrating the turbulence scales which are resolved and modelled in DNS, LES and RANS approaches is shown in Figure 2.2.

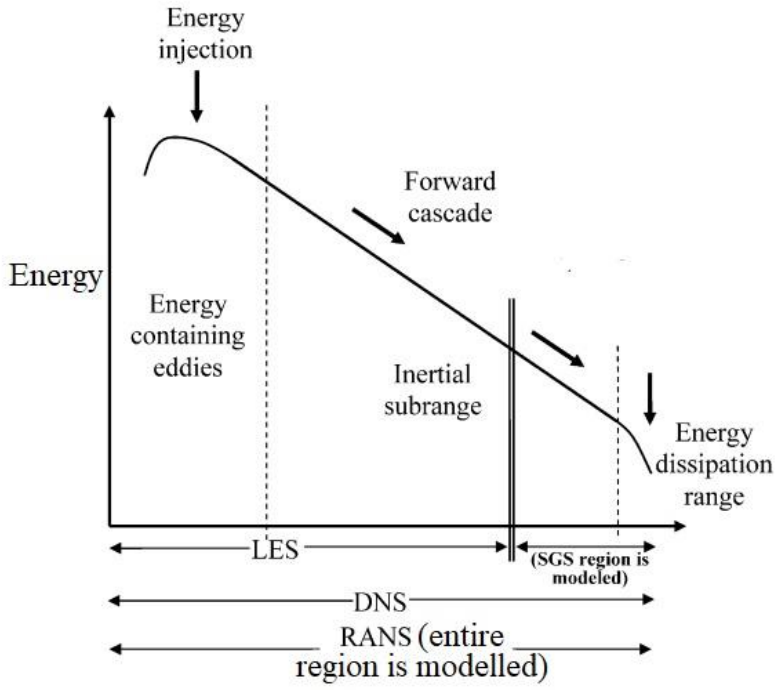

Figure 2.2: Energy spectrum of turbulence scales handled in various modelling approaches

(Source: Joshi et al. (2011))

In the DNS, continuity and momentum equations of fluid flow are solved exactly without using any turbulence modelling closure (Zhang et al. 2017b). Thus, it is possible to analyse the fully developed turbulent flow fields up to the micro-scale (Kolmogorov scale) and perform highly accurate calculations of the flow and transport processes (Joshi et al. 2011) respectively. However, the computational cost associated with the DNS is huge and it is impossible to employ this approach for modelling the large scale industrial vessels working even at moderate Reynolds numbers (Murthy and Joshi 2008). For example, the mesh size required for resolving all the energy containing and energy dissipating eddies in the mixing vessels is proportional to $R_e{}^{9/2}$ (Joshi et al. 2011). Hence, for the higher turbulent Reynolds numbers, the overall grid size becomes prohibitive and excessive computational time as well

as storage facilities is necessary for properly modelling the reactor flow fields (Liu 2016). Further, the time step for these transient simulations is very small as the temporal resolution is governed by the size of energy dissipating scales as compared to the mean flow or energy containing eddies (Joshi et al. 2011). Recently, with the advent of superior workstations and super computers, DNS approach was attempted by various authors such as Başbuğ et al. (2017, 2018), Steiros et al. (2017) and Zhang et al. (2017b) for modelling the reactor vessels working mainly in the laminar and transitional regimes.

In the LES approach, the computational cost of the simulations was reduced by providing appropriate treatments for the large scale and small scale eddies. The large scale eddies control the mixing and mass transport processes in the reactor vessels and varies according to the geometry and flow conditions associated with the reactor vessels. On the other hand, the small scale eddies are universal in nature and dissipates the energy transferred from the large scale eddies into the fluid contained within the reactor vessel (Joshi et al. 2011). In the LES approach, the energy containing (large scale) eddies are properly resolved due to its dynamic behaviour while the energy dissipating (small scale) eddies are properly modelled since its characteristics are invariant with the geometry and flow conditions in the reactor vessel (Murthy and Joshi 2008). The small scale eddies are modelled using sub-grid scale models which effectively represent the transfer of energy from large scale eddies to small scale eddies (Alcamo et al. 2005). In comparison with the DNS approach, the LES approach requires lesser computational cost and storage requirements and provides proper understanding of the local hydrodynamic characteristics of the agitated vessels (Joshi et al. 2011). In this regard, the LES approach has obtained wide acceptance among the researchers and often employed by several scholars such as Alcamo et al. (2005), Delafosse et al. (2008), Hartmann et al. (2004), Murthy and Joshi (2008) and Yeoh et al. (2004) for modelling the reactor vessels. However, the LES approach requires high resolution grids near the impeller and tank periphery so as to resolve the boundary layer gradients and thereby providing accurate predictions of turbulent quantities near the impeller and tank periphery respectively. Due to the restrictions in the computational facilities, many of the studies couldn't provide high resolution grids near the impeller and tank periphery and resulted in significant under prediction of the turbulent quantities (Gillissen and Van den Akker 2012; Menter 2012). In order to improve the computations of wall bounded flows from the LES approach, Detached Eddy Simulation (DES) approach was proposed. In the DES, the flow fields near the walls are simulated using the RANS approach while that away from the walls are simulated using the

LES approach (Lane 2017). This kind of LES-RANS blended scheme was often adopted by various scholars such as Gimbun et al. (2012) and Lane (2017) for modelling the agitated reactors.

From a practical point of view, the LES approach can't be used as a design tool due to the superior computational cost associated with the same. Moreover, the complex geometric conditions and high R_e of flow in the industrial reactor vessels pose difficulties in obtaining accurate flow field predictions within an affordable computational cost from the LES approach (Murthy and Joshi 2008). Due to these reasons, the RANS approach with adequate turbulence modelling closure is widely adopted for designing the reactor vessels by the industrial practitioners as well as the research community (Joshi et al. 2011). In the RANS approach, the governing equations of fluid flow are ensemble averaged over the entire energy spectrum of the reactor vessel, ie, all the turbulence scales present in the reactor vessel are modelled. The Reynolds stresses emerging from the ensemble averaging process are modelled using various turbulence models (Joshi et al. 2011). Although, the computational cost is significantly reduced due to the ensemble averaging process, it is difficult to achieve high quality predictions consistently from the RANS approach (Alcamo et al. 2005). However, the proper verification of various sources of numerical error was found to provide accurate and reliable predictions from the RANS approach (Coroneo et al. 2011) and hence this approach is extensively employed for modelling the complex flow pattern transitions (Montante et al. 2001), homogenization dynamics of the tracer (Coroneo et al. 2011), chemical reaction kinetics (Duan et al. 2016, 2018), thermal runaway and short stopping processes (Jiang et al. 2018; Zhang et al. 2017a) associated with the reactor vessels.

2.3.2 Turbulence modelling closures in the RANS approach

The fluctuating velocity components or the Reynolds stresses emerging from the ensemble averaging of the governing equations are generally modelled using zero, one or two equation turbulence models (Liu 2013). The background and performance of various turbulence models employed for modelling the flow fields in the reactor vessels are evaluated in the present sub-section and the advantages and limitations of the same are elucidated.

The standard $k-\varepsilon$ model is the most widely adopted turbulence model for analysing the flow field conditions associated with the reactor vessels (Deglon and Meyer 2006). This model provides transport equations for the turbulent kinetic energy and its dissipation rate for

calculating the turbulent viscosity and the Reynolds stresses associated with the fluid flow (Joshi et al. 2011). Although, this model assumes isotropic turbulence conditions and spectral equilibrium in solving the transport equations of turbulent kinetic energy and its dissipation rate, reliable and satisfactory performance obtained at affordable computational cost makes it as an attractive tool for the design of the reactor vessels (Joshi et al. 2011; Liu 2016).

In order to improve the flow field predictions from standard $k-\varepsilon$ model, Sahu et al. (1998) and Nere et al. (2001) have divided the reactor vessel into various zones based on the distinct flow physics and different sets of model parameters associated with standard $k-\varepsilon$ model were assigned to each zone so as to accurately predict the inhomogeneous flow conditions within the reactor vessel. The optimal values of the turbulence model parameters for each zone were obtained in a trial and error manner. Moreover, Nere et al. (2001) have formulated a new constitutive relationship for the eddy viscosity and obtained superior predictions of the various flow field characteristics associated with the reactor vessel. However, these approaches involving variations in the values of the turbulence model parameters from the standard $k-\varepsilon$ model are not recommended as the latter model is tested for wider range of fluid flow problems while the former models are applied only for limited range of fluid flow problems. Moreover, the studies of Coroneo et al. (2011), Deglon and Meyer (2006) and Montante et al. (2001) have exhibited significant improvements in the flow field predictions from the standard $k-\varepsilon$ model with proper verification of numerical errors related with the grid resolution and numerical discretization scheme respectively. Therefore, redundancies in the predictions from the standard $k-\varepsilon$ model is due to the underlying numerical errors while the adjustment of the parameters of the turbulence model just cover up these deficiencies and shows improvements in the flow field results (Liu 2016).

Several modifications in the formulation of the standard $k-\varepsilon$ model were attempted by various research scholars so as to improve the predictive performance of the same. In the Re-Normalization Group (RNG) $k-\varepsilon$ model, a modified eddy viscosity relationship based on the renormalization group theory was applied to obtain accurate predictions of the swirling flows within the reactor vessel (Joshi et al. 2011). This model provides effective formulation of the turbulence production and dissipation terms as well as the near wall flows within the reactor vessel. On the other hand, the realizable $k-\varepsilon$ model includes a new formulation of turbulent viscosity as well as an improved equation for the transport of turbulence dissipation rate based on the mean-squared vorticity fluctuation. This model formulation is capable of

effectively capturing the streamline curvature, rotation and vortices present in the reactor vessels (Basavarajappa et al. 2015). However, Jaworski et al. (1997) and Aubin et al. (2004) couldn't find much improvements in the performance of RNG and realizable $k-\varepsilon$ models as compared to the standard $k-\varepsilon$ model while Jaworski and Zakrzewska (2002) and Montante et al. (2001) have obtained poor predictions of turbulence quantities from the RNG and realizable $k-\varepsilon$ models as compared to the standard $k-\varepsilon$ model.

The multiscale model eliminates the assumption of spectral equilibrium related with the standard $k-\varepsilon$ model by providing separate transport equations for the turbulent kinetic energy of large scale vortices and inertial sub-range eddies respectively apart from the transport equation for the turbulence dissipation rate (Placek et al. 1986). This model formulation specifies separate time scales for the production and dissipation of turbulence and provides adequate prediction of the flow patterns associated with the reactor vessels (Joshi et al. 2011). In the Chen-Kim $k-\varepsilon$ model, an additional production range time scale is included into the transport equation of the turbulence dissipation rate which avoids the overshoot behaviour of the turbulent kinetic energy for the flow conditions involving higher values of mean strain rate (Chen and Kim 1987). However, the research works of Jaworski and Zakrzewska (2002) and Jenne and Reuss (1999) couldn't obtain even marginal improvements from these turbulence models as compared to the standard $k-\varepsilon$ model. Even though, Jenne and Reuss (1999) have reported improvements in the flow field predictions from the Chen-Kim $k-\varepsilon$ model after optimizing the underlying model parameters, the optimized Chen-Kim $k-\varepsilon$ model wasn't validated for variety of fluid flow problems related with the reactor vessels.

The wall functions associated with the standard $k-\varepsilon$ model provide inferior predictions of the flow fields in the near-wall region. In order to resolve this issue, transport equation of the turbulence dissipation rate is replaced by the transport equation of the turbulence eddy frequency (ω) which has led to the development of $k-\omega$ model (Singh et al. 2011). The $k-\omega$ model has performed well near the wall regions and properly modelled the behaviour of flow inside the boundary layers close to the impeller and tank periphery. However, the $k-\omega$ model provides poor performance away from the walls as the corresponding equations are over-sensitive to the free stream conditions (Lane 2017). Menter (1994) has derived the Shear Stress Transport (SST) model by combining the $k-\varepsilon$ and $k-\omega$ models and included a turbulence production limiter to accurately calculate the eddy viscosity term arising from

ensemble averaging process. Although, the SST model has provided accurate prediction of the flow fields involving separation and negative pressure gradients, excess damping of the turbulence terms has resulted in inadequate predictions of the turbulence features (Singh et al. 2011). Menter and Egorov (2005) have formulated the Scale Adaptive Simulation (SAS)-SST model in which a turbulence length scale is introduced and the respective value is adjusted to obtain proper predictions of the eddy viscosity and turbulence dissipation rate within the reactor vessel. The SAS-SST model can provide detailed characterization of turbulent structures present in the reactor vessel as the unsteady flow predictions are significantly improved with the use of the turbulence length scale (Egorov et al. 2010). Another improvement was also applied to SST model for capturing the swirl or curvature in the fluid flow by modifying the turbulence production term present in the transport equation of turbulent kinetic energy (Lane 2017). Singh et al. (2011) have analysed the performance of standard $k-\varepsilon$ model, SST model, SAS-SST model and SST model with curvature correction for predicting the flow fields associated with the reactor vessel. Although, these models provide adequate predictions of mean velocities and trailing vortex patterns, the predictions of turbulent kinetic energy and turbulence dissipation rate were found to be inferior as compared to the experimental values. Alonzo-Garcia et al. (2019) have also reported insignificant improvements with the SST model in predicting the mean and turbulent flow fields as compared to the RNG and realizable $k-\varepsilon$ models.

The Reynolds Stress Model (RSM) is an anisotropic turbulence model which provides six individual transport equations for the Reynolds stress terms and an additional transport equation for the turbulence dissipation rate for modelling the flow fields related with the reactor vessels (Jenne and Reuss 1999). The equations of Reynolds stress contain the terms related with the flux of Reynolds stress and pressure strain rate which can accurately model the streamline curvature, rotational strains and vortex characteristics associated with the reactor vessels (Joshi et al. 2011). Even though, the formulation of RSM is appropriate for modelling the anisotropic turbulence conditions as well as rotating flows within the reactor vessel, this approach wasn't much successful in modelling the flow fields associated with the reactor vessels. Due to the presence of large number of transport equations, computational cost associated with the RSM is much higher than that of the standard $k-\varepsilon$ model (Joshi et al. 2011; Liu 2016; Murthy and Joshi 2008) and poses difficulties in numerical convergence of the solutions (Aubin et al. 2004; Lane 2017). Moreover, the parameters associated with the RSM are non-universal in nature (Joshi et al. 2011) and several studies (Bakker et al. 1996;

Jaworski and Zakrzewska 2002; Montante et al. 2001; Singh et al. 2011) have reported insignificant improvements in the predictions from the RSM as compared to the standard $k-\varepsilon$ model. In order to reduce the computational difficulties associated with the RSM, an alternative turbulence model known as Algebraic Stress Model (ASM) was developed by Rodi (1976). The partial differential equations associated with the RSM are converted into a set of algebraic equations by suitably approximating the convection and diffusion terms present in the same. This transformation reduces the computational cost while keeps the anisotropic features of the RSM with the algebraic equations thus derived (Feng et al. 2012). Unfortunately, significant reduction in the computational cost wasn't achieved for the ASM in comparison with the RSM as the Reynolds stress terms are implicitly present in the algebraic expressions of ASM. In order to reduce the computational cost of ASM, an Explicit Algebraic Stress Model (EASM) was developed by Pope (1975) and later modified by various authors (Gatski and Speziale 1993; Sun et al. 2002; Wallin and Johansson 2000). In the EASM, the Reynolds stress terms present in the equations are replaced with an algebraic correlation of rotation rate, mean strain rate and turbulence characteristics in an explicit manner. The EASM has greatly simplified the CFD modelling process and improved the stability of the numerical solutions (Feng et al. 2012). Feng et al. (2012) have modelled the anisotropic turbulent flow conditions in the reactor vessels using the EASM and compared the respective predictions with the predictions from the standard $k-\varepsilon$ model, ASM, RSM and LES methods available in the literature. Although, the EASM has provided adequate predictions of mean velocities, the predictions of random velocity fluctuations and turbulent kinetic energy were similar to that obtained from the standard $k-\varepsilon$ model.

The comparative analysis of the performance of various turbulence models illustrate that there is no single turbulence model which can provide accurate predictions of the mean and turbulent flow fields within a satisfactory computational cost. The standard $k-\varepsilon$ model is an appropriate choice for modelling the flow conditions in the reactor vessels as it provides superior predictions of the mean and turbulent flow fields at an affordable computational cost. On the other hand, attempts in improving the accuracy of standard $k-\varepsilon$ model have resulted in the complex model formulations which have unnecessarily increased the computational requirements and numerical issues without producing substantial improvements in the flow field predictions from the standard $k-\varepsilon$ model.

2.3.3 Modelling of multiphase flows in reactor vessels

The multiphase flow regimes associated with the reactor vessels can be classified into three categories such as gas-liquid flows, liquid-solid flows and solid-liquid-gas flows respectively. The multiphase flow emphasizes the presence of a single or multiple materials which make adequate interaction and inertial response with the flow as well as with the potential field within which the same are immersed. The dynamics of multiphase flows in the reactor vessels is analysed using two approaches in the CFD viz. Euler-Euler approach and Euler-Lagrange approach respectively.

In the Euler-Euler method, the continuity and momentum equations corresponding to each phase of the system under consideration are coupled using empirical constitutive relationships and are solved to obtain the flow and transport characteristics associated with the system. In this method, different phases present in the system are considered mathematically as interpenetrating continua and the theory of phase volume fraction is adopted. The volume of each phase present in the system doesn't vary during the simulations and the sum of the volume fraction of all the phases is equal to unity. This method is widely preferred for modelling the flow and mass transfer processes associated with the various industrial reactor vessels (ANSYS 2013).

In the Euler-Lagrange method, the conservation (or Navier-Stokes) equations are solved in the fluid phase of the system while the dispersed phase is modelled by tracking the large number of droplets, particles and bubbles which move through the flow field thus calculated. The dispersed phase exchanges the mass, momentum and energy with the fluid phase. However, this method can be adopted only when the dispersed phase comprises of negligible volume fraction in the system although high mass loading of the same is permitted. The particle or bubble or droplet trajectories are calculated separately during the calculations of the fluid phase at specified intervals. This method is suited for modelling the particle laden flows, spray dryers and coal or liquid fuel combustion while unsuitable for modelling the liquid-liquid dispersions, fluidized beds and any other applications in which the volume fraction of the dispersed phases can't be ignored (ANSYS 2013).

The Euler-Euler multiphase models are classified into three categories such as Volume of Fluid (VOF) model, mixture model and Eulerian model respectively.

(1) Volume of Fluid (VOF) model: The VOF model solves a single set of momentum equations to model the volume fraction of each phase in the entire domain of the vessel as well as the location of different phases considered for the analysis (Kulkarni and Patwardhan 2014). Thus, the VOF model is highly suitable for tracking the position of interface between different phases and widely adopted by various researchers (Haque et al. 2006; Kulkarni and Patwardhan 2014; Mahmud et al. 2009; Yamamoto et al. 2019; Zhang et al. 2018) for analysing the characteristics of air-liquid interface (shape, location, extent) associated with various geometric configurations of the reactor vessels. The computational mesh for the VOF method is fixed in nature and this method is applied for the problems involving more than two immiscible fluids (ANSYS 2013). The VOF method is again divided into explicit scheme and implicit scheme respectively. The implicit scheme solves a standard scalar transport equation for each of the dispersed phases in an iterative manner at each time step to obtain the volume fraction values at the current time step. On the other hand, the explicit scheme doesn't require such iterative solutions of the scalar transport equation at each time step since the volume fraction values of the previous time step are adopted in the interpolation schemes.

(2) Mixture model: The mixture model is adopted to analyse the multiphase systems in which the different phases move at different velocities and a local equilibrium is assumed to exist over the short spatial length scales. The mixture model solves the continuity, momentum and energy equations for the mixture, volume fraction equations for the phases present in the system and the algebraic equations for the relative velocities associated with the various phases. The mixture model is an effective alternative for the full Eulerian model for various engineering applications. A full Eulerian multiphase flow model isn't feasible in the applications involving wider distribution of particulate phases, inadequate knowledge regarding the interphase laws and unreliable formulation of the interphase laws. The mixture model has the simplified formulation among the various multiphase models and often used to compute the non-Newtonian viscosity. The mixture model is mainly applied to analyse the bubbly flows, particle laden flows and sedimentation process associated with the various industrial systems (ANSYS 2013).

(3) Eulerian model: In the Eulerian model, continuity and momentum equations corresponding to each phase of the system are coupled using pressure and interface exchange coefficients and solved to obtain the underlying flow and transport characteristics. The Eulerian model is the most complicated formulation among the various multiphase models.

The exchange of momentum between the phases and the way of coupling of governing equations are different for the liquid-solid and liquid-liquid flows respectively. The Eulerian model is mainly applied to analyse the flow and transport conditions associated with the bubble columns and fluidized bed reactors respectively (ANSYS 2013).

2.3.4 Verification of numerical errors

A mathematical model represents a physical system in terms of a set of partial differential equations, allied auxiliary equations along with the proper boundary conditions and initial conditions respectively. In scientific computing, it is necessary to find approximate solutions to the mathematical model by discretizing the domain of the system as well as the underlying model equations. The approximation errors related with the discretization process are known as the discretization errors (Roy 2010). The discretization error emerges from the interplay between the grid resolution, numerical discretization scheme adopted, quality of grid and type of elements used for discretizing the geometry. The discretization error is the largest source of numerical error as compared to the other sources such as round-off error and statistical sampling error respectively (Phillips and Roy 2011). The discretization error is basically classified into two categories such as apriori estimates and posteriori estimates respectively. In the apriori method, approximate bounds on the solution derivatives are determined by relating the truncation error with the discretization error through discretization error transport equation (Cavallo et al. 2008; Celik and Hu 2004). However, the error bounds obtained from this method are usually much higher than the true discretization error and hence this method is not popular for quantifying the numerical discretization error (Roy 2010). A posteriori method is widely used for quantifying the discretization error associated with the various applications based on the solutions obtained from the numerical simulations along with the necessary additional information. The discretization error is computed relative to the exact solution of the mathematical model (Roy 2010). A posteriori estimates are again divided into two categories such as higher order methods and residual methods respectively. In the higher order method, solution with higher formal order of accuracy as compared to the underlying solutions is determined and considered as the exact solution of the mathematical model for quantifying the numerical error (Phillips and Roy 2011). In the residual method, detailed knowledge regarding the discretization error is obtained by incorporating the specific information related with the problem under consideration in the error estimates (Roy 2010). The higher order methods are widely adopted since the residual methods are code intrusive

and difficult to implement for the practical engineering applications (Phillips and Roy 2014). The Richardson extrapolation is the popular higher order method which is widely adopted and often recommended by the American Society of Mechanical Engineers (ASME) and the American Institute of Aeronautics and Astronautics (AIAA) for quantifying the discretization error (Xing and Stern 2010).

The discretization error is defined as the difference between exact solution to the mathematical model and exact solution to the discrete algebraic equations. The discretization error decreases with the grid refinement process. The theoretical rate of decrease of discretization error with the systematic grid refinement is known as formal order of accuracy of the numerical discretization scheme (Phillips and Roy 2013). In the Richardson extrapolation method, discrete solutions from two systematically refined grids which are in asymptotic range and order of accuracy of the numerical discretization scheme were used to calculate the discretization error (Phillips and Roy 2014). However, it is very difficult to obtain the discrete solutions which are in asymptotic range for the practical engineering applications which leads to unreliable discretization error estimates from the Richardson extrapolation method (Phillips and Roy 2014). In order to overcome this issue, absolute value of discretization error obtained from the Richardson extrapolation is considered as an uncertainty estimate which is multiplied by a factor of safety and specified as an error band for the solutions obtained from finer grids (Phillips and Roy 2011). The Grid Convergence Index (GCI) (Roache 1994) is the widely accepted method for this purpose in which the discretization error from any grid refinement study is converted into an equivalent uncertainty estimate which would have been obtained if the underlying grids are systematically refined. Roache (1994) has developed the uncertainty estimate based on the concept that doubling the number of grid elements (or halving the size of each element) with a second order accurate numerical discretization scheme can provide flow field solutions within the asymptotic range of convergence. The GCI produces reasonable error bars for the fine grid solutions obtained from the grid independence studies. That means, the GCI provides a level of confidence or certainty (mostly 95%) with which the fine grid solution is related to the true solution in 95% of cases. The indication of such level of confidence in the CFD simulations is the major goal associated with the grid independence studies (Roache 2003). In the GCI method, factor of safety is decided according to the knowledge of nearness to the asymptotic range of convergence of the flow field solutions (Phillips and Roy 2013). Roy (2010) has provided explicit guidelines for selecting the factor of safety so as to avoid infinite or unreasonably

smaller GCI estimates. Several other formulations have been developed to determine the factor of safety for calculating the GCI in the literature such as global averaging method (Cadafalch et al. 2002), Correction Factor method (Stern et al. 2001), Factor of Safety method (Xing and Stern 2010) and Least Squares method (Eça and Hoekstra 2009) respectively. However, these formulations were tested for limited number of problems and their applicability to the complex engineering problems needs to be studied further.

The analyses of discretization error associated with the flow fields of the agitated reactor vessels aren't popular among the research community. Although, the grid independence study has been performed by most of the researchers, these studies lack uniformity in analysing the performance of various grids and reporting of the results from the same. In other words, grid independence studies in the literature are not performed in a systematic manner and the corresponding results are reported in an inconsistent and confusing manner (Roache 1994). The systematic and uniform reporting of grid independence studies requires quantification of discretization error or uncertainty associated with the various flow field variables. The GCI is the most popular method for quantifying the numerical uncertainty related with the various engineering applications (Freitas 2002; Roy 2010). However, few scholars have only determined the numerical uncertainty of reactor flow fields in terms of GCI. Coroneo et al. (2011) have quantified the GCI associated with the global flow quantities such as power number based on torque of rotating or stationary walls (N_{pt}), power number based on overall turbulence dissipation rate ($N_{p\varepsilon}$) and N_q respectively. The GCI of these flow quantities were found to decrease with increase in the grid resolution. Moreover, this study has concluded that accurate and numerically converged predictions of turbulent flow fields can be obtained with high resolution or finer grids while the same for mean velocity fields, N_{pt} and N_q can be achieved with low resolution or coarser grids. Karimi et al. (2012) have used the GCI for quantifying the numerical uncertainty associated with the tangential and axial velocities of the hydrocyclone and concluded that the GCI is a methodical and practical tool for building confidence in the CFD predictions. Alonzo-Garcia et al. (2019) have also quantified the GCI of $N_{p\varepsilon}$ associated with the reactor configurations discretized using Cut-Cell and tetrahedral grid schemes respectively so as to determine the optimal grid scheme for discretizing the reactor vessel. These studies have mainly quantified the GCI associated with the mean flow quantities while the same related with the local turbulent flow fields weren't determined. However, the numerical convergence of local turbulent flow fields is much difficult as

compared to the mean flow fields (Roy 2010) and hence it is more important to quantify the GCI associated with local turbulent flow fields as compared to the mean flow fields so as to properly fix the adequate grid resolution for the modelling purposes. Moreover, the error bands associated with the predictions from the CFD models of reactor vessels weren't provided by any of the scholars although it is the main purpose of the grid independence studies.

The accuracy of the CFD predictions is also linked with the type of numerical scheme adopted for discretizing the underlying partial differential equations (Aubin et al. 2004). The comparative analyses of the performance of various discretization schemes done by Aubin et al. (2004), Coroneo et al. (2011) and Deglon and Meyer (2006) indicate that the first order upwind scheme significantly under predicts the turbulent kinetic energy and its dissipation rate while the higher order schemes such as second order upwind, central differencing and Quadratic Upstream Interpolation for Convective Kinematics (QUICK) schemes provide much better prediction of the same. However, the prediction of mean flow fields were unaffected by the type of the discretization scheme. Lane (2017) and Singh et al. (2011) have employed a high resolution discretization scheme for the discretization of the convective terms present in the governing equations of fluid flow. However, the efficiency of third order Monotone Upstream-Centered Schemes for Conservation Laws (MUSCL) scheme and convection-diffusion based Power-law scheme in predicting the mean and turbulent flow fields associated with the reactor vessels haven't been evaluated till now and the same needs to be studied further for possible improvements in the accuracy of CFD predictions.

The predictions from the RANS approach are also affected by the type of elements used for discretizing the domain of the agitated reactors. Majority of the studies have adopted the structured or unstructured hexahedral elements for discretizing the computational domain of the agitated vessel. The generation of structured grids comprising of hexahedral elements requires considerable efforts and time while the unstructured grids consisting of tetrahedral elements can be generated in a faster manner even for complex geometric configurations of the reactor vessel (Longest and Vinchurkar 2007). The structured grids provide accurate flow field predictions whereas the unstructured grids increase the numerical diffusion error resulting in inferior prediction of the reactor flow fields (Longest and Vinchurkar 2007). Alonzo-Garcia et al. (2019) have compared the performance of two unstructured grid schemes viz., cut-cell and tetrahedral grid schemes in modelling the flow fields associated with the

reactor vessel agitated using the PBT impeller. They have found that the predictions from the cut-cell grid scheme are better than that obtained from the tetrahedral grid scheme. Longest and Vinchurkar (2007) and Vinchurkar and Longest (2008) have observed that it is necessary to develop hybrid grid schemes by combining the tetrahedral and hexahedral elements for effectively modelling the reactor flow fields at less computational cost. Thus, the comparative study of the performance of various grid types in modelling the agitated vessels is required.

From the review of literature, it can be inferred that the RANS approach with standard $k-\varepsilon$ model closure is an efficient tool for effective modelling of the flow field characteristics associated with the reactor vessels at less computational cost. The numerical errors arising from grid resolution, numerical discretization scheme and type of elements adopted for discretizing the reactor domain considerably affect the accuracy and numerical convergence of the flow field predictions. Apart from the routine grid independence studies, discretization error or numerical uncertainty associated with the various flow fields weren't quantified in a systematic manner in the literature. Similarly, the performance of hybrid grids as well as the MUSCL and power-law numerical discretization schemes needs to be evaluated to select the appropriate grid and numerical discretization scheme for the accurate prediction of various flow field quantities.

2.3.5 Impeller modelling approaches

Impeller modelling schemes are necessary for simulating the relative movement between the rotating impeller and stationary periphery of the tank. The impeller modelling schemes are basically classified into steady state and unsteady state approaches. The steady state approach include Impeller Boundary Condition (IBC) method (Ranade and Joshi 1990), Source Sink (SS) method (Pericleous and Patel 1987), Inner-Outer (IO) method (Brucato et al. 1994), Multiple Reference Frame (MRF) method (Luo et al. 1994) and Snapshot method (Ranade and Dommeti 1996) respectively. In the IBC method (Gosman et al. 1992; Kresta and Wood 1991; Ranade and Joshi 1990), experimentally measured velocity and turbulence fields are provided as boundary conditions at a selected surface around the impeller. As a result, flow field characteristics within the impeller swept region can't be obtained. The variations in the geometry or flow conditions of the reactor vessel necessitate the corresponding experimental measurements of velocity and turbulent flow fields for the modelling purposes. Due to these reasons, IBC method isn't presently used for modelling the reactor vessels. In the SS

approach (Pericleous and Patel 1987; Xu and McGrath 1996), impeller is considered as the source of momentum while the baffles are considered as the sinks of momentum. The blades are divided into number of vertical strips from disc region to the tip of impeller blades. Each strip is considered as an aerofoil and the aerodynamics of the aerofoil is solved in each strip to obtain flow fields in the reactor vessel. However, this method is not widely applied by various researchers for modelling the reactor vessels. In the IO method (Brucato et al. 1994) and MRF method (Luo et al. 1994), the reactor vessel is divided into an inner zone containing impeller and an outer zone containing tank and baffle walls respectively. The interface (or boundary) between the inner and outer zones are partially overlapped for IO method while no overlapping is provided in the case of MRF method. The typical diagram showing the rotating and stationary zones associated with the reactor vessel is illustrated in Figure 2.3.

In the IO method, governing equations are solved in a rotating frame of reference in the inner zone using arbitrary boundary conditions applied on its boundary and the resulting flow fields are transferred to the inner boundary of the outer zone for computing the flow fields in the outer zone using the black box approach. The new flow fields at the inner boundary of outer zone are used as the boundary conditions for computing the flow fields in the inner zone in the next iteration. This iterative process is continued till the system achieves satisfactory numerical convergence.

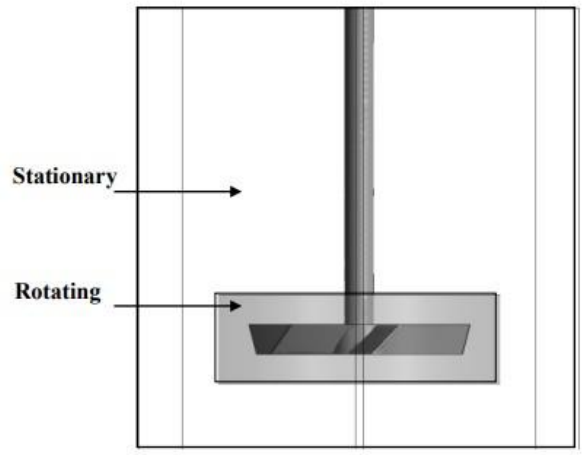

Figure 2.3: Rotating and stationary zones in the computational domain considered for the modelling purposes

(Source: Liu (2013))

In the MRF method, governing equations are solved in a rotating frame of reference in the inner zone and the resulting flow fields are used as the boundary conditions for computations in the outer zone in a stationary frame of reference. The new flow fields from the outer zone are used as the boundary conditions for the computations in the inner zone and this process is continued until the system achieves adequate numerical convergence. Since the frames of reference of inner and outer zones are different, solutions which are iteratively exchanged between both the zones are corrected for the relative movement between impeller and baffles and azimuthally averaged over the boundary separating both the zones in the IO and MRF methods. The MRF and IO methods provide appropriate modelling of the impeller rotation and the former method is computationally less intensive as compared to the latter method and widely adopted for modelling the reactor vessels (Joshi et al. 2011). In the snapshot approach (Ranade and Dommeti 1996), time derivative terms present in the inner zone are converted into spatial derivative terms and added to the source term present in the governing equations of fluid flow. Since, the time derivative terms associated with the outer zone are weak, the corresponding terms are neglected in the governing equations of fluid flow. Moreover, additional mass source and sink terms are included in the computational cells near the impeller so as to simulate the rotation effects of the impeller. However, this method is not properly validated for various types of fluid flow problems and hence not widely preferred for modelling the reactor vessels.

The unsteady approach for modelling the impeller rotation include Sliding Mesh (SM) method (Luo et al. 1994), Moving deforming grid technique (Perng and Murthy 1994) and Adaptive Force Field Technique (AFT) (Joshi et al. 2011) respectively. In the SM method (Luo et al. 1994; Murthy et al. 1994), the reactor vessel is divided into an inner domain containing impeller and an outer domain containing tank and baffle walls respectively. The inner and outer domains of the vessel are gridded separately as a block. The grid associated with the outer domain is considered as fixed while that associated with the inner domain is assumed to rotate with the speed of impeller. The rotation of the inner domain is incorporated into the model by explicitly adding the acceleration terms due to the rotation of the impeller into the momentum equations. The solutions from both the domains are corrected for the relative movement between the impeller and tank periphery, interpolated and coupled at the interface separating both the domains using the sliding grid algorithm. In the moving deforming grid technique (Perng and Murthy 1994), a single grid is employed for the rotating and stationary parts. The grid near the impeller is deformed according to the rotation of the

impeller and the deformation is further extended from impeller to the periphery of the reactor vessel. The grid is continuously deformed during the calculations until the minimum prescribed grid quality is achieved. Thereafter, the grid is restored back to its original form before the commencement of further simulation and the properties of the deformed grid are transferred to the restored grid in a conservative manner. Although, the concept of this technique properly accounts the impeller baffle interactions, computational requirements to maintain the necessary quality of the grid and to reduce the numerical error arising from such poor quality grids is enormous. The computational cost associated with this method is highest among the various impeller modelling approaches. In the AFT method (Joshi et al. 2011), the fluid is assumed as a system consisting of large number of particles and each particle occupies a corner of a lattice. The conservation equations of mass and momentum are solved for each particle so as to obtain the flow field characteristics in the reactor vessel. The impeller, baffle walls and tank periphery are described using a set of control points on their periphery. The tangential velocities of the control points on the impeller surface depends on the impeller speed while that on the baffle walls are zero. At each time step, force field in the reactor system is computed in such a way that the difference between the calculated and prescribed tangential velocities in the control points of the impeller and baffle walls is minimal. This method doesn't uses grid for the computational purposes and the new designs can be easily developed by adjusting the control points. Although, this method provides accurate prediction of flow fields in the reactor vessel, huge computational cost associated with the same makes it unsuitable for most of the practical engineering problems.

Among these impeller rotation models, SM method is an effective tool for analysing the time varying flow fields associated with the reactor vessels. On the other hand, this method demands excessive computational requirements in terms of higher simulation time, storage facilities and computer memory (Coroneo et al. 2011). This fact in turn provides restrictions in the computational cells to be used for the simulations and decreases the quality of the flow field predictions. Moreover, proper care needs to be provided to avoid numerical issues arising from interpolation procedure as well as rotating grid at the interface separating both the domains (Joshi et al. 2011). These reasons make the SM method less attractive as a tool for designing the industrial reactor vessels. Moreover, various research works (Aubin et al. 2004; Coroneo et al. 2011; Deglon and Meyer 2006; Wechsler et al. 1999) have reported that the predictions from the SM and MRF methods are highly comparable and the computational

cost of the latter method is much lower than that from the former method. Hence, the MRF method became a popular choice for modelling the industrial reactor vessels.

The position of MRF boundary separating the inner and outer zones is a crucial parameter which affects the accuracy of the flow field predictions in the reactor vessel. The transformation of velocity fields from inner zone to outer zone as well as from outer zone to inner zone occurs at the MRF boundary and hence its location or position significantly affects the numerical convergence and accuracy of the flow field predictions (Remaki et al. 2017). Although, the position of MRF boundary significantly affects the accuracy of the CFD predictions, there is no any clear-cut idea regarding the proper position of the same which produces accurate prediction of the flow field quantities. Majority of the studies have considered engineering judgements while selecting the MRF boundary and only few scholars have addressed the issue in a scientific manner. The studies of Brucato et al. (1998), Joshi et al. (2011), Luo et al. (1994) and Ochieng et al. (2008) have suggested to provide the MRF boundary at a location having minimum spatial and temporal variations of the flow field variables while Bartels et al. (2000), Coroneo et al. (2011), Deglon and Meyer (2006) and Wechsler et al. (1999) have assumed the extent of vortex and turbulence activity around the impeller as the MRF extents for modelling the flow fields in the stirred tank reactors. Norouzi-Firouz et al. (2018), Oshinowo et al. (2000), Patil et al. (2021), Shi and Rzehak (2018) and Zadravec et al. (2007) have varied the position of the MRF boundary and determined the optimal position of the same. Oshinowo et al. (2000) have kept the MRF boundary at the mid-way between impeller and baffle walls while Zadravec et al. (2007) and Norouzi-Firouz et al. (2018) have concluded to provide larger MRF boundaries for accurate predictions of the flow field variables. The conclusions from these studies are mutually contradicting in nature and needs further investigations to clarify this issue. Moreover, the recommendation of larger MRF boundary for modelling the impeller rotation by Zadravec et al. (2007) and Norouzi-Firouz et al. (2018) is technically incorrect as the researchers can adopt the tank periphery as the MRF boundary. But the MRF boundary should be located at a suitable position between the impeller and tank periphery for the proper transformation of the flow fields from the inner zone to the outer zone (Remaki et al. 2017). Apart from the above mentioned drawbacks in the literature, majority of the studies have considered the standard reactor configuration for determining the optimal extents of the MRF boundary. However, it is necessary to determine the optimal MRF extents for the non-standard reactor configurations which are either of research interest or widely used for the practical engineering applications.

Since the position of MRF boundary is sensitive to the geometric configuration, it is expensive to perform a series of numerical simulations for determining the optimal position of the same for various non-standard configurations of the reactor vessel. In this scenario, it is necessary to develop a generalized criterion for selecting the optimal position of the MRF boundary for any configuration of the reactor vessel agitated using any type of impeller.

2.4 Summary of review of literature and research gaps

From the comprehensive review of literature, it was found that the geometric and dynamic parameters of the reactor vessel affect the underlying flow field characteristics. The double loop pattern associated with the standard reactor vessel changes into single loop pattern with significant reduction in N_p under low and high clearance conditions respectively. Past studies have determined the critical impeller clearance causing such flow pattern transition and analysed the flow field characteristics associated with the standard, low and high clearance vessels respectively. However, physical reasons causing double loop to single loop pattern transition and consequent reduction in the N_p still remain as mystery among the research community. The high clearance vessels provide significant oxygen transfer into the reactor vessel and hence employed as surface aerators in the wastewater treatment plants. The past studies have evaluated the geometric and dynamic conditions of the vessel suitable for the surface aeration process and the flow field characteristics related with the respective configurations. However, the physical reasons causing surface aeration under various geometric and dynamic conditions of the vessel aren't properly explored in the literature. Similarly, flow field characteristics in a reactor vessel under various R_e of flow were analysed while the physical reasons causing variations in the performance goals with variations in the N and D aren't elucidated. Moreover, it is necessary to determine the optimal N_{bl} and N_{bf} required for achieving superior mixing conditions in the reactor vessels since a contradiction is persisting in this issue among the literature. Although, the effect of $\frac{h}{D}$ and R_e of flow on the reactor flow fields were widely analysed in the literature, the effect of $\frac{d}{D}$, N_{bl} and N_{bf} on the reactor flow fields aren't properly investigated so far which is necessary for optimal design of the aeration tanks. Therefore, the physical reasons causing variations in the power number, oxygen transfer and mixing performance with variations in the geometric and dynamic parameters of the reactor vessels weren't analysed so far. Such kind of analyses is extremely important for designing the optimal configurations of the reactor vessels (Başbuğ et al. 2018).

In other words, proper understanding of the linkage between the tank parameters, flow field characteristics and performance goals (power number, mixing and oxygen transfer) is the starting step for the design of the reactor vessels (Joshi et al. 2011; Karpinska and Bridgeman 2016).

The CFD is an efficient tool for the detailed characterization of mean and turbulent flow fields associated with the reactor vessels. The RANS approach with standard $k-\varepsilon$ model is an attractive tool for the design of reactor vessels since accurate predictions of flow field variables can be obtained at affordable computational cost. The numerical errors arising from grid resolution, numerical discretization scheme and grid type need to be properly minimized to obtain accurate predictions from the standard $k-\varepsilon$ model. Although, the grid independence study of the flow fields were performed by various researchers, discretization error or numerical uncertainty associated with the same weren't quantified in a systematic manner. Similarly, the performance of hybrid grid schemes as well as numerical discretization schemes such as MUSCL and power-law schemes need to be analysed. The pseudo-steady MRF method is widely adopted for modelling the impeller rotation as it provides accurate flow field predictions at lesser computational cost in comparison with the unsteady SM method. However, the literature didn't provide a clear-cut idea regarding the selection of optimal position of MRF boundary and it is necessary to develop a generalized criterion for obtaining the optimal position of the MRF boundary for non-standard configurations of the reactor vessels. Finally, the flow field predictions after the numerical verification process from the RANS approach with standard $k-\varepsilon$ model closure need to be validated by comparing the same with the corresponding results from the experimental approach as well as from the other complex turbulence models respectively.

2.5 Objectives

Based on the research gaps extracted from the comprehensive literature review, the following objectives are proposed for the present research work.

(1) To determine the optimal grid resolution, discretization scheme and type of grid for the development of CFD model of surface aeration tank

(2) To develop a generalized criterion for selecting the optimal extents of MRF boundary for any tank geometry agitated using any type of impeller

(3) To determine the optimal N_{bl} as well as N_{bf} for obtaining the optimal mixing performance of the surface aeration tanks

(4) To determine the physical reasons causing variations in the flow patterns and performance goals with the variations in the geometric and dynamic parameters of the tank such as $\frac{h}{D}$, $\frac{d}{D}$, N_{bl}, N_{bf} and N.

2.6 References

Adams, L. W., and M. Barigou. 2007. “CFD Analysis of Caverns and Pseudo-Caverns developed during Mixing of Non-Newtonian Fluids.” *Chem. Eng. Res. Des.*, 85 (5): 598–604. https://doi.org/10.1205/cherd06170.

Alcamo, R., G. Micale, F. Grisafi, A. Brucato, and M. Ciofalo. 2005. “Large-eddy simulation of turbulent flow in an unbaffled stirred tank driven by a Rushton turbine.” *Chem. Eng. Sci.*, 60 (8–9): 2303–2316. https://doi.org/10.1016/j.ces.2004.11.017.

Alonzo-Garcia, A., V. X. Mendoza-Escamilla, S. A. Martinez-Delgadillo, I. Gonzalez-Neria, C. Del C Gutiérrez-Torres, and J. A. Jiménez-Bernal. 2019. “On the performance of different RANS based models to describe the turbulent flow in an agitated vessel using non-structured grids and PIV validation.” *Brazilian J. Chem. Eng.*, 36 (1): 361–382. https://doi.org/10.1590/0104-6632.20190361s20180091.

ANSYS, Inc. 2013. *ANSYS Fluent Theory Guide*. USA: ANSYS.

Armenante, P. M., and E. U. Nagamine. 1998. “Effect of low off-bottom impeller clearance on the minimum agitation speed for complete suspension of solids in stirred tanks.” *Chem. Eng. Sci.*, 53 (9): 1757–1775.

Armenante, P. M., E. U. Nagamine, and J. Susanto. 1998. “Determination of Correlations to Predict the Minimum Agitation Speed for Complete Solid Suspension in Agitated Vessels.” *Can. J. Chem. Eng.*, 76: 413–419.

Aubin, J., D. F. Fletcher, and C. Xuereb. 2004. “Modeling turbulent flow in stirred tanks with CFD: The influence of the modeling approach, turbulence model and numerical scheme.” *Exp. Therm. Fluid Sci.* https://doi.org/10.1016/j.expthermflusci.2003.04.001.

Backhurst, J. R., J. H. Harker, and S. N. Kaul. 1988. “The performance of pilot and full-scale vertical shaft aerators.” *Water Res.*, 22 (10): 1239–1243. https://doi.org/10.1016/0043-1354(88)90110-8.

Bakker, A., A. H. Haidari, and L. M. Oshinowo. 2001. “Realize greater benefits from CFD, Fluid/Solid Handling.” *AIChE’s CEP Mag.*, March 2001.

Bakker, A., K. J. Myers, R. W. Ward, and C. K. Lee. 1996. “The laminar and turbulent flow pattern of a pitched blade turbine.” *Trans IChemE,* 74 (A): 485–491.

Bartels, C., M. Breuer, and F. Durst. 2000. “*Comparison between Direct Numerical Simulation and k-ε Prediction of the Flow in a Vessel Stirred by a Rushton Turbine.*” In *Proc., Tenth Eur. Conf. Mix.*, 239–246. Delft, The Netherlands: Elsevier Science B. V.

Basavarajappa, M., T. Draper, P. Toth, T. A. Ring, and S. Miskovic. 2015. “Numerical and experimental investigation of single phase flow characteristics in stirred tanks using Rushton turbine and flotation impeller.” *Miner. Eng.*, 83: 156–167. https://doi.org/10.1016/j.mineng.2015.08.018.

Başbuğ, S., G. Papadakis, and J. C. Vassilicos. 2017. “DNS investigation of the dynamical behaviour of trailing vortices in unbaffled stirred vessels at transitional Reynolds numbers.” *Phys. Fluids,* 29 (6): 064101. https://doi.org/10.1063/1.4983494.

Başbuğ, S., G. Papadakis, and J. C. Vassilicos. 2018. “Reduced power consumption in stirred vessels by means of fractal impellers.” *AIChE J.*, 64 (4): 1485–1499. https://doi.org/10.1002/aic.16096.

Bates, R. L., P. L. Fondy, and R. R. Corpstein. 1963. “An Examination of Some Geometric Parameters of Impeller Power.” *Ind. Eng. Chem. Process Des. Dev.*, 2 (4): 310–314. https://doi.org/10.1021/i260008a011.

Brucato, A., M. Ciofalo, F. Grisafi, and G. Micale. 1994. “*Complete Numerical Solution of Flow Fields in Baffled Stirred Vessels: The Inner–Outer Approach.*” In *Proc., Eighth Eur. Conf. Mix.*, 155–162. Rugby, England: Institution of Chemical Engineers.

Brucato, A., M. Ciofalo, F. Grisafi, and G. Micale. 1998. “Numerical prediction of flow fields in baffled stirred vessels: A comparison of alternative modelling approaches.” *Chem. Eng. Sci.*, 53 (21): 3653–3684. https://doi.org/10.1016/S0009-2509(98)00149-3.

Cadafalch, J., C. D. Pe´rez-Segarra, R. Co`nsul, and A. Oliva. 2002. “Verification of Finite Volume Computations on Steady-State Fluid Flow and Heat Transfer.” *J. Fluids Eng.*, 124 (1): 11–21. https://doi.org/10.1115/1.1436092.

Cavallo, P. A., N. Sinha, and M. R. O'Gara. 2008. "*Viscous Error Transport Equation for Error Quantification of Turbulent Flows.*" In *Proc., 38th Fluid Dyn. Conf. Exhib.*, 1–16. Seattle, WA: AIAA.

Celik, I., and G. Hu. 2004. "Single Grid Error Estimation Using Error Transport Equation." *J. Fluids Eng.*, 126 (5): 778–790. https://doi.org/10.1115/1.1792254.

Chen, Y. S., and S. W. Kim. 1987. *Computation of Turbulent Flows Using an Extended k − ε Turbulence Closure Model*. Marshall Space Flight Center, Alabama: NASA.

Conti, R., S. Sicardi, and V. Specchia. 1981. "Effect of the stirrer clearance on particle suspension in agitated vessels." *Chem. Eng. J.*, 22: 247–249. https://doi.org/10.1080/1023624021000019333.

Coroneo, M., G. Montante, A. Paglianti, and F. Magelli. 2011. "CFD prediction of fluid flow and mixing in stirred tanks: Numerical issues about the RANS simulations." *Comput. Chem. Eng.*, 35 (10): 1959–1968. https://doi.org/10.1016/j.compchemeng.2010.12.007.

Cutter, L. A. 1966. "Flow and Turbulence in a Stirred Tank." *AIChE J.*, 12 (1): 35–45.

Deglon, D. A., and C. J. Meyer. 2006. "CFD modelling of stirred tanks: Numerical considerations." *Miner. Eng.*, 19 (10): 1059–1068. https://doi.org/10.1016/j.mineng.2006.04.001.

Delafosse, A., A. Line, J. Morchain, and P. Guiraud. 2008. "LES and URANS simulations of hydrodynamics in mixing tank: Comparison to PIV experiments." *Chem. Eng. Res. Des.*, 86 (12): 1322–1330. https://doi.org/10.1016/j.cherd.2008.07.008.

Deshmukh, N. A., and J. B. Joshi. 2006. "Surface aerators: Power number, mass transfer coefficient, gas hold up profiles and flow patterns." *Chem. Eng. Res. Des.*, 84 (11 A): 977–992. https://doi.org/10.1205/cherd05066.

Duan, X., X. Feng, C. Yang, and Z. S. Mao. 2016. "Numerical simulation of micro-mixing in stirred reactors using the engulfment model coupled with CFD." *Chem. Eng. Sci.*, 140: 179–188. https://doi.org/10.1016/j.ces.2015.10.017.

Duan, X., X. Feng, C. Yang, and Z. Mao. 2018. “CFD modeling of turbulent reacting flow in a semi-batch stirred-tank reactor.” *Chinese J. Chem. Eng.,* 26 (4): 675–683. https://doi.org/10.1016/j.cjche.2017.05.014.

Eça, L., and M. Hoekstra. 2009. “Evaluation of numerical error estimation based on grid refinement studies with the method of manufactured solutions.” *Comput. Fluids,* 38 (8): 1580–1591. https://doi.org/10.1016/j.compfluid.2009.01.003.

Egorov, Y., F. R. Menter, R. Lechner, and D. Cokljat. 2010. “The Scale-Adaptive Simulation Method for Unsteady Turbulent Flow Predictions. Part 2: Application to Complex Flows.” *Flow, Turbul. Combust.,* 85 (1): 139–165. https://doi.org/10.1007/s10494-010-9265-4.

Escudié, R., D. Bouyer, and A. Liné. 2004. “Characterization of trailing vortices generated by a Rushton turbine.” *AIChE J.,* 50 (1): 75–86. https://doi.org/10.1002/aic.10007.

Escudié, R., and A. Liné. 2003. “Experimental analysis of hydrodynamics in a radially agitated tank.” *AIChE J.,* 49 (3): 585–603. https://doi.org/10.1002/aic.690490306.

Escudié, R., and A. Liné. 2006. “Analysis of turbulence anisotropy in a mixing tank.” *Chem. Eng. Sci.,* 61 (9): 2771–2779. https://doi.org/10.1016/j.ces.2005.09.022.

Feng, X., J. Cheng, X. Li, C. Yang, and Z.-S. Mao. 2012. “Numerical simulation of turbulent flow in a baffled stirred tank with an explicit algebraic stress model.” *Chem. Eng. Sci.,* 69 (1): 30–44. https://doi.org/10.1016/j.ces.2011.09.055.

Freitas, C. J. 2002. “The issue of numerical uncertainty.” *Appl. Math. Model.,* 26 (2): 237–248. https://doi.org/10.1016/S0307-904X(01)00058-0.

Galletti, C., E. Brunazzi, M. Yianneskis, and A. Paglianti. 2003. “Spectral and wavelet analysis of the flow pattern transition with impeller clearance variations in a stirred vessel.” *Chem. Eng. Sci.,* 58 (17): 3859–3875. https://doi.org/10.1016/S0009-2509(03)00230-6.

Gatski, T. B., and C. G. Speziale. 1993. “On explicit algebraic stress models for complex turbulent flows.” *J. Fluid Mech.,* 254: 59–78. https://doi.org/10.1017/S0022112093002034.

Gillissen, J. J. J., and H. E. A. Van den Akker. 2012. “Direct numerical simulation of the turbulent flow in a baffled tank driven by a Rushton turbine.” *AIChE J.*, 58 (12): 3878–3890. https://doi.org/10.1002/aic.13762.

Gimbun, J., C. D. Rielly, Z. K. Nagy, and J. J. Derksen. 2012. “Detached eddy simulation on the turbulent flow in a stirred tank.” *AIChE J.*, 58 (10): 3224–3241. https://doi.org/10.1002/aic.12807.

Gosman, A. D., C. Lekakou, S. Politis, R. I. Issa, and M. K. Looney. 1992. “Multidimensional modeling of turbulent two-phase flows in stirred vessels.” *AIChE J.*, 38 (12): 1946–1956. https://doi.org/10.1002/aic.690381210.

Guha, D., P. A. Ramachandran, M. P. Dudukovic, and J. J. Derksen. 2008. “Evaluation of Large Eddy Simulation and Euler-Euler CFD models for solids flow dynamics in a stirred tank reactor.” *AIChE J.*, 54 (3): 766–778. https://doi.org/10.1002/aic.11417.

Haque, J. N., T. Mahmud, K. J. Roberts, and D. Rhodes. 2006. “Modeling Turbulent Flows with Free-Surface in Unbaffled Agitated Vessels.” *Ind. Eng. Chem. Res.*, 45 (8): 2881–2891. https://doi.org/10.1021/ie051021a.

Hartmann, H., J. J. Derksen, C. Montavon, J. Pearson, I. S. Hamill, and H. E. A. van den Akker. 2004. “Assessment of large eddy and RANS stirred tank simulations by means of LDA.” *Chem. Eng. Sci.*, 59 (12): 2419–2432. https://doi.org/10.1016/j.ces.2004.01.065.

Iyer, D. K., and A. K. Patel. 2022. “Physical Reasoning of Double- to Single-Loop Transition in Industrial Reactors using Computational Fluid Dynamics.” *J. Appl. Fluid Mech.*, 15 (5), 1621-1634. https://doi.org/10.47176/jafm.15.05.1190.

Jaworski, Z., K. N. Dyster, I. P. T. Moore, A. W. Nienow, and S. Wyszynski. 1997. “*The Use of Angle Resolved LDA Data to Compare Two Differential Turbulence Models Applied to Sliding Mesh CFD Flow Simulations in a Stirred Tank.*” In *Proc., Ninth Eur. Conf. Mix.*, 11(51), 187–194. Paris, France: Institution of Chemical Engineers.

Jaworski, Z., and B. Zakrzewska. 2002. “Modelling of the Turbulent Wall Jet Generated by a Pitched Blade Turbine Impeller: The Effect of Turbulence Model.” *Chem. Eng. Res. Des.*, 80 (8): 846–854. https://doi.org/10.1205/026387602321143381.

Jenne, M., and M. Reuss. 1999. “A critical assessment on the use of k–ε turbulence models for simulation of the turbulent liquid flow induced by a Rushton-turbine in baffled stirred-tank reactors.” *Chem. Eng. Sci.*, 54 (17): 3921–3941. https://doi.org/10.1016/S0009-2509(99)00093-7.

Jiang, J., H. Wu, L. Ni, and M. Zou. 2018. “CFD simulation to study batch reactor thermal runaway behavior based on esterification reaction.” *Process Saf. Environ. Prot.*, 120: 87–96. https://doi.org/10.1016/j.psep.2018.08.029.

Joshi, J. B., N. K. Nere, C. V. Rane, B. N. Murthy, C. S. Mathpati, A. W. Patwardhan, and V. V. Ranade. 2011. “CFD simulation of stirred tanks: Comparison of turbulence models. Part I: Radial flow impellers.” *Can. J. Chem. Eng.*, 89 (1): 23–82. https://doi.org/10.1002/cjce.20446.

Karimi, M., G. Akdogan, K. H. Dellimore, and S. M. Bradshaw. 2012. “*Quantification of Numerical and Model Uncertainties in the CFD Simulation of the Gas Holdup and Flow Dynamics in a Laboratory Scale Rushton - turbine Flotation Tank.*” In *Proc., Ninth Int. Conf. CFD Miner. Process Ind.*, 1–7. CSIRO, Melbourne, Australia.

Karpinska, A. M., and J. Bridgeman. 2016. “CFD-aided modelling of activated sludge systems – A critical review.” *Water Res.*, 88: 861–879. https://doi.org/10.1016/j.watres.2015.11.008.

Karpinska, A. M., and J. Bridgeman. 2018. “CFD as a Tool to Optimize Aeration Tank Design and Operation.” *J. Environ. Eng.*, 144 (2): 05017008. https://doi.org/10.1061/(ASCE)EE.1943-7870.0001307.

Kresta, S. M., and P. E. Wood. 1991. “Prediction of the three-dimensional turbulent flow in stirred tanks.” *AIChE J.*, 37 (3): 448–460. https://doi.org/10.1002/aic.690370314.

Kresta, S. M., and P. E. Wood. 1993. “The mean flow field produced by a 45º pitched blade turbine: Changes in the circulation pattern due to off bottom clearance.” *Can. J. Chem. Eng.*, 71 (1): 42–53. https://doi.org/10.1002/cjce.5450710107.

Kulkarni, A. L., and A. W. Patwardhan. 2012. “Effect of scale on entrainment in stirred tanks.” *Chem. Eng. Res. Des.*, 90 (8): 1031–1037. Institution of Chemical Engineers. https://doi.org/10.1016/j.cherd.2011.11.012.

Kulkarni, A. L., and A. W. Patwardhan. 2014. “CFD modeling of gas entrainment in stirred tank systems.” *Chem. Eng. Res. Des.*, 92 (7): 1227–1248. Institution of Chemical Engineers. https://doi.org/10.1016/j.cherd.2013.10.025.

Lane, G. L. 2017. “Improving the accuracy of CFD predictions of turbulence in a tank stirred by a hydrofoil impeller.” *Chem. Eng. Sci.*, 169: 188–211. https://doi.org/10.1016/j.ces.2017.03.061.

Lee, K. C., and M. Yianneskis. 1998. “Turbulence properties of the impeller stream of a Rushton turbine.” *AIChE J.*, 44 (1): 13–24. https://doi.org/10.1002/aic.690440104.

Li, Z., Y. Bao, and Z. Gao. 2011. “PIV experiments and large eddy simulations of single-loop flow fields in Rushton turbine stirred tanks.” *Chem. Eng. Sci.*, 66 (6): 1219–1231. Elsevier. https://doi.org/10.1016/j.ces.2010.12.024.

Liu, L. 2013. “Computational Fluid Dynamics Modelling of Complex Fluid Flow in Stirred Vessels.” Ph.D. thesis, School of Chemical Engineering, College of Engineering and Physical Sciences, The University of Birmingham.

Liu, M. 2016. *Advances in Industrial Mixing- A Companion to the Handbook of Industrial Mixing. Chapter 5b: CFD Modeling of Stirred Tank Reactors,* 123–145. New Jersey, USA: John Wiley & Sons, Inc.

Longest, P. W., and S. Vinchurkar. 2007. “Effects of mesh style and grid convergence on particle deposition in bifurcating airway models with comparisons to experimental data.” *Med. Eng. Phys.*, 29 (3): 350–366. https://doi.org/10.1016/j.medengphy.2006.05.012.

Lu, W. M., H. Z. Wu, and M. Y. Ju. 1997. “Effects of baffle design on the liquid mixing in an aerated stirred tank with standard Rushton turbine impellers.” *Chem. Eng. Sci.*, 52 (21–22): 3843–3851. https://doi.org/10.1016/S0009-2509(97)88929-4.

Lu, W. M., and B. S. Yang. 1998. “Effect of Blade Pitch on the Structure of the Trailing Vortex around Rushton Turbine Impellers .” *Can. J. Chem. Eng.*, 76: 556–562.

Luo, J. Y., R. I. Issa, and A. D. Gosman. 1994. “*Prediction of impeller induced flows in mixing vessels using Multiple Frames of Reference.*” In *Proc., Eighth Eur. Conf. Mix.*, 549–556. United Kingdom: Institition of Chemical Engineers Symposium Series.

Mahmud, T., J. N. Haque, K. J. Roberts, D. Rhodes, and D. Wilkinson. 2009. “Measurements and modelling of free-surface turbulent flows induced by a magnetic stirrer in an unbaffled stirred tank reactor.” *Chem. Eng. Sci.*, 64 (20): 4197–4209. https://doi.org/10.1016/j.ces.2009.06.059.

Matsumura, M., H. Sakuma, T. Yamagata, and J. Kobayashi. 1982. “Gas Entrainment in a New Gas Entraining Fermentor.” *J. Ferment. Technol.*, 60 (5): 457–467.

Menter, F. R. 1994. “Two-equation eddy-viscosity turbulence models for engineering applications.” *AIAA J.*, 32 (8): 1598–1605. https://doi.org/10.2514/3.12149.

Menter, F. R. 2012. *Best Practice: Scale-Resolving Simulations in ANSYS CFD*. ANSYS, Inc.

Menter, F. R., and Y. Egorov. 2005. “*A scale-adaptive simulation model using two-equation models.*” In *Proc., 43rd AIAA Aerosp. Sci. Meet. Exhib.*, 271–283. Reno, NV, United States: AIAA.

Molnár, B., A. Egedy, and T. Varga. 2014. “Analysis of Mixing Efficiency of Rushton Turbines based on CFD Models.” *Period. Polytech. Chem. Eng.*, 58 (2): 93–102. https://doi.org/10.3311/PPch.2187.

Montante, G., A. Brucato, K. C. Lee, and M. Yianneskis. 1999. “An experimental study of double-to-single-loop transition in stirred vessels.” *Can. J. Chem. Eng.*, 77 (4): 649–659. https://doi.org/10.1002/cjce.5450770405.

Montante, G., K. C. Lee, A. Brucato, and M. Yianneskis. 2001. “Numerical simulations of the dependency of flow pattern on impeller clearance in stirred vessels.” *Chem. Eng. Sci.*, 56 (12): 3751–3770. https://doi.org/10.1016/S0009-2509(01)00089-6.

Montante, G., and F. Magelli. 2007. “Mixed Solids Distribution in Stirred Vessels: Experiments and Computational Fluid Dynamics Simulations.” *Ind. Eng. Chem. Res.*, 46 (9): 2885–2891. https://doi.org/10.1021/ie060616i.

Motamedvaziri, S., and P. M. Armenante. 2012. “Flow regimes and surface air entrainment in partially filled stirred vessels for different fill ratios.” *Chem. Eng. Sci.*, 81: 231–250. https://doi.org/10.1016/j.ces.2012.05.050.

Murthy, B. N., and J. B. Joshi. 2008. “Assessment of standard k-ε, RSM and LES turbulence models in a baffled stirred vessel agitated by various impeller designs.” *Chem. Eng. Sci.*, 63 (22): 5468–5495. https://doi.org/10.1016/j.ces.2008.06.019.

Murthy, J. Y., S. R. Mathur, and D. Choudhary. 1994. “*CFD Simulation of Flows in Stirred Tank Rectors using a Sliding Mesh Technique.*” In *Proc., Eighth Eur. Conf. Mix.*, 155–162. Cambridge, UK: Institution of Chemical Engineers.

Myers, K. J., M. F. Reeder, and J. B. Fasano. 2002. “Optimize Mixing by using the Proper Baffles.” *CEP Mag.*, February 2002.

Nere, N. K., A. W. Patwardhan, and J. B. Joshi. 2001. “Prediction of Flow Pattern in Stirred Tanks: New Constitutive Equation for Eddy Viscosity.” *Ind. Eng. Chem. Res.*, 40 (7): 1755–1772. https://doi.org/10.1021/ie0004951.

Nienow, A. W. 1968. “Suspension of solid particles in turbine agitated baffled vessels.” *Chem. Eng. Sci.*, 23 (12): 1453-1459. https://doi.org/10.1080/02726358708904551.

Nishikawa, M., K. Ashiwake, N. Hashimoto, and S. Nagata. 1979. “Agitation power and mixing time in off-centering mixing.” *Inst. Chem. Eng.*, 19 (1): 153–159.

Norouzi-Firouz, H., M.-H. Sarrafzadeh, and R. Zarghami. 2018. “Investigating the Effect of Multiple Reference Frame Approach on the Modelling of an Oxidation Ditch.” *Int. J. Environ. Res.*, 12 (4): 429–437. Springer International Publishing. https://doi.org/10.1007/s41742-018-0095-x.

Ochieng, A., and M. S. Onyango. 2008. “Homogenization energy in a stirred tank.” *Chem. Eng. Process. Process Intensif.*, 47 (9–10): 1853–1860. https://doi.org/10.1016/j.cep.2007.10.014.

Ochieng, A., M. S. Onyango, A. Kumar, K. Kiriamiti, and P. Musonge. 2008. “Mixing in a tank stirred by a Rushton turbine at a low clearance.” *Chem. Eng. Process. Process Intensif.*, 47 (5): 842–851. https://doi.org/10.1016/j.cep.2007.01.034.

Oshinowo, L., Z. Jaworski, K. N. Dyster, E. Marshall, and A. W. Nienow. 2000. “*Predicting the tangential velocity field in stirred tanks using the Multiple Reference Frames (MRF) model with validation by LDA measurements.*” In *Proc., 10th Eur. Conf. Mix.*, 281–288. Delft, The Netherlands: Elsevier.

Pakzad, L., F. Ein-Mozaffari, and P. Chan. 2008. “Using computational fluid dynamics modeling to study the mixing of pseudoplastic fluids with a Scaba 6SRGT impeller.” *Chem. Eng. Process. Process Intensif.*, 47 (12): 2218–2227. https://doi.org/10.1016/j.cep.2007.12.003.

Patil, H., A. K. Patel, H. J. Pant, and A. Venu Vinod. 2021. “CFD simulation model for mixing tank using multiple reference frame (MRF) impeller rotation.” *ISH J. Hydraul. Eng.*, 27 (2): 200–209. https://doi.org/10.1080/09715010.2018.1535921.

Patil, S. S., N. A. Deshmukh, and J. B. Joshi. 2004. “Mass-transfer characteristics of surface aerators and gas-inducing impellers.” *Ind. Eng. Chem. Res.*, 43 (11): 2765–2774. https://doi.org/10.1021/ie030428h.

Pericleous, K. A., and M. K. Patel. 1987. “The Modelling of Tangential and Axial Agitators in Chemical Reactors.” *Physicochem. Hydrodyn.*, 8 (2): 105–123.

Perng, C. Y., and J. Y. Murthy. 1994. “*A Moving Deforming Mesh Technique for Simulation of Flow in Mixing Tanks.*” In *Proc., Eighth Eur. Conf. Mix.*, 37–39. Cambridge, UK: Institution of Chemical Engineers.

Phillips, T. S., and C. J. Roy. 2011. “*Evaluation of Extrapolation-Based Discretization Error and Uncertainty Estimators.*” In *Proc., 49th AIAA Aerosp. Sci. Meet. Incl. New Horizons Forum Aerosp. Expo.*, 1–18. Orlando, Florida: American Institute of Aeronautics and Astronautics.

Phillips, T., and C. Roy. 2013. “*A New Extrapolation-Based Uncertainty Estimator for Computational Fluid Dynamics.*” In *Proc., 51st AIAA Aerosp. Sci. Meet. Incl. New Horizons Forum Aerosp. Expo.*, 1–15. Reston, Virigina: American Institute of Aeronautics and Astronautics.

Phillips, T. S., and C. J. Roy. 2014. “Richardson Extrapolation-Based Discretization Uncertainty Estimation for Computational Fluid Dynamics.” *J. Fluids Eng.*, 136 (12). https://doi.org/10.1115/1.4027353.

Placek, J., L. L. Tavlarides, G. W. Smith, and I. Fořt. 1986. “Turbulent flow in stirred tanks, Part II: A two-scale model of turbulence.” *AIChE J.*, 32 (11): 1771–1786. https://doi.org/10.1002/aic.690321103.

Pope, S. B. 1975. “A more general effective-viscosity hypothesis.” *J. Fluid Mech.,* 72 (02): 331. https://doi.org/10.1017/S0022112075003382.

Ranade, V. V., and S. M. S. Dommeti. 1996. “Computational Snapshot of Flow Generated by Axial Impellers in Baffled Stirred Vessels.” *Chem. Eng. Res. Des.,* 74: 476–484.

Ranade, V. V., and J. B. Joshi. 1990. “Flow Generated by a Disc Turbine: Part II Mathematical Modelling and Comparison with Experimental Data.” *Chem. Eng. Res. Des.,* 68 (A): 34–43.

Rao, A. R. 1999. “Prediction of reaeration rates in square stirred tanks.” *J. Environ. Eng.,* 125 (March): 215–223.

Rao, A. R., A. K. Patel, and B. Kumar. 2009. “Oxygen transfer in circular surface aeration tanks.” *Environ. Technol.,* 30 (7): 747–753. https://doi.org/10.1080/09593330902911705.

Rashidifar, M. A., and A. A. Rashidifar. 2013. “Turbulence Characteristics in a Rushton Stirring Vessel: A Numerical Investigation.” *Asian J. Sci. Appl. Technol.,* 2 (2): 25–42.

Remaki, L., A. Ramezani, J. M. Blanco, and I. Garcia. 2017. “New Simplified Algorithm for the Multiple Rotating Frame Approach in Computational Fluid Dynamics.” *J. Fluids Eng.,* 139 (8): 081104. https://doi.org/10.1115/1.4036300.

Roache, P. J. 1994. “Perspective: A Method for Uniform Reporting of Grid Refinement Studies.” *J. Fluids Eng.,* 116 (3): 405–413. https://doi.org/10.1115/1.2910291.

Roache, P. J. 2003. “*Error bars for CFD.*” In *Proc., 41st Aerosp. Sci. Meet. Exhib.,* 1–21. Reno, Nevada: American Institute of Aeronautics and Astronautics.

Rodi, W. 1976. “New Algebraic Relation for Calculating Reynolds Stresses.” *ZAMM - J. Appl. Math. Mech. / Zeitschrift für Angew. Math. und Mech.,* 56 (S1). https://doi.org/10.1002/zamm.19765613093.

Roy, C. 2010. “*Review of Discretization Error Estimators in Scientific Computing.*” In *Proc., 48th AIAA Aerosp. Sci. Meet. Incl. New Horizons Forum Aerosp. Expo.,* 1–29. Reston, Virigina: American Institute of Aeronautics and Astronautics.

Ryma, A., H. Dhaouadi, H. Mhiri, and P. Bournot. 2013. “CFD Study of Turbine Submergence Effects on Aeration of a Stirred Tank.” *Int. J. Chem. Mol. Eng.,* 7 (4): 173–178.

Sahu, A. K., P. Kumar, and J. B. Joshi. 1998. “Simulation of Flow in Stirred Vessels with Axial Flow Impeller: Zonal Modeling and Optimization of Parameters.” *Ind. Eng. Chem. Res.,* 37 (6): 2116–2130. https://doi.org/10.1021/ie970321s.

Shi, P., and R. Rzehak. 2018. “Bubbly flow in stirred tanks: Euler-Euler/RANS modeling.” *Chem. Eng. Sci.,* 190: 419–435. Elsevier Ltd. https://doi.org/10.1016/j.ces.2018.06.001.

Singh, H., D. F. Fletcher, and J. J. Nijdam. 2011. “An assessment of different turbulence models for predicting flow in a baffled tank stirred with a Rushton turbine.” *Chem. Eng. Sci.,* 66 (23): 5976–5988. https://doi.org/10.1016/j.ces.2011.08.018.

Sommerfeld, M., and S. Decker. 2004. “State of the Art and Future Trends in CFD Simulation of Stirred Vessel Hydrodynamics.” *Chem. Eng. Technol.,* 27 (3): 215–224. https://doi.org/10.1002/ceat.200402007.

Steiros, K., P. J. K. Bruce, O. R. H. Buxton, and J. C. Vassilicos. 2017. “Effect of blade modifications on the torque and flow field of radial impellers in stirred tanks.” *Phys. Rev. Fluids,* 2 (9): 094802. https://doi.org/10.1103/PhysRevFluids.2.094802.

Stern, F., R. V. Wilson, H. W. Coleman, and E. G. Paterson. 2001. “Comprehensive Approach to Verification and Validation of CFD Simulations—Part 1: Methodology and Procedures.” *J. Fluids Eng.,* 123 (4): 793–802. https://doi.org/10.1115/1.1412235.

Stoots, C. M., and R. V. Calabrese. 1995. “Mean velocity field relative to a Rushton turbine blade.” *AIChE J.,* 41 (1): 1–11. https://doi.org/10.1002/aic.690410102.

Sun, H., Z. S. Mao, and G. Yu. 2006. “Experimental and numerical study of gas hold-up in surface aerated stirred tanks.” *Chem. Eng. Sci.,* 61 (12): 4098–4110. https://doi.org/10.1016/j.ces.2005.12.029.

Sun, H. Y., W. J. Wang, and Z. S. Mao. 2002. “Numerical simulation of the whole three dimensional flow in a stirred tank with anisotropic algebraic stress model.” *Chinese J. Chem. Eng.,* 10 (1): 15–24.

Van Der Molen, K., and H. R. E. Van Maanen. 1978. “Laser-Doppler measurements of the turbulent flow in stirred vessels to establish scaling rules.” *Chem. Eng. Sci.*, 33 (9): 1161–1168. https://doi.org/10.1016/0009-2509(78)85081-7.

Versteeg, H. K., and Malalasekera, W. 1995. *An introduction to computational fluid dynamics- The finite volume method.* 1st ed. England: Longman Scientific and Technical, Longman Group Ltd.

Vinchurkar, S., and P. W. Longest. 2008. “Evaluation of hexahedral, prismatic and hybrid mesh styles for simulating respiratory aerosol dynamics.” *Comput. Fluids*, 37 (3): 317–331. https://doi.org/10.1016/j.compfluid.2007.05.001.

Wallin, S., and A. V. Johansson. 2000. “An explicit algebraic Reynolds stress model for incompressible and compressible turbulent flows.” *J. Fluid Mech.*, 403: 89–132. https://doi.org/10.1017/S0022112099007004.

Wechsler, K., M. Breuer, and F. Durst. 1999. “Steady and Unsteady Computations of Turbulent Flows Induced by a 4/45° Pitched-Blade Impeller.” *J. Fluids Eng.*, 121 (2): 318–329. https://doi.org/10.1115/1.2822210.

Wu, H., and G. K. Patterson. 1989. “Laser-Doppler measurements of turbulent-flow parameters in a stirred mixer.” *Chem. Eng. Sci.*, 44 (10): 2207–2221. https://doi.org/10.1016/0009-2509(89)85155-3.

Wu, J., Y. Zhu, and L. Pullum. 2001. “Impeller Geometry Effect on Velocity and Solids Suspension.” *Chem. Eng. Res. Des.*, 79 (8): 989–997. https://doi.org/10.1205/02638760152721857.

Xing, T., and F. Stern. 2010. “Factors of Safety for Richardson Extrapolation.” *J. Fluids Eng.*, 132 (6). https://doi.org/10.1115/1.4001771.

Xu, Y., and G. McGrath. 1996. “CFD Predictions in Stirred Tank Flows.” *Chem. Eng. Res. Des.*, 74 (4): 471–475.

Yamamoto, T., Y. Fang, and S. V. Komarov. 2019. “Surface vortex formation and free surface deformation in an unbaffled vessel stirred by on-axis and eccentric impellers.” *Chem. Eng. J.*, 367 (December 2018): 25–36. Elsevier. https://doi.org/10.1016/j.cej.2019.02.130.

Yapici, K., B. Karasozen, M. Schäfer, and Y. Uludag. 2008. “Numerical investigation of the effect of the Rushton type turbine design factors on agitated tank flow characteristics.” *Chem. Eng. Process. Process Intensif.*, 47 (8): 1340–1349. https://doi.org/10.1016/j.cep.2007.05.002.

Yeoh, S. L., G. Papadakis, K. C. Lee, and M. Yianneskis. 2004. “Large Eddy Simulation of Turbulent Flow in a Rushton Impeller Stirred Reactor with Sliding-Deforming Mesh Methodology.” *Chem. Eng. Technol.*, 27 (3): 257–263. https://doi.org/10.1002/ceat.200401994.

Yianneskis, M., Z. Popiolek, and J. H. Whitelaw. 1987. “An experimental study of the steady and unsteady flow characteristics of stirred reactors.” *J. Fluid Mech.*, 175 (1): 537. https://doi.org/10.1017/S002211208700051X.

Zadravec, M., S. Basic, and M. Hribersek. 2007. "The influence of rotating domain size in a rotating frame of reference appraoch for simulation of rotating impeller in a mixing vessel." *J. Eng. Sci. Technol.*,2 (2): 126-138.

Zhang, M., L. Ni, J. Jiang, and W. Zhang. 2017a. “Thermal runaway and shortstopping of esterification in batch stirred reactors.” *Process Saf. Environ. Prot.*, 111: 326–334. https://doi.org/10.1016/j.psep.2017.07.028.

Zhang, Y., Z. Gao, Z. Li, and J. J. Derksen. 2017b. “Transitional flow in a Rushton turbine stirred tank.” *AIChE J.*, 63 (8): 3610–3623. https://doi.org/10.1002/aic.15809.

Zhang, Y., X. Pan, Y. Wang, P. Luo, and H. Wu. 2018. “Numerical and experimental investigation on surface air entrainment mechanisms of a novel long-short blades agitator.” *AIChE J.*, 64 (1): 316–325. https://doi.org/10.1002/aic.15865.

Zhu, Q., H. Xiao, A. Chen, S. Geng, and Q. Huang. 2019. “CFD study on double- to single-loop flow pattern transition and its influence on macro mixing efficiency in fully baffled tank stirred by a Rushton turbine.” *Chinese J. Chem. Eng.*, 27 (5): 993–1000. https://doi.org/10.1016/j.cjche.2018.10.002.

Zlokarnik, M. 2006. *Scale-Up in Chemical Engineering*. 2nd ed. Germany: WILEY-VCH Verlag GmbH & Co. KGaA.

Chapter 3

Computational Methodology

3.1 Introduction

As discussed in the Chapters 1 and 2, energy efficient design of the surface aeration tank requires detailed knowledge regarding the relationships between the tank parameters, flow field characteristics and performance goals. The significant developments in the computer resources and model algorithms in the past two decades have led to widespread usage of the CFD technique for analyzing the flow field characteristics associated with the reactor vessels (Aubin et al. 2004; Joshi et al. 2011). Moreover, the CFD technique needs lesser time, man power and expenses for obtaining the flow field results as compared to the experimental techniques (Iyer and Patel 2022). Although, the CFD approach has distinct advantages over the experimental techniques, the reliability and accuracy of the underlying methodology should be carefully evaluated so as to enhance the confidence in the flow field predictions (Oberkampf and Trucano 2002). The present chapter discusses the details regarding the modelling approach, impeller rotation model, boundary conditions, numerical discretization schemes, computational grids and various performance goals adopted for the present research work. Further, the procedures employed for evaluating the reliability and accuracy of the CFD predictions and the aeration tank configurations used for the flow field analysis are also described in this chapter.

3.2 Overview of CFD modelling process

The CFD modelling consists of three stages such as pre-processing, solver and post-processing respectively. The pre-processing stage comprises of creating the geometry of the

surface aeration tanks, discretizing the geometric configurations of the tank into number of smaller volumes, selecting the appropriate governing equations to be solved and specifying the fluid properties, boundary conditions and initial conditions associated with the problem under consideration. The governing equations of flow and transport processes along with the boundary conditions and initial conditions are solved in a numerical manner in the second or solver stage. The post-processing stage is concerned with the analysis of the results obtained from the second stage so as to arrive at the conclusions. The flow field results from the second stage are extracted in the form of graphs or images or various kinds of plots for the further detailed analysis. The flow chart illustrating the CFD modelling process is shown in Figure 3.1.

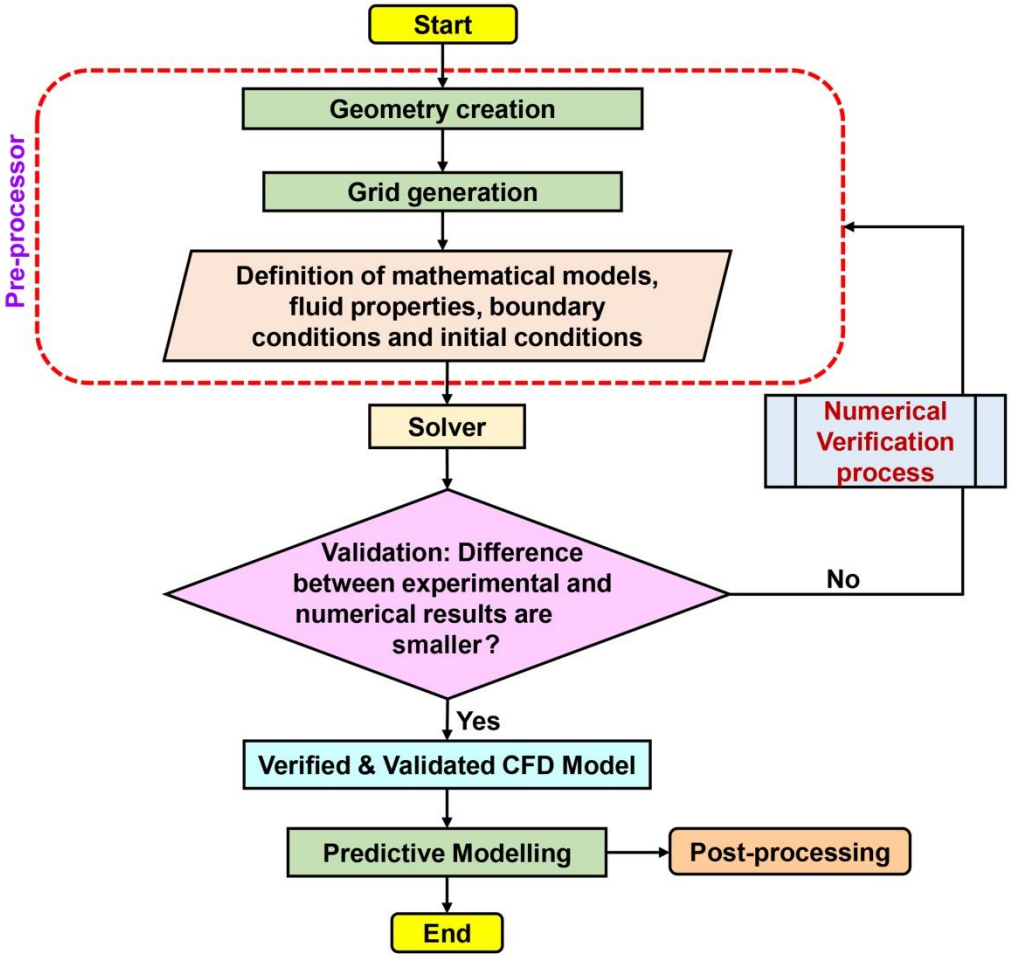

Figure 3.1: General flow chart of CFD process

The reliability and accuracy of the CFD methodology is evaluated using the Verification & Validation (V&V) process (AIAA 1998; Oberkampf and Trucano 2002). For this purpose, a reactor vessel configuration which is experimentally investigated in the literature (Wu and

Patterson 1989) is modeled using the CFD technique. Initially, a series of CFD simulations needs to be performed by increasing the resolution of the computational grid and employing the higher order discretization schemes until significant variations aren't observed in the flow field predictions (Coroneo et al. 2011; Deglon and Meyer 2006). This process is known as numerical verification process which determines the exact solutions or near exact solutions of the governing equations solved in the CFD model (Roy 2010). In order to ensure whether the discretized equations replicates the actual flow physics associated with the reactor vessel, the flow field predictions from the CFD model are compared with the corresponding experimental results (Roache 1998). The superior matching of the experimental and CFD results indicates that the CFD methodology is validated and the same can be confidently employed for analyzing the reactor vessel configurations which aren't investigated so far using the experimental techniques (Oberkampf and Trucano 2002). The inadequate matching of the experimental and CFD results necessitate careful evaluation of the underlying modelling approach and turbulence model closures adopted for the modelling process.

3.3 CFD methodology

The details of the computational methodology adopted for the present research work are explained in the sub-sections given below.

3.3.1 Modelling approach

The three dimensional steady and unsteady CFD simulations were performed using the commercially available ANSYS Fluent software (17.0 version) founded on the finite volume discretization method. The ANSYS Fluent is the major commercial CFD code which is extensively used and validated for wide range of natural and engineering problems. Several research works (Basavarajappa et al. 2015; Coroneo et al. 2011; Deglon and Meyer 2006; Kulkarni and Patwardhan 2014) have adopted this software for modelling the reactor vessels and have obtained accurate predictions of the mean and turbulent flow fields from the same. The usage of commercial software has considerably decreased the efforts and time required for modelling even the complex systems and hence received wide attention from the research community as well as from the industrial practitioners.

The RANS equations corresponding to the incompressible fluid flow under turbulent conditions were solved to obtain the flow field characteristics associated with the surface aeration tanks. The standard $k-\varepsilon$ model which is widely adopted as the closure condition for the Reynolds stress terms emerging from the Reynolds averaging of the Navier-Stokes equations (Coroneo et al. 2011; Deglon and Meyer 2006; Montante et al. 2001) was considered for the present research work. The present study has considered the pure water (ρ_w of 1000 Kg/m^3 and dynamic viscosity of 0.001 Ns/m^2) and air at standard conditions as the working fluids for the numerical simulations. The Navier-Stokes equations with standard $k-\varepsilon$ model closure was solved under single phase condition (water as the working fluid) as well as multiphase condition (air and water as working fluids) respectively. The single phase simulations of the surface aeration tanks were carried out under steady state conditions while the multiphase simulations of the same were carried out under the unsteady state conditions respectively. The Reynolds averaged continuity and momentum equations which are expressed in the Cartesian tensor form (ANSYS 2013) are given in the equations 3.1 and 3.2 respectively.

$$\frac{\partial \rho_q}{\partial t}+\frac{\partial(\rho_q u_i)}{\partial x_i}=0 \tag{3.1}$$

$$\frac{\partial(\rho_q u_i)}{\partial t}+\frac{\partial(\rho_q u_i u_j)}{\partial x_j}=-\frac{\partial p}{\partial x_i}+\frac{\partial}{\partial x_j}\left[\mu\left\{\frac{\partial u_i}{\partial x_j}+\frac{\partial u_j}{\partial x_i}-\frac{2}{3}\delta_{ij}\frac{\partial u_k}{\partial x_k}\right\}\right]+\frac{\partial\left(-\rho_q\overline{u_i'u_j'}\right)}{\partial x_j}+F_\sigma+F_B+F_g \tag{3.2}$$

Where ρ_q is the density of fluid (q represents the phase under consideration), u is the velocity of flow, p is the pressure, μ is the viscosity of fluid, δ_{ij} is the Kronecker delta ($\delta_{ij}=1$ if $i=j$ and $\delta_{ij}=0$ if $i\neq j$), $-\rho_q\overline{u_i'u_j'}$ is the Reynolds stress, F_σ is the surface tension force, F_B is the body force and F_g is the gravitational force. The term t specifies time, x represents the spatial coordinate and the subscripts i,j,k indicate the three coordinate directions respectively.

The Reynolds stress present in the equation 3.2 contains the product of fluctuating velocity terms which is converted into the mean velocity gradients using the Boussinesq hypothesis (ANSYS 2013) as given in the equation 3.3.

$$-\rho_q\overline{u_i'u_j'}=\mu_t\left[\frac{\partial u_i}{\partial x_j}+\frac{\partial u_j}{\partial x_i}\right]-\frac{2}{3}\left[\rho_q k+\mu_t\frac{\partial u_k}{\partial x_k}\right]\delta_{ij} \tag{3.3}$$

Where μ_t is the turbulence viscosity which is calculated using one or two equation turbulence models. In the standard $k-\varepsilon$ model, μ_t is represented as the function of turbulent kinetic energy (k) and turbulence dissipation rate (ε) as given in the equation 3.4 and the additional transport equations for calculating the k and ε are given in the equations 3.5 and 3.6 respectively.

$$\mu_t = \rho_q C_\mu \frac{k^2}{\varepsilon} \tag{3.4}$$

$$\frac{\partial(\rho_q k)}{\partial t} + \frac{\partial(\rho_q k u_i)}{\partial x_i} = \frac{\partial}{\partial x_j}\left[\left(\mu + \frac{\mu_t}{\sigma_k}\right)\frac{\partial k}{\partial x_j}\right] + G_k + G_b - \rho_q \varepsilon - Y_M + S_k \tag{3.5}$$

$$\frac{\partial(\rho_q \varepsilon)}{\partial t} + \frac{\partial(\rho_q \varepsilon u_i)}{\partial x_i} = \frac{\partial}{\partial x_j}\left[\left(\mu + \frac{\mu_t}{\sigma_\varepsilon}\right)\frac{\partial \varepsilon}{\partial x_j}\right] + C_{1\varepsilon}\frac{\varepsilon}{k}(G_k + C_{3\varepsilon}G_b) - C_{2\varepsilon}\rho_q \frac{\varepsilon^2}{k} + S_\varepsilon \tag{3.6}$$

Where σ_k and σ_ε are turbulent Prandtl numbers, G_k and G_b indicate the generation of turbulent kinetic energy from mean velocity gradients and buoyancy respectively. The Y_M specifies the contribution of fluctuating dilatation in compressible turbulence to the overall turbulence dissipation rate. The S_k and S_ε are the user defined source terms while $C_{1\varepsilon}$, $C_{2\varepsilon}$, $C_{3\varepsilon}$ and C_μ are the model constants. The default values of these model constants were found out from the experiments of fundamental turbulent flows including various types of shear flows such as boundary layers, jets and mixing layers and the corresponding values are given below.

$C_{1\varepsilon}$=1.44, $C_{2\varepsilon}$=1.92, C_μ=0.09, σ_k=1.0 and σ_ε=1.3

These values of model constants have worked well for various types of turbulent flows (ANSYS 2013) and hence adopted for the present research work.

The term F_B comprises of coriolis and centrifugal forces which are generated due to the rotation of the impeller and the expression for the same is given in the equation 3.7. In the present research work, the impeller rotation was modelled using the pseudo steady MRF method as it produces highly similar flow field predictions at a lesser computational cost as compared to unsteady SM method (Aubin et al. 2004; Wechsler et al. 1999). Although, the MRF method was initially developed for modelling the steady state flow conditions in the stirred tanks, it was later upgraded for modelling the transient flow features associated with

the same (Brucato et al. 1998). The term F_B is considered for the calculations only when the governing equations are solved in a rotating frame of reference in the MRF method.

$$F_B = \left(-2\rho_q \Omega \times u_i\right) - \left(-\rho_q \Omega \times \{\Omega \times x\}\right) \tag{3.7}$$

Where Ω is the angular speed of the impeller.

The water and air are regarded as the primary and secondary (dispersed) phases respectively for the numerical simulations. The present research work has employed the VOF model (Hirt and Nicholas 1981) for capturing the air-water interface and the distribution of air fraction in the vessel during the surface aeration process. The VOF model is a famous interface tracking method which is widely adopted for modelling the entrainment of air into the reactor vessels (Kulkarni and Patwardhan 2014; Yamamoto et al. 2019). The interfaces between the different phases are tracked by solving an additional continuity equation for the volume fraction of each phase under consideration. The continuity equation for the volume fraction of q^{th} phase is given in the equation 3.8.

$$\frac{1}{\rho_q}\left[\frac{\partial}{\partial t}\left(\alpha_q \rho_q\right) + \nabla.\left(\alpha_q \rho_q \overline{u_q}\right) = S_{\alpha q} + \sum_{p=1}^{n}\left(\dot{m}_{pq} - \dot{m}_{qp}\right)\right] \tag{3.8}$$

Where $\dot{m}_{pq}$ is the mass transfer from p^{th} phase to q^{th} phase, $\dot{m}_{qp}$ is the mass transfer from q^{th} phase to p^{th} phase, $S_{\alpha q}$ is the mass source term for each phase, α_q is the volume fraction of q^{th} phase in a computational cell and u_q is the velocity of q^{th} phase. The volume fraction α of any phase is defined as given in the equation 3.9. According to the value of α in each computational cell, corresponding properties of fluid and variables are assigned to each of the computational cell. The sum of volume fractions of various phases in any computational cell equals to unity.

$$\alpha = \begin{cases} 1 & Liquid \\ 0 & Gas \\ 0 < \alpha < 1 & Interface \end{cases} \tag{3.9}$$

In the present research work, the interface between the phases is depicted when the value of α is equal to 0.50. The above mentioned volume fraction equation is solved for the dispersed phases and the volume fraction of the primary phase is computed using the equation 3.10.

$$\sum_{q=1}^{n} \alpha_q = 1 \tag{3.10}$$

The implicit time discretization scheme was used for solving this volume fraction equation in the present study. The discretized form of this volume fraction equation in the implicit scheme requires volume fraction values at the current time step which are obtained by solving a standard scalar transport equation in an iterative manner at each time step for each of the dispersed phases present in the system. The term F_σ present in the equation 3.2 was modelled using the Continuum Surface Force Model (CSM). A constant value of 0.072 N/m was applied as the coefficient of surface tension which is highly appropriate for the air-water systems (Kulkarni and Patwardhan 2014).

In short, the surface aeration process in a reactor vessel is modelled by solving the volume fraction equation of air (equation 3.8) along with the continuity equation (equation 3.1), momentum equation (equation 3.2) and turbulence transport equations (equations 3.5 and 3.6) respectively.

3.3.2 Boundary conditions

The appropriate boundary conditions which reflect the actual flow behavior of the surface aeration tanks need to be provided for developing the CFD models of the same. The tank periphery, tank bottom, baffle walls and impeller were modelled as solid surfaces with no-slip boundary condition. On the other hand, the top surface of the tank was modelled using symmetry boundary condition in the single phase simulations and using pressure-outlet condition in the multiphase simulations respectively. The viscous flow near the solid boundaries was modelled using the standard wall function (Launder and Spalding 1974).

3.3.3 Impeller rotation model

The surface aeration tank configurations are divided into two zones such as inner zone enclosing the impeller and outer zone encompassing the tank and baffle walls respectively. The governing equations are solved in a rotating reference frame in the inner zone and in a stationary reference frame in the outer zone respectively. The effects of rotation of the impeller are included into the model by adding the corresponding coriolis and centrifugal force contributions in the momentum equations which are solved in the rotating frame of reference and removing the same from the momentum equations which are solved in the stationary frame of reference respectively. The velocity fields obtained from the inner zone

are iteratively exchanged to the outer zone after providing necessary transformations at the boundary separating the inner and outer zones and vice versa. This process is continued until satisfactory numerical convergence is achieved for the velocity fields computed in the inner and outer zones respectively.

As discussed in the subsection 2.3.4, position of the MRF boundary separating the inner and outer zones of the reactor vessel affects the accuracy of flow field predictions and hence it is necessary to determine the appropriate position of the same for accurate modelling of the flow behavior of the reactor vessels. A cylindrical shaped MRF boundary was used to divide the agitated vessel into an inner zone as well as outer zone respectively. The diameter of the cylindrical MRF boundary (radial extent) is defined as D_r while the axial distance between the top and bottom horizontal faces of the MRF boundary (axial extent) is defined as H_r respectively. The H_r is equally divided above and below the impeller centre-plane (which is represented using the '±' symbol). A series of computational trials (simulations) were performed by varying either D_r or H_r at a time and the proper magnitudes of the same were determined by comparing the flow field predictions with the corresponding experimental results. The upper and lower limits of D_r and H_r employed for the simulations are given in Table 3.1 as well as shown in Figure 3.2 respectively. The values of D_r and H_r for the initial trial were assumed as 14 cm and 4 cm respectively based on the study of Lane et al. (2000).

Table 3.1: Upper and lower limit of D_r and H_r for implementing the MRF scheme

MRF boundary extent	General limits for any geometry	Possible limits for the current study
D_r	$D < D_r < (d - 2B)$	9.3 cm <D_r< 21.6 cm
H_r	$h < H_r < 2h$	1.86 cm <H_r< 18 cm

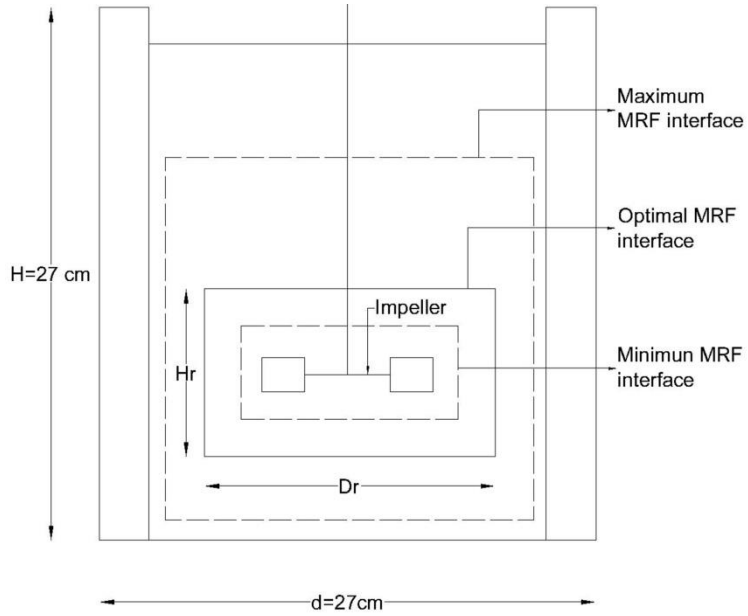

Figure 3.2: Upper and lower limits of MRF boundary for modelling the flow fields

3.3.4 Computational grids

The full three dimensional geometry of the surface aeration tanks were created using ANSYS Design Modeler tool (version 17.0) and the various geometric features such as RT impeller and the baffle walls were accurately represented in the models developed. The full three dimensional geometry of the aeration tanks were considered in the present study since the modelling of half or quarter geometric configurations of the same was reported to be unsuitable for modelling the associated flow field characteristics (Jenne and Reuss 1999). The surface aeration tanks were discretized using the finite volume based grids with sufficient local refinements to capture the flow gradients using the ANSYS Meshing tool (version 17.0). The complex shape of the RT impeller as well as the baffle walls were properly represented in the discretized domain of the reactor vessels. The computational domain was discretized using two different grid types viz: (1) Hybrid grid type and (2) Tetrahedral grid type as shown in Figures 3.3(a)-3.3(d) respectively.

In both the grid types, the computational domain was divided into a sub-domain surrounding the impeller as well as another sub-domain enclosing the remaining portions of the vessel. The sub-domain surrounding the impeller coincides with the inner zone generated in the MRF model for providing effects of rotation of the impeller and the other sub-domain coincides with the outer zone created in the MRF model for encompassing the tank and baffle walls.

The performance of hybrid and tetrahedral grid types were compared so as to select the appropriate grid type for modeling the flow features associated with the reactor vessels.

The hybrid grid was developed by splitting the computational domain of the reactor vessel into various blocks. The block around the impeller which coincides with the inner zone was discretized using the unstructured tetrahedral elements so as to properly define the complex shape of the RT impeller. In the other blocks generated above and below the inner zone, the hexahedral elements were developed by sweeping a surface mesh consisting of unstructured quadrilateral-dominant elements along the axial direction of the tank. The tetrahedral elements were distributed based on the Patch Confirming Algorithm (ANSYS 2013) and the hexahedral elements were provided according to the General Sweeping Algorithm available in ANSYS (2013). On the other hand, the generation of tetrahedral grid doesn't require any block-wise treatment as that of the hybrid grid and the entire tank geometry was discretized using the unstructured tetrahedral elements based on the Patch Confirming Algorithm.

The grid independence study was performed for each grid type using five grids of significantly different resolutions as given in the Table 3.2. The size of the elements comprising the RT impeller was successively reduced to obtain the computational grids used for the grid independence study. The finer grids near the impeller help in resolving the sharp velocity gradients, trailing vortices and high turbulence regions around the impeller. The thickness of impeller disc, blades and baffles are accounted in the finer grids developed for the present research work. Moreover, the inflation layers were provided around the impeller so as to resolve the boundary layer gradients by refining the grid elements in a direction perpendicular to the impeller walls.

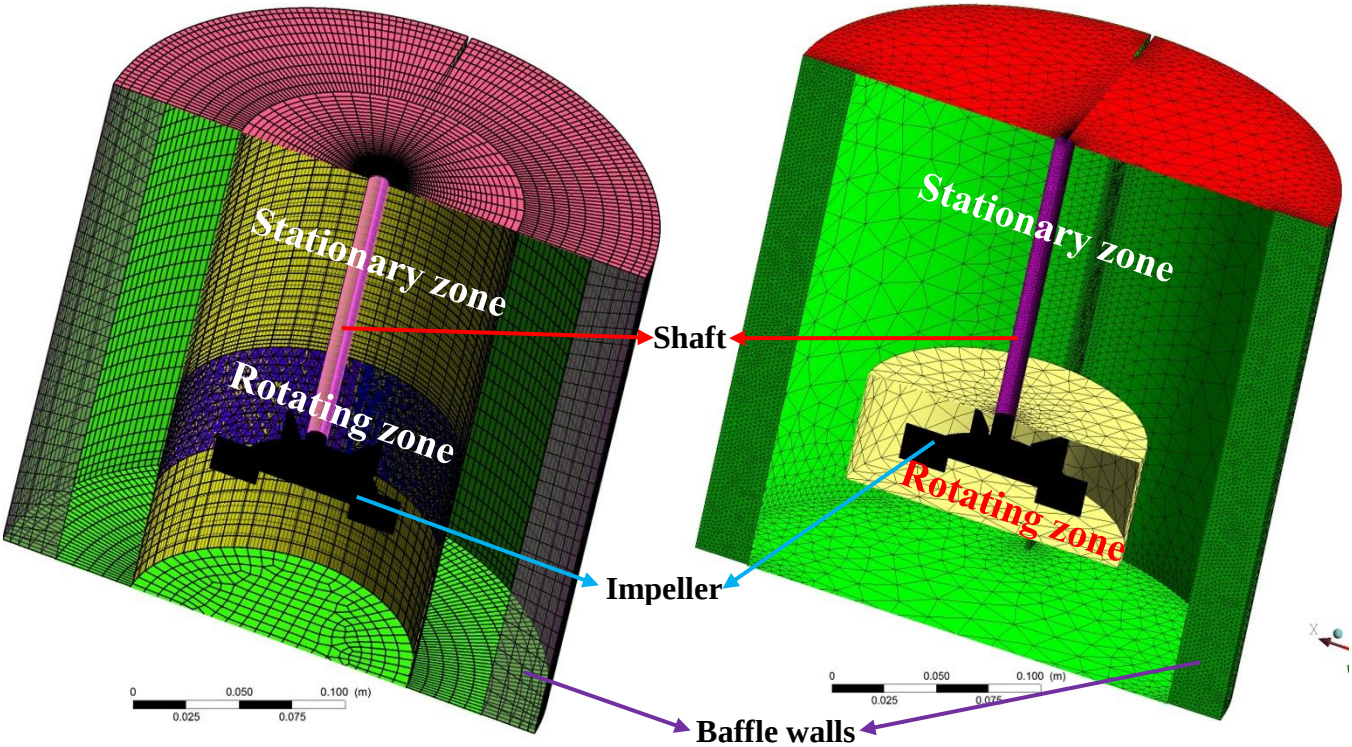

(a) (b)

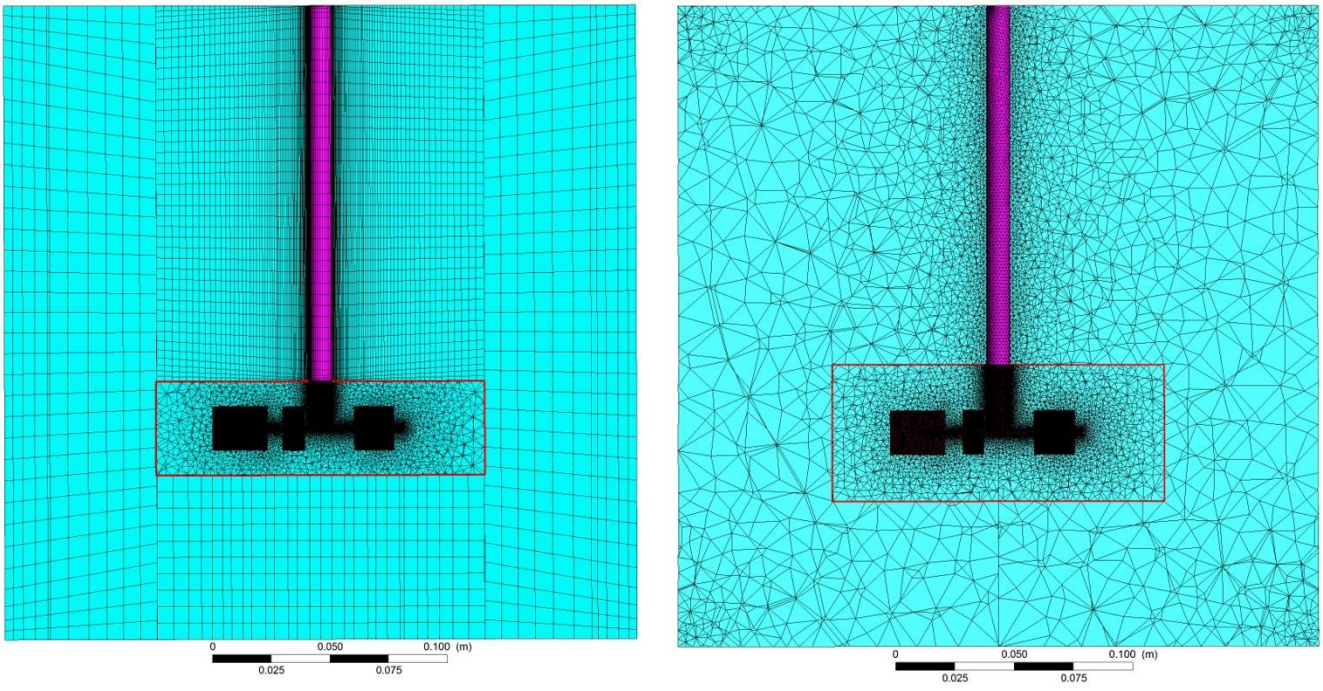

(c) (d)

Figure 3.3: Isometric and sectional elevation views of [(a) & (c)] hybrid grid type and [(b) & (d)] tetrahedral grid type

Table 3.2: Features of the grids generated for the grid independence study under the hybrid and tetrahedral grid types

Grid	Element size of impeller (m)	Number of elements of blade		Overall number of elements	Overall number of nodes
		L_r	L_z		
Hybrid grid type					
Grid 1	0.004	6	5	300573	304574
Grid 2	0.0008	36	25	996072	361096
Grid 3	0.00035	66	44	4497937	1325522
Grid 4	0.000258	86	65	7418360	2329381
Grid 5	0.00024	96	77	8451837	2607928
Tetrahedral grid type					
Grid 1	0.005	5	4	266733	56882
Grid 2	0.002	10	8	869340	168494
Grid 3	0.0015	16	13	1001202	193513
Grid 4	0.0005	53	41	3874542	732154
Grid 5	0.000258	90	72	7142519	1332020

3.3.5 Numerical discretization schemes

The continuity and momentum equations were coupled using the Semi-Implicit Method for Pressure Linked Equations (SIMPLE) pressure-velocity coupling scheme and the resulting equations were numerically discretized using various higher and lower order discretization schemes respectively. The performance of various higher and lower order discretization schemes were compared to select the most appropriate discretization scheme for modelling the reactor vessels. The lower order schemes consist of first order upwind and power-law schemes whereas the higher order schemes include second order upwind, third order QUICK and MUSCL schemes respectively. During the multiphase modelling, the pressure term was discretized using the PRESTO scheme and the volume fraction term was discretized using the Geo-reconstruct scheme respectively. The details regarding the pressure-velocity coupling schemes and the various numerical discretization schemes are available in ANSYS (2013).

3.3.6 Numerical convergence

The time step adopted for the unsteady simulations was 0.0002s and the total time of simulation was 10s which is equal to or more than the mixing time required for the baffled tanks agitated using the RT impeller (Kulkarni and Patwardhan 2014). Particular care was given for the convergence of turbulent quantities since the mean flow quantities converges in a faster manner as compared to the turbulent quantities (Coroneo et al. 2011; Deglon and Meyer 2006). Also, the number of iterations necessary to achieve superior convergence of the turbulent quantities is much higher than that required for the mean flow quantities. In order to achieve superior convergence of the turbulent quantities, a higher convergence criterion of 10^{-7} was adopted for the mean as well as turbulent flow fields. The residuals of continuity equation, X-velocity, Y-velocity, Z-velocity, k and ε were carefully monitored and the simulations were considered as converged when the residuals of the same were dropped below the level of 10^{-7}. Apart from the residuals of flow fields, impeller torque and volume integrated turbulence dissipation rate were also monitored during the simulations which attained constant magnitudes when the numerical simulations were stopped. The careful monitoring of the turbulent quantities assures accurate predictions from the CFD model.

The computations were carried out in a workstation having double precision 64 bit Intel (R) Xeon (R) E5-1620 3.6 GHz processor. The parallel processing with 12 cores was adopted for each simulation and the time required for each simulation was also noted.

3.4 Numerical Verification & Validation process

The present study minimizes the numerical error arising from four sources such as grid resolution, grid type, numerical discretization scheme and position of MRF boundary separating the inner and outer zones of the reactor vessel. At first, the grid independence study of the hybrid and tetrahedral grids were performed in a systematic manner using five grids of significantly different resolutions so as to minimize the numerical error arising from the grid resolution. This numerical error associated with the hybrid and tetrahedral grids were quantified using the GCI method and the computational grid providing minimum GCI (optimal grid) was selected for further analysis. The details of the GCI method adopted to quantify the numerical error are described in the next paragraph. The computational time, accuracy and numerical convergence of the flow field predictions from the optimal grids of

hybrid and tetrahedral grid types were compared to determine the optimal grid type for the modelling. The performance of various higher and lower order discretization schemes was analysed on the optimal grid type thus selected to obtain the appropriate numerical discretization scheme for the modelling. Finally, a series of numerical simulations were performed by varying the D_r and H_r in the optimal grid type with appropriate discretization scheme obtained from the previous steps and the optimal D_r and H_r were found out by comparing the flow field predictions from the simulations with the corresponding experimental results. The flow chart elucidating the step by step procedure of the numerical verification process is shown in Figure 3.4.

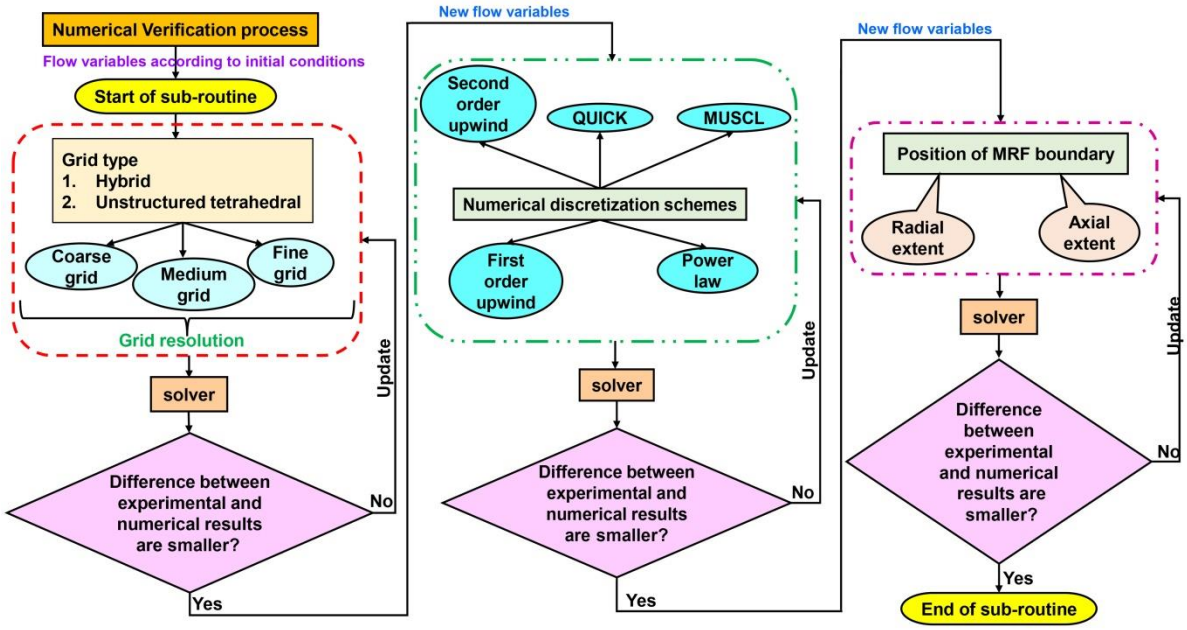

Figure 3.4: Numerical verification process adopted for the present research work

The numerical error or uncertainty associated with the global and local flow fields were determined using the GCI method (Roache 1994). The GCI is determined from three systematically refined grids namely coarse, medium and fine grids respectively. The flow field solutions from the fine, medium and coarse grids are represented as f_1, f_2 and f_3 respectively. The grid refinement factor between the medium and fine grids is expressed as given in the equation 3.11.

$$r'_{21} = \left(\frac{M_{fine}}{M_{medium}}\right)^{1/3} \tag{3.11}$$

Where M is the number of elements or control volumes in the grids and r'_{21} is the refinement factor between the medium and fine grids. The difference between the f_3 and f_2 is indicated as v_{32} and that between f_2 and f_1 is specified as v_{21} respectively. The Convergence ratio (R^*) is computed as given in the equation 3.12.

$$R^* = \frac{v_{21}}{v_{32}} \tag{3.12}$$

The positive values of R^* between zero and one ($0<R^*<1$) indicate monotonic convergence of the solutions while the negative values of the same represent the oscillatory convergence of the solutions. The GCI as well as the absolute relative error (e_r) of the flow quantities associated with the fine grids are estimated using the equations 3.13 and 3.14 respectively.

$$GCI_{fine}^{21} = \frac{F_s * e_r^{21}}{(r'_{21})^{\hat{p}} - 1} \tag{3.13}$$

$$e_r^{21} = \left|\frac{f_1 - f_2}{f_1}\right| \tag{3.14}$$

Where $\hat{p}$ indicates the observed order of accuracy and the F_s specifies the Factor of Safety provided to achieve 95% confidence in the estimation of GCI related with the various flow quantities. The asymptotic convergence of various flow quantities with the grid resolution was tested by determining the $\hat{p}$ using the expressions given in the equations from 3.15 to 3.17.

$$\hat{p} = \frac{1}{ln(r'_{21})}\left|ln\left|\frac{v_{32}}{v_{21}}\right| + q(\hat{p})\right| \tag{3.15}$$

$$q(\hat{p}) = ln\left(\frac{(r'_{21})^{\hat{p}} - s}{(r'_{32})^{\hat{p}} - s}\right) \tag{3.16}$$

$$s = 1.sign\left(\frac{v_{32}}{v_{21}}\right) \tag{3.17}$$

For the complex geometries having turbulent flow features, the $\hat{p}$ can exhibit deviations from the formal order of accuracy of the discretization scheme (p_f) either due to unstructured nature of grids or due to non-uniform refinement factor between the coarse, medium and fine grids respectively. The considerable difference between the $\hat{p}$ and p_f leads to unreliable estimates of the GCI (Phillips and Roy 2011; Roy 2010). In order to avoid the unrealistic large or small magnitudes of GCI due to lower or higher values of $\hat{p}$, the recommendations

provided by Roy (2010) were adopted for the present work as given in the equations 3.18 and 3.19 respectively.

$$\hat{p} = min\left(max(0.1, \hat{p}), p_f\right) \tag{3.18}$$

$$F_s = \begin{cases} 1.25, & \frac{p_f - \hat{p}}{p_f} < 10\% \\ 3.0, & \frac{p_f - \hat{p}}{p_f} > 10\% \end{cases} \tag{3.19}$$

A lower F_s of 1.25 was applied when the $\hat{p}$ is close to p_f indicating asymptotic convergence of the flow quantities whereas a higher F_s of 3.0 was applied when considerable deviations exist in the magnitudes of $\hat{p}$ and p_f indicating non-asymptotic convergence of the flow quantities (Roy 2010).

The mean and turbulent flow field predictions from the CFD model after the verification of various sources of numerical error were compared with the corresponding results from the experiments, LES and other complex turbulence models respectively. This process is known as validation process.

3.5 Performance goals and flow field characteristics of surface aeration tanks

The performance goals of the surface aeration tanks considered in the present research work are the impeller power number, pumping number and gas hold-up respectively. The impeller power number was computed from the torque of the rotating impeller (N_{pt}) as well as from the volume integrated turbulence dissipation rate ($N_{p\varepsilon}$) respectively. The percentage difference between N_{pt} and $N_{p\varepsilon}$ represents the effective dissipation of the power drawn from the impeller in the entire domain of the reactor vessel (Başbuğ et al. 2018). In other words, this quantity is known as energy imbalance associated with the reactor vessel. The smaller values of energy imbalance indicate the energy efficiency of the flow and transport processes associated with the reactor vessels (Başbuğ et al. 2018). The concept of energy imbalance can also be used for analyzing the accuracy and consistency of the standard $k-\varepsilon$ model in predicting the turbulent quantities related with the reactor vessels (Coroneo et al. 2011; Liu 2016). The expressions of the various performance goals considered for the present study are given in the equations 3.20-3.24 respectively.

$$N_{pt} = \frac{P'}{\rho_q N^3 D^5} \tag{3.20}$$

Where $P' = 2\pi N\tau$, P' indicates the impeller power drawn and τ is the net torque on the impeller blades

$$N_{p\varepsilon} = \frac{\iiint \rho_q \varepsilon \, dV}{\rho_q N^3 D^5} \tag{3.21}$$

$$\text{Energy imbalance} = \frac{N_{pt} - N_{p\varepsilon}}{Npt} \tag{3.22}$$

Pumping number (N_q) is defined as given in the equation 3.23.

$$N_q = \frac{Q_r}{ND^3} \tag{3.23}$$

Where Q_r is the volume flow rate in the radial direction.

Gas hold-up (e) is specified as given in the equation 3.24.

$$e = \frac{H_D - H}{H_D} \tag{3.24}$$

Where H_D and H are the height of the liquid in the presence of the gas as well as in the absence of the gas respectively. The gas hold-up is represented as percentage values.

The flow field parameters such as N_{pt}, $N_{p\varepsilon}$, normalized mean radial velocity $\left(\frac{u_r}{u_{tip}}\right)$, normalized mean tangential velocity $\left(\frac{u_t}{u_{tip}}\right)$ and normalized turbulent kinetic energy $\left(\frac{k}{u_{tip}^2}\right)$ in the reactor vessel were considered for the V&V process. The radial and axial profiles of $\frac{u_r}{u_{tip}}$, $\frac{u_t}{u_{tip}}$ and $\frac{k}{u_{tip}^2}$ at various locations within the tank were considered for the respective analyses. The physical reasons causing variations in the performance goals of the surface aerators with variations in the tank parameters were evaluated using the contours of pressure coefficient (C_p), trailing vortices, $\frac{k}{u_{tip}^2}$, normalized turbulence intensity $\left(\frac{TI}{u_{tip}}\right)$, vorticity ($G$) and strain rate ($S$) respectively. The expression for C_p is given in the equation 3.25.

$$C_p = \frac{p}{\frac{1}{2}\rho_q u_{tip}^2} \tag{3.25}$$

Where u_{tip} is the impeller tip velocity.

The trailing vortices associated with the reactor vessels were plotted using the Q-criterion (Huang and Green 2015) and the expression for the same is given in the equation 3.26.

$$Q = \frac{1}{2}(\|w\|^2 - \|S\|^2) \tag{3.26}$$

Where $\|w\|$ represents the Euclidean norm of rotation rate tensor and $\|S\|$ indicates the Euclidean norm of strain rate tensor respectively. The formation of a vortex is inferred when $Q > 0$, ie, the rotation rate of a fluid element dominates over the respective strain rate.

3.6 Configurations of surface aeration tanks

The flat bottomed tanks having circular cross-sections were adopted for the flow field analyses concerned with the present research work. The RT impeller was employed for agitating the fluid contained within the reactor vessel. The tank parameters such as $\frac{h}{D}$, $\frac{d}{D}$, N, N_{bl} and N_{bf} were varied and the corresponding impacts on the flow fields and performance goals were analysed. These tank parameters were varied in the range as given in the Table 3.3. The effect of variations of $\frac{h}{D}$, $\frac{d}{D}$ and N on the flow field characteristics of the reactor vessels were analysed under the single phase as well as multiphase conditions respectively. On the other hand, the effect of variations of N_{bl} and N_{bf} on the flow field characteristics were analysed only under the single phase conditions as the main purpose of the respective studies is to compare the mixing performance of the reactor vessel configurations rather than the features of entrainment of air into the reactor vessels.

Table 3.3: Range of the geometric and dynamic parameters of the surface aeration tank varied during the simulations

Tank type	h (m)	N (rpm)	d (m)	N_{bl}	N_{bf}
Circular baffled	0.03-0.26	100-500	0.27-0.40	2-32	0-10

The standard configuration of the reactor vessel was employed for the V&V process. The mean and turbulent flow fields associated with the standard configuration of the reactor vessel were widely investigated in the literature using the advanced experimental and computational

approaches (Delafosse et al. 2008; Escudié et al. 2004; Escudié and Liné 2003; Singh et al. 2011; Yeoh et al. 2004). Thus, the corresponding flow field results can be confidently used for assessing the accuracy of the present CFD model. The geometric details of the standard configuration of the reactor vessel used for the present research work are given in Table 3.4.

Table 3.4: Geometric details of standard configuration of the reactor vessel

Geometric parameter	Value (m)
d	0.27
H	0.27
$h\ (H/3)$	0.09
$B\ (d/10)$	0.027
$D\ (d/3)$	0.093
$l\ (D/4)$	0.02325
$b\ (D/5)$	0.0186
N_{bl}	6
N_{bf}	4

The impeller was rotated at a speed of 200 rpm so as to generate the turbulent flow conditions in the reactor vessel. The diagram of the standard configuration of the reactor vessel used for the present research work is illustrated in Figure 3.5.

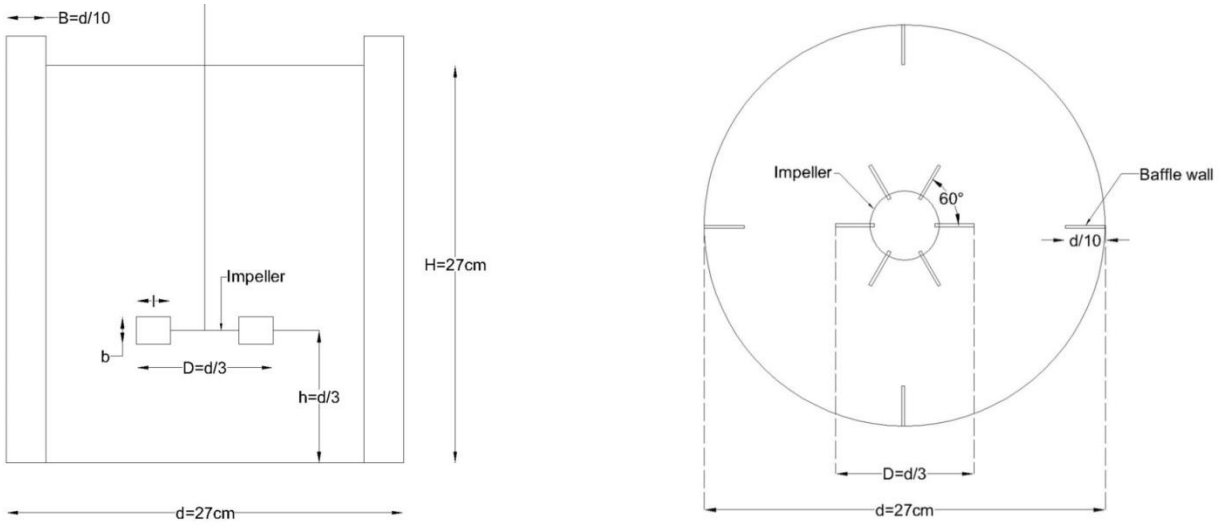

(a) **(b)**

Figure 3.5: (a) Sectional elevation and (b) Plan of the standard configuration of the reactor vessel (Source: Wu and Patterson (1989))

3.7 Summary

The single phase and multiphase CFD simulations were performed using the methodology described in the previous sections. In order to ascertain the reliability and accuracy of the CFD methodology, systematic and scientific V&V process was conducted on the widely investigated standard configuration of the stirred vessel. Based on the confidence obtained from the validation process, the methodology was employed for analyzing the flow field characteristics related with the non-standard configurations of the reactor vessels. Finally, the predicted flow fields were used to explain the physical reasons behind the variations in the performance goals with the variations in the geometric and dynamic parameters of the surface aeration tank.

3.8 References

AIAA (American Institute of Aeronautics and Astronautics). 1998. *Guide for the Verification and Validation of Computational Fluid Dynamics Simulations (AIAA G-077-1998(2002)).* Washington, DC: AIAA, Inc.

ANSYS, Inc. 2013. *ANSYS Fluent Theory Guide*. USA: ANSYS.

Aubin, J., D. F. Fletcher, and C. Xuereb. 2004. "Modeling turbulent flow in stirred tanks with CFD: The influence of the modeling approach, turbulence model and numerical scheme." *Exp. Therm. Fluid Sci.* https://doi.org/10.1016/j.expthermflusci.2003.04.001.

Basavarajappa, M., T. Draper, P. Toth, T. A. Ring, and S. Miskovic. 2015. "Numerical and experimental investigation of single phase flow characteristics in stirred tanks using Rushton turbine and flotation impeller." *Miner. Eng.*, 83: 156–167. https://doi.org/10.1016/j.mineng.2015.08.018.

Başbuğ, S., G. Papadakis, and J. C. Vassilicos. 2018. "Reduced power consumption in stirred vessels by means of fractal impellers." *AIChE J.*, 64 (4): 1485–1499. https://doi.org/10.1002/aic.16096.

Brucato, A., M. Ciofalo, F. Grisafi, and G. Micale. 1998. "Numerical prediction of flow fields in baffled stirred vessels: A comparison of alternative modelling approaches." *Chem. Eng. Sci.*, 53 (21): 3653–3684. https://doi.org/10.1016/S0009-2509(98)00149-3.

Coroneo, M., G. Montante, A. Paglianti, and F. Magelli. 2011. "CFD prediction of fluid flow and mixing in stirred tanks: Numerical issues about the RANS simulations." *Comput. Chem. Eng.*, 35 (10): 1959–1968. https://doi.org/10.1016/j.compchemeng.2010.12.007.

Deglon, D. A., and C. J. Meyer. 2006. "CFD modelling of stirred tanks: Numerical considerations." *Miner. Eng.*, 19 (10): 1059–1068. https://doi.org/10.1016/j.mineng.2006.04.001.

Delafosse, A., A. Line, J. Morchain, and P. Guiraud. 2008. "LES and URANS simulations of hydrodynamics in mixing tank: Comparison to PIV experiments." *Chem. Eng. Res. Des.*, 86 (12): 1322–1330. https://doi.org/10.1016/j.cherd.2008.07.008.

Escudié, R., D. Bouyer, and A. Liné. 2004. "Characterization of trailing vortices generated by a Rushton turbine." *AIChE J.*, 50 (1): 75–86. https://doi.org/10.1002/aic.10007.

Escudié, R., and A. Liné. 2003. “Experimental analysis of hydrodynamics in a radially agitated tank.” *AIChE J.*, 49 (3): 585–603. https://doi.org/10.1002/aic.690490306.

Hirt, C. W., and B. D. Nicholas. 1981. "Volume of fluid method for the dynamics of free surface boundaries." *J. Comput. Phys.*, 39: 201-225.

Huang, Y., and M. A. Green. 2015. “Detection and tracking of vortex phenomena using Lagrangian coherent structures.” *Exp. Fluids*, 56 (7): 1–12. Springer Berlin Heidelberg. https://doi.org/10.1007/s00348-015-2001-z.

Iyer, D. K., and A. K. Patel. 2022. “Physical Reasoning of Double- to Single-Loop Transition in Industrial Reactors using Computational Fluid Dynamics.” *J. Appl. Fluid Mech.*, 15 (5), 1621-1634. https://doi.org/10.47176/jafm.15.05.1190.

Jenne, M., and M. Reuss. 1999. “A critical assessment on the use of k–ε turbulence models for simulation of the turbulent liquid flow induced by a Rushton-turbine in baffled stirred-tank reactors.” *Chem. Eng. Sci.*, 54 (17): 3921–3941. https://doi.org/10.1016/S0009-2509(99)00093-7.

Joshi, J. B., N. K. Nere, C. V. Rane, B. N. Murthy, C. S. Mathpati, A. W. Patwardhan, and V. V. Ranade. 2011. “CFD simulation of stirred tanks: Comparison of turbulence models. Part I: Radial flow impellers.” *Can. J. Chem. Eng.*, 89 (1): 23–82. https://doi.org/10.1002/cjce.20446.

Kulkarni, A. L., and A. W. Patwardhan. 2014. “CFD modeling of gas entrainment in stirred tank systems.” *Chem. Eng. Res. Des.*, 92 (7): 1227–1248. Institution of Chemical Engineers. https://doi.org/10.1016/j.cherd.2013.10.025.

Lane, G. L., M. P. Schwarz, and G. M. Evans. 2000. “*Comparison of CFD Methods for Modelling of Stirred Tanks.*” In *Proc., Tenth Eur. Conf. Mix.*,273-280. Delft, The Netherlands: Elsevier Science.

Launder, B. E., and D. B. Spalding. 1974. “The numerical computation of turbulent flows.” *Comput. Methods Appl. Mech. Eng.*, 3 (2): 269–289. https://doi.org/10.1016/0045-7825(74)90029-2.

Liu, M. 2016. *Advances in Industrial Mixing- A Companion to the Handbook of Industrial Mixing. Chapter 5b: CFD Modeling of Stirred Tank Reactors*, 123–145. New Jersey, USA: John Wiley & Sons, Inc.

Montante, G., K. C. Lee, A. Brucato, and M. Yianneskis. 2001. “Numerical simulations of the dependency of flow pattern on impeller clearance in stirred vessels.” *Chem. Eng. Sci.*, 56 (12): 3751–3770. https://doi.org/10.1016/S0009-2509(01)00089-6.

Oberkampf, W. L., and T. G. Trucano. 2002. “Verification and validation in computational fluid dynamics.” *Prog. Aerosp. Sci.*, 38 (3): 209–272. https://doi.org/10.1016/S0376-0421(02)00005-2.

Phillips, T. S., and C. J. Roy. 2011. “*Evaluation of Extrapolation-Based Discretization Error and Uncertainty Estimators.*” In *Proc., 49th AIAA Aerosp. Sci. Meet. Incl. New Horizons Forum Aerosp. Expo.*, 1–18. Orlando, Florida: American Institute of Aeronautics and Astronautics.

Roache, P. J. 1994. “Perspective: A Method for Uniform Reporting of Grid Refinement Studies.” *J. Fluids Eng.*, 116 (3): 405–413. https://doi.org/10.1115/1.2910291.

Roache, P. J. 1998. “Verification of codes and calculations.” *AIAA J.*, 36: 696–702. https://doi.org/10.2514/3.13882.

Roy, C. J. 2010. “*Review of Discretization Error Estimators in Scientific Computing.*” In *Proc., 48th AIAA Aerosp. Sci. Meet. Incl. New Horizons Forum Aerosp. Expo.*, 1–29. Orlando, Florida: American Institute of Aeronautics and Astronautics.

Singh, H., D. F. Fletcher, and J. J. Nijdam. 2011. “An assessment of different turbulence models for predicting flow in a baffled tank stirred with a Rushton turbine.” *Chem. Eng. Sci.*, 66 (23): 5976–5988. https://doi.org/10.1016/j.ces.2011.08.018.

Wechsler, K., M. Breuer, and F. Durst. 1999. “Steady and Unsteady Computations of Turbulent Flows Induced by a 4/45° Pitched-Blade Impeller.” *J. Fluids Eng.*, 121 (2): 318–329. https://doi.org/10.1115/1.2822210.

Wu, H., and G. K. Patterson. 1989. “Laser-Doppler measurements of turbulent-flow parameters in a stirred mixer.” *Chem. Eng. Sci.*, 44 (10): 2207–2221. https://doi.org/10.1016/0009-2509(89)85155-3.

Yamamoto, T., Y. Fang, and S. V. Komarov. 2019. “Surface vortex formation and free surface deformation in an unbaffled vessel stirred by on-axis and eccentric impellers.” *Chem. Eng. J.*, 367 (December 2018): 25–36. Elsevier. https://doi.org/10.1016/j.cej.2019.02.130.

Yeoh, S. L., G. Papadakis, K. C. Lee, and M. Yianneskis. 2004. “Large Eddy Simulation of Turbulent Flow in a Rushton Impeller Stirred Reactor with Sliding-Deforming Mesh Methodology.” *Chem. Eng. Technol.*, 27 (3): 257–263. https://doi.org/10.1002/ceat.200401994.

Chapter 4

Verification and Validation (V&V) process

4.1 Introduction

The Verification & Validation (V&V) are the scientific methods employed for quantifying and building confidence in the CFD simulations (Oberkampf and Trucano 2002). The verification process is concerned with the minimization of various sources of numerical error (Cadafalch et al. 2002) so as to determine whether the CFD methodology accurately characterizes the conceptual modelling approach developed for the problem under consideration (Suard et al. 2011). On the other hand, the validation process asses the degree to which the CFD model represents the real world conditions by comparing the flow field predictions with the experimental/benchmark results (Freitas 2002; Suard et al. 2011). In the present study, four sources of numerical error such as grid resolution, grid type, numerical discretization scheme and position of MRF boundary separating the rotating and stationary zones of the reactor vessel were minimized and the corresponding predictions were validated against the results from the experimental studies, LES approach and other complex turbulence models available in the literature. The standard configuration of the reactor vessel as specified in the section 3.6 of Chapter 3 was adopted for the V&V process. The flow field characteristics as described in the section 3.5 of Chapter 3 were considered for the V&V process. These flow field characteristics include both the global flow quantities as well as local flow quantities respectively. The global flow quantities include N_{pt} and $N_{p\varepsilon}$ while the local flow quantities comprises of radial and axial profiles of $\frac{u_r}{u_{tip}}$, $\frac{u_t}{u_{tip}}$ and $\frac{k}{u_{tip}^2}$ respectively. The radial and tangential velocities are selected for the analyses as the standard reactor vessel produces strong flow in the radial and tangential directions surrounding the impeller

(Yianneskis et al. 1987). Moreover, the distribution of turbulent kinetic energy provides a clear picture of the trailing vortices around the impeller and turbulence action in the entire domain of the reactor vessel (Schäfer et al. 1998).

4.2 Grid resolution and grid type

The present section evaluates the effects of grid resolution and grid type on the accuracy and numerical convergence of the flow field predictions associated with the reactor vessel. The grid independence study of the hybrid and tetrahedral grid types were performed in a manner as specified in the sub-section 3.3.4 of Chapter 3. The grid independence study was performed in the discharge stream of the impeller since the grid convergence of the underlying anisotropic turbulence fields are much difficult as compared to that in the remaining parts of the reactor vessel (Feng et al. 2012). Therefore, the grid independence study was performed until the mean and turbulent flow fields near the impeller become almost invariant with the grid resolution. The computational grid producing accurate flow field predictions near the impeller will be adequate for the remaining portions of the reactor vessel as the flow gradients decreases with increase in the radial distance from the impeller (Feng et al. 2012). The variations of N_{pt}, $N_{p\varepsilon}$, axial profiles of $\frac{u_r}{u_{tip}}$ and $\frac{k}{u_{tip}^2}$ near the impeller with the grid resolution for both the grid types are shown in Figures 4.1(a)-4.1(f) respectively.

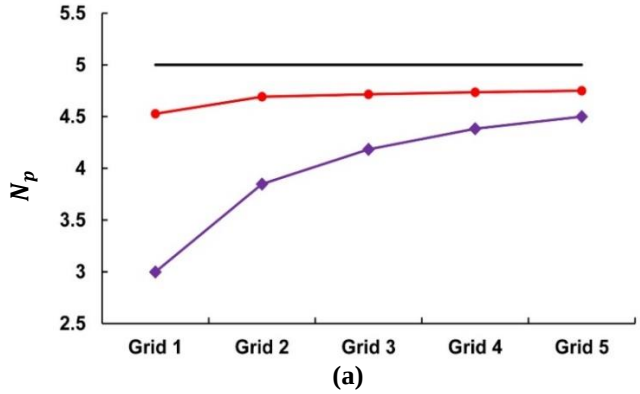

(a)

——: Experimental study (Bates et al. 1963), ●: N_{pt}, ◆: $N_{p\varepsilon}$

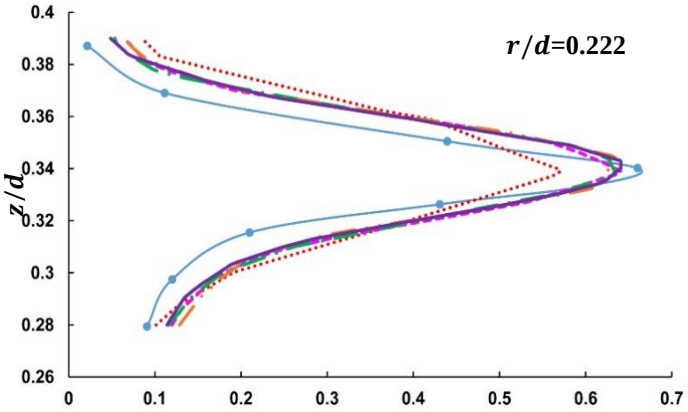

(b)

: Experimental study (Wu and Patterson 1989), : Grid 1, : Grid 2, : Grid 3, : Grid 4, : Grid 5

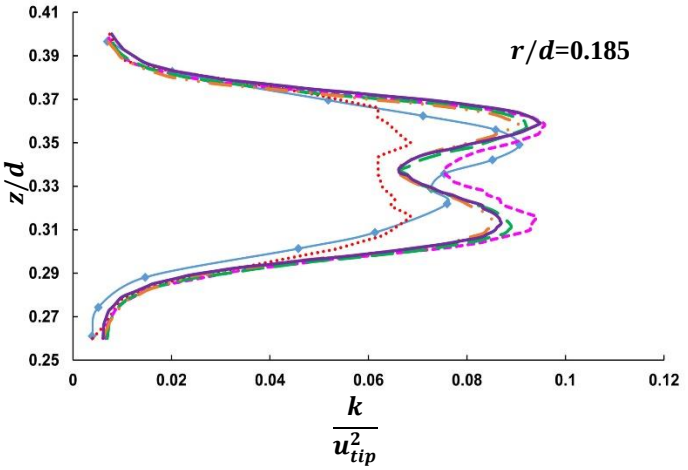

(c)

: Experimental study (Hartmann et al. 2004), : Grid 1, : Grid 2, : Grid 3, : Grid 4, : Grid 5

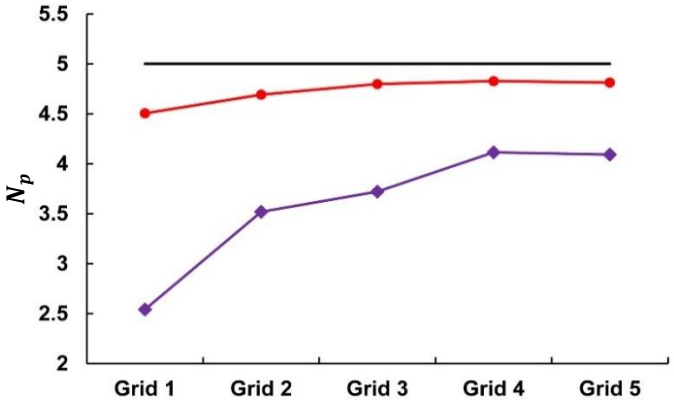

(d)

: Experimental study (Bates et al. 1963), : N_{pt}, : $N_{p\varepsilon}$

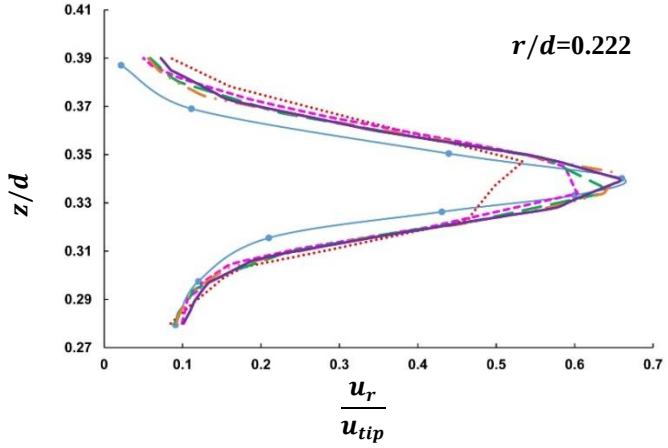

(e)

: Experimental study (Wu and Patterson 1989), : Grid 1, : Grid 2, : Grid 3, : Grid 4, : Grid 5

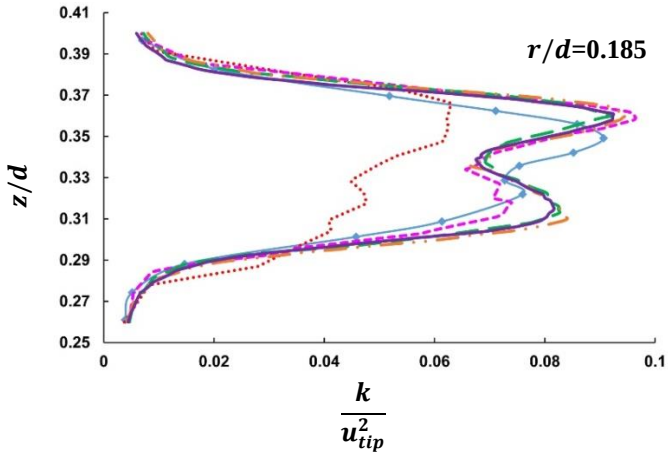

(f)

: Experimental study (Hartmann et al. 2004), : Grid 1, : Grid 2, : Grid 3, : Grid 4, : Grid 5

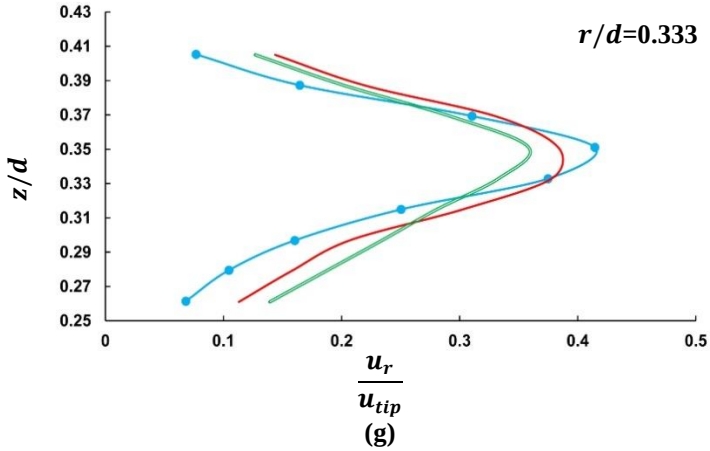

(g)

: Experimental study (Wu and Patterson 1989), : Hybrid grid, : Tetrahedral grid

Figure 4.1: Variation of N_{pt}, $N_{p\varepsilon}$ and axial profiles of $\frac{u_r}{u_{tip}}$ and $\frac{k}{u_{tip}^2}$ close to the impeller with grid resolution for [(a)-(c)] hybrid and [(d)-(f)] tetrahedral grid types and (g) comparison of axial profiles of $\frac{u_r}{u_{tip}}$ away from the impeller from the hybrid and tetrahedral grid types

As shown in Figures 4.1(a)-4.1(f), the predictions of N_{pt}, $\frac{u_r}{u_{tip}}$ and $\frac{k}{u_{tip}^2}$ close to the impeller exhibit considerable changes from Grid-1 to Grid-3 and remains constant thereafter for the hybrid as well as tetrahedral grid types. On the other hand, the prediction of $N_{p\varepsilon}$ increases from Grid-1 to Grid-4 and produces marginal improvements with Grid-5 for both the grid types. These observations indicate that the grid independency of N_{pt}, $\frac{u_r}{u_{tip}}$ and $\frac{k}{u_{tip}^2}$ is achieved with Grid-3 while the grid independency of $N_{p\varepsilon}$ is obtained with Grid-4 of both the grid types. Therefore, the high resolution grids are needed for the appropriate convergence of $N_{p\varepsilon}$ as compared to the remaining flow field variables and the computational grid producing superior convergence of the $N_{p\varepsilon}$ will provide excellent convergence of the remaining mean and turbulent flow quantities. Thus, the $N_{p\varepsilon}$ can be considered as a monitoring parameter for analyzing the grid convergence of the CFD simulations of the reactor vessels. However, the discussions related with the selection of proper monitoring parameter for the grid independence studies of the CFD simulations of the reactor vessels weren't performed in the past research works.

The N_{pt} and $N_{p\varepsilon}$ increases by 4.7% and 33.4% respectively from Grid 1 to Grid 5 for the hybrid grid type while the same increases by 6.4% and 38% respectively from Grid 1 to Grid 5 for the tetrahedral grid type. The peak $\frac{u_r}{u_{tip}}$, $\frac{u_t}{u_{tip}}$ and $\frac{k}{u_{tip}^2}$ increases by 11%, 10% and 27% from Grid 1 to Grid 5 for the hybrid grid type while the same increases by 19%, 10% and 32% from Grid 1 to Grid 5 for the tetrahedral grid type respectively. Hence, the grid convergence of the hybrid grid type is faster as compared to the tetrahedral grid type.

The numerical error associated with the mean and turbulent flow fields of hybrid and tetrahedral grids were estimated based on the GCI method (Roache 1994). The recommendations provided by Roy (2010) regarding the selection of F_s based on the value of $\hat{p}$ were adopted wherever necessary. Among the five grids generated for each grid type, three grids were used for quantifying the numerical error and the details of the same are given in the Table 4.1. The particulars related with the quantification of numerical error associated with the N_{pt}, $N_{p\varepsilon}$, $\frac{u_r}{u_{tip}}$, $\frac{u_t}{u_{tip}}$ and $\frac{k}{u_{tip}^2}$ of the hybrid and tetrahedral grids using the GCI concept are given in the Table 4.2. The GCI associated with the N_{pt}, $N_{p\varepsilon}$, $\frac{u_r}{u_{tip}}$, $\frac{u_t}{u_{tip}}$ and $\frac{k}{u_{tip}^2}$ are represented

in the form of error bars for the hybrid and tetrahedral grids as shown in Figures 4.2-4.4 respectively.

Table 4.1: Details of the grids used for the quantification of GCI associated with the mean and turbulent flow fields of the hybrid and tetrahedral grid types

Grid designation	Grid size	Element size of the impeller (m)	r	Computational time (Hrs.)
Hybrid grid type				
Grid 1	300573	0.00400	-	4
Grid 2	996072	0.00080	1.49	20
Grid 5	7418360	0.000258	1.95	40
Tetrahedral grid type				
Grid 1	266733	0.005000	-	5
Grid 3	1001202	0.001500	1.55	27
Grid 5	7142519	0.000258	1.93	60

Table 4.2: Particulars related with the quantification of GCI associated with the mean and turbulent flow fields for the hybrid and tetrahedral grid types

Flow field parameter	Hybrid grid			Tetrahedral grid		
	R^*	e_r^{21} (%)	GCI_{fine}^{21} (%)	R^*	e_r^{21} (%)	GCI_{fine}^{21} (%)
N_{pt}	0.2709	0.92	1.00	0.0523	0.32	0.35
$N_{p\varepsilon}$	0.6305	12.20	5.44	0.3148	9.07	10.0
u_{rp}	0.0396	0.42	1.27	0.4568	6.73	7.07
u_{tp}	0.2740	1.84	0.12	-1.1463	10.20	5.05
k_p	0.0340	0.98	1.73	-0.0475	1.68	3.19

The hybrid grid type provides monotonic convergence ($0<R^*<1$) for all the mean and turbulent flow quantities considered for the analysis while the tetrahedral grid type produces monotonic convergence for the N_{pt}, $N_{p\varepsilon}$ and u_{rp} and oscillatory convergence ($R^*<0$) for the u_{tp} and k_p respectively. The hybrid and tetrahedral grids develop small values of GCI (< 1%) for the N_{pt}. On the other hand, the GCI associated with the $N_{p\varepsilon}$ of hybrid grid was found to be almost half of the tetrahedral grid type. The hybrid grid develop small values of GCI (< 2%) related with the u_{rp}, u_{tp} and k_p which considerably increases for the tetrahedral grid type.

Moreover, it is clear from Figures 4.3 and 4.4 that the GCI of $\frac{u_r}{u_{tip}}$ and $\frac{k}{u_{tip}^2}$ at various locations (z/d=0.28, 0.36 and 0.4) above and below the impeller centre-plane especially close to the impeller blades from the hybrid grid are lesser than that from the tetrahedral grid. The higher GCI associated with the mean and turbulent flow fields of the tetrahedral grid type might be stemming from the numerical diffusion errors allied with the underlying elements (Longest and Vinchurkar 2007). Thus, the hybrid grid develops reliable predictions of various mean and turbulent flow fields as the corresponding GCI magnitudes are considerably smaller than that from the tetrahedral grid type. Further, as given in the Table 4.1, the computational time required for the grids of hybrid type are much lesser than that of the tetrahedral type indicating that the hybrid grid is more economical for modelling the complex multiphase flows associated with the agitated reactors.

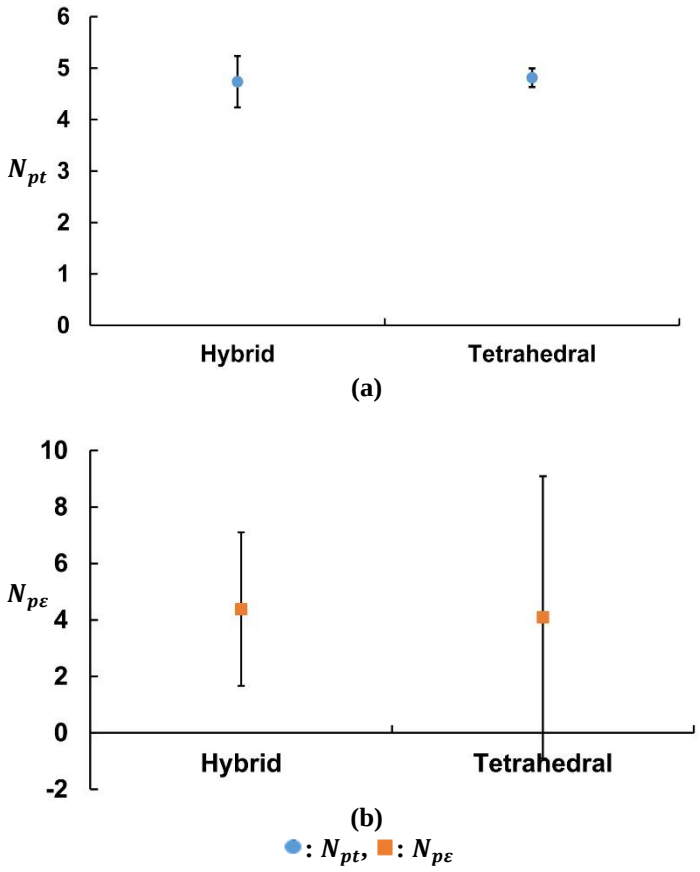

Figure 4.2: Error bars of (a) N_{pt} and (b) $N_{p\varepsilon}$ related with the hybrid and tetrahedral grid types

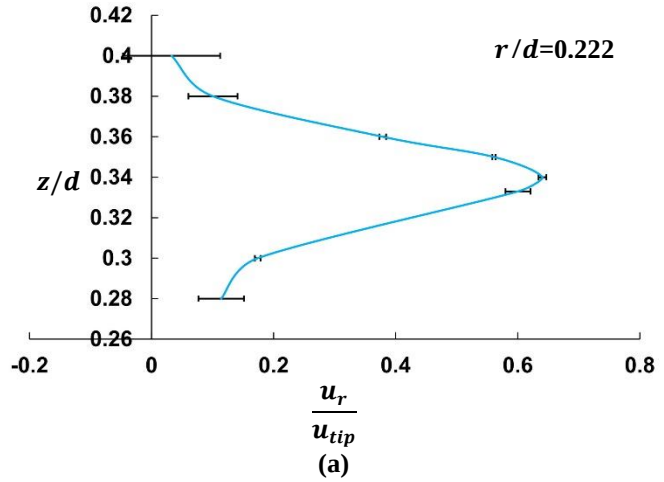

(a)

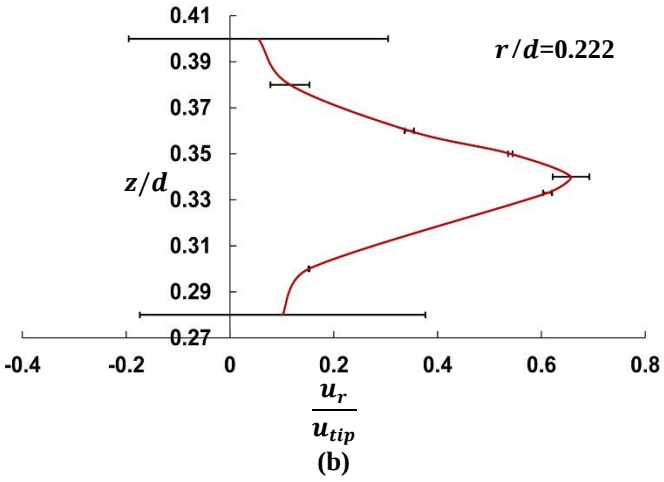

(b)

Figure 4.3: Error bars of $\frac{u_r}{u_{tip}}$ associated with the (a) hybrid and (b) tetrahedral grid types

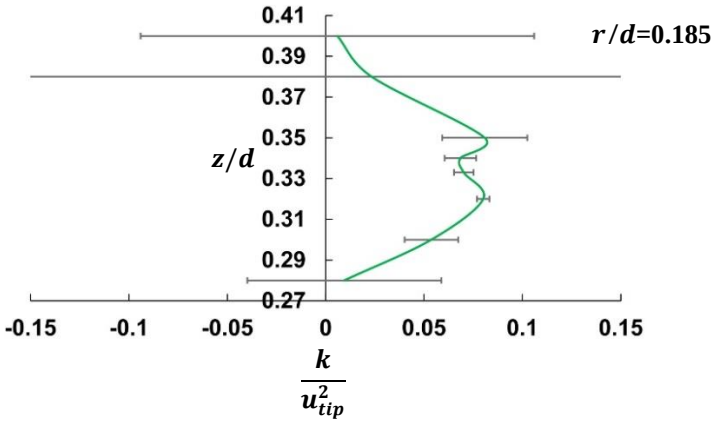

(a)

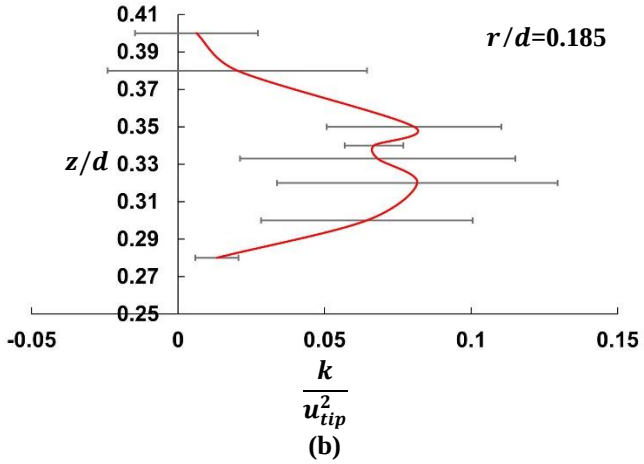

Figure 4.4: Error bars of $\frac{k}{u_{tip}^2}$ associated with the (a) hybrid and (b) tetrahedral grid types

The accuracy of flow field predictions from the hybrid and tetrahedral grids were analysed by comparing the corresponding predictions of N_{pt}, $N_{p\varepsilon}$, axial profiles of $\frac{u_r}{u_{tip}}$ and $\frac{k}{u_{tip}^2}$ close to the impeller with the experimental results as illustrated in Figures 4.1(a)-4.1(g) respectively. Both the grid types accurately predicted the single peaked curve of $\frac{u_r}{u_{tip}}$ representing the liquid jets emerging from the impeller blades and double peaked curve of $\frac{k}{u_{tip}^2}$ representing the trailing vortices generated near the top and bottom corners of impeller blades. Hybrid and tetrahedral grids accurately predicted the N_{pt} with error less than 5%. The hybrid grid accurately predicts the $N_{p\varepsilon}$ with an error of 10% while the tetrahedral grid provides inferior prediction of the same as the underlying error considerably increases to 18%. Moreover, the hybrid grid type provides lesser energy imbalance of about 5.3% in the reactor vessel which significantly increases to 15% for the tetrahedral grid type. The axial profiles of $\frac{u_r}{u_{tip}}$ and $\frac{k}{u_{tip}^2}$ near the impeller tip predicted by the hybrid and tetrahedral grids are highly similar and close to the corresponding profiles obtained from the experimental studies. The magnitude and location of peak $\frac{u_r}{u_{tip}}$ were accurately predicted by both grid types. Although, the upper peak value of $\frac{k}{u_{tip}^2}$ was accurately predicted, the lower peak magnitude of the same was slightly over predicted by both the grid types. Moreover, the locations of upper and lower peak values of $\frac{k}{u_{tip}^2}$ obtained from both the grid types were slightly shifted above and below the corresponding locations obtained from the experimental studies. Even though, both the grid types accurately predict the axial profile of $\frac{u_r}{u_{tip}}$ near the impeller blades, the hybrid grid

provides superior predictions of the same away from the impeller in comparison with the tetrahedral grid type as illustrated in Figure 4.1(g). Thus, the hybrid grid type provides accurate prediction of various mean and turbulent flow fields as compared to the tetrahedral grid type.

In general, hybrid grid type provides accurate predictions of mean and turbulent flow fields with lesser numerical discretization error and computational time as compared to the tetrahedral grid type. The Grid-5 of the hybrid grid type was employed for the further analyses in the following sections.

4.3 Numerical discretization scheme

The predictions of N_{pt}, $N_{p\varepsilon}$ and axial profiles of $\frac{u_r}{u_{tip}}$, $\frac{u_t}{u_{tip}}$ and $\frac{k}{u_{tip}^2}$ obtained from the various numerical discretization schemes are displayed in Figures 4.5(a)-4.5(d) respectively.

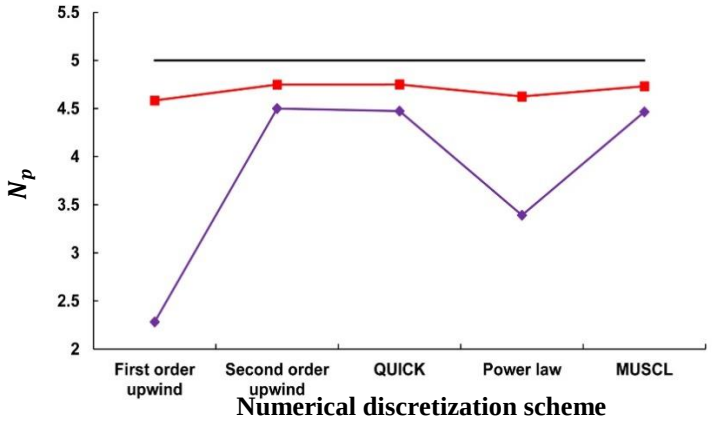

(a)

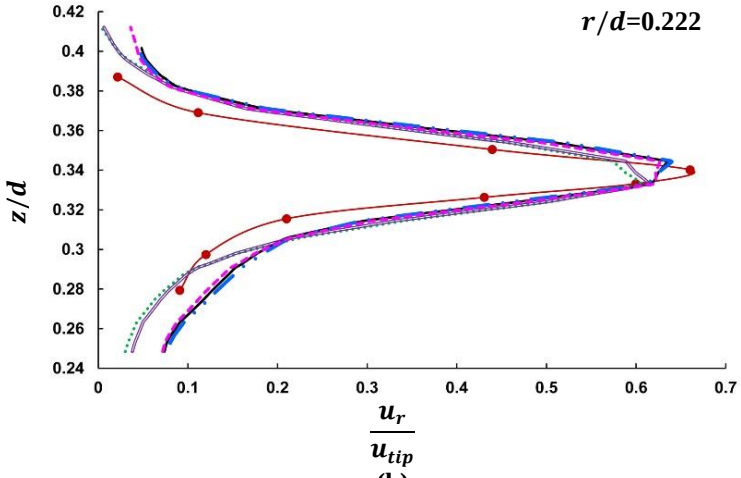

(b)

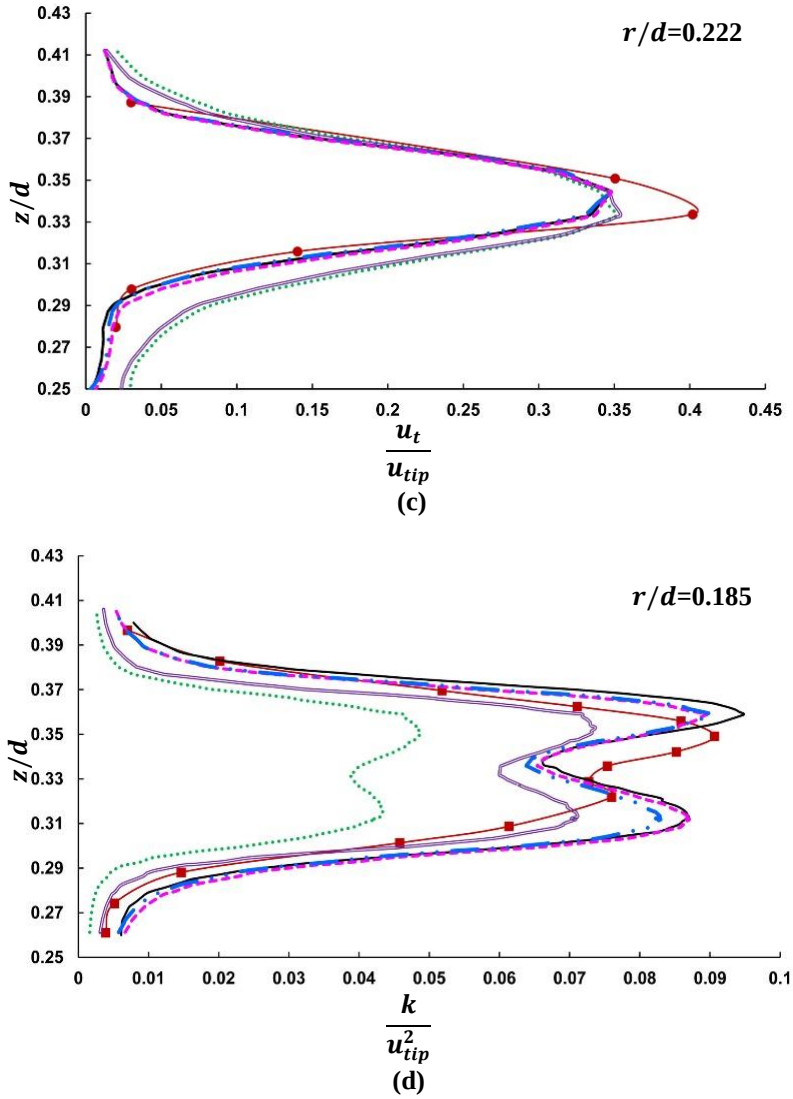

: Experimental study (Wu and Patterson 1989), : Experimental study (Hartmann et al. 2004), : Experimental study (Bates et al. 1963), : N_{pt}, : $N_{p\varepsilon}$, : First order upwind scheme, : Second order upwind scheme, : QUICK scheme, : Power law scheme, : MUSCL scheme

Figure 4.5: Variation of N_{pt}, $N_{p\varepsilon}$ and axial profiles of $\frac{u_r}{u_{tip}}$, $\frac{u_t}{u_{tip}}$ and $\frac{k}{u_{tip}^2}$ close to the impeller with the numerical discretization schemes

The general flow field characteristics of the standard reactor vessel such as single peaked curve of $\frac{u_r}{u_{tip}}$ and $\frac{u_t}{u_{tip}}$ as well as double peaked curve of $\frac{k}{u_{tip}^2}$ were accurately predicted by the various discretization schemes. The N_{pt} and $N_{p\varepsilon}$ were accurately predicted by the higher order discretization schemes with a smaller energy imbalance of 5.3% (Fig. 4.5(a)). On the other hand, the lower order discretization schemes developed inferior predictions of the N_{pt}

and $N_{p\varepsilon}$ with a significant energy imbalance of 30% (Fig. 4.5(a)). It can be observed from Figure 4.5(b) that the higher order discretization schemes provide axial profiles of $\frac{u_r}{u_{tip}}$ which are close to the corresponding experimental profile as compared to the lower order discretization schemes. Moreover, the magnitude and location of peak $\frac{u_r}{u_{tip}}$ were accurately predicted by the higher order discretization schemes as compared to the lower order discretization schemes. The axial profiles of $\frac{u_r}{u_{tip}}$ predicted by the various higher order discretization schemes were found to be highly similar in nature. On the other hand, the lower order discretization schemes qualitatively predicted the axial profile of $\frac{u_r}{u_{tip}}$ and under predicted the magnitude of peak $\frac{u_r}{u_{tip}}$ by 7%. Moreover, the location of peak $\frac{u_r}{u_{tip}}$ was found to be below the corresponding experimental location. It is clear from Figure 4.5(c) that the higher and lower order discretization schemes develop similar and accurate predictions of $\frac{u_t}{u_{tip}}$ above the impeller centre-plane while the predictions of $\frac{u_t}{u_{tip}}$ below the impeller centre-plane from the higher order discretization schemes are superior as compared to the lower order discretization schemes. It is understood from Figure 4.5(d) that the higher order schemes provide similar and accurate predictions of $\frac{k}{u_{tip}^2}$ in the entire axial profile considered for the analysis. The upper peak magnitude of the axial profile of $\frac{k}{u_{tip}^2}$ was accurately predicted with deviations less than 5% by the higher order discretization schemes. On the other hand, the first order upwind scheme provides inferior predictions of $\frac{k}{u_{tip}^2}$ along the entire axial profile considered while the power-law scheme produces improved predictions of the same above and below the impeller centre-plane which are similar to the higher order discretization schemes.

In general, the higher order discretization schemes develop similar and accurate predictions of the various mean and turbulent flow quantities. Coroneo et al. (2011) have also reported similar conclusions after comparing the predictive performance of various discretization schemes. Among the various higher order discretization schemes, the second order upwind scheme can be confidently used for modelling the reactor vessels as it provides accurate and highly similar flow field predictions in line with the third order QUICK and MUSCL schemes respectively. The QUICK and MUSCL schemes are basically developed for the CFD

simulations involving structured grids (ANSYS 2013). The usage of these third order schemes for the CFD simulations comprising of unstructured grids can reduce the predictive performance of the same (ANSYS 2013). This might be a possible reason for similar flow field predictions from the second order upwind and the remaining third order discretization schemes. However, accurate predictions of the mean and turbulent flow fields were obtained from the second order upwind scheme and the same was adopted for the further CFD simulations of the reactor vessels. The $N_{p\varepsilon}$ again becomes a critical parameter for selecting the appropriate discretization scheme as the respective magnitude significantly varies with the order of the numerical discretization scheme.

4.4 Position of MRF boundary

The proper simulation of the rotation of RT impeller in the reactor vessels requires appropriate balance between the torque applied by the impeller walls and the torque applied by the tank and baffle walls respectively (Başbuğ et al. 2017). Moreover, the velocity fields produced within the tank due to the rotation of the impeller needs to be properly modeled (ANSYS 2013). In this view, the N_{pt} computed from the torques of rotating walls $(N_{pt} - imp)$ and the stationary walls $(N_{pt} - baff)$ of the tank as well as the rate of decay of dominant velocities in the standard configuration of the reactor vessel such as mean radial velocity and mean tangential velocity were considered for the analysis. The expressions for the rate of decay of $\frac{u_r}{u_{tip}}$ and $\frac{u_t}{u_{tip}}$ in the discharge stream of the RT impeller were derived by Molen and Maanen (1978) and Wu and Patterson (1989) the same are given in the equations 4.1 and 4.2 respectively.

$$\frac{u_r}{u_{tip}} = 0.85\left(\frac{r}{R}\right)^{-a} \tag{4.1}$$

$$\frac{u_t}{u_{tip}} = 0.54\left(\frac{r}{R}\right)^{-\beta} \tag{4.2}$$

The variable R represents the radius of the impeller and the exponents a and β elucidate the rate of decay of $\frac{u_r}{u_{tip}}$ and $\frac{u_t}{u_{tip}}$ in the discharge stream of the impeller.

The variations of $N_{pt}-imp$, $N_{pt}-baff$, $N_{p\varepsilon}$, a and β with the $\frac{D_r}{D}$ and $\frac{H_r}{D}$ are shown in Figures 4.6 and 4.7 respectively. It is clear from Figures 4.6 and 4.7 that the medium $\frac{D_r}{D}$ (1.51 – 1.94) and large $\frac{H_r}{D}$ (0.43 – 1.51) develops superior matching of the $N_{pt}-imp$ and $N_{pt}-baff$ and provides accurate decay of mean radial and tangential velocities in the discharge stream of the impeller. On the other hand, the small $\frac{D_r}{D}$ (1.02 - 1.29), small $\frac{H_r}{D}$ (0.22) and large $\frac{D_r}{D}$ (2.04 - 2.26) generates inadequate matching of the $N_{pt}-imp$ and $N_{pt}-baff$ and produces inaccurate decay of the mean radial and tangential velocities in the discharge stream of the impeller. Thus, the medium $\frac{D_r}{D}$ (1.51 – 1.94) and large $\frac{H_r}{D}$ (0.43 – 1.51) can be considered as the optimal radial (D_r^*) and axial extents (H_r^*) for modelling the rotation of the RT impeller. The $D_r \times H_r$ of 14 cm×5.75 cm ($1.51D\times\pm0.31D$) provides excellent predictions of the N_{pt}, $N_{p\varepsilon}$, a and β with error less than 10% and hence the flow field predictions from the corresponding CFD model were used for analyzing the predictive capability of the present CFD modelling approach as described in the subsequent sections (ie, section 4.5 and 4.6).

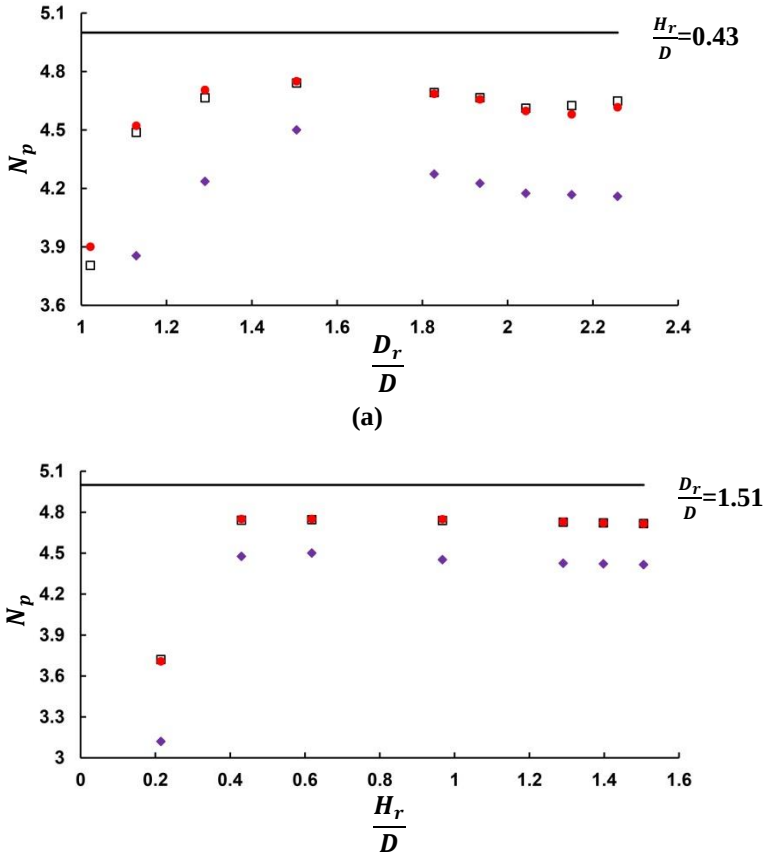

——: Experimental study (Bates et al. 1963) □:$N_{pt}-baff$, ●:$N_{pt}-imp$, ◆: $N_{p\varepsilon}$

Figure 4.6: Variation of $N_{pt}-imp$, $N_{pt}-baff$ and $N_{p\varepsilon}$ with the (a) $\frac{D_r}{D}$ and (b) $\frac{H_r}{D}$

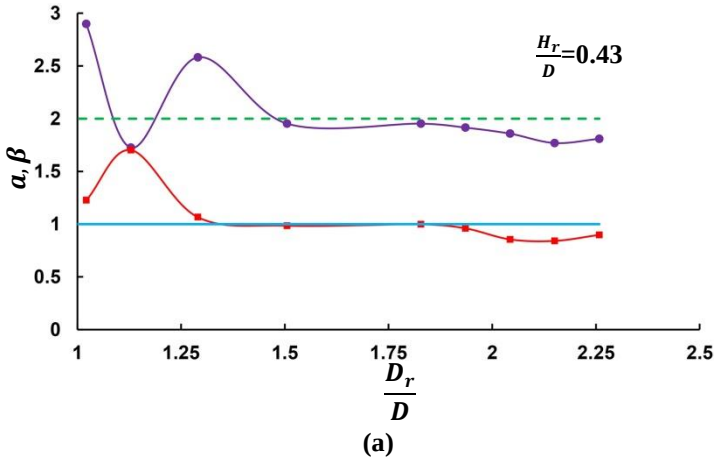

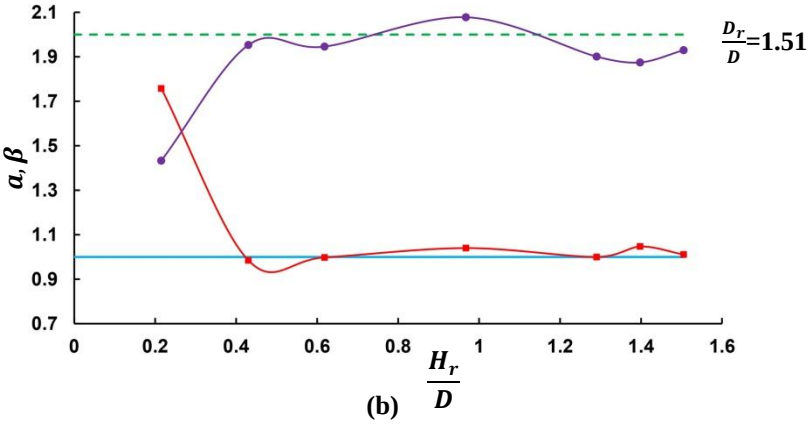

(b)

——: a based on experimental study of Molen and Maanen (1978), - - -: β based on experimental study of Wu and Patterson (1989), —■—: a, —●—: β

Figure 4.7: Variation of a and β with the (a) $\frac{D_r}{D}$ and (b) $\frac{H_r}{D}$

The suitability of limited range of $\frac{D_r}{D}$ and larger range of $\frac{H_r}{D}$ for modelling the impeller rotation indicates that the accuracy of model predictions is well controlled by the former parameter as compared to the latter parameter. The observations described in the previous paragraph indicate that the small as well as large $\frac{D_r}{D}$ are unsuitable for modelling the impeller rotation and there exists a specific range of $\frac{D_r}{D}$ which accurately predicts the various flow features associated with the standard reactor vessel. Therefore, the conclusion of suitability of large MRF boundaries for modelling the impeller rotation as given by Norouzi-Firouz et al. (2018) and Zadravec et al. (2007) cannot be followed. The small and large $\frac{D_r}{D}$ breaks the underlying steady state assumption of the MRF method (Tabor et al. 1996) which leads to inappropriate transformation of the velocity fields and inferior prediction of the flow fields associated with the standard reactor vessel. The D_r^* obtained from this study isn't close to either impeller walls or tank periphery and provides accurate prediction of various flow field quantities associated with the standard reactor vessel. Therefore, the D_r^* is located at a proper distance from the impeller walls which provides accurate transformation of the velocity fields from the inner zone to the outer zone and vice versa (ANSYS 2013; Tabor et al. 1996) for modelling the flow features associated with the standard reactor vessel. The optimal MRF extents reported by Patil et al. (2021) lies within the D_r^* obtained from this study. Moreover, the optimal MRF extents reported by Oshinowo et al. (2000) is close to the D_r^* obtained from this study while the strict comparison of the results is difficult due to slight variations in the

geometric configuration used by Oshinowo et al. (2000) and that adopted in the present research work.

The proper balance between the $N_{pt} - imp$ and $N_{pt} - baff$ can be adopted as a generalized criterion for selecting the D_r^* and H_r^* for modelling the impeller rotation associated with the reactor vessels. This condition represents the transport of angular momentum from the impeller walls to the periphery of the reactor vessel (Başbuğ et al. 2017, 2018). Since the transport of angular momentum within the reactor vessel is conserved (Başbuğ et al. 2017), the above mentioned criterion can be employed for selecting the D_r^* and H_r^* for any geometric configuration of the reactor vessel agitated using any type of impeller. Moreover, the N_{pt} can be accurately determined even from coarser computational grids which can considerably decrease the time required to select the optimal MRF boundary.

4.5 General flow features of standard reactor vessel

The general flow characteristics of the standard reactor vessel were studied using the angular profiles of $\frac{u_r}{u_{tip}}$, $\frac{u_t}{u_{tip}}$ and $\frac{u_a}{u_{tip}}$ behind the impeller blades at various radial distances from the centre of the impeller and at various axial planes above and below the impeller centre-plane as elucidated in Figures 4.8(a)-4.8(e) respectively. The main purpose of the study is to compare the mean velocity fields predicted by the present CFD model with the corresponding results reported in the literature. The radial distances are normalized by R and indicated as r^* (r/R) while the axial distances are normalized by $b/2$ and represented as z^* $(2z/b)$ respectively. The study was conducted in four regions surrounding the impeller such as (1) within the impeller blades (r^* between 0.753 and 0.968), (2) in the discharge stream of the impeller (r^* between 1.022 and 2.15), (3) within the axial extents of the impeller blades (z^* of ± 0.86) and (4) outside the axial extents of the impeller blades (z^* of ± 2.58). The ± sign indicates the z^* above and below the impeller centre-plane.

As shown in Figures 4.8(a) and 4.8(b), $\frac{u_t}{u_{tip}}$ dominates over the $\frac{u_r}{u_{tip}}$ within the region between the impeller blades while the $\frac{u_t}{u_{tip}}$ decays in a faster rate as compared to the $\frac{u_r}{u_{tip}}$ in the discharge stream of the impeller. The acceleration of fluid over the impeller blades is the major reason behind the high magnitude of tangential velocity between the impeller blades as compared to the radial velocity (Stoots and Calabrese 1995). The zero degree specified in the

graphs corresponds to the centre of the leading blade while the sixty degree corresponds to the centre of the successive blade. The peak $\frac{u_r}{u_{tip}}$ was found to be 0.907 at 5º behind the impeller blades while the peak $\frac{u_t}{u_{tip}}$ was found to be 1.37 at 10º behind the impeller blades. Moreover, the peak $\frac{u_a}{u_{tip}}$ was found to be 0.496 at 10º behind the impeller blades. The peak magnitude of $\frac{u_a}{u_{tip}}$ was less than the peak magnitude of $\frac{u_r}{u_{tip}}$ and $\frac{u_t}{u_{tip}}$ respectively. These flow features observed in the present CFD model are much similar to that reported by Molen and Maanen (1978) and Stoots and Calabrese (1995) for the RT agitated reactor vessels.

The sinusoidal variation of $\frac{u_r}{u_{tip}}$, $\frac{u_t}{u_{tip}}$ and $\frac{u_a}{u_{tip}}$ as displayed in Figures 4.8(a) to 4.8(c) represent periodic behaviour of the mean velocity field surrounding the impeller. The flat profile of the mean velocity field as illustrated in these figures indicate the non-periodic behaviour of the same. The periodic nature of mean velocity depict the presence of trailing vortex structures and the extent of periodicity in the mean velocity around the impeller represent the active region of the trailing vortex structure (Rutherford et al. 1996; Stoots and Calabrese 1995). Along the impeller centre-plane, $\frac{u_r}{u_{tip}}$ exhibit periodic behaviour from the r^* of 0.914 to 1.022 and decays further in the discharge stream of the impeller whereas the $\frac{u_t}{u_{tip}}$ display periodic behaviour from the r^* of 0.753 to 1.022 and decays further in the discharge stream of the impeller (Fig. 4.8(a) and 4.8(b)). The angular variation of $\frac{u_r}{u_{tip}}$ and $\frac{u_t}{u_{tip}}$ at various r^* along the z^* of -1.72 and 1.72 (Fig. 4.8(d) and 4.8(e)) exhibit similar results as that obtained for the same along the impeller centre-plane. The periodicity of $\frac{u_r}{u_{tip}}$ and $\frac{u_t}{u_{tip}}$ completely vanishes at the r^* of 1.505 for the axial planes along the impeller centre-plane as well as that along the z^* corresponding to ±1.72. However, the magnitude of periodicity associated with $\frac{u_r}{u_{tip}}$ and $\frac{u_t}{u_{tip}}$ along the impeller centre-plane are much higher than that along the z^* of -1.72 and 1.72 respectively. The periodic behaviour of $\frac{u_r}{u_{tip}}$ and $\frac{u_t}{u_{tip}}$ completely vanishes at the axial planes corresponding to z^* of -2.58 and 2.58 respectively. The high magnitude and periodicity of $\frac{u_t}{u_{tip}}$ between the impeller blades represents swirling motion of the fluid emerging from the impeller blades which results in the formation of trailing vortex structure (Stoots and Calabrese 1995). The high magnitude of radial velocity in the discharge stream of the impeller represents strong jet action of the fluid emerging from the impeller (Escudié and Liné 2003).

The periodicity in $\frac{u_a}{u_{tip}}$ is quite less along the impeller centre-plane and increases above and below the impeller centre-plane up to the z^* of ±0.86 (Fig. 4.8(c)) and decreases thereafter. The $\frac{u_a}{u_{tip}}$ become completely non-periodic at the z^* of ±2.58 above and below the impeller centre-plane (Fig. 4.8(f) and 4.8(g)). Thus, strongest periodicity of $\frac{u_a}{u_{tip}}$ is present within the height of the impeller blades and decays outside the axial extents of the impeller blades. The periodic behaviour of $\frac{u_a}{u_{tip}}$ is observed from the r^* of 0.753 to 0.86 and decreases further in the discharge stream of the impeller (Fig. 4.8(c)). The $\frac{u_a}{u_{tip}}$ become completely non-periodic at the r^* of 1.505 (Fig. 4.8(c)) like the other two mean velocity fields. The inferences regarding the periodic variation of mean velocity fields are much similar to that reported by Molen and Maanen (1978), Stoots and Calabrese (1995) and Yianneskis et al. (1987) respectively.

Thus, $\frac{u_r}{u_{tip}}$, $\frac{u_t}{u_{tip}}$ and $\frac{u_a}{u_{tip}}$ develop strong periodicity near the impeller blades which decreases radially as well as axially in the discharge stream of the impeller. The strongest periodicity of $\frac{u_r}{u_{tip}}$ and $\frac{u_t}{u_{tip}}$ is observed along the centre-plane of the impeller while that of $\frac{u_a}{u_{tip}}$ is observed along the axial planes at z^* of ±0.86. The three dimensional variation of the mean velocity surrounding the impeller indicates that the periodicity of $\frac{u_r}{u_{tip}}$ and $\frac{u_t}{u_{tip}}$ varies in the radial direction of the vessel whereas the periodicity of $\frac{u_a}{u_{tip}}$ varies in the axial direction above and below the impeller centre-plane. The flow periodicity in the present configuration of the reactor vessel is confined within a cylindrical region around the impeller having a diameter of $1.505D$ and a height of $0.323D$ above and below the impeller centre-plane. The region of flow periodicity around the RT impeller of the standard reactor vessel obtained from the present study is close to that reported by Deglon and Meyer (2006), Lee and Yianneskis (1994) and Stoots and Calabrese (1995) respectively. Thus, the present CFD model accurately predicts the general flow characteristics of the standard reactor vessel.

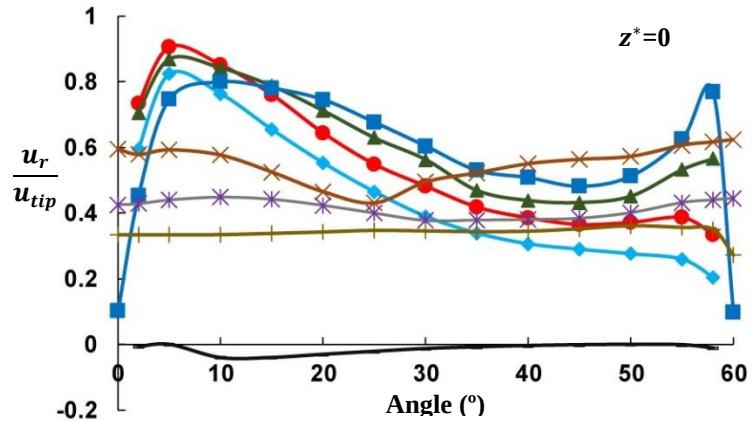
z^*=0
$\frac{u_r}{u_{tip}}$
1
0.8
0.6
0.4
0.2
0
-0.2
0
10
20
30
40
50
60
Angle (º)

(a)

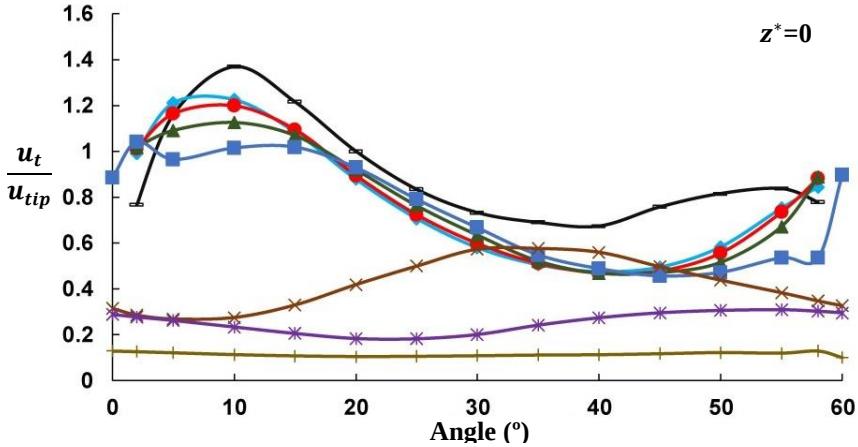
z^*=0
$\frac{u_t}{u_{tip}}$
1.6
1.4
1.2
1
0.8
0.6
0.4
0.2
0
0
10
20
30
40
50
60
Angle (º)

(b)

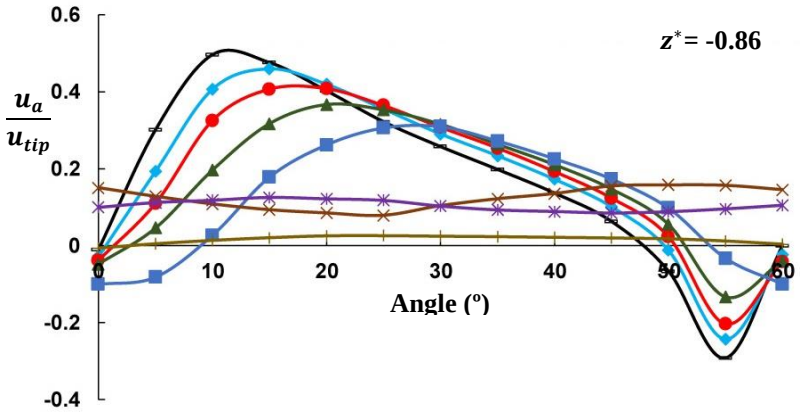
z^*= -0.86
$\frac{u_a}{u_{tip}}$
0.6
0.4
0.2
0
-0.2
-0.4
0
10
20
30
40
50
60
Angle (º)

(c)

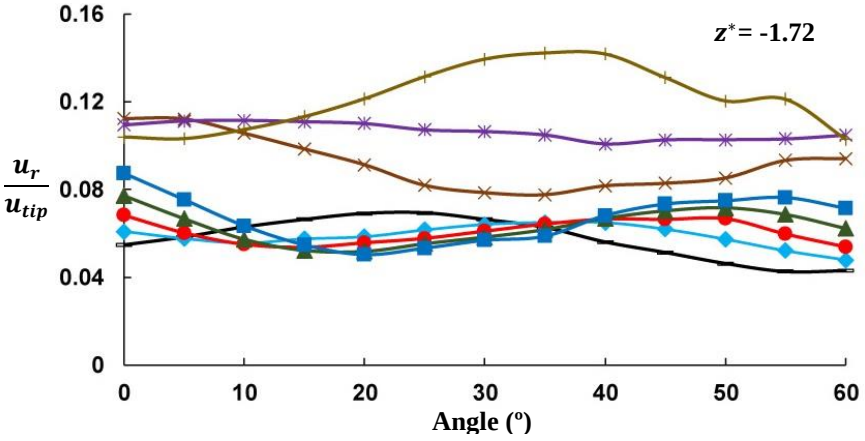
z^*= -1.72
$\frac{u_r}{u_{tip}}$
0.16
0.12
0.08
0.04
0
0
10
20
30
40
50
60
Angle (º)

(d)

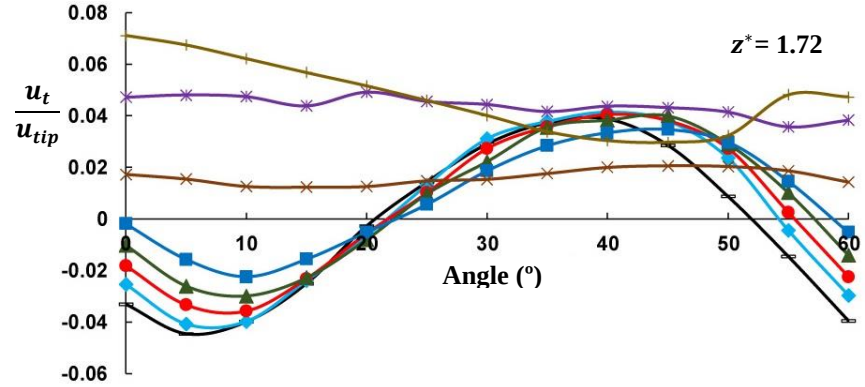
z^*= 1.72
$\frac{u_t}{u_{tip}}$
0.08
0.06
0.04
0.02
0
-0.02
-0.04
-0.06
0
10
20
30
40
50
60
Angle (º)

(e)

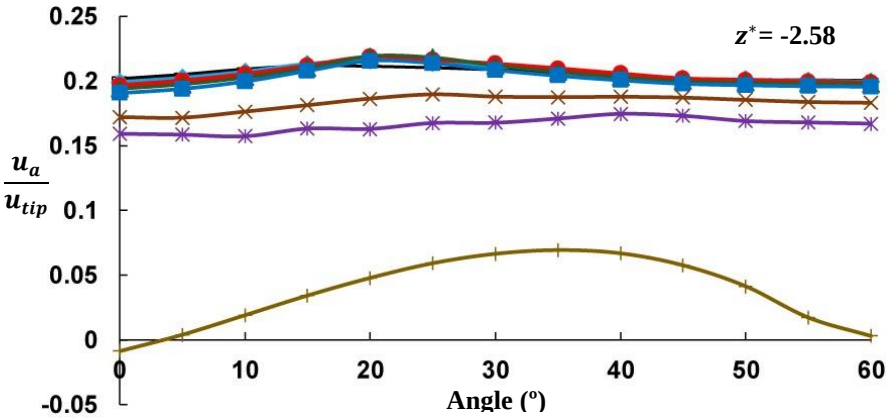
z^*= -2.58
$\frac{u_a}{u_{tip}}$
0.25
0.2
0.15
0.1
0.05
0
-0.05
0
10
20
30
40
50
60
Angle (º)

(f)

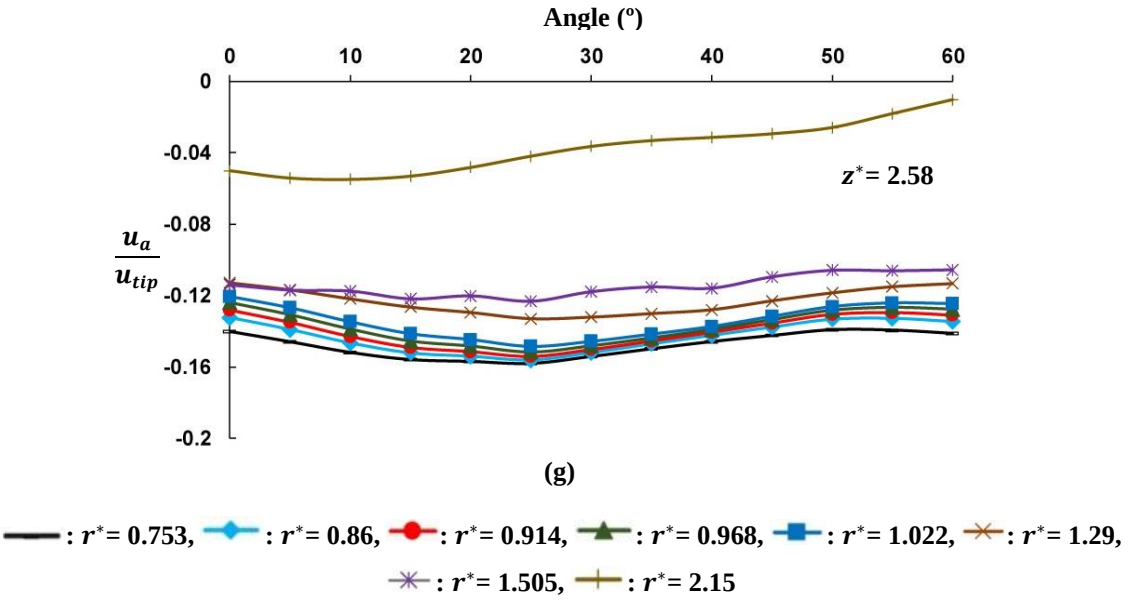

Figure 4.8: Angular profiles of $\frac{u_r}{u_{tip}}$, $\frac{u_t}{u_{tip}}$ and $\frac{u_a}{u_{tip}}$ at various r^* around the impeller

4.6 Predictive capability of the present CFD model

The present section evaluates the predictive performance of the completely verified CFD model by comparing the predictions of N_{pt}, $N_{p\varepsilon}$ and local profiles of $\frac{u_r}{u_{tip}}$ and $\frac{k}{u_{tip}^2}$ with the corresponding results from the experiments, LES approach and other complex turbulence models available in the literature. The particular care was given to the turbulent kinetic energy and turbulence dissipation rate which are normally under predicted in the majority of the CFD modelling works related with the stirred reactors. The axial and radial profiles of $\frac{u_r}{u_{tip}}$ and $\frac{k}{u_{tip}^2}$ from the present study and that from the various other literature are compared in Figures 4.9(a)-4.9(d) respectively.

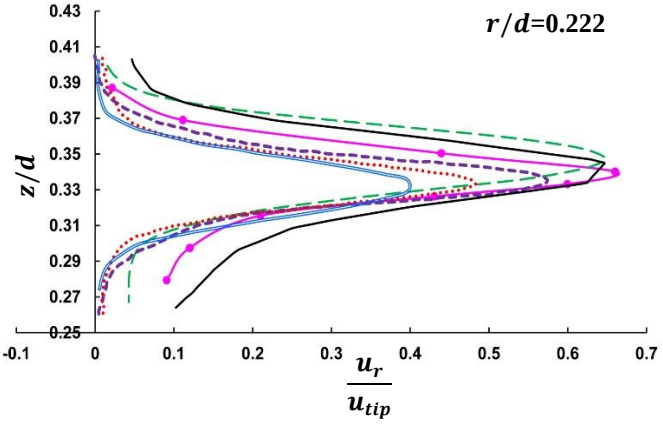

(a)

: Experimental study (Wu and Patterson 1989), : LES (Derksen and Van den Akker 1999), : EASM (Feng et al. 2012), : ASM (Sun et al. 2002), : $sk-\varepsilon$ model (Sun et al. 2002), : Present study

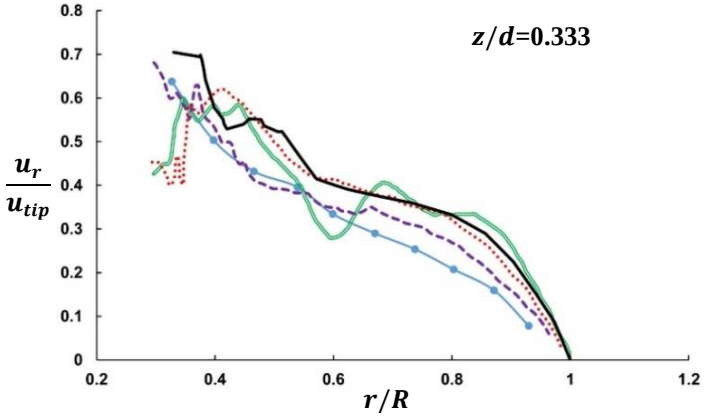

(b)

: Experimental study (Murthy and Joshi 2008), : LES (Murthy and Joshi 2008), : $sk-\varepsilon$ model (Murthy and Joshi 2008), : RSM (Murthy and Joshi 2008), : Present study

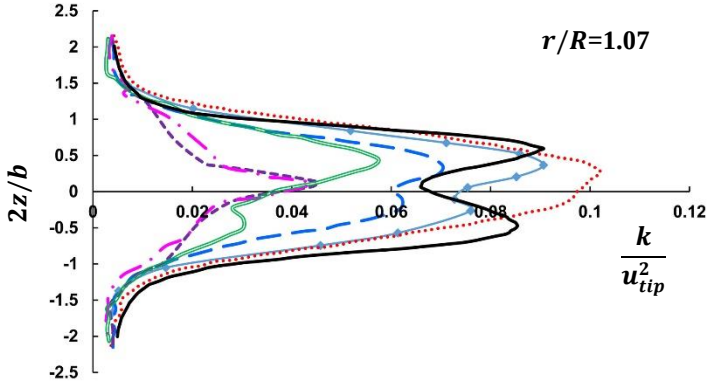

(c)

: Experimental study (Wu and Patterson 1989), : $sk-\varepsilon$ model (Singh et al. 2011), : SST model (Singh et al. 2011), : SST-CC model (Singh et al. 2011), : SSG-RSM (Singh et al. 2011), : SAS-SST model (Singh et al. 2011), : Present study

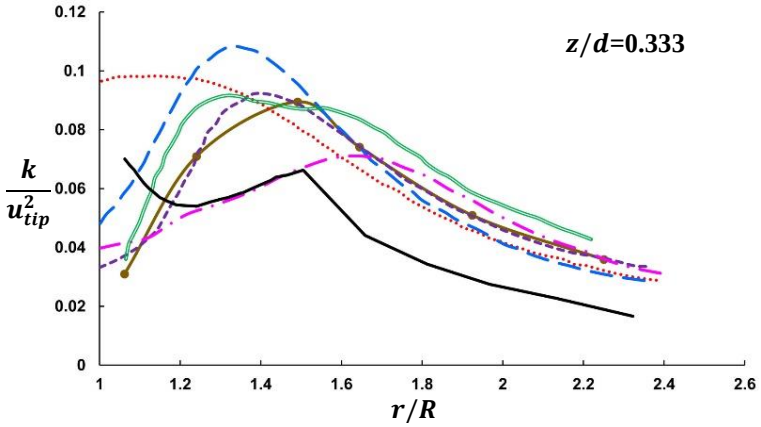

(d)

: Experimental study (Wu and Patterson 1989), : $sk-\varepsilon$ model (Singh et al. 2011), : SST model (Singh et al. 2011), : SST-CC model (Singh et al. 2011), : SSG-RSM (Singh et al. 2011), : SAS-SST model (Singh et al. 2011), : Present study

Figure 4.9: Comparison of local profiles of $\frac{u_r}{u_{tip}}$ and $\frac{k}{u_{tip}^2}$ from the present study with that from the various other literature

The axial profiles of $\frac{u_r}{u_{tip}}$ at a radial distance of 6 cm from the impeller tip predicted from the present CFD model and that reported in the various literature are compared in Figure 4.9(a). The axial profile of $\frac{u_r}{u_{tip}}$ predicted by the present CFD model closely matches with the corresponding profiles given by Derksen and Van den Akker (1999) through experimental and LES approaches respectively. Moreover, the axial profile of $\frac{u_r}{u_{tip}}$ predicted by the present CFD model was found to be better than that reported by Feng et al. (2012) using the EASM as well as by Sun et al. (2002) using the ASM and standard $k-\varepsilon$ model respectively. The present CFD model accurately predicts the magnitude and location of peak $\frac{u_r}{u_{tip}}$ whereas the EASM of Feng et al. (2012) as well as ASM and standard $k-\varepsilon$ model of Sun et al. (2002) substantially under predict the peak magnitude of $\frac{u_r}{u_{tip}}$. However, the location of peak $\frac{u_r}{u_{tip}}$ from the latter studies were found to be below the corresponding location specified by Wu and Patterson (1989) using the experimental approach.

The radial profiles of $\frac{u_r}{u_{tip}}$ along the impeller centre-plane obtained from the present CFD model and that reported in the various literature are illustrated in Figure 4.9(b). The radial profile of $\frac{u_r}{u_{tip}}$ obtained from the present CFD model is in good agreement with the

corresponding profile obtained from the experimental study of Murthy and Joshi (2008). The magnitudes of $\frac{u_r}{u_{tip}}$ near the impeller as well as in the bulk circulation region of the vessel were accurately predicted by the present CFD model. However, the LES and standard $k-\varepsilon$ models of Murthy and Joshi (2008) under predict the $\frac{u_r}{u_{tip}}$ near the impeller and over predict the same in the bulk circulation region of the vessel. Moreover, both of these models exhibit significant fluctuations of $\frac{u_r}{u_{tip}}$ along the entire radial profile considered for the analysis. The RSM approach employed by Murthy and Joshi (2008) provides adequate predictions of the $\frac{u_r}{u_{tip}}$ along the entire radial profile considered for the analysis.

The axial profiles of $\frac{k}{u_{tip}^2}$ near the impeller tip predicted from the present CFD model and that reported in the various literature are shown in Figure 4.9(c). The axial profile of $\frac{k}{u_{tip}^2}$ predicted from the present CFD model is close to the corresponding profile given by Wu and Patterson (1989) using experimental approach and better than obtained from the various turbulence models employed by Singh et al. (2011). The upper peak magnitude of $\frac{k}{u_{tip}^2}$ is accurately predicted while the lower peak magnitude of $\frac{k}{u_{tip}^2}$ is slightly over-predicted by the present CFD model. The standard $k-\varepsilon$ model of Singh et al. (2011) over-predicts $\frac{k}{u_{tip}^2}$ in the major portion of the axial profile considered while the SAS-SST, SST-CC and SSG-RSM models of Singh et al. (2011) considerably under predict the same and failed even to capture the trend of corresponding experimental profile. The SST model employed by Singh et al. (2011) significantly under predicts the magnitude of $\frac{k}{u_{tip}^2}$ along the entire axial profile considered although the corresponding axial profile qualitatively matches with the experimental profile reported by Wu and Patterson (1989).

The radial profiles of $\frac{k}{u_{tip}^2}$ along the impeller centre-plane obtained from the present CFD model as well as that reported in the various other literature are illustrated in Figure 4.9(d). The $\frac{k}{u_{tip}^2}$ increases with increase in the radial distance from the impeller, attain peak magnitude at r/R of 1.5 and decrease further towards the periphery of the reactor vessel (Singh et al. 2011). The SST model of Singh et al. (2011) considerably over predicts the magnitude of $\frac{k}{u_{tip}^2}$

along the radial profile considered for the analysis while the SSG-RSM of Singh et al. (2011) under predicts the respective magnitude and generates a wider profile of the same. The standard $k-\varepsilon$ model of Singh et al. (2011) provides higher magnitude of $\frac{k}{u_{tip}^2}$ near the impeller which decrease considerably with the radial distance from the impeller and failed even to qualitatively capture the trend of variation of $\frac{k}{u_{tip}^2}$ as obtained from the experimental study of Wu and Patterson (1989). The SAS-SST and SST-CC models employed by Singh et al. (2011) qualitatively predict the radial profile of $\frac{k}{u_{tip}^2}$ while the location of the peak $\frac{k}{u_{tip}^2}$ obtained from both the models were shifted away from the corresponding location specified in the experimental profile. The radial profile of $\frac{k}{u_{tip}^2}$ obtained from the present CFD model qualitatively matches with the respective experimental profile although the magnitude was under predicted at several locations in the radial profile. Moreover, the predictions of $\frac{k}{u_{tip}^2}$ from the present CFD model were found to be better than that obtained from the standard $k-\varepsilon$ model of Singh et al. (2011).

The percentage errors associated with the predictions of N_{pt} and $N_{p\varepsilon}$ as well as the energy imbalance allied with the present CFD model and various other modelling approaches available in the literature are specified in Table 4.3.

Table 4.3: Comparison of the percentage errors associated with N_{pt} and $N_{p\varepsilon}$ from the present study as well as from the various other literature considered for the analysis

Sl No.	Authors	Turbulence model adopted	Percentage error related with N_{pt}	Percentage error related with $N_{p\varepsilon}$	Energy imbalance $\left\{\frac{N_{pt}-N_{p\varepsilon}}{N_{pt}}\right\}$ (%)
1	Singh et al. (2011)	Standard $k-\varepsilon$ model	14.00	2.00	10.53
2	Singh et al. (2011)	SST	30.00	2.00	21.54
3	Singh et al. (2011)	SAS-SST	38.00	4.00	24.64
4	Singh et al. (2011)	SSG-RSM	30.00	10.00	15.38
5	Singh et al. (2011)	SST-CC	32.00	10.00	31.82
6	Murthy and Joshi (2008)	Standard $k-\varepsilon$ model	3.92	23.53	20.41
7	Murthy and Joshi (2008)	RSM	1.96	19.61	18.00
8	Murthy and Joshi (2008)	LES	1.96	7.84	9.62
9	Yeoh et al. (2004)	LES	-	15.00	-
10	Yeoh et al. (2004)	RANS	-	45.00	-
11	Delafosse et al. (2008)	URANS	20.00	10.00	25.00
12	Delafosse et al. (2008)	LES	20.00	20.00	33.33
13	**Present study**	**Standard $k-\varepsilon$ model**	**5.00**	**10.00**	**5.26**

The N_{pt} and $N_{p\varepsilon}$ were accurately predicted with errors less than 5% and 10% respectively by the present CFD model as well as the LES approach employed by Murthy and Joshi (2008). Although, the N_{pt} was accurately predicted by the standard $k-\varepsilon$ model and RSM adopted by Murthy and Joshi (2008), the $N_{p\varepsilon}$ was significantly under predicted by these models with errors more than 15%. On the other hand, the $N_{p\varepsilon}$ was accurately predicted by the standard $k-\varepsilon$, SST, SST-CC, SSG-RSM and SAS-SST models used by Singh et al. (2011) whereas the N_{pt} was considerably under predicted by these models with errors more than 12%. Moreover, the LES and URANS models adopted by Delafosse et al. (2008) under predicted the N_{pt} and $N_{p\varepsilon}$ by errors more than 10%. Further, the LES and RANS models employed by Yeoh et al. (2004) provide inferior predictions of $N_{p\varepsilon}$ with errors more than 15%. Also, the present CFD model produces least energy imbalance within the reactor vessel among the various other modelling approaches considered for the comparative analysis. Various

researchers (Murthy and Joshi 2008; Singh et al. 2011) have mentioned that N_{pt} is a more reliable and accurate estimate of the impeller power number as compared to the $N_{p\varepsilon}$ since the standard $k-\varepsilon$ model considerably under predicts the turbulence dissipation rate which is used for the calculation of $N_{p\varepsilon}$. However, results from the present research work illustrates that the proper minimization of various sources of numerical error significantly improves the prediction of turbulence dissipation rate from the standard $k-\varepsilon$ model which in turn provides superior prediction of the $N_{p\varepsilon}$ which is equally reliable and accurate as N_{pt} (energy imbalance of 5.26%).

The extensive comparative analyses performed so far elucidates that RANS approach with standard $k-\varepsilon$ model closure can provide accurate predictions of the mean and turbulent flow fields if various sources of numerical error are properly minimized. The mean and turbulent flow field predictions from the present CFD model were found to be close to the corresponding results from the experimental and LES methods specified in the literature. Moreover, the predictions from the present CFD model were found to be better than that obtained from the various complex turbulence models specified in the literature. The prediction of turbulent kinetic energy needs to be emphasized since the present study accurately predicts the same near the impeller while many of the researchers have experienced even 50% under prediction of the same close to the impeller (Liu 2016). The past studies have attempted to improve the accuracy of flow field predictions, turbulent quantities in particular by adopting complex or advanced turbulence model closures. However, such attempts failed to specify a single turbulence model which can accurately predict the various mean and turbulent flow fields related with the reactor vessels. For example, the SST-CC model recommended by Singh et al. (2011) has accurately predicted the radial profile of turbulent dissipation rate as compared to the remaining turbulence models considered for the analysis while the N_{pt} and $N_{p\varepsilon}$ were significantly under predicted. On the other hand, the SSG-RSM adopted by Singh et al. (2011) has provided accurate predictions of N_{pt} and $N_{p\varepsilon}$ while the local profiles of mean velocity and turbulent kinetic energy were considerably under predicted as compared to the remaining turbulence models considered for the analyses. The mixed and confusing conclusions obtained from the various turbulence model closure have posed difficulties in selecting a single turbulence model for simulating the flow features related with the reactor vessels. Moreover, various research works considered for the comparative analyses weren't properly minimized the numerical errors arising from the grid resolution and

numerical discretization scheme respectively. The studies of Delafosse et al. (2008), Singh et al. (2011), Sun et al. (2002) and Yeoh et al. (2004) didn't perform any stringent grid independence studies while Feng et al. (2012) have used lower order power-law scheme for modelling the flow fields associated with the reactor vessels. In addition to this, Singh et al. (2011) and Yeoh et al. (2004) have adopted half of the geometry of the reactor vessel for the CFD simulations which isn't an appropriate assumption for a reactor system involving complex three dimensional inhomogeneous turbulent flows (Jenne and Reuss 1999). Therefore, one of the possible reasons for the mixed conclusions regarding the performance of various turbulence models is the inadequate verification of numerical errors associated with the CFD model. The increase in the complexity of the turbulence model closure increases the number of closure equations to be solved along with the conservation equations. The solution of large number of algebraic equations increases the numerical diffusion errors and eventually affects the accuracy of the flow field predictions (Joshi et al. 2011). This is another possible reason for the mixed conclusions regarding the performance of various turbulence models. However, the present study illustrates that the proper minimization of various sources of numerical error associated with the CFD model can provide accurate predictions of the various mean and turbulent flow fields from the standard $k-\varepsilon$ model. Thus, the verification of numerical errors associated with the CFD model plays a crucial role in the accuracy of the flow field predictions regardless of the complexity of the turbulence model employed.

4.7 Conclusions

A CFD model for the standard configuration of the reactor vessel was successfully developed and numerical errors arising from grid resolution, grid type, numerical discretization scheme and position of MRF boundary associated with the CFD model were properly minimized so as to achieve reliable predictions of the mean and turbulent flow fields. Finally, the mean and turbulent flow fields obtained from the completely verified CFD model were compared with the corresponding results obtained from the experimental studies, LES approach and other complex turbulence models specified in the literature so as to evaluate the accuracy of the predictions from the present CFD model.

The grid resolution significantly affects the accuracy and numerical convergence of the various flow field quantities and its impact on the turbulent flow fields is more predominant as compared to the mean flow fields. The grid having more than 7 million elements was found

to provide grid independent solutions of the various mean and turbulent flow fields. The grid convergence of $N_{p\varepsilon}$ was difficult and required more number of iterations among the various mean and turbulent flow fields and hence recommended as a monitoring parameter for evaluating the grid independence of the CFD models of the reactor vessels. Among the hybrid and tetrahedral grid types, the hybrid grid provides accurate prediction of the mean and turbulent flow fields with less magnitude of GCI and computational time as compared to the tetrahedral grid. Thus, the hybrid grid was used for the further CFD simulations in the present research work. The higher order schemes such as second order upwind, third order QUICK and third order MUSCL schemes provided accurate predictions of various mean and turbulent flow fields as compared to the lower order schemes such as first order upwind and power-law scheme respectively. Therefore, the second order upwind scheme was employed for further CFD simulations in the present research work. The impact of position of MRF boundary on the flow fields associated with the reactor vessel was analysed by varying D_r and H_r in a systematic manner around the impeller. The medium $\frac{D_r}{D}$ (1.51-1.94) and large $\frac{H_r}{D}$ (±0.2) were found to be optimal for modelling the rotation of the impeller and the proper balance between the $N_{pt} - imp$ and $N_{pt} - baff$ was specified as a general criterion for selecting the D_r^* and H_r^* for modelling the impeller rotation. Since this criterion is based on the principle of conservation of angular momentum, it can be applied to any configuration of the reactor vessel agitated using any type of impeller.

The present CFD model accurately predicts the general features of mean velocities and periodic characteristics of the same surrounding the RT impeller. The completely verified CFD model provides accurate predictions of N_{pt} and $N_{p\varepsilon}$ which are better than that obtained from the LES approach and other complex turbulence models respectively. Moreover, the energy imbalance associated with the present CFD model was found to be the least among the various modelling approaches considered for the comparative analysis. The local profiles of $\frac{u_r}{u_{tip}}$ predicted from the present CFD model were close to the corresponding profiles obtained from the experimental and LES approaches respectively. Moreover, the local profiles of $\frac{u_r}{u_{tip}}$ obtained from the present CFD model were better than that obtained from the other complex turbulence models reported in the literature. The local profiles of $\frac{k}{u_{tip}^2}$ predicted from the present CFD model were close to the corresponding profiles obtained from the experimental studies and better than that obtained from the other complex turbulence models reported in the

literature. Thus, the RANS approach with standard $k-\varepsilon$ model closure is an effective tool for modelling the reactor vessels if the various sources of numerical error are properly minimized.

4.8 References

ANSYS, Inc. 2013. *ANSYS Fluent Theory Guide*. USA: ANSYS.

Başbuğ, S., G. Papadakis, and J. C. Vassilicos. 2017. "DNS investigation of the dynamical behaviour of trailing vortices in unbaffled stirred vessels at transitional Reynolds numbers." *Phys. Fluids*, 29 (6): 064101. https://doi.org/10.1063/1.4983494.

Başbuğ, S., G. Papadakis, and J. C. Vassilicos. 2018. "Reduced power consumption in stirred vessels by means of fractal impellers." *AIChE J.*, 64 (4): 1485–1499. https://doi.org/10.1002/aic.16096.

Bates, R. L., P. L. Fondy, and R. R. Corpstein. 1963. "Examination of Some Geometric Parameters of Impeller Power." *Ind. Eng. Chem. Process Des. Dev.*, 2 (4): 310–314. https://doi.org/10.1021/i260008a011.

Cadafalch, J., C. D. Pérez-Segarra, R. Cònsul, and A. Oliva. 2002. "Verification of Finite Volume Computations on Steady-State Fluid Flow and Heat Transfer." *J. Fluids Eng.*, 124 (1): 11. https://doi.org/10.1115/1.1436092.

Coroneo, M., G. Montante, A. Paglianti, and F. Magelli. 2011. "CFD prediction of fluid flow and mixing in stirred tanks: Numerical issues about the RANS simulations." *Comput. Chem. Eng.*, 35 (10): 1959–1968. https://doi.org/10.1016/j.compchemeng.2010.12.007.

Deglon, D. A., and C. J. Meyer. 2006. "CFD modelling of stirred tanks: Numerical considerations." *Miner. Eng.*, 19 (10): 1059–1068. https://doi.org/10.1016/j.mineng.2006.04.001.

Delafosse, A., A. Line, J. Morchain, and P. Guiraud. 2008. "LES and URANS simulations of hydrodynamics in mixing tank: Comparison to PIV experiments." *Chem. Eng. Res. Des.*, 86 (12): 1322–1330. https://doi.org/10.1016/j.cherd.2008.07.008.

Derksen, J., and H. E. A. Van den Akker. 1999. "Large eddy simulations on the flow driven by a Rushton turbine." *AIChE J.*, 45 (2): 209–221. https://doi.org/10.1002/aic.690450202.

Escudié, R., and A. Liné. 2003. "Experimental analysis of hydrodynamics in a radially agitated tank." *AIChE J.*, 49 (3): 585–603. https://doi.org/10.1002/aic.690490306.

Feng, X., J. Cheng, X. Li, C. Yang, and Z.-S. Mao. 2012. “Numerical simulation of turbulent flow in a baffled stirred tank with an explicit algebraic stress model.” *Chem. Eng. Sci.*, 69 (1): 30–44. https://doi.org/10.1016/j.ces.2011.09.055.

Freitas, C. J. 2002. “The issue of numerical uncertainty.” *Appl. Math. Model.*, 26 (2): 237–248. https://doi.org/10.1016/S0307-904X(01)00058-0.

Hartmann, H., J. J. Derksen, C. Montavon, J. Pearson, I. S. Hamill, and H. E. A. van den Akker. 2004. “Assessment of large eddy and RANS stirred tank simulations by means of LDA.” *Chem. Eng. Sci.*, 59 (12): 2419–2432. https://doi.org/10.1016/j.ces.2004.01.065.

Jenne, M., and M. Reuss. 1999. “A critical assessment on the use of k–ε turbulence models for simulation of the turbulent liquid flow induced by a Rushton-turbine in baffled stirred-tank reactors.” *Chem. Eng. Sci.*, 54 (17): 3921–3941. https://doi.org/10.1016/S0009-2509(99)00093-7.

Joshi, J. B., N. K. Nere, C. V. Rane, B. N. Murthy, C. S. Mathpati, A. W. Patwardhan, and V. V. Ranade. 2011. “CFD simulation of stirred tanks: Comparison of turbulence models. Part I: Radial flow impellers.” *Can. J. Chem. Eng.*, 89 (1): 23–82. https://doi.org/10.1002/cjce.20446.

Lee, K. C., and M. Yianneskis. 1994. “*The extent of periodicity of the flow in vessels stirred by Rushton impellers.*” In *AIChE Symp. Ser., Industrial Mixing Technology: Chemical and Biological Applications*, 90 (5), 5–18. AIChE.

Liu, M. 2016. *Advances in Industrial Mixing- A Companion to the Handbook of Industrial Mixing. Chapter 5b: CFD Modeling of Stirred Tank Reactors*, 123–145. New Jersey, USA: John Wiley & Sons, Inc.

Longest, P. W., and S. Vinchurkar. 2007. “Effects of mesh style and grid convergence on particle deposition in bifurcating airway models with comparisons to experimental data.” *Med. Eng. Phys.*, 29 (3): 350–366. https://doi.org/10.1016/j.medengphy.2006.05.012.

Murthy, B. N., and J. B. Joshi. 2008. “Assessment of standard k-e, RSM and LES turbulence models in a baffled stirred vessel agitated by various impeller designs.” *Chem. Eng. Sci.*, 63 (22): 5468–5495. https://doi.org/10.1016/j.ces.2008.06.019.

Norouzi-Firouz, H., M.-H. Sarrafzadeh, and R. Zarghami. 2018. “Investigating the Effect of Multiple Reference Frame Approach on the Modelling of an Oxidation Ditch.” *Int. J. Environ. Res.*, 12 (4): 429–437. Springer International Publishing. https://doi.org/10.1007/s41742-018-0095-x.

Oberkampf, W. L., and T. G. Trucano. 2002. “Verification and validation in computational fluid dynamics.” *Prog. Aerosp. Sci.*, 38 (3): 209–272. https://doi.org/10.1016/S0376-0421(02)00005-2.

Oshinowo, L., Z. Jaworski, K. N. Dyster, E. Marshall, and A. W. Nienow. 2000. “*Predicting the tangential velocity field in stirred tanks using the Multiple Reference Frames (MRF) model with validation by LDA measurements.*” In *Proc., 10th Eur. Conf. Mix.*, 281–288. Delft, The Netherlands: Elsevier.

Patil, H., A. K. Patel, H. J. Pant, and A. Venu Vinod. 2021. “CFD simulation model for mixing tank using multiple reference frame (MRF) impeller rotation.” *ISH J. Hydraul. Eng.*, 27 (2): 200–209. https://doi.org/10.1080/09715010.2018.1535921.

Roache, P. J. 1994. “Perspective: A Method for Uniform Reporting of Grid Refinement Studies.” *J. Fluids Eng.*, 116 (3): 405–413. https://doi.org/10.1115/1.2910291.

Roy, C. 2010. “*Review of Discretization Error Estimators in Scientific Computing.*” In *Proc., 48th AIAA Aerosp. Sci. Meet. Incl. New Horizons Forum Aerosp. Expo.*, 1–29. Reston, Virigina: American Institute of Aeronautics and Astronautics.

Rutherford, K., K. C. Lee, S. M. S. Mahmoudi, and M. Yianneskis. 1996. “Hydrodynamic characteristics of dual Rushton impeller stirred vessels.” *AIChE J.*, 42 (2): 332–346. https://doi.org/10.1002/aic.690420204.

Schäfer, M., M. Yianneskis, P. Wächter, and F. Durst. 1998. “Trailing vortices around a 45° pitched-blade impeller.” *AIChE J.*, 44 (6): 1233–1246. https://doi.org/10.1002/aic.690440602.

Singh, H., D. F. Fletcher, and J. J. Nijdam. 2011. “An assessment of different turbulence models for predicting flow in a baffled tank stirred with a Rushton turbine.” *Chem. Eng. Sci.*, 66 (23): 5976–5988. https://doi.org/10.1016/j.ces.2011.08.018.

Stoots, C. M., and R. V. Calabrese. 1995. “Mean velocity field relative to a Rushton turbine blade.” *AIChE J.*, 41 (1): 1–11. https://doi.org/10.1002/aic.690410102.

Suard, S., C. Lapuerta, F. Babik, and L. Rigollet. 2011. “Verification and validation of a CFD model for simulations of large-scale compartment fires.” *Nucl. Eng. Des.*, 241 (9): 3645–3657. https://doi.org/10.1016/j.nucengdes.2011.08.012.

Sun, H. Y., W. J. Wang, and Z. S. Mao. 2002. “Numerical simulation of the whole three dimensional flow in a stirred tank with anisotropic algebraic stress model.” *Chinese J. Chem. Eng.*, 10 (1): 15–24.

Tabor, G., A. D. Gosman, and R. I. Issa. 1996. “*Numerical simulation of the flow in a mixing vessel stirred by a rushton turbine.*” In *IChemE Symp. Ser., Fluid Mixing 5*, 140, 25-34. IChemE.

Van Der Molen, K., and H. R. E. Van Maanen. 1978. “Laser-Doppler measurements of the turbulent flow in stirred vessels to establish scaling rules.” *Chem. Eng. Sci.*, 33 (9): 1161–1168. https://doi.org/10.1016/0009-2509(78)85081-7.

Wu, H., and G. K. Patterson. 1989. “Laser-Doppler measurements of turbulent-flow parameters in a stirred mixer.” *Chem. Eng. Sci.*, 44 (10): 2207–2221. https://doi.org/10.1016/0009-2509(89)85155-3.

Yeoh, S. L., G. Papadakis, K. C. Lee, and M. Yianneskis. 2004. “Large Eddy Simulation of Turbulent Flow in a Rushton Impeller Stirred Reactor with Sliding-Deforming Mesh Methodology.” *Chem. Eng. Technol.*, 27 (3): 257–263. https://doi.org/10.1002/ceat.200401994.

Yianneskis, M., Z. Popiolek, and J. H. Whitelaw. 1987. “An experimental study of the steady and unsteady flow characteristics of stirred reactors.” *J. Fluid Mech.*, 175 (1): 537. https://doi.org/10.1017/S002211208700051X.

Zadravec, M., S. Basic, and M. Hribersek. 2007. "The influence of rotating domain size in a rotating reference frame appraoch for simulation of rotating impeller in a mixing vessel." *J. Eng. Sci. Technol.* 2 (2): 126-138.

Chapter 5

Effect of aeration tank parameters on flow field characteristics and performance goals

5.1 General

The geometric and dynamic parameters of the surface aeration tanks control the entrainment of air into the vessel. Earlier studies (Deshmukh and Joshi 2006; Patil et al. 2004; Rao et al. 2009) have determined the optimal configuration of the same for achieving maximum oxygen transfer into the reactor vessel. The study of Motamedvaziri and Armenante (2012) has found considerable variations in the flow patterns and power number under aeration conditions as compared to the non-aeration conditions. However, the physical reasons causing such variations in the flow patterns and power number during the aeration process are unknown to the research community which need to be studied in detail so as to obtain the optimal design of the surface aeration tanks. Thus, the present chapter attempts to provide physical reasons causing variations in the flow patterns, N_{pt} and oxygen transfer (in terms of gas hold-up) with variations in the geometric and dynamic parameters of the surface aeration tank. The flow behaviour of the surface aeration tank under various geometric and dynamic conditions was analysed for this purpose using the mean pressure coefficient, trailing vortex patterns, turbulent kinetic energy and turbulent intensity field near the impeller as well as in the bulk circulation region of the vessel. The key parameters affecting the aeration process such as $\frac{h}{D}$, $\frac{d}{D}$ and N were considered for the analysis. Moreover, the optimal N_{bl} and N_{bf} required for achieving superior mixing conditions in the aeration tank was also determined using the underlying patterns of turbulent kinetic energy and turbulent intensity respectively. The

comprehensive flow field analysis pertaining to each tank parameter is described in the sections given below.

5.2 Impeller clearance

The effect of impeller clearance on the flow patterns, N_{pt}, N_q, oxygen transfer and mixing characteristics of the reactor vessel were analysed in the sub-sections from 5.2.1 to 5.2.4. The $\frac{h}{D}$ was varied in a wide spectrum ranging between 0.32-2.79. Both the single phase and multiphase simulations were performed to understand the physical reasons causing variations in the performance goals with $\frac{h}{D}$.

5.2.1 Flow patterns

The mean flow patterns developed under various $\frac{h}{D}$ were analysed and following inferences were drawn. The $\frac{h}{D}$ in the range of 0.65-1.94 (medium $\frac{h}{D}$ or medium clearance) develops discharge streams which move radially behind the impeller blades and strike on the tank periphery to provide two circulation loops below the impeller and two circulation loops above the impeller respectively. This type of flow pattern is known as double re-circulation or double loop or double eight pattern (Zhu et al. 2019). The double loop pattern is characterised by high magnitude of velocity around the impeller representing strong jet action of the discharge stream and substantial velocity magnitude in the bulk circulation region. The high velocities in major part of the double loop pattern leads to bulk mixing of the fluid contained within the vessel. The double loop pattern associated with the vessel having $\frac{h}{D}$ of 0.97 is shown in Figure 5.1(b). The $\frac{h}{D}$ less than 0.65 (low $\frac{h}{D}$ or low clearance vessel) provide discharge streams which move axially downward, strike on the bottom surface of the reactor vessel to generate two major vortices above the impeller. This type of flow pattern is known as single re-circulation or single loop or single eight pattern (Montante et al. 2001). The single loop pattern associated with $\frac{h}{D}$ of 0.32 is shown in Figure 5.1(a). Since the discharge streams are directed downward under the low clearance conditions, this pattern can be precisely called as single loop down-pumping pattern. The single loop down-pumping pattern produces high velocities near the bottom surface of the tank and inferior velocities in the other portions of the tank resulting in localized mixing near the bottom surface of the tank. The secondary

circulation loops can be seen near the top surface of the tank, near the top corners of the tank and below the bottom surface of the blades as shown in Figure 5.1(a). The $\frac{h}{D}$ more than 1.94 (high $\frac{h}{D}$ or high clearance vessel) provide discharge streams which move axially upward, strike on the free liquid surface of the vessel to develop single loop pattern. The single loop pattern associated with $\frac{h}{D}$ of 2.58 is illustrated in Figure 5.1(c). Since, the discharge streams are directed upward under the high clearance conditions, this pattern can be named as single loop up-pumping pattern. The single loop up-pumping pattern produces high velocities near the free liquid surface and inferior velocities in the remaining portions of the vessel resulting in localized mixing near the free liquid surface of the reactor vessel. The secondary circulation loops can be seen above the top surface of the blades and near the free liquid surface as shown in Figure 5.1(c). Thus, the low clearance as well as high clearance conditions cause transition from standard double loop to single loop pattern and significant variations in the underlying mixing characteristics.

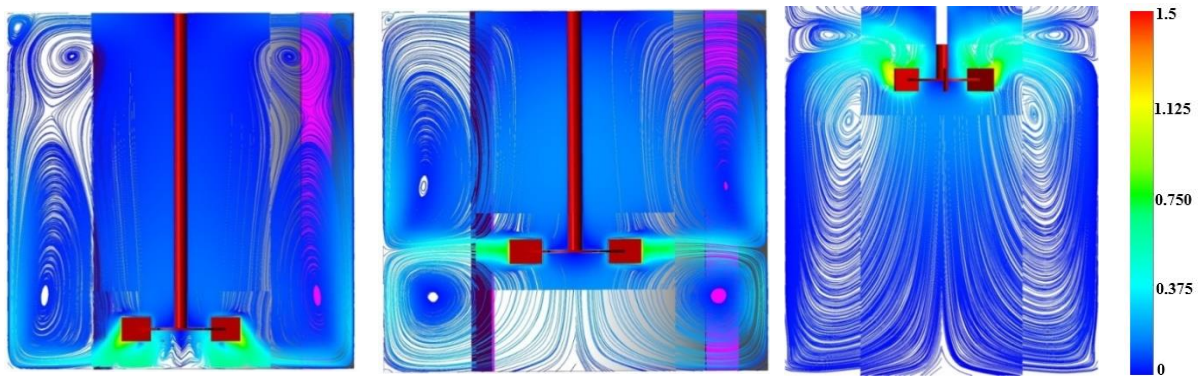

(a) **(b)** **(c)**

Figure 5.1: Flow patterns along the mid-baffle plane associated with the $\frac{h}{D}$ of (a) 0.32, (b) 0.97 and (c) 2.58

The contours of C_p along the mid baffle plane associated with the $\frac{h}{D}$ of 0.32, 0.97 and 2.58 are considered for explaining the physical reasons causing the transition from double loop to single loop pattern as illustrated in Figures 5.2(a)-5.2(c) respectively. The vessel with $\frac{h}{D}$ of 0.97 develops low pressure region behind the impeller blades and uniform distribution of high pressure in the remaining portions of the reactor vessel (Fig. 5.2(b)) resulting in the formation of radial flow fields behind the impeller blades and the classic double re-circulation pattern within the reactor vessel. On the other hand, the vessel with $\frac{h}{D}$ of 0.32 develops distinct low pressure region below the impeller (Fig. 5.2(a)) which drags the discharge streams towards

the bottom surface of the reactor vessel leading to the development of single loop down-pumping pattern. Similarly, the vessel with $\frac{h}{D}$ of 2.58 provides a distinct low pressure region above the impeller (Fig. 5.2(c)) which pulls the discharge streams towards the free-liquid surface resulting in formation of single loop up-pumping pattern. Thus, the distribution of low pressure region surrounding the impeller causes transition from double loop to single loop pattern under low clearance as well as high clearance conditions respectively.

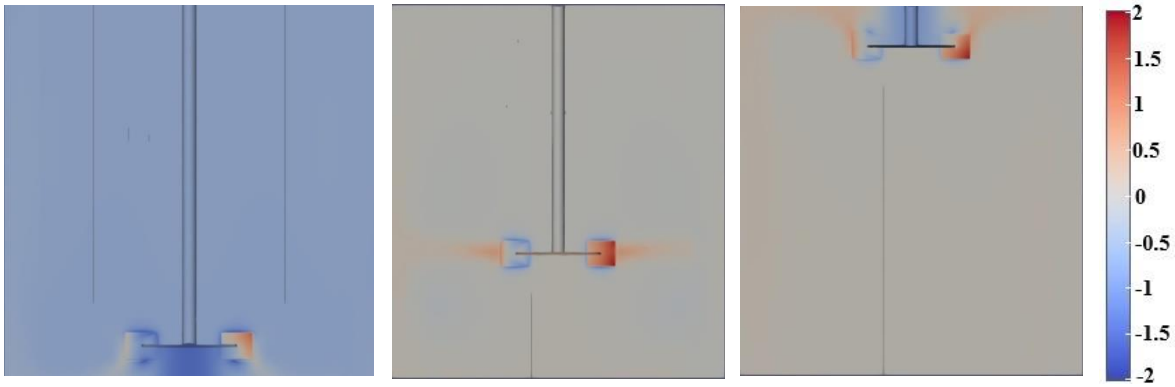

(a) **(b)** **(c)**

Figure 5.2: Contours of C_p along the mid-baffle plane associated with the $\frac{h}{D}$ of (a) 0.32, (b) 0.97 and (c) 2.58

5.2.2 Power number

The variation of N_{pt} with $\frac{h}{D}$ is shown in Figure 5.3. The vessels with medium $\frac{h}{D}$ exhibit similar values of N_{pt} which are 35% more than that obtained for the low $\frac{h}{D}$ as well as high $\frac{h}{D}$ respectively (Montante et al. 1999, 2001; Motamedvaziri and Armenante 2012). The low clearance as well as high clearance vessels also provide similar values of N_{pt}. Therefore, the reactor vessels with $\frac{h}{D}$ of 0.32, 0.97 and 2.58 were considered further for elucidating the physical reasons causing the reduction in the N_{pt} under low $\frac{h}{D}$ and high $\frac{h}{D}$ conditions.

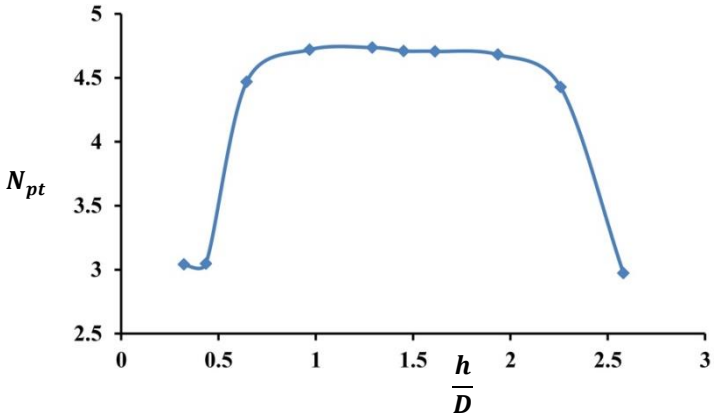

Figure 5.3: Variation of N_{pt} with $\frac{h}{D}$

The contours of trailing vortices along the impeller centre-plane associated with $\frac{h}{D}$ of 0.32, 0.97 and 2.58 are shown in Figures 5.4(a)-5.4(c) respectively. The $\frac{h}{D}$ of 0.97 develops large trailing vortices (Fig. 5.4(b)) which increases the intensity of low pressure regions (or flow separation regions) behind the impeller blades. The strong flow separation regions decrease the pressure on the suction side of the blades which in turn increase the pressure difference between the suction and pressure sides of the blades (Fig. 5.2(b)). The high pressure difference between the suction and pressure sides of the blades increase the form drag and torque related with the impeller. The high value of the impeller torque increases the corresponding N_{pt} magnitude. The front side of the impeller blade is indicated as the pressure side of the blade which is shown on the right side of the shaft in the contour plots (Fig. 5.2(a)-5.2(c)) while rear side of the impeller blade is indicated as the suction side of the blade which is shown on the left side of the shaft in the contour plots (Fig. 5.2(a)-5.2(c)). The $\frac{h}{D}$ of 0.32 and 2.58 provide small trailing vortices (Fig. 5.4(a) and 5.4(c)) which decrease the intensity of flow separation regions behind the impeller blades. The weak flow separation regions increase the pressure on the suction side of the blades which in turn decrease the pressure difference between the suction and pressure sides of the blades (Fig. 5.2(a) and 5.2(c)). The low pressure difference between the suction and pressure sides of the blades decrease the form drag and torque related with the impeller. The low value of impeller torque decreases the corresponding N_{pt} magnitude. Thus, the reduction in the intensity and extent of trailing vortices under the low clearance and high clearance conditions decrease the corresponding N_{pt} magnitude as compared to the medium clearance conditions. Hence, the distribution of trailing vortices surrounding the impeller controls the power number of the corresponding reactor vessel.

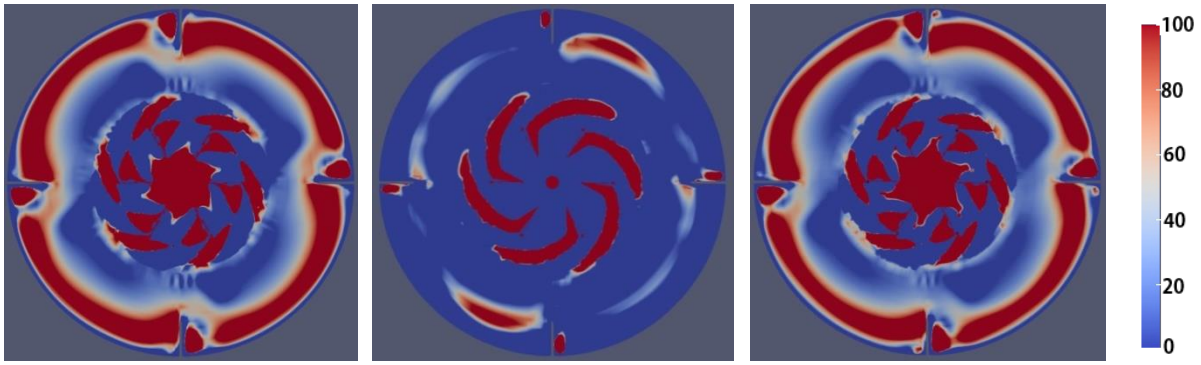

(a) **(b)** **(c)**

Figure 5.4: Contours of trailing vortices along impeller centre-plane for the $\frac{h}{D}$ of (a) 0.32, (b) 0.97 & (c) 2.58

The variation of N_q with $\frac{h}{D}$ is shown in Figure 5.5. The medium clearance vessels provide similar magnitude of N_q which are 35% more than that from the low clearance as well as high clearance vessels respectively. Moreover, N_q values of the low clearance and high clearance vessels are also similar in nature. Thus, the medium clearance vessels provide superior pumping of the liquid within the vessel as compared to the low and high clearance vessels respectively. As represented in Figure 5.3, the medium clearance vessels develop high N_{pt} as compared to the low clearance and high clearance vessels respectively. The pattern of variation of N_q with $\frac{h}{D}$ is highly similar to the pattern of variation of N_{pt} with $\frac{h}{D}$ indicating that the power drawn by the impeller is mainly used for pumping the liquid contained within the reactor vessel. Therefore, the high power consumed by the medium clearance vessels is used for pumping the liquid which in turn increases the mixing performance of the same in comparison with the low and high clearance vessels respectively.

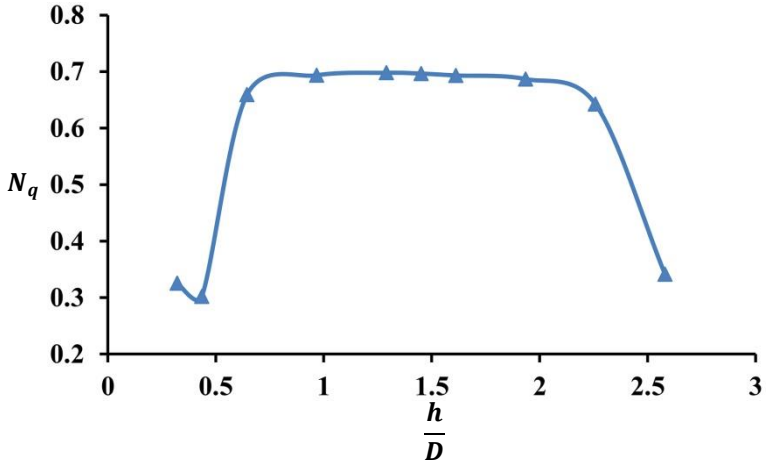

Figure 5.5: Variation of N_q with $\frac{h}{D}$

5.2.3 Oxygen transfer

The variation of gas hold-up with $\frac{h}{D}$ is shown in Figure 5.6. It can be seen that the standard reactor vessel with $\frac{h}{D}$ of 0.97 produces negligible gas hold-up while the high clearance vessels increases the gas hold-up and the vessel with the $\frac{h}{D}$ of 2.79 provides maximum entrainment of air into the reactor vessel. Therefore, the reactor vessels with $\frac{h}{D}$ of 0.97, 2.26 and 2.79 were considered for the further analysis including the description of physical reasons causing the oxygen transfer into the reactor vessel.

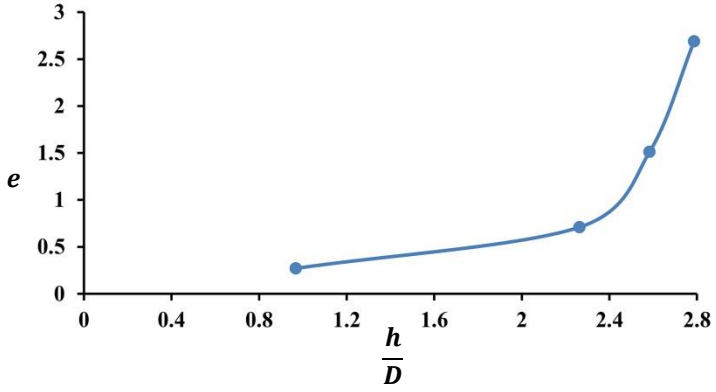

Figure 5.6: Variation of gas hold-up with $\frac{h}{D}$

The contours of volume fraction of air along the mid baffle plane for $\frac{h}{D}$ of 0.97, 2.26 and 2.79 are illustrated in Figures 5.7(a)-5.7(c) respectively. The vessel with $\frac{h}{D}$ of 0.97 provides

undisturbed air-water interface (Fig. 5.7(a)) while $\frac{h}{D}$ of 2.26 causes deformation and deflection of the air-water interface resulting in the formation of a free surface vortex around the impeller shaft (Fig. 5.7(b)). The free surface vortex increases the interfacial area manifold times as that of the undisturbed air-water interface due to high shearing action of the impeller which leads to considerable increase in the entrainment of air into the reactor vessel (Motamedvaziri and Armenante 2012). At $\frac{h}{D}$ of 2.79, the free surface vortex touches the impeller surface leading to the flooding of air bubbles into the reactor vessel. The vessel with $\frac{h}{D}$ of 2.79 provides 53% increase in the gas hold-up as compared to the vessel with $\frac{h}{D}$ of 2.26, indicating significant rise in the oxygen transfer under the impeller flooding conditions. In general, the high clearance vessels are suitable for the surface aeration process and the RT impeller located near the free liquid surface provides maximum entrainment of air with less power consumption.

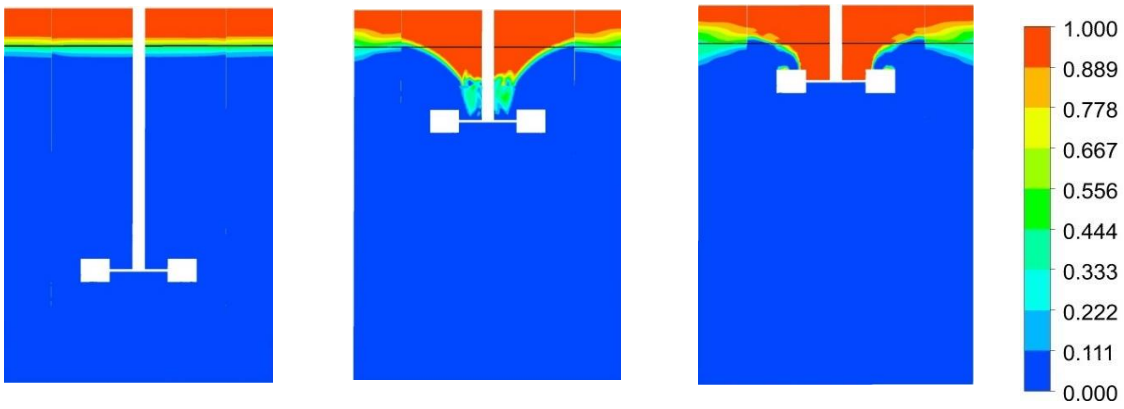

Figure 5.7: Contours of volume fraction of air along the mid-baffle plane associated with the $\frac{h}{D}$ of (a) 0.97, (b) 2.26 and (c) 2.79 (Black line in figures indicate air-water interface before the commencement of simulations)

It is evident from Figure 5.2(c) that the high clearance vessels develop a low pressure region near the free liquid surface which pulls the discharge streams towards the free liquid surface. The strong discharge streams behave like liquid jets which strike on the free liquid surface to develop significant wave action and subsequent deformation of the same (Patil et al. 2004). The contours of G and S along the mid-baffle plane associated with $\frac{h}{D}$ of 0.97, 2.26 and 2.79 are shown in Figures 5.8-5.9 respectively. The $\frac{h}{D}$ of 2.26 and 2.79 develop high magnitudes of G and S above the impeller up to the free liquid surface resulting in the formation of a free

surface vortex around the impeller shaft. Moreover, high magnitude of $\frac{k}{u_{tip}^2}$ can be observed near the free liquid surface of the vessels with $\frac{h}{D}$ of 2.26 and 2.79 (Fig. 5.10(b) and 5.10(c)) which also helps in deformation of the free liquid surface and subsequent entrainment of air into the reactor vessel. The shearing action of the impeller breaks the deformed surface causing entrapment of air bubbles and subsequent dispersion of the same in the bulk liquid contained within the vessel (Durve and Patwardhan 2012). Thus, the low pressure region developed near the free liquid surface and the presence of high turbulent quantities near the free liquid surface causes the entrainment of air into the reactor vessel.

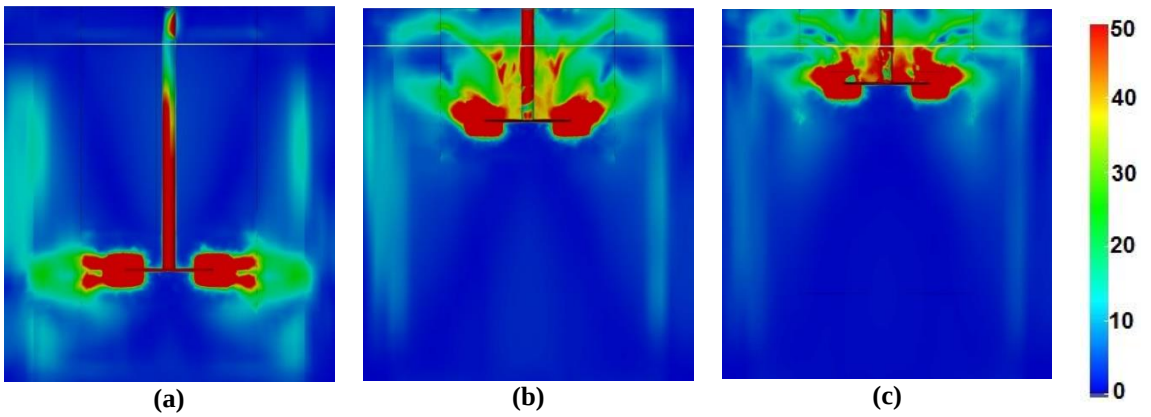

(a) **(b)** **(c)**

Figure 5.8: Contours of G along the mid-baffle plane associated with $\frac{h}{D}$ of (a) 0.97, (b) 2.26 and (c) 2.79 (White line in figures indicate air-water interface before the commencement of simulations)

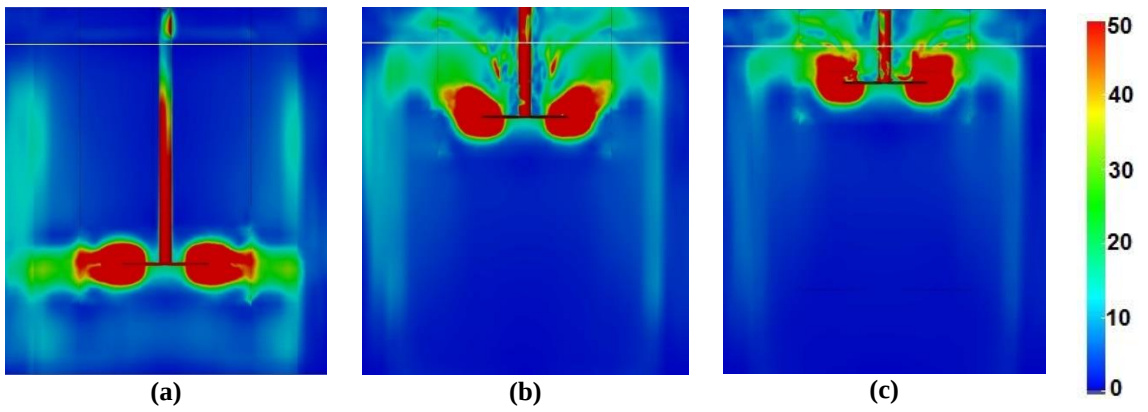

(a) **(b)** **(c)**

Figure 5.9: Contours of S along the mid-baffle plane associated with $\frac{h}{D}$ of (a) 0.97, (b) 2.26 and (c) 2.79 (White line in figures indicate air-water interface before the commencement of simulations)

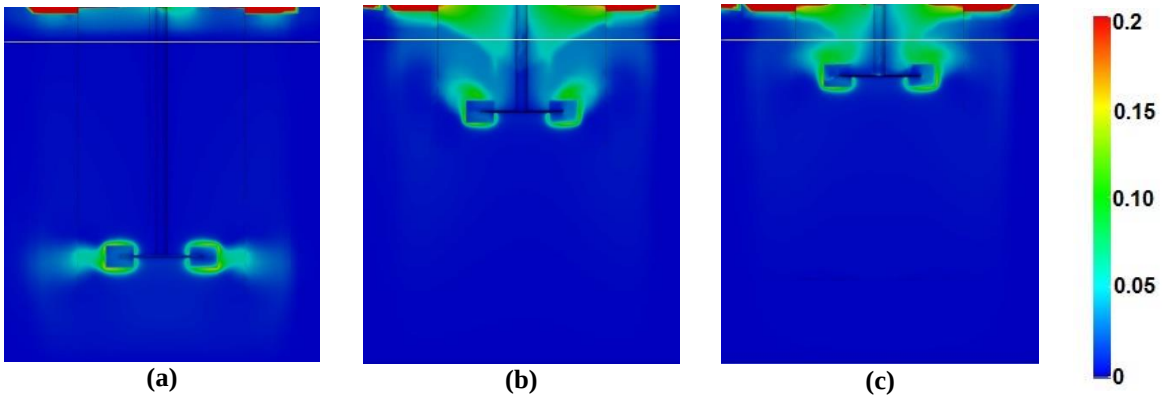

Figure 5.10: Contours of $\frac{k}{u_{tip}^2}$ along the mid-baffle plane associated with $\frac{h}{D}$ of (a) 0.97, (b) 2.26 and (c) 2.79 (White line in figures indicate air-water interface before the commencement of simulations)

5.2.4 Mixing characteristics

The mixing characteristics associated with the reactor vessels having $\frac{h}{D}$ of 0.32, 0.97 and 2.58 are evaluated using the contours of trailing vortices and $\frac{k}{u_{tip}^2}$ along the mid-baffle plane as shown in Figures 5.11 and 5.12 respectively. The $\frac{h}{D}$ of 0.97 (standard configuration) provides symmetric pair of trailing vortices above and below the impeller centre-plane which move radially towards the tank periphery and strike on the tank periphery to develop superior vortex activity in the entire domain of the reactor vessel (Fig. 5.11(b)). Similarly, high magnitude of $\frac{k}{u_{tip}^2}$ can be observed around the impeller as well as in bulk circulation region of the vessel having $\frac{h}{D}$ of 0.97 as shown in Figure 5.12(b). The superior vortex and turbulent activity in the entire domain of the vessel results in bulk mixing of the fluid contained within the reactor vessel. The $\frac{h}{D}$ of 0.32 generates a pair of trailing vortices below the impeller and no vortex activity can be observed above the impeller (Fig. 5.11(a)). However, these trailing vortices are shed out in axial manner which enhances the mixing near the bottom surface of the reactor vessel (Fig. 5.11(a)). Also, significant vortex activity was generated below the impeller which extends towards the bottom surface of the reactor vessel. The contour of $\frac{k}{u_{tip}^2}$ exhibits superior turbulence activity near the bottom region of the vessel at $\frac{h}{D}$ of 0.32 as illustrated in Figure 5.12(a). The high vortex and turbulence activity below the impeller leads to the development of localized mixing effect which helps in lifting the solid particles off the bottom surface of

the vessel and keep them suspended in the bulk liquid. Thus, the low clearance vessels are widely adopted for the solid-liquid suspension processes in the industries. The $\frac{h}{D}$ of 2.58 generates a pair of trailing vortices above the impeller and no vortex action can be observed below the impeller (Fig. 5.11(c)). However, these trailing vortices are shed in axial manner which enhances the mixing above the impeller (Fig. 5.11(c)). Also, considerable vortex activity was produced above the impeller which extends towards the top surface of the reactor vessel. The contour of $\frac{k}{u_{tip}^2}$ also shows significant turbulence activity in the region above the impeller of the reactor vessel at $\frac{h}{D}$ of 2.58 as illustrated in Figure 5.12(c). The high vortex and turbulence activity near the tank top surface results in the development of localized mixing which helps in the entrainment of air into the reactor vessel. Thus, the high clearance vessels are adopted for the surface aeration process in the wastewater treatment industries.

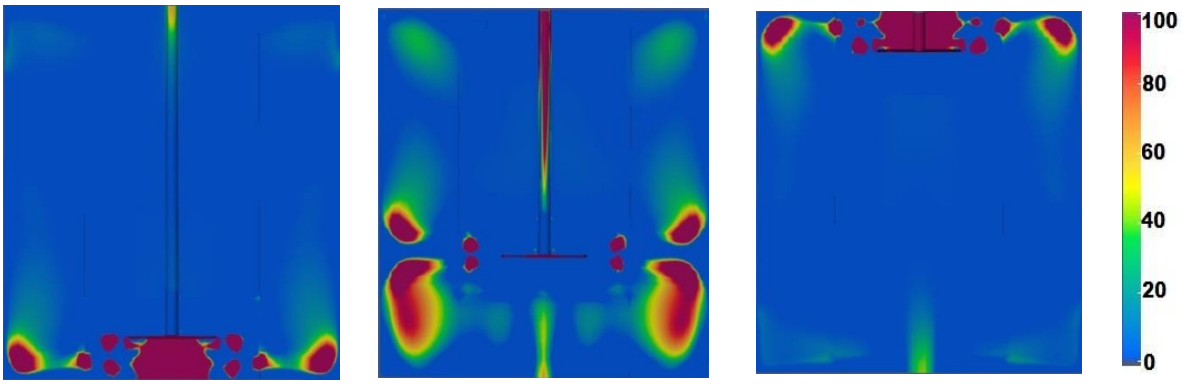

(a) **(b)** **(c)**

Figure 5.11: Contours of trailing vortices along the mid-baffle plane associated with $\frac{h}{D}$ of (a) 0.32, (b) 0.97 and (c) 2.58

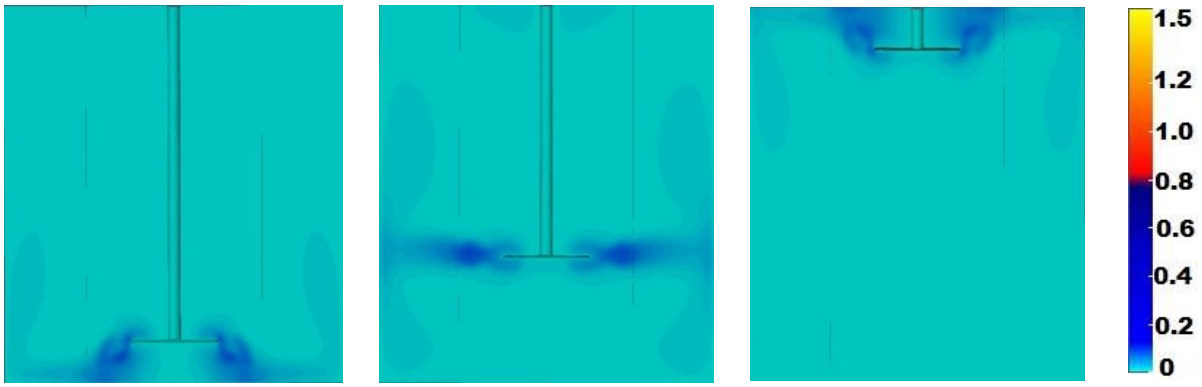

(a) **(b)** **(c)**

Figure 5.12: Contours of $\frac{k}{u_{tip}^2}$ along the mid-baffle plane associated with $\frac{h}{D}$ of (a) 0.32, (b) 0.97 and (c) 2.58

Thus, the medium impeller clearance provides double loop pattern and high vortex and turbulence activity in the entire domain of the vessel resulting in bulk mixing. On the other hand, the low clearance vessels develop single loop down-pumping pattern and high vortex and turbulence activity below the impeller leading to localized mixing near the bottom surface of the reactor vessel. The high clearance vessels generate single loop up-pumping pattern and high vortex and turbulence activity above the impeller resulting in localized mixing near the top surface of the reactor vessel. Hence, the variations in $\frac{h}{D}$ causes changes in the underlying flow patterns, vortex and turbulence characteristics which eventually controls the mixing performance of the same.

The $\frac{h}{D}$ is a key geometric parameter which considerably affects the flow fields and performance characteristics of the reactor vessels. The double loop pattern associated with the medium clearance conditions changes into single loop pattern under low and high clearance conditions respectively. The development of low pressure region above the impeller of high clearance vessels direct the discharge stream upwards resulting in the formation of single loop up-pumping pattern. On the other hand, the development of low pressure region below the impeller of low clearance vessels direct the discharge stream downwards resulting in the formation of single loop down-pumping pattern. The radial discharge stream and trailing vortices associated with the medium clearance vessels are directed upwards and downwards under the high and low clearance conditions respectively. The upward and downward movement of trailing vortices associated with the high and low clearance vessels reduce the length of trailing vortices which in turn reduce the form drag and N_{pt} associated with the respective reactor configurations. The double loop pattern provide bulk mixing of the fluid contained within the reactor vessel while the single loop up-pumping and down-pumping patterns develop localized mixing near the top and bottom surfaces of the reactor vessel respectively. The high clearance vessels provide substantial oxygen transfer into the reactor vessel due to the development of free surface vortex around the impeller shaft. The free surface vortex is produced due to the low pressure region generated above the impeller and significant increase in the turbulent quantities near the free liquid surface. The free surface vortex touches the impeller surface of the reactor vessel at $\frac{h}{D}$ of 2.79 resulting in the flooding of air bubbles and significant increase in the gas hold-up in the reactor vessel.

5.3 Tank diameter

The physical reasons causing variations in the performance goals with $\frac{d}{D}$ are analysed in the following sub-sections from 5.3.1 to 5.3.3. The $\frac{d}{D}$ was varied in the range of 2.5-4.5 so that the variations of the flow fields from the standard reactor configuration can be analysed.

5.3.1 Flow patterns

The flow patterns developed under various $\frac{d}{D}$ were analysed and the following inferences were drawn. The standard reactor vessel with $\frac{d}{D}$ of 2.90 provides double loop pattern while the large reactor vessel with $\frac{d}{D}$ of 4.30 (large $\frac{d}{D}$) produces single loop pattern as shown in Figures 5.13(a) and 5.13(b) respectively. The double loop pattern is characterised by high velocities near the impeller as well as in the bulk circulation region of the reactor vessel. These conditions provide bulk mixing of the fluid contained within the reactor vessel. The vessel with $\frac{d}{D}$ of 4.30 develops discharge stream which move axially downwards, strike on the bottom surface of the reactor vessel to generate two major vortices in the reactor vessel. This type of flow pattern is known as single loop pattern. Since the discharge stream is directed towards the bottom surface of the reactor vessel, the flow pattern thus developed can be precisely called as single loop down-pumping pattern which is similar to that obtained from low $\frac{h}{D}$. However, two secondary circulation loops can also be observed below the impeller as well as near the free liquid surface as shown in Figure 5.13(b). Thus, increase in the diameter of the reactor vessel causes transition from standard double loop to single loop down-pumping pattern and significant variations in the underlying mixing characteristics.

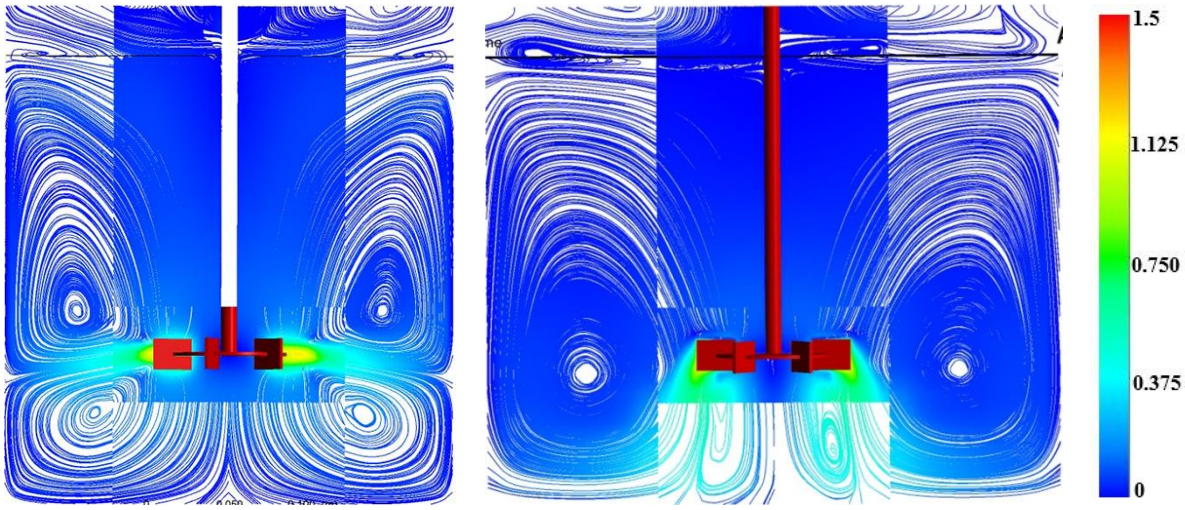

(a) **(b)**

Figure 5.13: Flow patterns along the mid-baffle plane associated with the $\frac{d}{D}$ of (a) 2.90 and (b) 4.30 (Black line in figures indicates air-water interface before the commencement of simulations)

The contours of C_p along the mid-baffle plane for the reactor vessels with $\frac{d}{D}$ of 2.90 and 4.30 as shown in Figures 5.14(a) and 5.14(b) were analysed to explain the physical reasons causing the transition from double loop to single loop down-pumping pattern. The reactor vessel with $\frac{d}{D}$ of 2.90 develops low pressure region behind the impeller blades and uniform distribution of high pressure in the remaining portions of the reactor vessel (Fig. 5.14(a)) resulting in the formation of standard double loop pattern. On the other hand, the vessel with $\frac{d}{D}$ of 4.30 generates distinct low pressure region below the impeller (Fig. 5.14(b)) which drags the discharge stream towards the bottom surface of the reactor vessel leading to the formation of single loop down-pumping pattern. Thus, the development of low pressure region below the impeller with increase in $\frac{d}{D}$ causes the transition from double loop pattern to single loop down-pumping pattern.

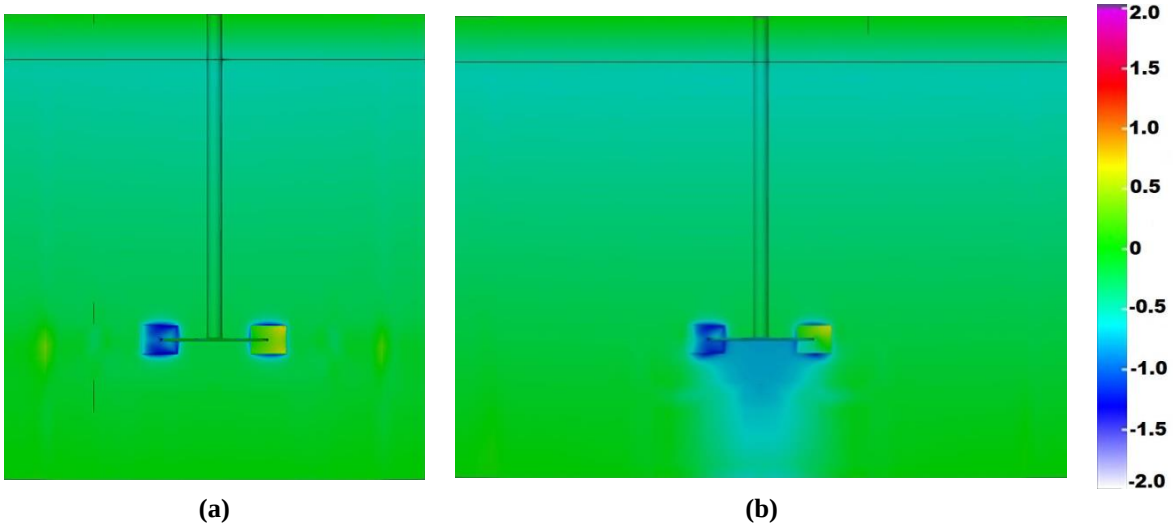

(a) **(b)**

Figure 5.14: Contours of C_p along the mid-baffle plane associated with the $\frac{d}{D}$ of (a) 2.90 and (b) 4.30 (Black line in figures indicates air-water interface before the commencement of simulations)

5.3.2 Power number

The variation of N_{pt} with $\frac{d}{D}$ is shown in Figure 5.15. The N_{pt} was found to decrease with the increase in $\frac{d}{D}$ of the reactor vessel. The vessels with $\frac{d}{D}$ of 2.58 and 2.90 have provided similar values of N_{pt} which decreased by 30% with the increase in $\frac{d}{D}$ to 4.30. The vessels with $\frac{d}{D}$ of 3.76 and 4.30 have provided similar values of N_{pt}. Thus, $\frac{d}{D}$ of the reactor vessel considerably affects the N_{pt} magnitude and based on this pattern of variation, the reactor configurations having $\frac{d}{D}$ of 2.90 and 4.30 were considered for the further analysis.

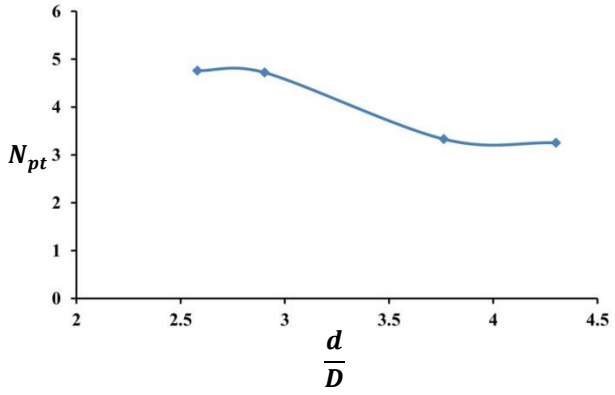

Figure 5.15: Variation of $N_{pt}$with $\frac{d}{D}$

The contours of trailing vortices along the impeller centre-plane for the reactor configurations having $\frac{d}{D}$ of 2.90 and 4.30 as shown in Figures 5.16(a) and 5.16(b) are considered for explaining the physical reasons behind the variations of N_{pt} with $\frac{d}{D}$. The standard reactor vessel with $\frac{d}{D}$ of 2.90 develops large trailing vortices (Fig. 5.16(a)) which significantly increases the intensity of flow separation region behind the impeller blades. The strong flow separation region decrease the pressure on the suction side of the blades resulting in high pressure difference between the suction and pressure sides of the blades (Fig. 5.14(a)). The high pressure difference between the suction and pressure sides of the blades increase the form drag and torque related with the impeller. The high value of impeller torque in turn increases the corresponding N_{pt} magnitude of the impeller. On the other hand, the reactor vessel with $\frac{d}{D}$ of 4.30 provides small trailing vortices (Fig. 5.16(b)) which significantly decrease the intensity of flow separation region behind the impeller blades. The weak flow separation region increase the pressure on the suction side of the blades resulting in small pressure difference between the suction and pressure sides of the blades (Fig. 5.14(b)). The small pressure difference between the suction and pressure sides of the blades decrease the form drag and the torque related with the impeller. The low value of impeller torque in turn decreases the corresponding N_{pt} magnitude of the impeller. Thus, the distribution of trailing vortices behind the impeller blades controls the form drag and N_{pt} associated with the reactor vessels of various scales.

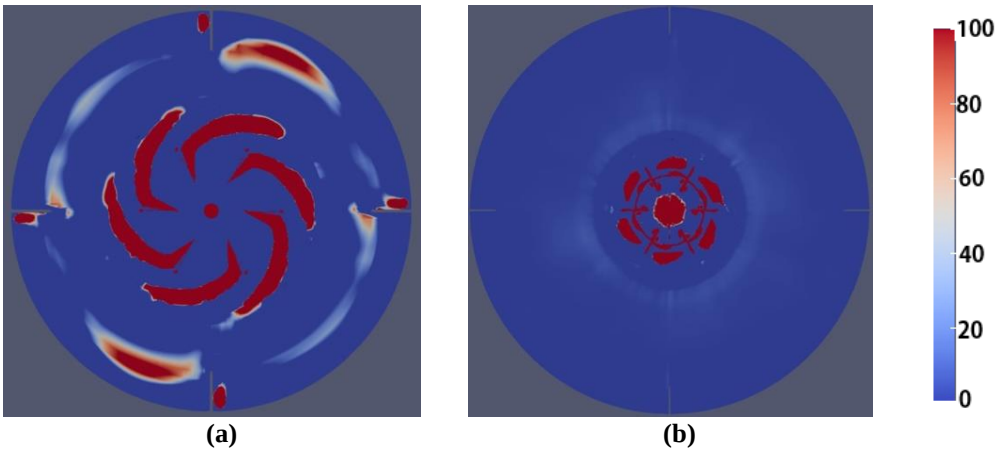

(a) **(b)**

Figure 5.16: Contours of trailing vortices along the impeller centre-plane associated with $\frac{d}{D}$ of (a) 2.90 and (b) 4.30

The variation of N_q with $\frac{d}{D}$ of the reactor vessel is shown in Figure 5.17. The N_q was found to decrease with increase in $\frac{d}{D}$ of the reactor vessel. The reactor vessels with $\frac{d}{D}$ of 2.58 and 2.90 provide similar magnitude of N_q which decreases by 62% with increase in $\frac{d}{D}$ to 4.30. Moreover, the larger vessel with $\frac{d}{D}$ of 3.76 and 4.30 develop similar values of N_q. Thus, the reactor vessel with $\frac{d}{D}$ of 2.90 provides superior pumping of the liquid within the reactor vessel as compared to the larger reactor vessels. The variation of N_q with $\frac{d}{D}$ of the reactor vessel is much similar to the variation of the N_{pt} with $\frac{d}{D}$ as illustrated in Figure 5.15. Therefore, the higher power consumed by the standard reactor vessel configuration is used for pumping the liquid which in turn increases the mixing performance of the same in comparison with the larger reactor vessels.

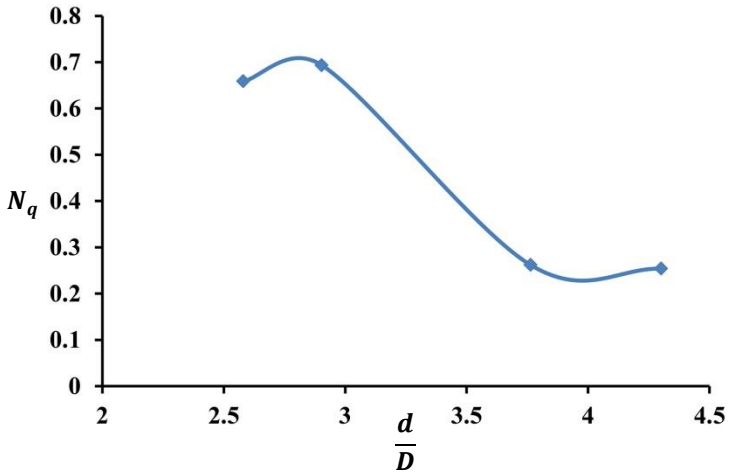

Figure 5.17: Variation of N_q with $\frac{d}{D}$

5.3.3 Oxygen transfer

The variation of gas hold-up with $\frac{d}{D}$ of the reactor vessel is shown in Figure 5.18. The gas hold-up was found to increase with increase in $\frac{d}{D}$ of the reactor vessel and attained peak magnitude for the vessel having $\frac{d}{D}$ of 4.30. However, the gas hold-up increased only by 12% with increase in $\frac{d}{D}$ from 2.90 to 4.30. The vessel with $\frac{d}{D}$ of 2.58 has provided inferior gas hold-up which is 51% smaller than that obtained for the vessel with $\frac{d}{D}$ of 4.30. The contours of

volume fraction of air along the mid-baffle plane associated with the vessels having $\frac{d}{D}$ of 2.90 and 4.30 are shown in Figures 5.19(a) and 5.19(b) respectively. The reactor vessel with $\frac{d}{D}$ of 2.90 develops flat air-water interface as shown in Figure 5.19(a). The reactor vessel with $\frac{d}{D}$ of 4.30 produces slight deformation of the air-water interface as illustrated in Figure 5.19(b) which has resulted in minor improvements in the entrainment of air as compared to the standard reactor vessel. Although, significant increase in the entrainment of air doesn't occurs with the increase in $\frac{d}{D}$ of the vessel, physical reasons causing such improvements in aeration are analysed based on the distributions of mean pressure and turbulent quantities near the free liquid surface. The vessel with $\frac{d}{D}$ of 4.30 develops low pressure magnitude near the free liquid surface which increases the wave action along the free liquid surface and results in the deformation of the same. Moreover, high magnitude of $\frac{k}{u_{tip}^2}$ developed near the free liquid surface of the vessel with $\frac{d}{D}$ of 4.30 (as shown in Fig. 5.20(b)) increase the deformation of the free liquid surface. The deformation of the free liquid surface increases the contact area between the air and water resulting in the entrainment of air into the reactor vessel. Thus, the low pressure region developed near the free liquid surface and the presence of high turbulent kinetic energy near the free liquid surface causes the entrainment of air into the reactor vessel.

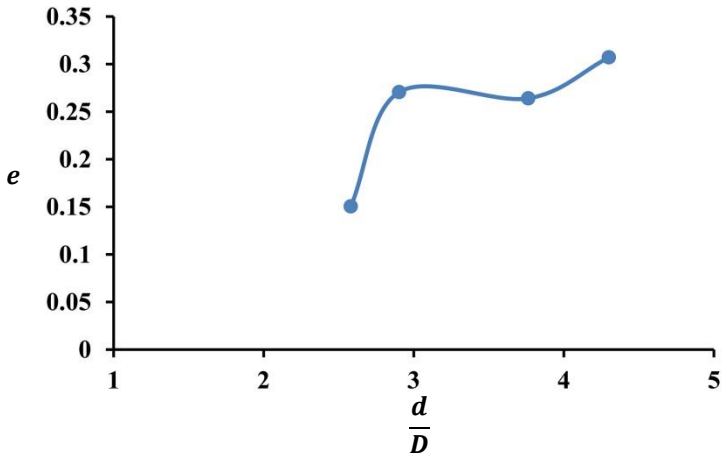

Figure 5.18: Variation of gas hold-up with $\frac{d}{D}$

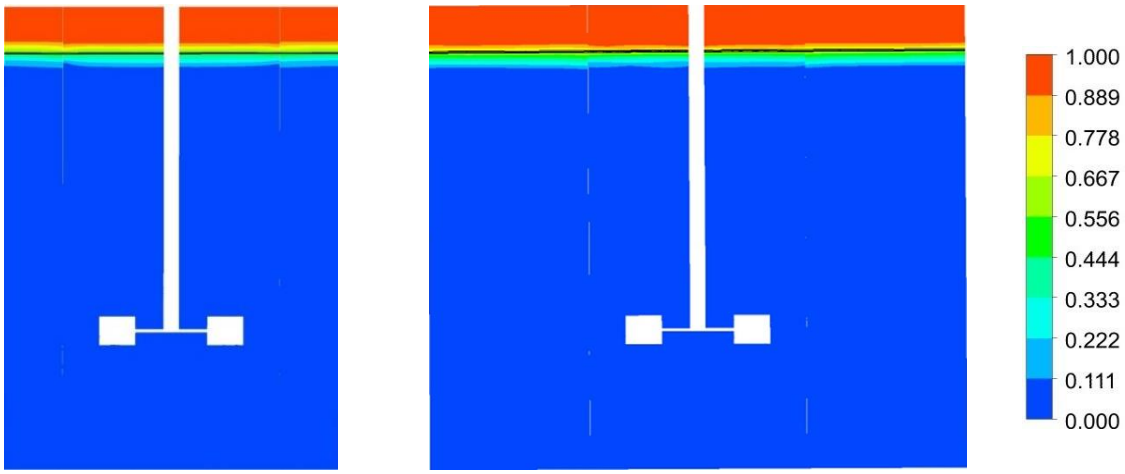

(a) (b)

Figure 5.19: Contours of volume fraction of air along the mid-baffle plane associated with $\frac{d}{D}$ of (a) 2.90 and (b) 4.30 (Black line in figures indicates the air-water interface before the commencement of simulations)

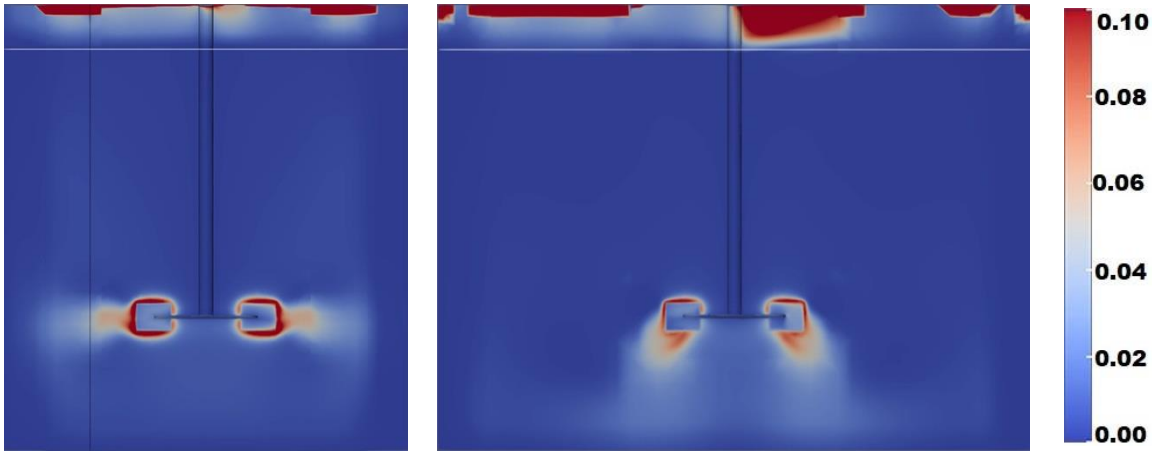

(a) (b)

Figure 5.20: Contours of $\frac{k}{u_{tip}^2}$ along the mid-baffle plane associated with $\frac{d}{D}$ of (a) 2.90 and (b) 4.30 (White line in figures indicates the air-water interface before the commencement of simulations)

5.3.4 Mixing characteristics

The mixing characteristics associated with the vessels having $\frac{d}{D}$ of 2.90 and 4.30 are evaluated using the contours of $\frac{k}{u_{tip}^2}$ and trailing vortices along the mid-baffle plane as illustrated in Figures 5.20 and 5.21 respectively. The reactor vessel with $\frac{d}{D}$ of 2.90 develops symmetric pair of trailing vortices above and below the impeller centre-plane, which move radially outwards and strike on the periphery of the vessel to develop superior vortex activity in the entire

domain of the reactor vessel (Fig. 5.21(a)). Similarly, high magnitude of $\frac{k}{u_{tip}^2}$ can be observed near the impeller as well as in the bulk circulation region of the vessel with $\frac{d}{D}$ of 2.90 indicating significant turbulence action within the reactor vessel (Fig. 5.20(a)). The significant vortex and turbulence activity in the entire domain of the vessel results in bulk mixing of the fluid contained within the reactor vessel. On the other hand, $\frac{d}{D}$ with 4.30 develops only a single pair of trailing vortices from the bottom corners of the blades which move downwards and strike on the tank bottom to provide superior vortex activity near the bottom surface of the reactor vessel (Fig. 5.21(b)). Moreover, high vortex action can be observed below the impeller region. Similarly, contours of $\frac{k}{u_{tip}^2}$ exhibits high magnitude of $\frac{k}{u_{tip}^2}$ below the impeller region as illustrated in Figure 5.20(b). However, no vortex or turbulence activity was observed above the impeller region. The superior vortex and turbulence activity near the bottom surface of the reactor vessel generates localized mixing effect which helps in suspending the solid particles within the fluid contained within the reactor vessel. Thus, the vessel with $\frac{d}{D}$ of 2.90 can be used for bulk mixing applications while that with $\frac{d}{D}$ of 4.30 can be applied for solid-liquid suspension process respectively.

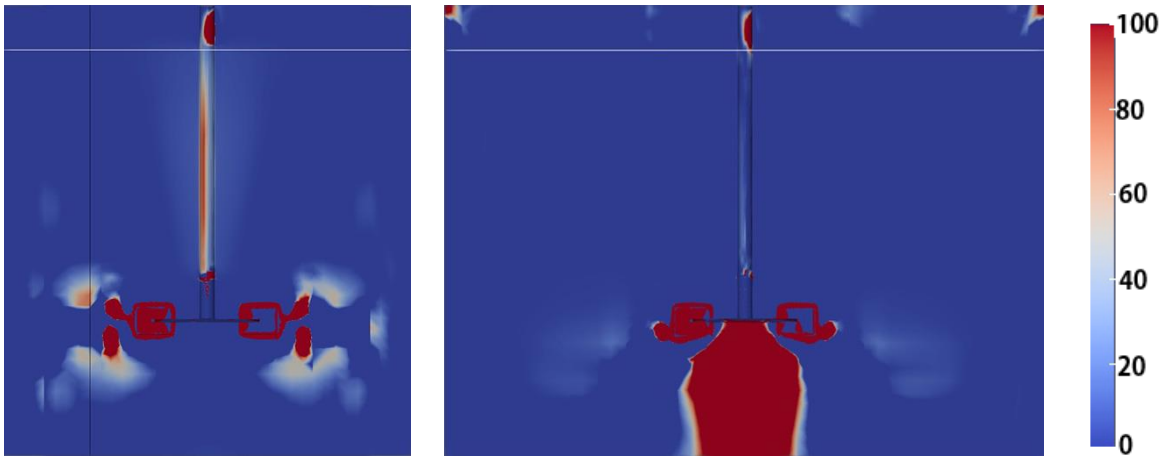

(a) **(b)**

Figure 5.21: Contours of trailing vortices along the mid-baffle plane associated with $\frac{d}{D}$ of (a) 2.90 and (b) 4.30 (White line in figures indicates air-water interface before the commencement of simulations)

Thus, $\frac{d}{D}$ is a key geometric parameter which significantly affects the flow fields and performance characteristics of the reactor vessels. The double loop pattern associated with the standard configuration of the vessel ($\frac{d}{D}$ of 2.90) changes into single loop pattern with the

increase in $\frac{d}{D}$ of the vessel to 4.30. The low pressure region developed below the impeller of the vessel with $\frac{d}{D}$ of 4.30 deflects the radially moving discharge streams downwards resulting in the formation of single loop down-pumping pattern. The downward movement of the discharge streams and trailing vortices associated with the vessel having $\frac{d}{D}$ of 4.30 decreases the length of trailing vortices behind the blades. The decrease in the length of trailing vortices reduces the strength of flow separation region behind the impeller blades which in turn decreases the form drag and N_{pt} associated with the impeller. The double loop pattern associated with the standard reactor vessel generates bulk mixing of the fluid contained within the reactor vessel while the single loop down-pumping pattern provides localized mixing near the bottom surface of the reactor vessel. Although, the gas hold-up associated with the vessel having $\frac{d}{D}$ of 4.30 is less, the development of low pressure region as well as high magnitude of $\frac{k}{u_{tip}^2}$ near the free liquid surface was found to cause the entrainment of air into the reactor vessel.

5.4 Impeller speed

The variation of the performance goals with N are elucidated in the sub-sections given below. The N was varied in a wide spectrum ranging between 100 rpm to 400 rpm. The entire analysis was performed in the turbulent regime. The impeller was located at the standard clearance condition for the whole analysis and both the single phase as well as multiphase simulations were performed to study the hydrodynamic reasons causing the variations of the performance goals with N.

5.4.1 Power number

The variation of N_{pt} with N is shown in Figure 5.22. The N_{pt} was found to increase with the increase in N from 100 rpm to 200 rpm and became constant thereafter. The magnitude of N_{pt} increased by 10% with increase in N from 100 rpm to 200 rpm. Thus, N significantly affects the N_{pt} magnitude and based on the pattern of variation obtained, the reactor vessels agitated at 100 rpm, 200 rpm and 400 rpm were considered for the further flow field analysis.

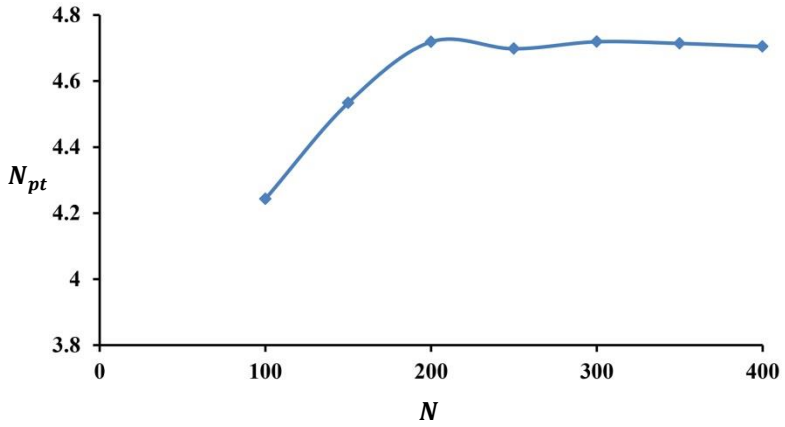

Figure 5.22: Variation of N_{pt} with N

The contours of trailing vortices along the impeller centre-plane for the reactor configurations agitated at 100 rpm, 200 rpm and 400 rpm are shown in Figures 5.23(a)-5.23(c) respectively. The impellers rotated at 200 rpm and 400 rpm develop large trailing vortices (Fig. 5.23(b) and 5.23(c)) which significantly increase the intensity of flow separation region behind the impeller blades. The strong flow separation region decrease the pressure on the suction side of the blades resulting in high pressure difference between the suction and pressure side of the blades (Fig. 5.24(b) and 5.24(c)). The high pressure difference between the suction and pressure side of the blades increase the impeller form drag and torque. The high impeller torque increases the corresponding N_{pt} magnitude of the impeller. On the other hand, the impeller rotated at 100 rpm provides small trailing vortices (Fig. 5.23(a)) which considerably decrease the intensity of flow separation region behind the impeller blades. The weak flow separation region increase the pressure on the suction side of the blades leading to smaller pressure difference between the suction and pressure side of the blades (Fig. 5.24(a)). The small pressure difference between the suction and pressure side of the blades decrease the impeller form drag and torque. The less magnitude of impeller torque decreases the corresponding N_{pt} magnitude of the impeller. Thus, the distribution of trailing vortices behind the impeller blades control the impeller form drag and N_{pt} at different rotational speeds.

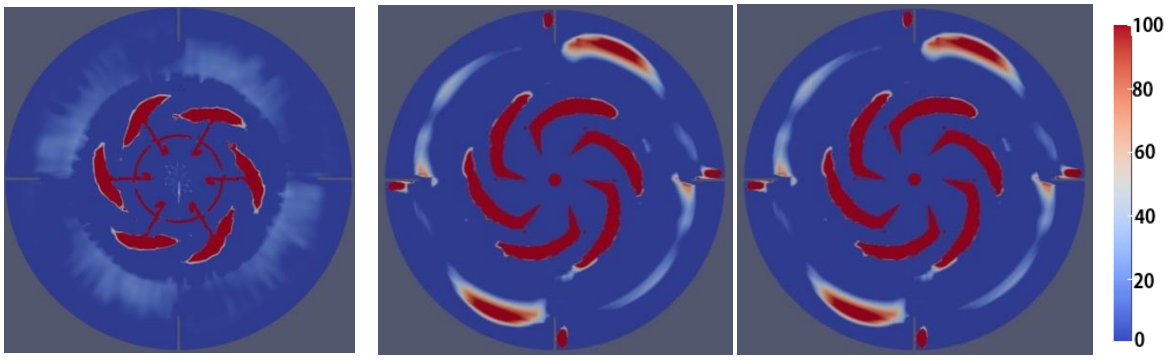

(a) **(b)** **(c)**

Figure 5.23: Contours of trailing vortices along the impeller centre-plane for the reactor vessels agitated at (a) 100 rpm, (b) 200 rpm and (c) 400 rpm

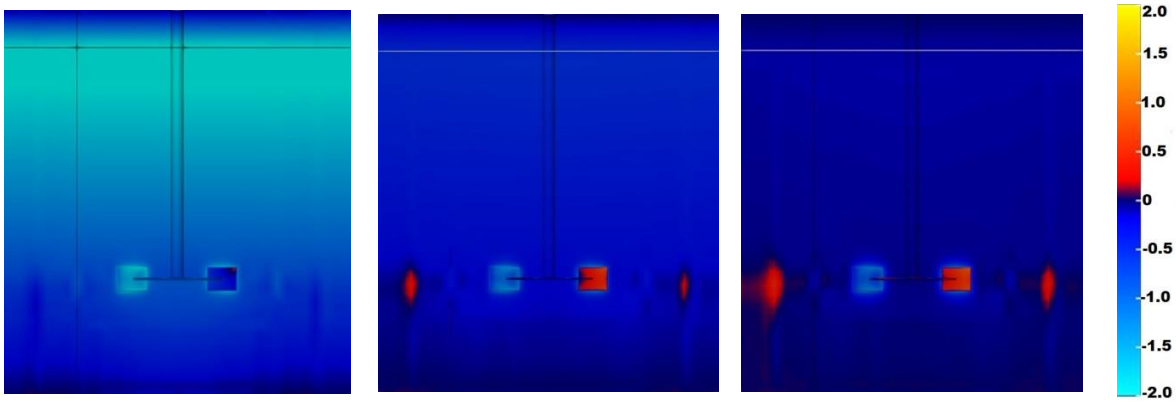

(a) **(b)** **(c)**

Figure 5.24: Contours of C_p along the mid-baffle plane for the reactor vessels agitated at (a) 100 rpm, (b) 200 rpm and (c) 400 rpm (White and black lines in figures indicate the air-water interface before the commencement of simulations)

The variation of N_q with N is shown in Figure 5.25. The N_q increases with the increase in N from 100 rpm to 200 rpm and becomes constant thereafter. Thus, the impeller rotated at higher speed increases the pumping of the liquid within the reactor vessel. According to Figure 5.22, impeller rotated at higher speed also develop higher N_{pt} magnitude as compared to the impeller rotated at smaller speeds. Therefore, the high power consumed by the impeller rotated at higher speed is used for pumping the liquid which in turn increases the mixing performance of the reactor vessel.

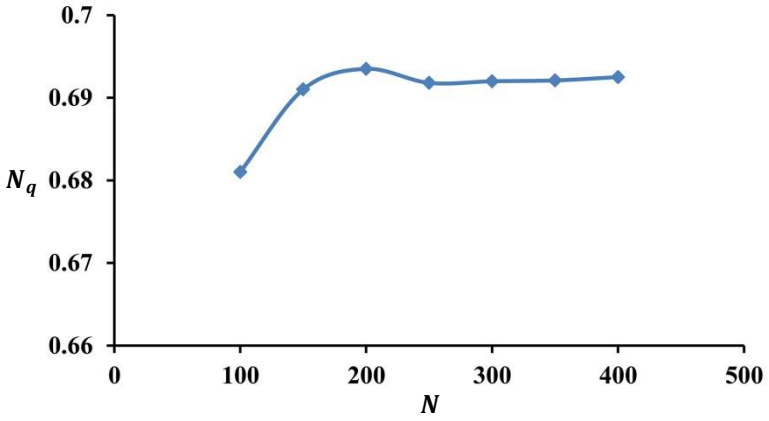

Figure 5.25: Variation of N_q with N

5.4.2 Oxygen transfer

The variation of gas hold-up with N is shown in Figure 5.26. The gas hold-up was found to increase with increase in N of the impeller. Based on the pattern of variation of gas hold-up, the reactor vessels agitated at 100 rpm, 200 rpm and 400 rpm were considered for the further analyses. The contours of volume fraction of air along the mid-baffle plane associated with the reactor vessels agitated at 100 rpm, 200 rpm and 400 rpm are shown in Figures 5.27(a)-5.27(c) respectively. The reactor vessels agitated at 100 rpm and 200 rpm provide undisturbed air-water interface as illustrated in Figures 5.27(a) and 5.27(b) respectively. On the other hand, the reactor vessel agitated at 400 rpm provides deformation of the free liquid surface resulting in increase in the interfacial contact area and subsequent entrainment of air into the reactor vessel (Fig. 5.27(c)).

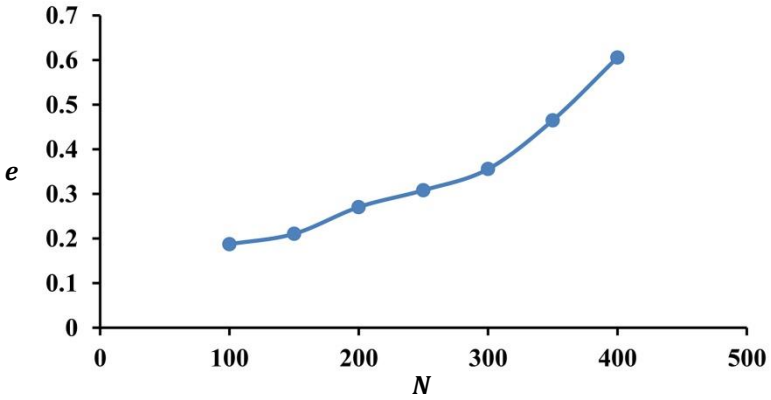

Figure 5.26: Variation of gas hold-up with N

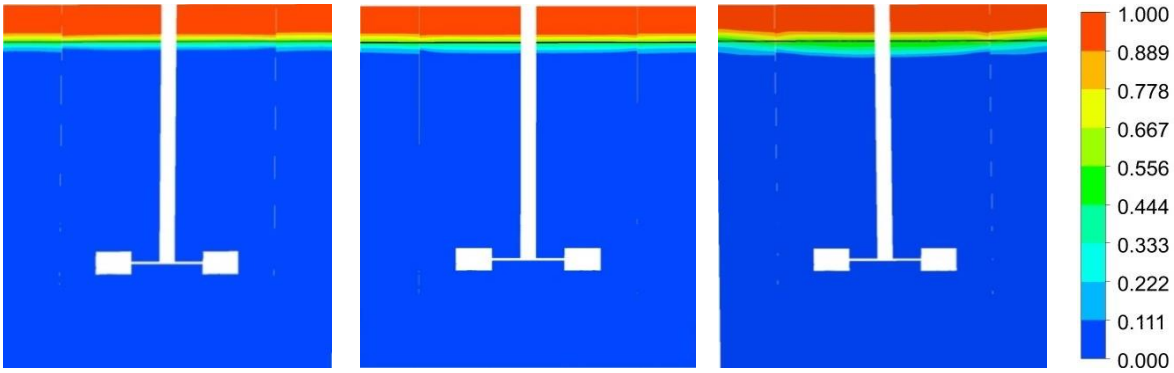

Figure 5.27: Contours of volume fraction of air along the mid-baffle plane for the reactor vessels agitated at (a) 100 rpm, (b) 200 rpm and (c) 400 rpm (Black line in figures indicates air-water interface before the commencement of simulations)

The physical reasons causing the entrainment of air under the high N are evaluated using the contours of mean flow patterns and trailing vortices along the mid-baffle plane as shown in Figures 5.28 and 5.29 respectively. As illustrated in Figures 5.28(a)-5.28(c), the reactor vessels agitated at 100 rpm and 200 rpm provide normal double loop pattern while the reactor vessel agitated at 400 rpm produces another small re-circulation loop below the air-water interface and induces another flow pattern in the form of a free surface vortex around the impeller shaft near the free liquid surface. The contours of trailing vortices associated with the reactor vessel agitated at 400 rpm also indicates the presence of a high vortex region in the form of a free surface vortex extending from the free liquid surface to the impeller as shown in Figure 5.29(c). However, such high vortex region around the impeller shaft is absent for the reactor vessels agitated at 100 rpm and 200 rpm respectively (Fig. 5.29(a) and 5.29(b)). Moreover, high G and S magnitude can be observed around the impeller shaft from the free liquid surface to the impeller for the reactor vessel agitated at 400 rpm as shown in Figures 5.30(c) and 5.31(c) respectively. But such patterns of high G and S regions around the impeller shaft are absent for the reactor vessels agitated at 100 rpm and 200 rpm as illustrated in Figures 5.30(a)-5.30(b) and 5.31(a)-5.31(b) respectively. The high vortex and turbulence region around the impeller shaft obtained for the reactor vessel agitated at 400 rpm causes the deformation of the free liquid surface and subsequent entrainment of air into the reactor vessel. Thus, the high vortex and turbulence activity developed around the impeller shaft from the free liquid surface to the near impeller region causes the air entrainment into the reactor vessel.

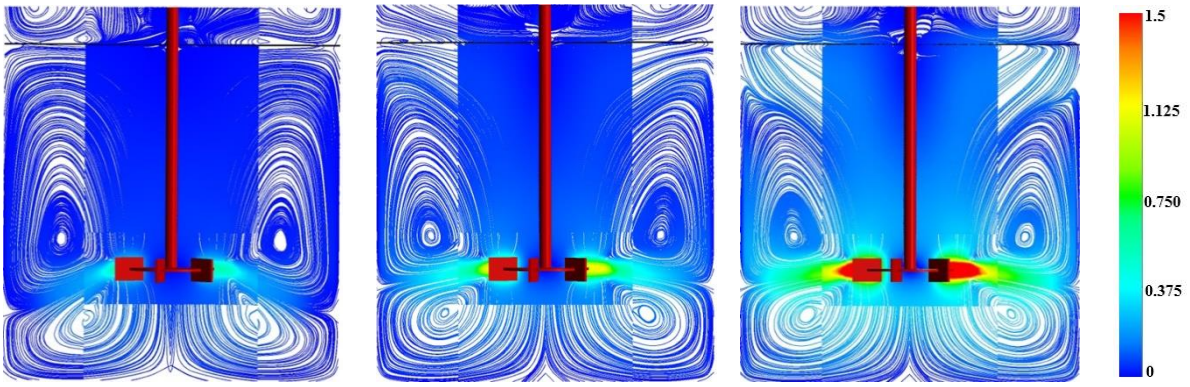

(a) (b) (c)

Figure 5.28: Re-circulation patterns along mid-baffle plane developed for the reactor vessels agitated at (a) 100 rpm, (b) 200 rpm and (c) 400 rpm (Black line in figures indicates air-water interface before the commencement of simulations)

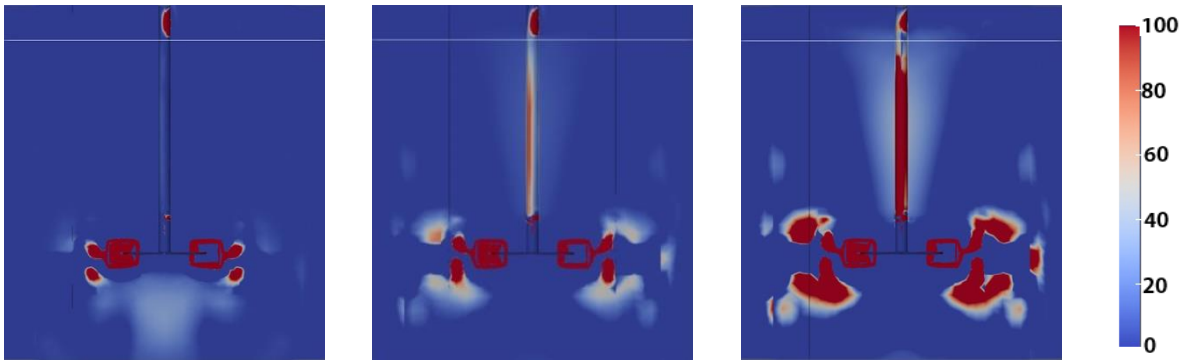

(a) (b) (c)

Figure 5.29: Contours of trailing vortices along the mid-baffle plane developed for the reactor vessels agitated at (a) 100 rpm, (b) 200 rpm and (c) 400 rpm (White line in figures indicates air-water interface before the commencement of simulations)

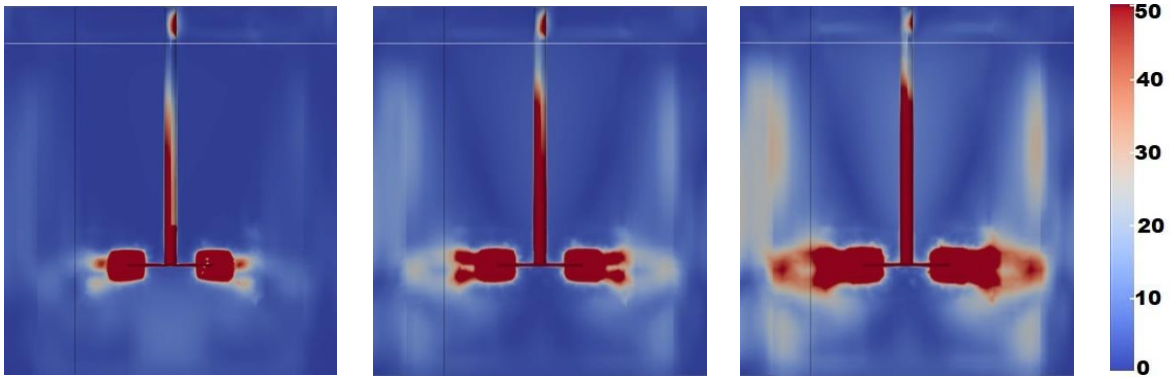

(a) (b) (c)

Figure 5.30: Contours of G along the mid-baffle plane developed for the reactor vessels agitated at (a) 100 rpm, (b) 200 rpm and (c) 400 rpm (White line in figures indicates air-water interface before the commencement of simulations)

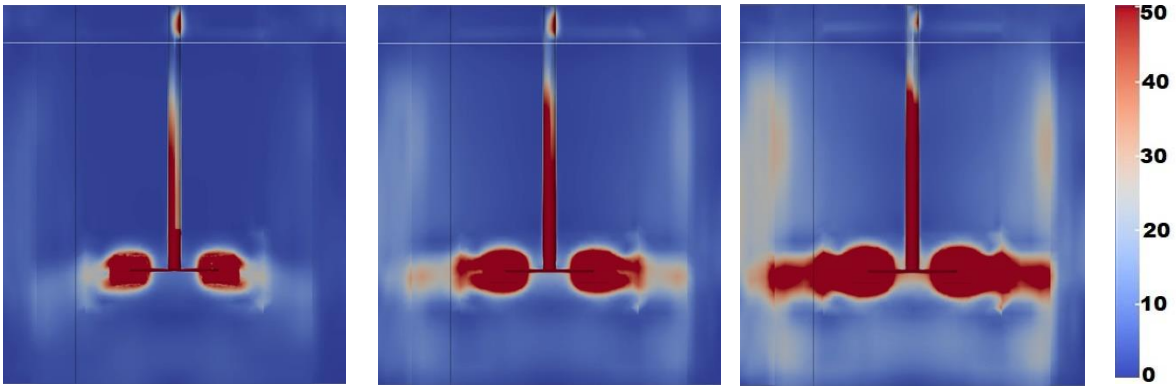

(a) **(b)** **(c)**

Figure 5.31: Contours of S along the mid-baffle plane developed for the reactor vessels agitated at (a) 100 rpm, (b) 200 rpm and (c) 400 rpm (White line in figures indicates air-water interface before the commencement of simulations)

As shown in Figure 5.28, reactor vessels agitated at various N provide double loop pattern and the intensity of discharge stream increases with increase in N of the impeller. The reactor vessel agitated at 400 rpm produces high magnitude of velocity near the impeller blades and significant velocity magnitude in the bulk circulation region of the vessel. Moreover, the intensity and extent of vortex activity around the impeller increases with increase in N of the impeller as illustrated in Figure 5.29. The reactor vessel agitated at 100 rpm generates two small trailing vortices above and below the impeller centre-plane as shown in Figure 5.29(a) while the size of trailing vortices increase with further increase in N as shown in Figures 5.29(b) and 5.29(c) respectively. Also, the magnitude of G and S near the impeller as well as in the bulk circulation region increase with increase in N of the impeller as shown in Figures 5.30 and 5.31 respectively. Thus, the reactor vessel agitated at 400 rpm develops double loop pattern, strong discharge streams, superior vortex and turbulence activity in the entire domain of the vessel resulting in the bulk mixing of the fluid contained within the reactor vessel. The bulk mixing conditions thus developed will help in uniformly distributing the entrained air within the reactor vessel. Hence, the reactor vessel agitated at high N by keeping the impeller at the standard clearance condition is an effective configuration for the surface aeration process.

Thus, N is an important dynamic parameter which significantly affects the flow field and performance goals of the reactor vessels. The impeller agitated at higher speed (200 rpm and 400 rpm) provide large trailing vortices which increase the strength of flow separation region behind the impeller blades. These strong flow separation regions increase the impeller form

drag and N_{pt} magnitude as compared to the impeller agitated at smaller speed (100 rpm). The gas hold-up was found to increase with the increase in N of the impeller. At higher N of 400 rpm, a region of high vortex and turbulence activity is developed from the free liquid surface towards the impeller around the impeller shaft resulting in the deformation of the free liquid surface and subsequent increase in entrainment of air into the reactor vessel. The increase in N increases the intensity of discharge stream, circulation pattern, vortex and turbulence activity in the entire domain of the vessel leading to bulk mixing of the fluid contained within the reactor vessel.

5.5 Number of blades

The steady state single phase simulations were performed by varying the N_{bl} of the RT impeller so as to determine the optimal N_{bl} for achieving superior mixing performance of the reactor vessel. The stirred reactor with four N_{bf} agitated using a RT impeller maintained at the standard clearance level and rotated at the speed of 200 rpm was used for all the simulations. The N_{bl} was varied from zero to thirty and the corresponding effect on the performance goals and flow fields were analysed.

5.5.1 Power number

The variation of N_{pt} with N_{bl} is shown in Figure 5.32. The N_{pt} increases with increase in N_{bl} from zero to eighteen, becomes constant upto the RT impeller having twenty blades and decreases thereafter. The impellers with eighteen and twenty blades attain maximum magnitude of N_{pt} which are 46.5% more than that of the standard reactor vessel (impeller with six blades) and 10.87% more than that with thirty blades respectively. Based on this pattern of variation, the RT impeller with six blades, eighteen blades and thirty blades were considered for the further analyses.

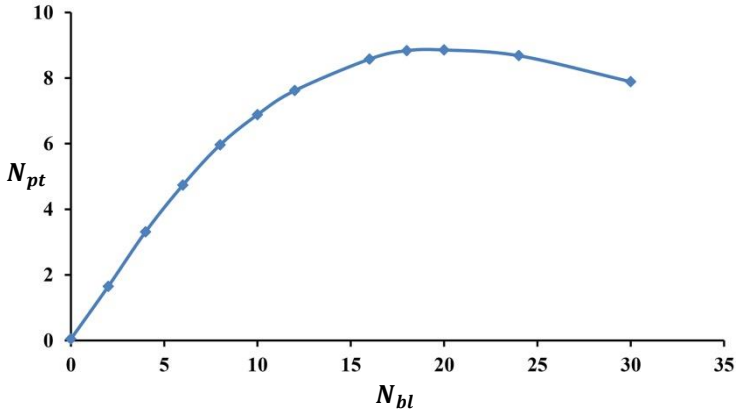

Figure 5.32: Variation of $N_{pt}$with N_{bl}

In order to elucidate the physical reasons causing variation of N_{pt} with N_{bl}, contours of C_p along the mid-baffle plane and contours of trailing vortices along the impeller centre-plane as shown in Figures 5.33 and 5.34 are considered. The RT impeller with six blades develop large trailing vortices (Fig. 5.34 (a)) which considerably increase the intensity of flow separation region behind the impeller blades. The strong flow separation region decreases the pressure on the suction side of the blades resulting in high pressure difference between the suction and pressure side of the blades (Fig. 5.33(a)). The high pressure difference between the suction and pressure side of blades increase the impeller form drag and torque. The higher impeller torque in turn increases the corresponding N_{pt} magnitude of the impeller with six blades. The RT impeller with eighteen blades develops small trailing vortices (Fig. 5.34(b)) which decrease the intensity of flow separation region behind the impeller blades. The weak flow separation region increases the pressure on the suction side of the blades resulting in low pressure difference between the suction and pressure side of the blades (Fig. 5.33(b)). Although, the contribution of form drag from each blade of the RT impeller with eighteen blades is smaller than that of the RT impeller with six blades, the cumulative form drag, torque and N_{pt} of impeller with eighteen blades is higher as compared to the impeller with six blades. The RT impeller with thirty blades develops a different kind of vortex pattern as compared to the RT impellers with six and eighteen blades respectively (Fig. 5.34(c)). The vortices are no longer trailing behind the blades and they are shed away from the tip of the impeller blades towards the periphery of the reactor vessel (Fig. 5.34(c)). In other words, the RT impeller with thirty blades behaves like a solid disc as the spacing between the impeller blades is small for the development of the trailing vortex structure. The insignificant trailing vortices behind the blades of the RT impeller with thirty blades develop weak flow separation region which increases the pressure on the suction side of the blades. The small pressure

difference between the suction and pressure side of the blades (Fig. 5.33(c)) decreases the impeller form drag and torque as compared to the impeller with eighteen blades. The smaller magnitude of the impeller torque in turn decreases the corresponding N_{pt} magnitude of the impeller. Thus, the distribution of trailing vortices behind the impeller blades control the impeller form drag and N_{pt}.

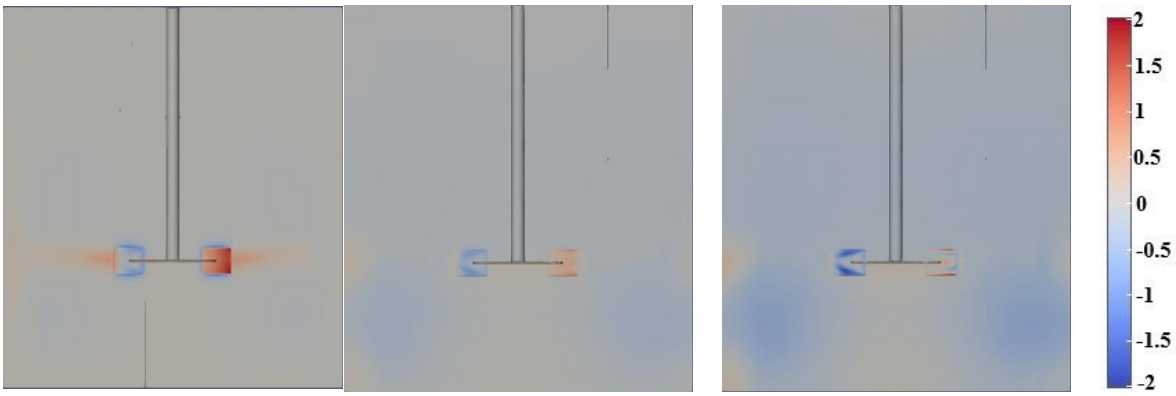

(a) **(b)** **(c)**

Figure 5.33: Contours of C_p along the mid-baffle plane for the RT impeller with (a) six blades, (b) eighteen blades and (c) thirty blades

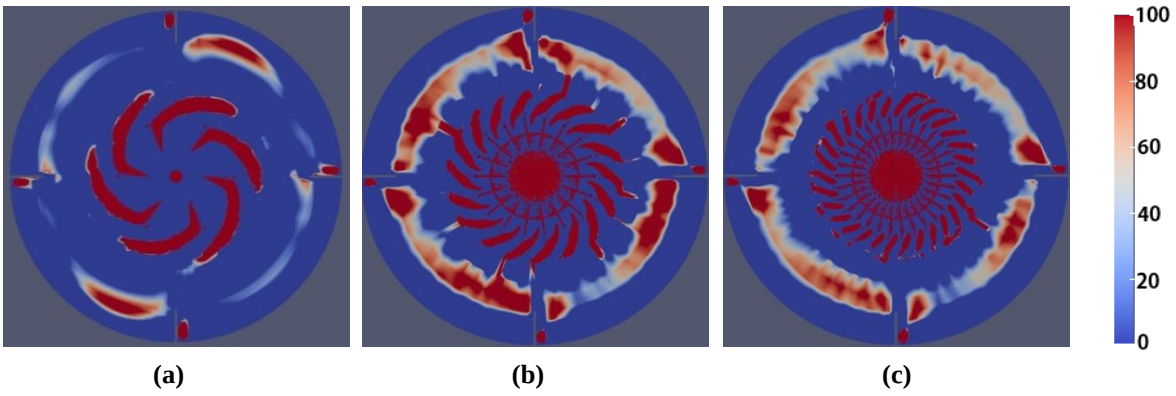

(a) **(b)** **(c)**

Figure 5.34: Contours of trailing vortices along the impeller centre-plane for the RT impeller with (a) six blades, (b) eighteen blades and (c) thirty blades

The variation of N_q with N_{bl} is shown in Figure 5.35. The N_q increases with increase in N_{bl} from zero to eighteen, becomes constant upto twenty blades and decreases thereafter. The maximum N_q is 25% more than that of RT impeller with six blades and 10.81% more than that with thirty blades respectively. Thus, RT impellers with eighteen and twenty blades generate superior pumping of liquid as compared to the reamining impeller configurations considered for the analysis. Also, according to Figure 5.32, RT impellers with eighteen and twenty blades provide maximum N_{pt} in comparison with other impeller configurations

considered for the analysis. Therefore, the high power consumed by the RT impellers with eighteen and twenty blades is used for pumping the liquid within the reactor vessel.

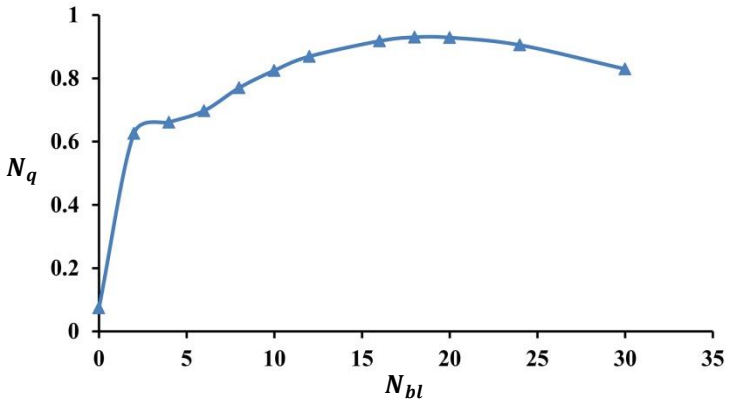

Figure 5.35: Variation of N_q with N_{bl}

5.5.2 Mixing characteristics

The mixing characteristics associated with the impellers having six blades, eighteen blades and thirty blades were analysed using the contours of trailing vortices and turbulent quantities in the present sub-section. The contours of $\frac{k}{u_{tip}^2}$ and $\frac{TI}{u_{tip}}$ along the impeller centre-plane for the impellers are shown in Figures 5.36 and 5.37 respectively. As shown in Figure 5.34(a), the RT impeller with six blades develops superior vortex action around the impeller while the RT impellers with eighteen and thirty blades develop inferior vortex action (Fig. 5.34(b) and 5.34 (c)). Moreover, RT impeller with six blades develop high $\frac{k}{u_{tip}^2}$ and $\frac{TI}{u_{tip}}$ around the impeller (Fig. 5.36(a) and 5.37(a)) which significantly decrease for the RT impellers having eighteen and thirty blades (Fig. 5.36(b)-5.36(c) and Fig. 5.37(b)-5.37(c)) respectively. The peak $\frac{k}{u_{tip}^2}$ and $\frac{TI}{u_{tip}}$ for six blade RT impeller is higher than that for other impellers. Further, six blade RT impeller develop adequate turbulence activity in the bulk circulation region which decreases for other impellers. It is to be noted that the RT impeller with thirty blades generates small magnitude of $\frac{k}{u_{tip}^2}$ and $\frac{TI}{u_{tip}}$ (Fig. 5.36(c) and 5.37(c)) in the reactor vessel as it behaves like a solid disc and results in generating inferior mixing in the reactor vessel. Therefore, RT impeller with six blades develops strong vortex and turbulence activity in the entire domain of the vessel which results in superior bulk mixing of the fluid as compared to RT impellers with

eighteen and thirty blades respectively. Hence, the RT impeller with six blades can be considered as optimal for the mixing processes. Although, the RT impeller with eighteen blades provides higher N_q in the vessel as compared to the RT impeller with six blades, the corresponding mixing performance is inferior than that of the RT impeller with six blades. Thus, there is a negative correlation between N_q and mixing performance of the reactor vessel agitated by the RT impellers with various N_{bl}.

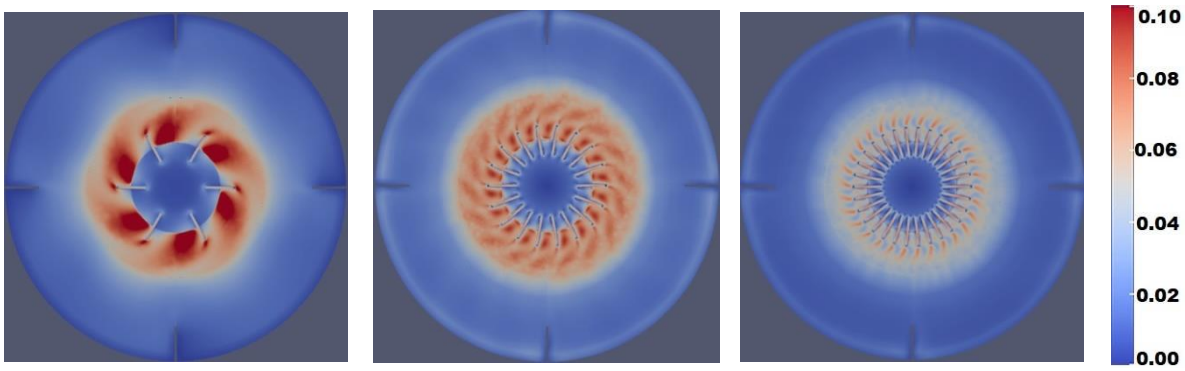

(a) **(b)** **(c)**

Figure 5.36: Contours of $\frac{k}{u_{tip}^2}$ along the impeller centre-plane for the RT impeller with (a) six blades, (b) eighteen blades and (c) thirty blades

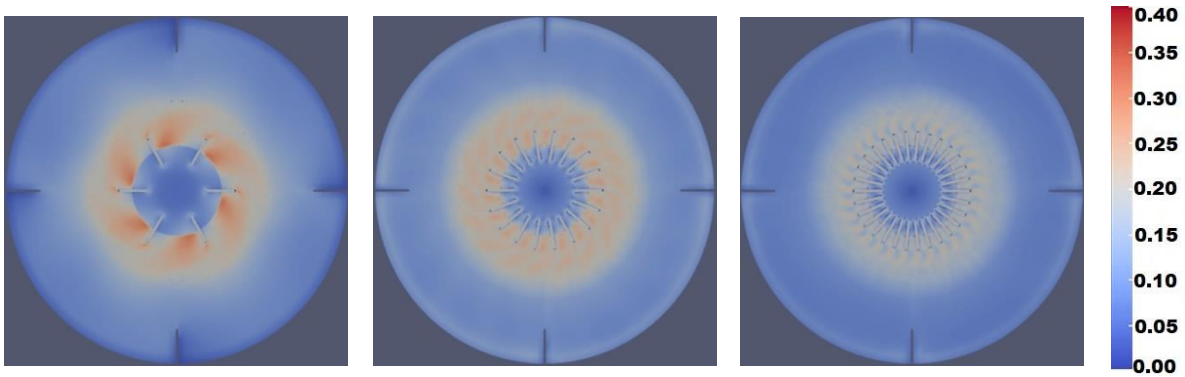

(a) **(b)** **(c)**

Figure 5.37: Contours of $\frac{TI}{u_{tip}}$ along the impeller centre-plane for the RT impeller with (a) six blades, (b) eighteen blades and (c) thirty blades

Thus, N_{bl} is a key geometric parameter which significantly affects the flow field and performance goals of the reactor vessels. The RT impeller with six blades develop large trailing vortices and strong flow separation region behind the blades. The strong flow separation region increase the impeller form drag and N_{pt}. Although, RT impeller with eighteen blades develop small trailing vortices and weak flow separation region behind the blades, the cumulative impeller form drag of eighteen blades increase the torque and N_{pt}

magnitude as compared to impeller with six blades. The insignificant trailing vortices developed by RT impeller having thirty blades generate weak flow separation region behind the blades. The weak flow separation region decrease the impeller form drag and N_{pt}. The RT impeller with six blades develop superior vortex and turbulence activity in the entire domain of the reactor vessel resulting in strong bulk mixing as compared to other RT impellers. Hence, the RT impeller with six blades was found to be optimal for the mixing process in the reactor vessels.

5.6 Number of baffle walls

The steady state single phase simulations of a reactor vessel under various N_{bf} were performed to determine the optimal N_{bf} for achieving superior mixing conditions in the reactor vessel. The RT impeller with six blades was maintained at standard clearance level and rotated at the speed of 200 rpm for all the simulations. The N_{bf} was varied from zero to ten and the corresponding effects on the flow fields and performance goals were analysed.

5.6.1 Power number

The variation of N_{pt} with N_{bf} is shown in Figure 5.38. The N_{pt} increases with increase in N_{bf} from zero to four and becomes constant thereafter. The vessels having N_{bf} greater than or equal to four develop similar N_{pt} which is 41.1% more than that of unbaffled reactor vessel. Based on this pattern of variation, unbaffled reactor, baffled reactor with four and ten baffles was considered for further analyses. In order to explain the physical reasons behind the variation of N_{pt} with N_{bf}, contours of C_p along the mid-baffle plane and contours of trailing vortices along the impeller centre-plane were considered as shown in Figures 5.39 and 5.40 respectively.

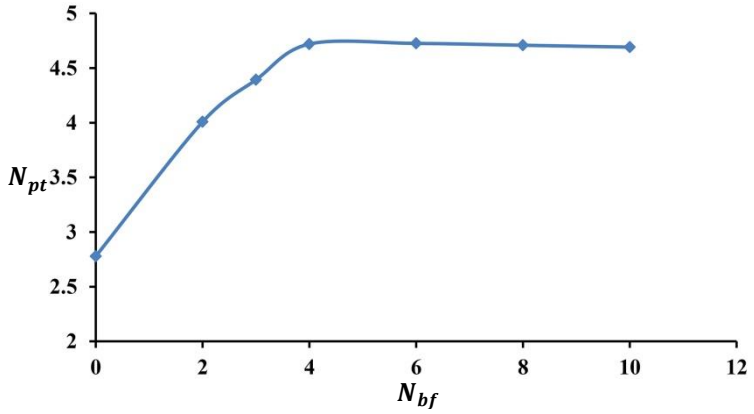

Figure 5.38: Variation of N_{pt} with N_{bf}

The reactor vessels with four and ten baffles develop large trailing vortices (Fig. 5.40(b) and 5.40(c)) which significantly increase the strength of flow separation region behind the impeller blades. The stronger flow separation region decrease the pressure on the suction side of the blades resulting in high pressure difference between the suction and pressure side of the blades (Fig. 5.39(b) and 5.39(c)). The high pressure difference leads to high impeller form drag and torque for the vessels with four and ten baffles respectively. The high impeller torque in turn increases the N_{pt} magnitude of the reactor vessels with four and ten baffles respectively. The unbaffled vessel develops small trailing vortices (Fig. 5.40(a)) which considerably decrease the intensity of flow separation region behind the impeller blades. The weak flow separation region increase the pressure on the suction side of the blades resulting in small pressure difference between the suction and pressure side of the blades (Fig. 5.39(a)). The small pressure difference leads to small impeller form drag and torque for the unbaffled reactor vessel. The small impeller torque in turn decreases the N_{pt} magnitude of the unbaffled reactor vessel.

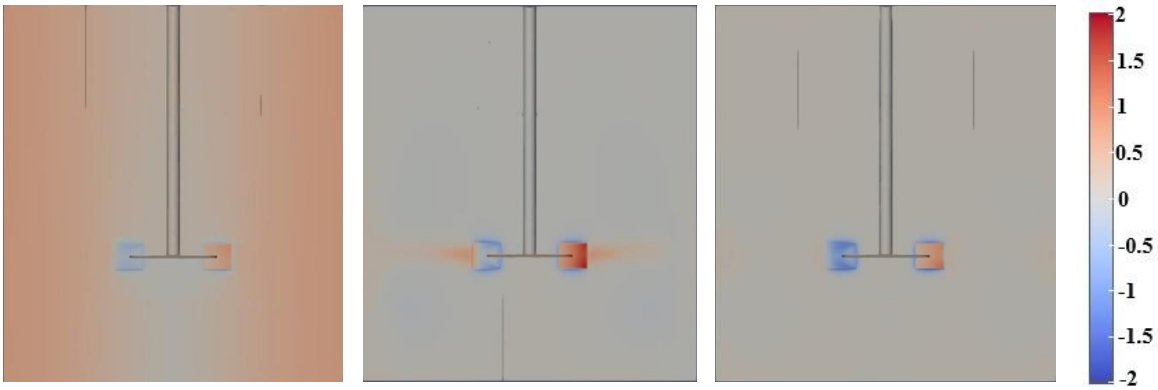

(a) (b) (c)

Figure 5.39: Contours of C_p along the mid-baffle plane for (a) unbaffled reactor vessel, (b) standard reactor vessel and (c) reactor vessel with ten baffle walls

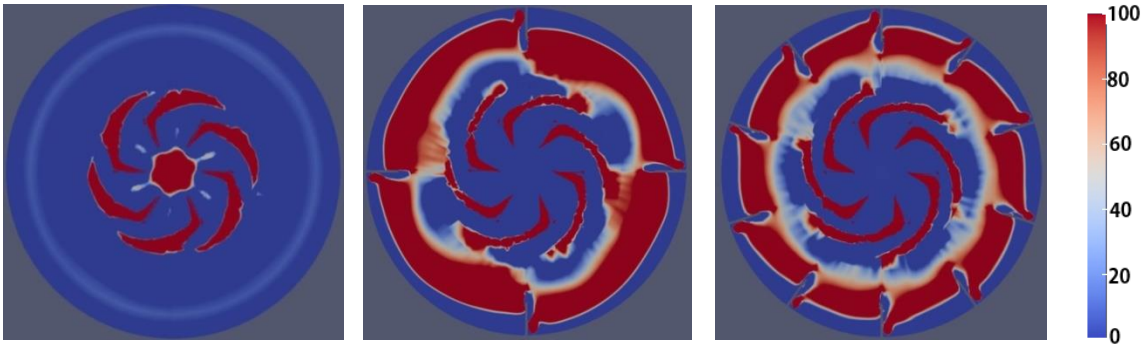

(a) (b) (c)

Figure 5.40: Contours of trailing vortices along the impeller centre-plane for (a) unbaffled reactor vessel, (b) standard reactor vessel and (c) reactor vessel with ten baffle walls

The variation of N_q with N_{bf} is shown in Figure 5.41. The N_q increases with increase in N_{bf} from zero to four, attains a peak magnitude for the reactor vessel with four baffles and decreases thereafter. The N_q associated with the reactor vessel having four baffles is 23.85% more than that for unbaffled reactor vessel and 8.03% more than that for reactor vessel with ten baffles respectively. Therefore, the standard reactor with four baffles develop superior pumping of the liquid within the reactor vessel. As shown in Figure 5.38, the reactor vessels with four and ten baffles develop high and similar magnitude of N_{pt} as compared to unbaffled reactor vessel. Therefore, the high power consumed by the standard reactor vessel with four baffles is used for pumping the liquid which in turn increases the mixing performance of the same as compared to the other reactor configurations considered for analysis. Moreover, the reactor vessel with ten baffles develop less pumping action as compared to the reactor vessel with four baffles although the former reactor configuration provides equal N_{pt} as that of the latter.

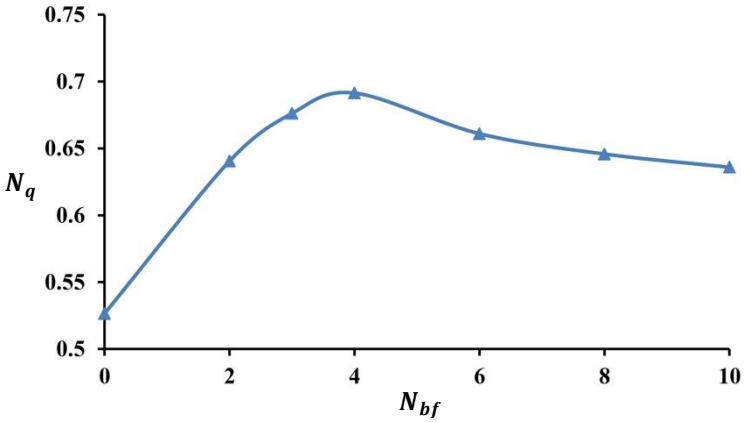

Figure 5.41: Variation of N_q with N_{bf}

5.6.2 Mixing characteristics

The mixing characteristics associated with the reactor vessels having various N_{bf} were analysed using the corresponding distributions of trailing vortices and turbulent quantities in the present sub-section. The contours of $\frac{k}{u_{tip}^2}$ and $\frac{TI}{u_{tip}}$ along the impeller centre-plane for the unbaffled reactor vessel, reactor vessel with four baffles and reactor vessel with ten baffles are illustrated in Figures 5.42 and 5.43 respectively. As shown in Figures 5.40(b) and 5.40(c), the reactor vessels with four and ten baffles provide significant vortex activity surrounding the impeller as well as in the bulk circulation region while the unbaffled reactor vessel develops small trailing vortices around the impeller and no vortex activity can be observed in the bulk circulation region of the reactor vessel (Fig. 5.40(a)). The reactor vessel with four baffles develop high magnitude of $\frac{k}{u_{tip}^2}$ and $\frac{TI}{u_{tip}}$ around the impeller as well as in the bulk circulation region (Fig. 5.42(b) and 5.43(b)) which decreases with further increase in N_{bf} to ten (Fig. 5.42(c) and 5.43(c)). The peak $\frac{k}{u_{tip}^2}$ and $\frac{TI}{u_{tip}}$ of the reactor vessels with four and ten baffles are higher than that from the unbaffled reactor vessel. The small magnitude of $\frac{k}{u_{tip}^2}$ and $\frac{TI}{u_{tip}}$ around the impeller as well as in the bulk circulation region of unbaffled vessel (Fig. 5.42(a) and 5.43(a)) results in poor mixing conditions. Therefore, the reactor vessel with four baffles develop superior vortex and turbulence activity in the entire domain of the reactor vessel resulting in strong bulk mixing as compared to the reactor vessel with ten baffles and the unbaffled reactor vessel respectively. Hence, the reactor vessel with four baffle walls can be considered as optimal configuration for the mixing processes. Also, the reactor vessel with

four baffles provide high magnitude of N_q as compared to the reactor vessels with ten baffles and unbaffled reactor vessel respectively. Thus, there exists a positive correlation between N_q and mixing performance of the reactor vessels with various N_{bf}.

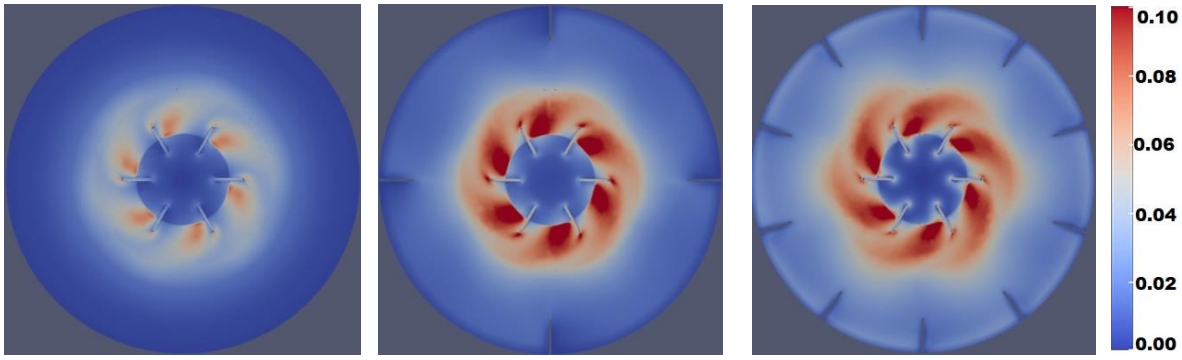

(a) **(b)** **(c)**

Figure 5.42: Contours of $\frac{k}{u_{tip}^2}$ along the impeller centre-plane for (a) unbaffled reactor vessel, (b) standard reactor vessel and (c) reactor vessel with ten baffle walls

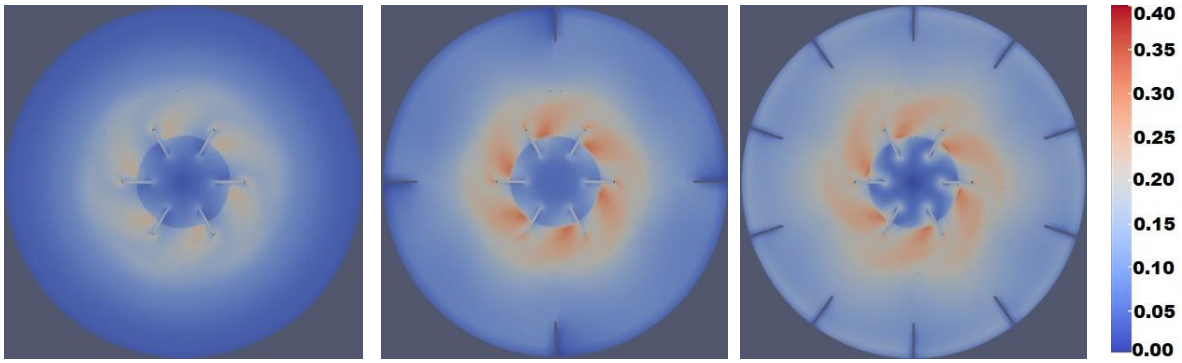

(a) N_{bf}=0 **(b) N_{bf}=4** **(c) N_{bf}=10**

Figure 5.43: Contours of $\frac{TI}{u_{tip}}$ along the impeller centre-plane for (a) unbaffled reactor vessel, (b) standard reactor vessel and (c) reactor vessel with ten baffle walls

Thus, N_{bf} is a key geometric parameter which significantly affects the flow field and performance goals of the reactor vessels. The reactor vessels with four and ten baffles develop large trailing vortices and strong flow separation region behind the impeller blades. The strong flow separation region increase the impeller form drag and N_{pt} of the corresponding reactor vessels. On the other hand, the unbaffled reactor vessel develop small trailing vortices and weak flow separation regions behind the impeller blades. The weak flow separation region lead to smaller impeller form drag and N_{pt} of the unbaffled reactor vessel. The superior vortex and turbulence activity developed in the reactor vessel with four baffles results in strong bulk mixing conditions as compared to the reactor vessel with ten baffles and

unbaffled reactor vessel respectively. Hence, the reactor vessel with four baffle walls can be considered as optimal configuration for the mixing processes.

5.7 Summary

The effect of tank parameters such as $\frac{h}{D}$, $\frac{d}{D}$, N, N_{bl} and N_{bf} on the flow field and performance characteristics associated with the reactor vessels were analysed using the CFD modelling approach. The medium $\frac{h}{D}$ provides radial flow field surrounding the impeller and double re-circulation pattern within the reactor vessel while large $\frac{d}{D}$ and low $\frac{h}{D}$ develop down-pumping discharge stream and single re-circulation pattern within the reactor vessel. On the other hand, the high $\frac{h}{D}$ develops upward moving discharge stream and single re-circulation pattern within the reactor vessel. The increase in N of the standard reactor vessel also generates strong radial flow field and double re-circulation pattern within the reactor vessel. The low pressure region behind the impeller blades and uniform distribution of high pressure in the remaining portions of the reactor vessel was found to cause the development of double re-circulation pattern. The distinct low pressure region generated below the impeller of large $\frac{d}{D}$ and low $\frac{h}{D}$ deflect the discharge stream towards the bottom surface of the reactor vessel resulting in the formation of single loop down-pumping pattern. Similarly, the distinct low pressure region produced above the impeller of high $\frac{h}{D}$ deflects the discharge stream upwards towards the top surface of the reactor vessel leading to the formation of single loop up-pumping pattern. Hence, the distribution of pressure around the impeller controls the flow pattern developed within the reactor vessel.

The double loop pattern develops radial discharge stream around the impeller while the single loop pattern provides axial discharge stream which move either towards the bottom or top surfaces of the reactor vessel. The trailing vortices and turbulence field were found to follow the trajectory of the discharge stream emerging from the impeller. The downward or upward movement of trailing vortices associated with low $\frac{h}{D}$, large $\frac{d}{D}$ and high $\frac{h}{D}$ reduces the radial extent of trailing vortices which decreases the intensity of flow separation region behind the impeller blades. The weak flow separation region increases the pressure on the suction side of the blades and decrease the pressure difference between the suction and pressure side of the blades. The small pressure difference between the suction and pressure side of the blades

decrease the impeller form drag and torque of low $\frac{h}{D}$, large $\frac{d}{D}$ and high $\frac{h}{D}$ respectively. On the other hand, the medium $\frac{h}{D}$ and the standard reactor vessel agitated at high N develop large trailing vortices and strong flow separation region behind the impeller blades. The strong flow separation region decrease the pressure on the suction side of the blades which increases the pressure difference between the suction and pressure side of the blades. The high pressure difference between the suction and pressure side of the blades increases the impeller form drag and torque of the corresponding reactor vessel configurations. The increase or decrease of the impeller torque results in corresponding increase or decrease in the magnitude of N_{pt}. The increase in N_{bl} from standard conditions decrease the length of trailing vortices while the cumulative strength of flow separation region increases the impeller form drag and N_{pt} of the vessels. The reactor vessel with ten baffles provides large trailing vortices which increase the intensity of flow separation region behind the blades while the unbaffled reactor vessel develops small trailing vortices which decrease the intensity of flow separation region behind the impeller blades. The strong flow separation region increase the impeller form drag and N_{pt} and vice versa. Thus, the distribution of trailing vortices surrounding the impeller controls the N_{pt} associated with the reactor vessels.

The double loop pattern associated with the reactor vessels provide significant vortex and turbulence activity in the entire domain of the vessel resulting in the development of bulk mixing conditions in the reactor vessel. The single loop down-pumping and up-pumping patterns generate superior vortex and turbulence activity near the bottom and top surfaces of the reactor vessel leading to the development of localized mixing conditions near the bottom and top surfaces of the reactor vessel respectively. The variations in $\frac{h}{D}$, $\frac{d}{D}$ and N of the reactor vessel illustrated a positive correlation between N_{pt}, N_q and mixing performance of the reactor vessel while a negative correlation was found for reactor vessels with various N_{bl} and N_{bf} respectively. The reactor vessel with four baffles and the six bladed RT impeller was found to be optimal for the mixing processes as the underlying vortex and turbulence activity are much higher than that obtained with other N_{bl} and N_{bf} respectively.

The single loop up-pumping pattern associated with high $\frac{h}{D}$ develops a low pressure region near the free liquid surface. This low pressure region as well as high vortex and turbulence activity developed near the free liquid surface deforms the free liquid surface and leads to the

formation of a free surface vortex around the impeller shaft. The development of free surface vortex significantly increases the interfacial contact area between the air and water and the entrainment of air into the reactor vessel. The reactor vessel with $\frac{h}{D}$ of 2.79 provides maximum surface aeration as the free surface vortex touches the impeller surface and causes flooding of air bubbles within the reactor vessel. The increase in N and $\frac{d}{D}$ of the reactor vessel also increase the vortex and turbulence activity near the free liquid surface resulting in increase in entrainment of air into the reactor vessel. The increase in *N* of the standard reactor vessel is a suitable option for the surface aeration process as the air entrained into the reactor vessel is uniformly distributed in the entire domain due to strong bulk mixing conditions associated with the same. Thus, the oxygen transfer into the reactor vessel is caused by the development of low pressure region as well as higher vortex and turbulence activity near the free liquid surface. Hence, the mixing and oxygen transfer performance of the agitated reactors are controlled by the distribution of pressure, trailing vortex structures and turbulence in the entire domain of the reactor vessel.

5.8 References

Deshmukh, N. A., and J. B. Joshi. 2006. “Surface aerators: Power number, mass transfer coefficient, gas hold up profiles and flow patterns.” *Chem. Eng. Res. Des.,* 84 (11 A): 977–992. https://doi.org/10.1205/cherd05066.

Durve, A. P., and A. W. Patwardhan. 2012. “Numerical and experimental investigation of onset of gas entrainment phenomenon.” *Chem. Eng. Sci.,* 73: 140–150. https://doi.org/10.1016/j.ces.2012.01.030.

Montante, G., A. Brucato, K. C. Lee, and M. Yianneskis. 1999. “An experimental study of double-to-single-loop transition in stirred vessels.” *Can. J. Chem. Eng.,* 77 (4): 649–659. https://doi.org/10.1002/cjce.5450770405.

Montante, G., K. C. Lee, A. Brucato, and M. Yianneskis. 2001. “Numerical simulations of the dependency of flow pattern on impeller clearance in stirred vessels.” *Chem. Eng. Sci.,* 56 (12): 3751–3770. https://doi.org/10.1016/S0009-2509(01)00089-6.

Motamedvaziri, S., and P. M. Armenante. 2012. “Flow regimes and surface air entrainment in partially filled stirred vessels for different fill ratios.” *Chem. Eng. Sci.,* 81: 231–250. https://doi.org/10.1016/j.ces.2012.05.050.

Patil, S. S., N. A. Deshmukh, and J. B. Joshi. 2004. “Mass-transfer characteristics of surface aerators and gas-inducing impellers.” *Ind. Eng. Chem. Res.,* 43 (11): 2765–2774. https://doi.org/10.1021/ie030428h.

Rao, A. R., A. K. Patel, and B. Kumar. 2009. “Oxygen transfer in circular surface aeration tanks.” *Environ. Technol.,* 30 (7): 747–753. https://doi.org/10.1080/09593330902911705.

Zhu, Q., H. Xiao, A. Chen, S. Geng, and Q. Huang. 2019. “CFD study on double- to single-loop flow pattern transition and its influence on macro mixing efficiency in fully baffled tank stirred by a Rushton turbine.” *Chinese J. Chem. Eng.,* 27 (5): 993–1000. https://doi.org/10.1016/j.cjche.2018.10.002.

Chapter 6

Summary and Conclusions

6.1 Conclusions

The energy efficient design of the surface aeration tanks requires detailed analysis of the underlying hydrodynamic features while the present design practises doesn't account the same resulting in non-optimal design of the surface aeration tanks. This issue can be resolved by analysing the physical reasons causing variation in the oxygen transfer, power consumption and flow patterns with variation in the geometric and dynamic parameters of the vessel and selecting a configuration which provides optimal flow conditions necessary for obtaining maximum oxygen transfer at less power consumption in the reactor vessel. The CFD technique is widely used for obtaining detailed characterisation of the flow field associated with the surface aeration tanks owing to significant development in the computational facilities and the availability of results with less manpower, cost and time as compared to the experimental techniques. In the present work, physical reasons causing variation in the oxygen transfer, power consumption and flow patterns with variation in the geometric and dynamic parameters of the tank were analysed which will help in the proper design of the surface aeration tanks. The reliability and accuracy of the CFD predictions were evaluated using the systematic and scientific V&V procedures. The conclusions derived from the present thesis work are summarised in this chapter.

6.1.1 Verification and Validation of CFD model predictions

The numerical error arising due to the choice of grid resolution, grid type, numerical discretization scheme and the position of MRF boundary were minimized and the CFD model

predictions were validated with the corresponding results from the experimental studies, LES model and other complex turbulence models respectively.

1. The numerical convergence of the turbulent quantities require high resolution grid as compared to the mean flow quantities for both the grid types. The $N_{p\varepsilon}$ was found to be the critical flow parameter for evaluating the grid independence conditions, as its convergence is most difficult among the various flow field parameters considered for the analysis.

2. The GCI associated with the flow field of hybrid grid was found to be less than that obtained from the tetrahedral grid. The hybrid grid provides accurate predictions of the mean and turbulent quantities at less computational cost as compared to the tetrahedral grid. Thus, the hybrid grid outperforms the tetrahedral grid in terms of numerical convergence, accuracy of predictions and computational time.

3. Among the various numerical discretization schemes, the second order upwind scheme provides accurate predictions of the mean and turbulent flow fields which are similar to the third order schemes (QUICK, MUSCL schemes) and better than that obtained from the various lower order schemes (first order upwind, power-law schemes).

4. The D_r as well as H_r were systematically varied and the medium $\frac{D_r}{D}$ (1.51-1.94) as well as large $\frac{H_r}{D}$ (0.43 – 1.51) were found to be optimal for modeling the impeller rotation. The D_r was found to be more sensitive to the CFD predictions as compared to H_r. The optimal D_r and H_r provide accurate rate of decay of mean radial as well as tangential velocities in the discharge stream of the impeller. The proper balance between $N_{pt} - imp$ and $N_{pt} - baff$ was derived as the general criterion for selecting the optimal extents of the MRF boundary. This criterion is based on the principle of conservation of angular momentum and thus can be implemented for any configuration of the impeller in the reactor vessels.

5. The predictions of N_{pt}, $N_{p\varepsilon}$ and the local profiles of $\frac{u_r}{u_{tip}}$ and $\frac{k}{u_{tip}^2}$ from the present CFD model were close to the experimental results and better than that obtained from the other turbulence models in the literature. Moreover, the energy imbalance obtained from the present CFD model was least in comparison with the energy imbalance provided by the other turbulence models in the literature. Thus, the proper verification of various sources of numerical error provides superior predictions from the RANS approach with the standard

$k-\varepsilon$ model closure and hence considered for further flow field analysis in the present research work.

6.1.2 Physical reasons causing variations in the oxygen transfer, power consumption and flow patterns in the surface aeration tanks

1. The low pressure behind the impeller blades and uniform distribution of high pressure in the entire domain of the medium $\frac{h}{D}$ (0.65-2.26) provides radial flow field around the impeller and double loop pattern within the reactor vessels. The double loop pattern was also obtained with continuous increase in N of the impeller maintained at standard clearance condition. On the other hand, the low $\frac{h}{D}$ ($\frac{h}{D}$<0.65) and large $\frac{d}{D}$ ($\frac{d}{D}$>2.90) generate a low pressure region below the impeller which deflects the discharge stream towards the bottom surface of the vessel leading to the formation of single loop down-pumping pattern. Also, the high $\frac{h}{D}$ ($\frac{h}{D}$>2.26) produces a low pressure region above the impeller which deflects the discharge stream towards the free liquid surface resulting in the development of single loop up-pumping pattern. Thus, the pressure distribution surrounding the impeller controls the flow patterns associated with the reactor vessels.

2. The double loop pattern provides radial discharge stream behind the blades while the single loop down-pumping and up-pumping patterns generate axial discharge stream moving downwards and upwards from the impeller respectively. The trailing vortices and turbulence field were found to follow the trajectory of the discharge stream emerging from the impeller. The downward/upward movement of trailing vortices associated with the single loop patterns of low $\frac{h}{D}$, large $\frac{d}{D}$ and high $\frac{h}{D}$ reduces the radial extent of trailing vortices behind the impeller blades. The decrease in the length of trailing vortices decreases the intensity of flow separation region behind the blades which in turn increases the pressure on the suction side of the blades. The small pressure difference between the suction and pressure side of the blades decreases the impeller form drag and torque. On the other hand, the large trailing vortices related with the double loop pattern of medium $\frac{h}{D}$ and the standard reactor vessel agitated at high N develop strong flow separation region behind the blades which reduces the pressure on the suction side of the blades. The high pressure difference between the suction and pressure side of blades increases the impeller form drag and torque. The increase or decrease in the

impeller torque results in the corresponding increase or decrease in the magnitude of N_{pt}. Even though, the increase in N_{bl} from standard condition decreases the length of trailing vortices behind the blades, the cumulative strength of all flow separation regions increases the impeller form drag and N_{pt}. Moreover, increase in N_{bf} from the standard condition provides large trailing vortices which increase the intensity of flow separation region, impeller form drag and N_{pt}. On the other hand, the unbaffled reactor vessel provides small trailing vortices which reduces the intensity of flow separation region, impeller form drag and N_{pt}. Thus, the distribution of trailing vortices around the impeller controls the N_{pt} associated with the reactor vessels.

3. The double loop pattern associated with medium $\frac{h}{D}$ and the standard reactor vessel agitated at high N provides high vortex and turbulence activity in the entire domain of the vessel resulting in superior bulk mixing of the liquid contained within the reactor vessel. On the other hand, the single loop down-pumping pattern related with low $\frac{h}{D}$ and large $\frac{d}{D}$ increases the vortex and turbulence activity near the bottom surface of the vessel which helps in suspending the solid particles within the reactor vessel.

4. The single loop up-pumping pattern related with high $\frac{h}{D}$ provides a low pressure region near the free liquid surface. The low pressure region deforms the free liquid surface into a free surface vortex around the impeller shaft. The free surface vortex increases the interfacial contact area between the air and water which eventually increases the oxygen transfer into the reactor vessel. Moreover, the high vortex and turbulence activity obtained near the free liquid surface helps in continued deformation of the free liquid surface and subsequent entrainment of air into the reactor vessel. The maximum surface aeration was found to occur at $\frac{h}{D}$ of 2.79 as the free surface vortex touches the impeller surface causing flooding of air bubbles in the reactor vessel. The increase in N of the standard reactor vessel and the large $\frac{d}{D}$ develop high vortex and turbulence activity near the free liquid surface and increases the entrainment of air into the reactor vessel. The increase in N of the standard reactor vessel is a viable option for increasing the surface aeration process since the entrained air will be uniformly distributed in the entire domain of the vessel due to the superior bulk mixing conditions associated with the same. Thus, the oxygen transfer into the reactor vessel is caused by the development of low pressure region as well as high vortex and turbulence activity near the free liquid surface.

6.1.3 Optimal N_{bl} and N_{bf} for the mixing process in the surface aeration tank

The RT impeller with six blades provides high vortex and turbulence activity in the entire domain of the vessel which decreases with further increase or decrease in N_{bl} of the impeller. Moreover, the RT impeller with six blades provides superior bulk mixing at less N_{pt} which reduces with further increase or decrease in N_{bl}. Also, the vessel with four baffle walls provides high pumping action as well as high vortex and turbulence activity in the entire domain of the vessel as compared to the unbaffled reactor vessel and the reactor vessel with ten baffles respectively. Thus, the RT impeller with six blades and the reactor vessel with four baffles can be considered as optimal for the mixing operations in the surface aeration tanks.

6.2 Suggestions for the future work

In the present research work, the physical reasons causing the variation in the performance goals with the variation in the geometric and dynamic parameters of the surface aeration tank were analysed in detail. The CFD approach was adopted for modelling the flow field characteristics under various geometric and dynamic conditions of the reactor vessel. The CFD approach was properly verified and validated so as to obtain the reliable as well as accurate flow field predictions from the same. The GCI was used to determine the numerical error/uncertainty associated with the flow field variables. But the asymptotic convergence of the local flow fields at various locations in the tank was found to be difficult due to complex geometric conditions as well as turbulent flow conditions associated with the reactor vessel. Therefore, it is necessary to develop an error estimator exclusively for the agitated reactor vessels for properly quantifying the numerical error associated with the flow field variables.

The tank parameters such as $\frac{h}{D}$, $\frac{d}{D}$, N, N_{bl} and N_{bf} were considered for the present study while the effects of remaining parameters such as $\frac{H}{D}$, $\frac{B}{D}$, $\frac{l}{D}$ and $\frac{b}{D}$ on the mixing characteristics need to be investigated further. Presently, the physical reasons causing variation in the performance goals with the variation in the tank parameters are explained in terms of low pressure region developed around the impeller, characteristics of trailing vortices and the features of turbulence field developed in the entire domain of the reactor vessel. Apart from these features, the flow instabilities (macro as well as micro levels) present in the tank play a crucial

role in the underlying mixing and oxygen transfer processes which should be studied to provide detailed understanding of physical reasons behind the behaviour of the surface aeration process. The present study utilized the RANS approach for modelling the surface aeration tanks. The modelling of surface aeration tanks with LES will provide detailed as well as accurate predictions of the mean and turbulent quantities associated with the same. This will be useful for developing better design of the surface aeration tanks as well as for analysing the flow instabilities present in the tank as mentioned above. Moreover, the balance between the angular momentum flux associated with the impeller and the tank periphery can be analysed to quantify the flux properly transported to the tank periphery, dissipated in the tank periphery and lost in the tank domain during its movement. This may lead to proper inferences regarding the utilization of available energy for the development of various flow features in the surface aeration tank.

Publications

Journals:

[1] **Iyer, D. K.**, and A. K. Patel. 2022. "Physical Reasoning of Double- to Single-Loop Transition in Industrial Reactors using Computational Fluid Dynamics." *J. Appl. Fluid Mech.*, 15 (5), 1621-1634. https://doi.org/10.47176/jafm.15.05.1190. [**SCIE indexed**]

[2] **Iyer, D. K.**, and A. K. Patel. 2019. "Periodic Behaviour of Mean Velocity Fields in Rushton Turbine (RT) Driven Stirred Tank." *Int. J. Math. Eng. Manag. Sci.*, 4 (6), 1341-1351. https://dx.doi.org/10.33889/IJMEMS.2019.4.6-105 [**ESCI indexed**]

[3] **Iyer, D. K.**, and A. K. Patel. 2020. "CFD study of the effect of impeller clearance on the turbulence characteristics of the baffled stirred tank reactors." *Int. J. Eng. Sci.*, 1 (Special issue on 2nd International Conference on NHTFF-2020), 41-45.

Book Chapters:

[1] **Iyer, D. K.,** and A. K. Patel. 2022. *Lecture Notes in Civil Engineering. Chapter 50: Effect of Grid Type on the Flow Field Predictions in Baffled Circular Surface Aeration Tanks,* 713-725. Singapore: Springer Nature Singapore Pte Ltd., eBook ISBN 978-981-19-0304-5. https://doi.org/10.1007/978-981-19-0304-5_50 [**Scopus indexed**]

[2] **Iyer, D. K.,** and A. K. Patel. 2018. *Urbanization Challenges in Emerging Economies. Chapter 6: CFD Modelling of Circular Baffled Aeration Tanks,* 47-58. Virginia, USA: American Society of Civil Engineers, eBook ISBN 978-0-7844-8202-5 (PDF). https://doi.org/10.1061/9780784482025 [**Scopus indexed**]

Conferences:

[1] **Devarajan, K.**, and A. K. Patel. 2021. "Effect of Grid Type on the Flow Field Predictions in Baffled Circular Surface Aeration Tanks." In *Proc., International Virtual Conference on Innovative Trends in Hydrological and Environmental Systems (ITHES-2021)*, 145-146. Warangal, India: NIT Warangal.

[2] **Devarajan, K.**, and A. K. Patel. 2021. "Numerical Modelling of Turbulent Flows in Surface Aerators." In *Proc., 6th IAHR Europe Congress.* Warsaw, Poland: IAHR.

[3] **Devarajan, K.**, and A. K. Patel. 2020. “CFD study of the effect of impeller clearance on the turbulence characteristics of the baffled stirred tank reactors.” In *Proc., 2nd International Conference on Numerical Heat Transfer and Fluid Flow (NHTFF-2020),* O-32. Warangal, India: NIT Warangal.

[4] **Devarajan, K.**, and A. K. Patel. 2019. “Periodic Behaviour of Mean Velocity Fields in Rushton Turbine (RT) Driven Stirred Tank.” In *Proc., National Conference on Computational Modelling of Fluid Dynamics Problems (CMFDP-2019).* Warangal, India: NIT Warangal.

[5] **Devarajan, K.**, and A. K. Patel. 2017. “Modelling of Free Surface Profiles in Unbaffled Surface Aerators.” In *Proc., International Conference on Modelling of Environmental and Water Resources Systems (ICMEWRS-2017).* Kanpur, India: HBTU Kanpur.

Manuscripts under preparation:

[1] **Devarajan, K.**, and A. K. Patel. “CFD Simulation of Turbulent Flows in Stirred Tank Reactors: Issues and Challenges Related with MRF Impeller Modelling Approach.”

[2] **Devarajan, K.,** and A. K. Patel. “Flow Field Characterisation of Industrial Reactors of Various Scales using Computational Fluid Dynamics.”

Acknowledgements

I am highly indebted to my supervisor **Dr. Ajey Kumar Patel** for his guidance, valuable contributions, timely appreciation and support during the whole time of my doctoral study. He boosted the fire of research in me and motivated to apply this knowledge for carrying out this Ph.D work. His vision towards the research and valuable ideas were the precious inputs for the research work. The enlightening discussions with him have inculcated the skills of critical evaluation of research findings as well as systematic and scientific approach towards carrying out the work. His positive attitude at any adverse situations taught me the way of tackling the difficulties at any stage with happiness and enthusiasm. This opportunity has provided exceptional platform for the growth of my professional and personal life.

I would like to express my sincere gratitude to **Prof. N. V. Ramana Rao**, Director, National Institute of Technology Warangal for providing me a chance for carrying out the research work.

Immemorable appreciation and deepest gratitude are extended to the following dignitaries.

Prof. Rathish Kumar P., Head, Department of Civil Engineering, National Institute of Technology Warangal for his valuable supports.

Prof. Jayakumar K. V., **Prof. Umamahesh N. V.** and **Dr. Rajesh Khana Raju V. who are the Doctoral Scrutiny Committee members,** for their valuable suggestions, words of encouragement, valuable comments and worthy support for the successful completion of this work.

I register my wholehearted gratitude to all the faculty members in the Department of Civil Engineering for their encouragement during the work.

I owe deep sense of gratitude to all the technical and supporting staffs of Department of Civil Engineering for their kind help.

I profusely thank my fellow research scholars especially **Dr. Harshal Somnath Patil**, **Dr. Uday Dasharath Bagale** and **Dr. Nikhil M. Thoppil** for their kind help, cooperation and fruitful conversations.

It is a genuine pleasure to acknowledge the financial assistance received from **Science and Engineering Research Board (SERB), Department of Science and Technology (DST), Government of India** for this work.

I wish to dedicate this Ph.D. work to my parents for their constant encouragement.

DEVARAJAN K